# Time-resolved and Continuous Wave Spectroscopic Imaging of Biological Media

by

Mohammad AL-Rubaiee

A dissertation submitted to the Graduate Faculty in Physics in partial fulfillment of the requirements for the degree of Doctor of Philosophy,

The City University of New York

**2007**

UMI Number: 3283588





ProQuest Information and Learning Company
300 North Zeeb Road
P.O. Box 1346
Ann Arbor, MI 48106-1346

This manuscript has been read and accepted for the Graduate Faculty in Physics in satisfaction of the dissertation requirement for the degree of Doctor of Philosophy.

| | |
|---|---|
| **Date** | **Professor: R. R. Alfano**<br>**Co-Chair of Examining Committee** |
| **Date** | **Professor: S. K. Gayen**<br>**Co-Chair of Examining Committee** |
| **Date** | **Professor: Sultan Catto**<br>**Executive Officer** |

Supervisory Committee:

Prof. Joel I. Gersten (CCNY Physics)

Prof. Vladimir Petricevic (CCNY Physics)

Prof. M. Xu (Fairfield University Physics)

Dr. Howard Savage (New York Eye and Ear Infirmary)

THE CITY UNIVERSITY OF NEW YORK

# Abstract

## Time-resolved and Continuous Wave Spectroscopic Imaging of Biological Media

**by**

**Mohammad AL-Rubaiee**

**Advisors: Professor R. R. Alfano and Professor S. K. Gayen**

Time-resolved and spectroscopic imaging approaches were developed and adapted and developed to detect and localize tumors in *ex vivo* breast tissue samples and tumorlike inhomogeneities breastlike phantoms. The experimental arrangement for time-sliced optical imaging used 120 fs, 1 kHz repetition-rate, 800 nm light pulses from a Ti:sapphire laser system for sample illumination and a 80 ps resolution ultrafast gated intensified camera system for recording 2-D time-sliced images. The spectroscopic imaging arrangement used 1225-1300 nm tunable output of a Cr: forsterite laser for sample illumination, a Fourier space gate to discriminate against multiple-scattered light and a near-infrared area camera to record 2-D images.

Results of these direct time-resolved imaging measurements on thin (5 mm – 10 mm ) breast tissue specimens revealed that early-light images highlight cancerous regions of the specimens, while late arriving light accentuates the normal fibroglandular tissues. These differences are attributed to the difference in light scattering characteristics of normal and cancerous tissues. In direct spectroscopic imaging measurements, when light

was tuned closer to the 1203 nm absorption resonance of adipose tissues, a marked enhancement in contrast between the images of adipose and fibro-glandular tissues was observed. A similar wavelength-dependent difference between normal and cancerous tissues was observed. These results correlate well with pathology and nuclear magnetic resonance based analyses of the samples, and indicate the diagnostic potential of optical imaging approaches.

Detection and localization of targets in thick breast tissue specimens and phantoms was accomplished using independent component analysis (ICA) from information theory. The approach known as Optical Tomography using Independent Component Analysis (OPTICA) made use of multi-source probing of the samples, multi-detector transillumination signal acquisition, and analysis of resulting data using ICA for detection and three-dimensional localization of targets in turbid media. OPTICA was able to detect and determine the location of small scattering, absorptive, and fluorescence targets embedded in turbid media within a few millimeter in all three dimensions.

*Dedicated to my parents*

*and my bothers Haider and Laith*

# *Acknowledgements*

I am very grateful to my mentors Prof. Alfano and Prof. S.K. Gayen for their patient guidance and rigorous training. They provided me with the opportunity to work directly with them and gave me the independence to pursue this and other topics. They motivated me to reach higher level inspiring me that we can compete with the best researchers in the world. Their professional knowledge, sense, especially passions and ideas on science and technology has been the greatest help in the preparation of this thesis and wealth of knowledge for my future career.

I would like to take this opportunity to thank all the members of IUSL who have helped and supported me to mature from a beginning student to an accomplished researcher during this thesis work. I especially thank to Dr. M. Xu who guided me in the theoretical and computational work. I thank Dr. B. B. Das, Dr. W. Cai, Dr. A. Katz, Dr. J. M. Evans, Mr. Yuri Bondasky, Ms. X. Liang, and Mr. G. Tang for useful discussion and helping with experimental issues, and Dr. K. Sutkus, for all the help in the past eight years. I will like to thank the administrative staff at IUSL, Ms. Joan Brijlall, Ms. Megan Gibbs, and Ms. Lauren Gohara, for help everyday at IUSL. I would like to thank the members of committee Prof. Joel I. Gersten, Prof. Vladimir Petricevic and Dr. Howard Savage for serving in my committee and for their advice. In particular, Dr. Savage provided useful help on tissue histology and pathology. I thank Prof. Jeremy Hebden of University College London for the loan of the breast phantom used in the experiments.

I sincerely thank my friends Demetrios Kalamidas, Merlin Brito, Igor Shtau, David Matten, Selenne Wellette, Nicole Carnevale, Dermot O'Reilly, H. Rehman, M. Siddique, and others friends who were with me in the PhD program.

Financial support for this research was provided by Army Medical Research and Material Commands, New York State Science Technology and Academic Research, NASA University Research for Optical Sensing and Imaging at City College of New York, and by the National Science Foundation through an Advance Placement Fellowship (2003-2004). Finally, I thank my parents (Mom and Dad) and my brothers Haider and Laith for being there through "thick and thin".

# Time-resolved and Continuous Wave Spectroscopic Imaging of Biological Media

## Table of Contents

## Table of Tables

# Table of Figures

# Chapter 1
# Introduction

## 1.1 Introduction

In one second approximately $10^{18}$ photons are emitted from a 1 Watt laser. What happens when these photons interact with matter is a complicated process. Optical physics makes use of these photons to probe the physical and chemical process of microscopic and macroscopic world. An avenue of optical physics is optical imaging, and over the past twenty years, biomedical optical imaging has been developed as a new modality that employs non-ionizing radiation to detect and possibly diagnose tumors in human body organs, such as, breast and prostate. However, light is absorbed and multiple scattered by biological tissues that deteriorate any information for direct imaging of targets of thickness under one centimeter. Therefore, the challenge is to retrieve useful information in the form of images or wavelength fingerprint that locate and distinguished between normal and cancerous tissues.

To tackle the problem of optical imaging of thick (> 1 cm) biological tissue, various optical imaging techniques, such as, time-resolved (TR), frequency modulation (FM), and spatial continuous wave (CW) imaging have been developed. Light emerging from a thick realistic biological tissue will be multiply scattered and completely diffusive, and will lack information for direct imaging. However, multiple-scattered light carry useful image information that has to be retrieved using sophisticated numerical algorithms.

## 1.2 Thesis Statement

The aim of this thesis is to develop optical imaging methods and algorithms for detection, diagnosis, and three-dimensional localization of targets in turbid media, in general, and tumors in human breast, in particular. A time-resolved optical approach that uses ultrafast near-infrared light for probing and an ultrafast gated image intensified camera system (UGICS) for sensing of transmitted light has been developed and used to study *ex vivo* normal and cancerous human breast tissues. A spectroscopic imaging method that uses tunable near-infrared radiation to explore the diagnostic potential of optical imaging based on optical resonances in tissue constituents has been developed and used on excised breast tissue specimens. Results of optical measurements have been compared against x-ray and nuclear magnetic resonance (NMR) results for validation. A method based on the independent component analysis (ICA) of information theory has been used with multi-source-multi-detector measurements to obtain location of scattering, absorptive, and fluorescent targets in turbid media with high accuracy.

## 1.3 Background

### 1.3.1 Light propagation through turbid media

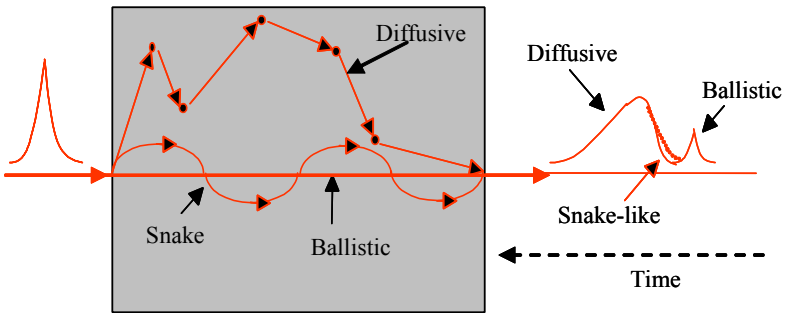


Figure 1.1 Pulse propagates through a turbid medium

When an ultrashort light pulse propagates through a turbid medium, as shown schematically in Figure 1.1, it suffers attenuation due to scattering and absorption and spread out due to scattering so that it gets much weaker and broadens into early and diffusive components. The diffusive light is attributed to multiple scattered photons that traverse long distances within the medium. It is described by the transport theory and its diffusion approximation. The early light includes ballistic component [1] and snake-like component [2]. The ballistic photons propagate in the incident direction, traverse the shortest path and arrive early. The snake-like photons undergo few scattering in the forward direction and retain significant initial properties. The ballistic component decay as $exp\ (-z/l_s)$ where z is the distance in the medium and $l_s$ is the scattering length, and is too weak to form direct image for $z>>l_t$. where $l_t$ is the transport length For very thick samples such as the human breast ($z>50l_t$), multiple scattered light dominates.

Aside for the process of light scattering that is shown in Figure 1.1, absorption and florescence process still occurs in turbid media. Figure 1.2 shows photons

interacting with simple polyatomic organic molecule, where fluorescence [3] is the emission of radiation that occurs when the molecule in an excited electronic state returns to ground state and emitting light usually $\lambda_{emission} > \lambda_{excitation}$ (where $\lambda_{emission}$ = transition wavelength from higher state to lower state, and $\lambda_{excitation}$ = transition wavelength from lower state to higher state). Absorption [4] refers to the process when photons of appropriate energy cause an atom or molecules to make a transition to an excited state.

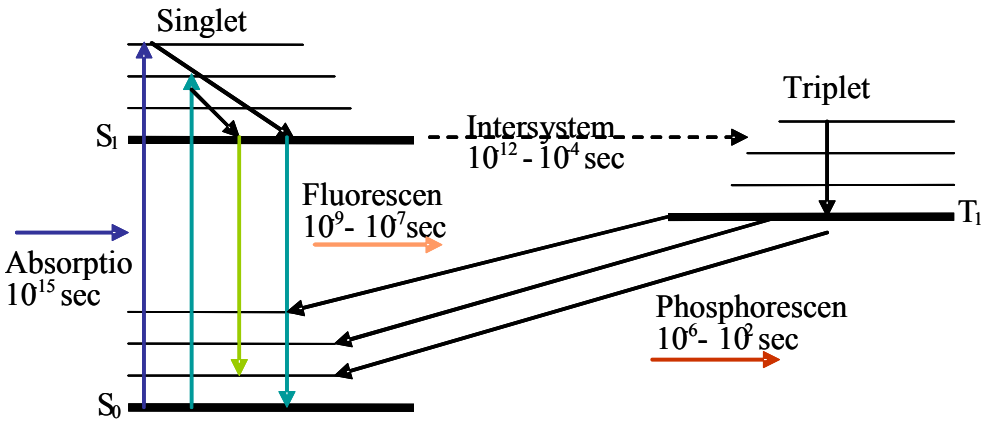


Figure 1.2 Simplified energy level diagram of a polyatomic organic molecule

In general scattering, absorption and fluorescence can be studied in two ways: steady state and time-resolved. A steady state approach uses continuous wave (CW) light to study the characteristics of absorption and florescence spectra of the materials [5]. A time-resolved method uses a pulsed light source to study the dynamical process in the material [6].

An understanding of light scattering and photon migration in biomedical and model turbid media is central to developing optical imaging (direct and indirect) methods with diagnostic potential. Key parameters to understand and quantify the behavior of light traversing through biological media are: *scattering length ($l_s$),*

*absorption length ($l_a$), transport length ($l_t$), and mean cosine of the angle of scattering (g).* The absorption length ($l_a$) is the average distance a photon travels in the medium before it is absorbed. Furthermore, the length depends on the chemical species, concentration and quantum yield of the medium [7]. The scattering length ($l_s$) is the mean distance between scattering events, which is inversely dependent on the density of particles, and scattering cross-section. The scattering cross-section depends on the shape and size of particle in comparison to the incident wavelength of light and index of refraction with respect to the surrounding medium [8]. The usual symbol for the scattering cross-section $\sigma_s$ is related to the differential scattering cross-section $\sigma_d$ $(\theta,\phi)$ giving by the equation below

$$\sigma_s = \int \sigma_d(\theta,\varphi)\sin\theta d\theta d\varphi \qquad (1.1)$$

The differential scattering cross-section $\sigma_d$ $(\theta,\phi)$ tells how light scatters in the direction of $(\theta,\phi)$ by the particle. For example, if the particle is much smaller than the incident wavelength (Rayleigh scattering) the light is scattered almost uniformly in all directions (isotropically). Rayleigh scattering [9] explained why the sky is blue, since the strong wavelength dependence of the scattering ($\sim\lambda^{-4}$) means the blue light is scattered much more strongly than the red light. Rayleigh scattering is wavelength dependent. As the wavelength decreases, scattering increases.

$$I = I_0 \frac{8\pi^4 N\alpha^2}{\lambda^4 R^2}\left(1+\cos^2\theta\right) \qquad (1.2)$$

Anisotropic scattering occurs when the particle size much larger than incident wavelength, light will scatter more in forward direction [10]. As the particle

dimension reaches the incident wavelength $\sigma_d$ $(\theta,\phi)$ depends strongly on the scattering angle $\theta$. To achieve a complete solution we refer to Lorenz-Mie theory [11], which treat electromagnetic wave scattering by spherical particle.

When light incident on a particle with an index of refraction different from the surrounding, the light refracts at an angle. The angle is function of size, shape of the particle, incident wavelength and angle of incidence. Each particle has a scattering profile or what is commonly used is phase function $p(\theta,\phi)$ [20-21, 22].

The anisotropic scattering of light by a particle can be characterized by an anisotropic factor $g$, which is the mean cosine of the scattering directions [g in (-1,1): g<0: backward scattering; g>0: forward scattering; g=0: isotropic scattering]

$$g = \langle \cos\theta \rangle = \frac{\int_{4\pi} p(\theta,\varphi)\cos\theta d\Omega}{\int_{4\pi} p(\theta,\varphi) d\Omega} \tag{1.3}$$

The properties of light scattering by random media are characterized by three key length parameters: the scattering mean free path $l_s$, the transport mean free path $l_t$, and the absorption length $l_a$. $l_s$ is the mean distance between scatterings

$$l_s = \frac{1}{n\sigma_s} \tag{1.4}$$

where $n$ is the number density of the scatterer in the medium. $l_s$ describes the average distance photons travel before deviating significantly from their original direction of propagation.

$$l_t = \frac{1}{(1-g)} \tag{1.5}$$

### 1.3.2 Diffusion Equation

Light scattering in turbid media can be described by wave theory, which starts with Maxwell's equation, or transport theory, which deals directly with the transport of power through turbid media [24-25]. Because the mathematical complexities of wave equation, transport theory has now been widely used to describe light scattering in random media.

Transport theory, also called radiative transfer theory, on the other hand, does not start with the wave equation. It deals directly with the transport of energy through a medium containing particles. The classical approach, which assumes that phases are uncorrelated on scales larger than the elastic mean free path leads to an intensity transport equation of the Boltzmann type in which any interference effects are neglected. The scalar transport equation can be expressed as [26-29].

$$\frac{\partial}{c\partial t} I(\mathbf{r},\mathbf{s},t) + s\cdot\nabla I(\mathbf{r},\mathbf{s},t) + \mu_s I(\mathbf{r},\mathbf{s},t) + \mu_a I(\mathbf{r},\mathbf{s},t) = S(\mathbf{r},t) + \mu_s \int ds' P(\mathbf{s},\mathbf{s}') I(\mathbf{r},\mathbf{s}',t) \tag{1.6}$$

where ***I(r,s,t),*** the specific intensity, is the photon distribution function; c is the light velocity inside the medium; $\mu_a$ and $\mu_s$ are the absorption and scattering coefficients, P(**s**, **s**') is the phase function, and represents the probability of scattering into a direction s' from s. We review the diffusion approximation of the transport theory for a highly scattering medium. The essential approximation underlying the diffusion approach is that after going through a large number of scattering events the phases of the scattered waves are randomized so that any interference effects in the medium can be neglected [26]. As a result, only the light intensity needs to be

considered in the description of light propagation [27]. The diffuse light intensity of a pulse is given by the following diffusion equation [28-29]

$$\frac{\partial I(\mathbf{r},t)}{\partial t} = \nabla\left(D\nabla I(\mathbf{r},t)\right) - \nu\mu_a I(\mathbf{r},t) + q^{(0)}(\mathbf{r},t) \qquad (1.7)$$

where $q^{(0)}(\mathbf{r},t) = \delta(\mathbf{r})\delta(t)$ represents the impulse incident source at t=0 and position $\mathbf{r} = 0$, $D = \frac{v}{3\mu_s(1-g)}$ is the diffusion coefficient and ν is the speed of light in the scattering medium. It should be noted that *Cai et al.*[30] has shown that the diffusion coefficient to be time dependent, and independent of absorption coefficient $\mu_a$,. For a slab sample the transmitted pulse can be described by the solution of diffusion Eq.(1.8) for the slab geometry,[29]

$$I_z(t) = \frac{1}{4d^2t}\sum_{m=1}^{\infty} m\sin\left(\frac{m\pi z}{d}\right)\exp\left[-Dt\left(\frac{m\pi}{d}\right)^2\right]\exp\left(\frac{-vt}{l_a}\right) \qquad (1.8)$$

where $d = z + 2z_0$, $z_0 = 0.71l_t$ the extrapolation length and z is the thickness of the slab. In obtaining the above solution, perfectly absorbing boundary conditions at the extrapolated surfaces are used in Eq. (1.7). The transport length and the absorption length can be calculated by numerically fitting the experimental temporal profile to Eq. (1.7) [31-32], or for the case of slab geometry Eq. (1.8).

The diffusion equation cannot describe the ballistic and snake-like parts of the scattered pulse profile [distance > 10 $l_t$ at least is needed for DA to hold (33)]. It can be an excellent approximation for large z / $l_t$ and smaller g factor. An analytic solution for the scalar transport equation has been developed by *Cai et al.* [34] that

provides a more accurate description of photon distribution in space as well as photon velocity direction.

## 1.4 Review of Current Research

Cutler [39], fist attempted optical mammography by transillumination of the female breast with a bright light source in a darkened room, revealed that multiple scattering, causes features below the surface to appear extremely blurred. Optical mammography is being developed as noninvasive imaging modality that uses the non-ionizing near infrared (NIR) light in the wavelength range of 700 nm to 1300 nm for both detecting and diagnosing breast cancer [35]. Diagnostic potential based on molecular spectroscopic signatures is the key advantage that optical mammography promises over other breast imaging modalities, such as, x-ray mammography and ultrasound in healthcare for women (2,3) [36]. Over the last decade and a half, with the advent of broadly tunable near-infrared (NIR) lasers, highly sensitive detectors, charge coupled device (CCD) cameras, amplitude modulation schemes, and image reconstruction algorithms, the field has been rejuvenated [37].

The concepts, techniques, components, and algorithms have developed sufficiently to enable design and testing of some optical mammography systems (14-20). These systems use either frequency domain or time resolved optical approaches in an attempt to obtain two-dimensional (2-D) projection images, or three-dimensional (3-D) tomographic images of the breast. While the results are promising, the ultimate goal of high spatial resolution and genuine diagnostic ability remains elusive. The time-resolved approach has higher potential to enhance resolution since time-resolved measurements provide data over a multitude of frequencies that is essential for high-resolution image reconstruction. However, the diagnostic potential that makes optical mammography more attractive than x-ray mammography and

provides the best spatial resolution compared to other modalities. Spectroscopic imaging offers that diagnostic potential, since the wavelength of light can be tuned to molecular changes in tissue constituents that are associated with cancer. The key is to identify those changes, and the wavelengths needed to interrogate the effects of those changes.

Despite attempts to improve breast transillumination by employing NIR sources and detectors, clinical trials have demonstrated that its clinical utility is severely limited [40]. In general, researchers have approached the task of improving the performance of transillumination. The goal in optical tomography is to reconstruct an interior map of optical characteristics (absorption and scattering coefficients) within the medium by using transmission data acquired on the surface of the object. The reconstruction of these parameters is a nonlinear inverse problem. The problem now is to reconstruct images of the internal distribution of the media optical properties from the measurements of light intensity at the sample boundaries. Unlike CT [37], this problem is highly nonlinear [44-46], and analytical solutions exist only for a limited number of simple geometries [47]. The reconstruction of the absorption and scattering maps is an ill-posed problem i.e. even small errors in the measured data can produce arbitrarily large errors in the reconstructed images. Thus, the image reconstruction process necessitates linearization on the assumption of a week inhomogeneity and regularization [29]. One way to regularize is to augment the original optimization problem with additional penalty function. These penalty functions can be viewed as additional measurements, which are based on the prior information (assumptions) about the wanted solution. In general, we must resort to

numerically solving the problem using either Monte Carlo simulation or any iterative approach [29,48]. and converge to the solution by minimizing the error The image reconstruction method depends on developing a Forward Model for simulating boundary measurements for a given experimental setup and known optical tissue parameters, and using it to determine the medium parameters from a given experimental setup and a given set of measurements (the Inverse problem). Various groups have developed a light transport model based on the Finite Element Method (FEM) that solves the diffusion equation numerically [49], and a preliminary approach to the inverse problem that shows great promise.

## 1.5 Breast Cancer

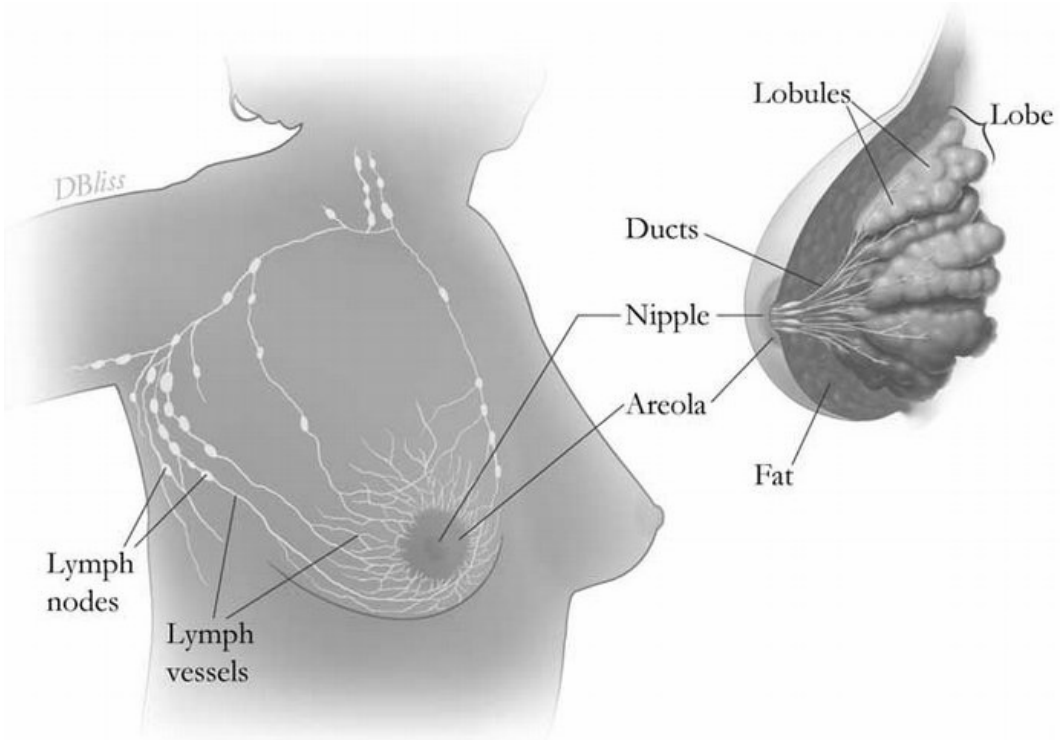


Figure 1.3 Anatomy of Female Breast (Ref. 52)

Cancer occurs when cells throughout parts of the body begin to grow out of control. Each form of cancer exhibits characteristic behavior [50]. In 2003, approximately 212,600 women in United States were found with invasive breast cancer, and about 25 (white female) to 35 (African American female) per 100,000 died from the disease in year 2002 [50-52].

The female human breast is composed of lobules, ducts, and fat, connective and lymphatic tissue, which are illustrated in Figure 1.3. The glands inside the female breast will produce and release milk. Lobules are the glands that produce milk, and the tubes that attach them to the nipple are called ducts. Lymph is a clear liquid that contains immune system cells and tissue waste products. The lymph vessels carry the fluid to small pea-sized musters of tissue called the lymph nodes.

Axillary nodes are situated under the arm, where the majority of lymph nodes are located [50-52] .Tumors in breast are separated into two types, benign and malignant. Benign breast tumors are abnormal growths that do not spread outside the female breast, and are not life threatening. Some of the lumps are not tumors at all. Fibrocystic, Cysts that are sacs filled with fluid cause these lumps and fibrosis changes, which leads to the formation of either scar tissue or connective tissue. Fibrocystic changes in the breast cause swelling, soreness lumpiness. .

The malignant tumors are life threatening, especially if not detected and treated in time. The most common breast cancers listed and defined by the American Cancer Society (ACS)[52], National Cancer Institute (NCI)[51], and Nation Institute of Health (NIH)[50] include.

•**Ductal carcinoma *in situ*** (DCIS): This is breast cancer at its earliest stage (stage 0). Here, the cancer is only restricted to the ducts and has not spread from the walls of the ducts into the fatty tissue of the female breasts. Just about all women with cancer at this stage 0 can be cured. The best way to find DCIS is with a X-ray mammogram.

•**Infiltrating (invasive) ductal carcinoma** (IDC): IDC starts in either the milk passage or duct. The cancer would then crack through the wall of the duct and attack the adipose tissue of the breast. From there, the cancer can broaden to other parts of the body. IDC is the most common type of breast cancer, and it accounts for nearly 80% of diagnosed breast cancer.

•**Infiltrating (invasive) lobular carcinoma** (ILC): This cancer starts in the milk glands (lobules). The cancer can then spread to other parts of the body. Invasive breast cancer, ILC, accounts for about 10% to 15% for diagnosed cases.

•**Lobular carcinoma *in situ*** (LCIS): A tumor that has not spread beyond the area where it developed is an *in situ* tumor. Although it is not a exact cancer, LCIS increases a woman's risk of developing cancer later in life.

The less common types of known breast cancer and diseases are the following; inflammatory breast cancer, medullary carcinoma, mucinous carcinoma, Paget's disease of the nipple, Phyllodes tumor and tubular carcinoma.

## 1.6 Motivation

The main thrust of this dissertation is to develop of near-infrared (NIR) system of light propagation in biological media and for transillumination imaging inside a turbid media i.e. breast optical mammography and tomography. While, a lot of groups have chosen their path on the techniques of using frequency domain imaging with limited result, I chose to expand time-resolved imaging, because of the limitless potential, that a femtosecond ($10^{-15}$) laser pulses translate in frequency domain into the hundred of Terahertz ($10^{12}$) which is unavailable with conventional technology. Continuous wave NIR spectroscopic imaging offers diagnostic potential over clinical x-ray imaging, and can enhance direct optical imaging. The knowledge acquired from direct imaging will used to develop indirect (tomography) imaging.

**First objective** is to show experimentally that time-resolved imaging can distinguish normal and cancerous breast tissue, and that spectroscopic continuous wave imaging can differentiate between soft tissue and tumors.

**Second objective** is to obtain position of the tumor target inside turbid media. Almost all research groups in optical mammography / tomography rely on analytical or numerical solution of the transport equation or its diffusion approximation, analytically to generate a two-dimensional 2-D image (pixels) or three-dimensional 3-D (voxals is 3-D pixel) map of scattering or absorption properties of interiors of breast from experimentally measured light intensity distributions. We will take a different approach of analyzing transillumination intensity signals. First scanning the source is grid-like fashion to gain a multi-source illumination of the desire medium, and utilizing the charge couple device (CCD) and pixels in each two-dimensional

(2-D) image as multiple-detector to gain a multi-angular view of the sample. This information can be analyzed using a power tools from information theory called independent component analysis (ICA). ICA can uncouple the background and targets from each other. The thesis demonstrates the use of ICA to obtain location of scattering, absorptive, or fluorescent targets in tissue simulating turbid media, as wells as, tumor in *ex vivo* breast tissue.

## 1.7 Thesis organization

The thesis is organized as follows.

- **Chapter 2** will present the time-gated and spectroscopic imaging techniques that we developed and this efficiency in imaging cancerous and normal *ex vivo* breast tissue specimens. The results of these optical imaging experiments are coupled with the use of clinical imaging techniques such as NMR and histopathology.
- **Chapter 3** presents the developments of optical tomography using independent components analysis (OPTICA) and its application to obtain location of scattering, absorbing and florescent targets in breastlike phantoms.
- **Chapter 4** OPYICA formulism is used detect, locate, and cross-section shape reconstruct tumors in an ex vivo breast tissue specimen.
- **Chapter 5** presents a Monte Carlo simulation analysis of measurements on *ex vivo* breast tissues to extract two key parameters, the transport length $l_t$ and the anisotropy factor (g)
- **Chapter 6** summarizes the results and outlines futures extension of this work.

## 1.8 References


1. L. Wang, P. P. Ho, C. Liu, G. Zhang, and R. R. Alfano, "Ballistic 2-D Imaging Through Scattering Walls Using an Ultrafast Optical Kerr Gate", Science **253** 769, (1991)
2. R. R. Alfano and Britton Chance, chairs/editors, "Optical Tomography, Photon Migration, and Spectroscopy of Tissue and Model Media: Theory, Human Studies, and Instrumentation", Progress in Biomedical Optics, SPIE vol. **2389** Parts 1&2, February (1995).
3. I. D. Campbell and R. A. Dwek, "Biological Spectroscopy", Benjamin/Cummins Publishing Co. Inc. California (1984).
4. A. Ishimaru, "Wave Propagation and Scattering in Random Media", Academic, New York, 1978).
5. S. Udenfriend, "Fluorescence Assay in Biology and Medicine", New York Academic, **1**, (1962), **2**, (1963).
6. B. B. Das, Feng Liu and R. R. Alfano, "Time-resolved fluorescence and photon migration studies in biomedical and model random media", Rep. Prog. Phys. **60**, 227-292, (1997)
7. R. R. Alfano, S. K. Gayen, A. Katz, "Advances in Mediphotonic Imaging and Biopsy", IS&T/OSA Optics & Imaging in the Information Age, **299** (1997).
8. Nelson A. Logan, "Survey of some early studies of the scattering of plane waves by a sphere, Selected papers on light scattering", Milton Kerker, editor, pp.3-15(1988).

9. L. Rayleigh, "On the scattering of light by small particles", Phil. Mag. **41**, 447 (1871).
10. M. I. Mishchenko, L. D. Travis, and A. A. Lacis, "Scattering, Absorption, and Emission of light by Small Particles", Cambridge University Press, UK, (2002).
11. G. Mie, "Beitzrâge zur optik truber Medien, speziell kolloidaler Metalolsungen," Ann. Phys. **25**, 377 (1908).
12. H. C. van de Hulst, "Light scattering by small particles", Dover, New York, (1981).
13. J. A. Stratton, "Electromagnetic Theory", McGraw-Hill, New York, (1941).
14. F. Bohren, D. R. Huffmann, "Absorption and scattering of light by small particles", Wiley-Innterscience, New York, (1983).
15. S. A. Prahl. "Light Transport in Tissue". PhD thesis, University of Texas at Austin, (1988).
16. S. A. Prahl, M. J. C. van Gemert, and A. J. Welch, "Determining the optical properties of turbid media by using the adding-doubling method". Appl. Opt., **32**:559-568, (1993).
17. J. W. Pickering, C. J. M. Moes, H. J. C. M. Sterenborg, S. A. Prahl, and M. J. C. van Gemert. "Two integrating spheres with an intervening scattering sample", J. Opt. Soc. Am. A, **9**:621-631, (1992).

18. W. F. Cheong, S. A. Prahl, and A. J. Welch. "A review of the optical properties of biological tissues", IEEE J. Quantum Electron., **26**:2166-2185, (1990).
19. M. Kerker, "The scattering of light and other electromagnetic radiation", Academic, New York, (1969).
20. S. Chandrasekhar, "Radiative Transfer", Clarendon, Oxford, (1950).
21. A. Ishimaru, "Diffusion of light in turbid material", Appl. Opt. **28**, 2210 (1989).
22. S. L. Jacques, C. A. Alter, S. A. Prahl, "Angular dependence of HeNe laser light scattering by human dermis," Lasers Life Sci.,**1**, 309-333 (1987).
23. L. G. Henyey, J. L. Greenstein, "Diffuse radiation in the galaxy", Astrophysical Journal, **93**, 70 (1941).
24. M. Lax, V. Narayanamurti, and R. C. Fulton, "Classical diffusive photon transport in a slab", in Proc. Symp. on Laser Optics and Condensed Matter, Leningrad, June 1987, edited by J. L. Birman and H. Z. Cummins (Plenum, New York).
25. W. Cai, M. Lax, and R. R. Alfano, "Analytical solution of the polarized photon transport equation in an infinite uniform medium using cumulant expansion", Phys. Rev. E **61**, 3871 (2000).
26. J. Crank, "The mathematics of diffusion", Clarendon Press, Oxford, (1956)

27. M. Xu, W. Cai, M. Lax, and R. R. Alfano, "A photon transport forward model for imaging in turbid media," Opt. Lett. **26**, 1066-1068 (2001).
28. B. B. Das, "Time-resolved light scattering and fluorescence spectroscopy in biomedical and model random media", PhD thesis, City University of New York (1993).
29. M. Xu, "Optical image reconstruction in highly scattering media", PhD thesis, City University of New York (2001).
30. W. Cai, M. Xu, M. Lax, and R. R. Alfano, "Diffusion coefficient depends on time, not on absorption", Opt. Lett. **27**, 731 (2002).
31. R. Garg, R. K. Prud'homme, A. Aksay, F. Liu, and R. R. Alfano, "Optical transmission in highly concentrated dispersions", J. Opt. Soc. Am. A **15**, 932 (1998).
32. R. Garg, R. K. Prud'homme, A. Aksay, F. Liu, and R. R. Alfano, "Absorption length for photon propagation in highly dense colloidal dispersions", J. Mater. Res. **13**, 3463 (1998).
33. K. M. Yoo, F. Liu, and R. R. Alfano, "When does the diffusion approximation fail to describe photon transport in random media?", Phys. Rev. Lett. **64**, 2647 (1990).
34. W. Cai, M. Xu, and R. R. Alfano, " Analytical form of the particle distribution based on the cumulant solution of the elastic Boltzmann transport equation" Phys. Rev. E **71**, 041202 (2005).
35. R. R. Alfano Guest Editor, "Advances in Optical Breast Imaging," Technology in Cancer Research and Treatment **4** (2005, special issue).

36. S. K. Gayen, M. E. Zevallos, M. Alrubaiee, and R. R. Alfano, "Near-infrared laser spectroscopic imaging: a step towards diagnostic optical imaging of human tissues," Laser Life Sci. **8**, 187-198, (1999).
37. William R. Hendee and E. Russell Ritenour," Medical Imaging Physics ",Wiley-Liss; 4th edition (2002)
38. Chance, B. "Near infrared images using continuous, phase modulated and pulsed light with quantitation of blood and oxygenation". Ann. New Acad. Sci. **838**:29-45. (1997)
39. Cutler M. "Transillumination as an aid in the diagnosis of breast lesions". Surg Gynecol Obstet;**48**:721–729, (1929)
40. R. R. Alfano, S. G. Demos, S. K. Gayen "Advances in Optical Imaging of Biomedical Media", Annals of the New York Academy of Sciences **248**, 820, (1997).
41. J. C. Hebden, S. R. Arridge and D. T. Delpy, "Optical imaging in medicine I: experimental techniques," Physics in Medicine and Biology, **42**, 825-840. (1997).
42. S. R. Arridge and J. C. Hebden, "Optical imaging in medicine II: modeling and reconstruction," Physics in Medicine and Biology, **42**, 841-854. (1997).
43. S. K. Gayen and R. R. Alfano, "Emerging optical biomedical imaging techniques," Opt. Photon. News **7**, 17-22 (1996).
44. S. R. Arridge, "Optical tomography in medical imaging," Inverse Probl. **15**, R41-R93 (1999).

45. W. Cai, S. K. Gayen, M. Xu, M. Zevallos, M. Alrubaiee, M. Lax, R. R. Alfano “Optical tomographic image reconstruction from ultrafast time-sliced transmission measurements,” Appl. Opt. **38**, 4237-4246 (1999).

46. A. P. Gibson, J. C. Hebden, and S. R. Arridge, "Recent advances in diffuse optical imaging," Physics in Medicine and Biology, **50**, R1-R43. (2005).

47. Li, X.D., T. Durduran, A.G. Yodh, B. Chance and D.N. Pattanayak, “Diffraction tomography for biochemical imaging with diffuse-photon density waves”. Optics Lett. **22**:573-575. (1997)

48. Arridge, S.R., Schweiger, M., Hiraoka, M., Delpy, D.T., "A Finite Element approach to modeling photon transport in tissue", Medical Physics, **20(2)**, 299-309. (1993)

49. Schweiger, M., Arridge, S.R., Delpy, D.T., "Application of the Finite Element Method for the forward and inverse problem in optical tomography", Journal of Mathematical Imaging and Vision, **3(3)**, 263-283, (1993)

50. http://health.nih.gov/

51. http://www.nci.nih.gov/

52. http://www.cancer.org/docroot/home/index.asp

# Chapter 2

# *Ex vivo* cancerous and normal breast tissue investigated using time sliced and near-infrared spectroscopic imaging

## 2.1 Introduction

Optical mammography, imaging of the interior structure and optical properties of human breast using light, is an actively pursued area of research that derives from a need for safe, non-invasive, and affordable modality for early detection and diagnosis of breast cancer [1-20]. Diagnostic potential based on molecular spectroscopic signatures is the key advantage that optical mammography promises over other breast imaging modalities, such, as x-ray mammography and ultrasound in healthcare for women [2,3]. In 1929, Cutler made the first attempt at optical imaging of breast using white light to illuminate the breast and looked for pathology in the transmitted light [1]. The paucity of adequate light sources, poor spatial resolution of the images, and the rapid advance of x-ray mammography stymied the development of diaphanography, as the approach was then known [21]. Over the last decade and a half, with the advent of broadly tunable near-infrared (NIR) lasers, highly sensitive detectors, charge coupled device (CCD) cameras, amplitude modulation schemes, and image reconstruction algorithms, the field has been rejuvenated.

Light-based imaging techniques capitalize on the changes in the characteristics of light resulting from its interaction with the turbid medium. The photons of an incident short pulse of light that emerge after transiting through a turbid medium, such as, human breast tissues consist of ballistic, snake, and diffusive components [5,6]. The ballistic component consists of ‘unscattered’ or coherently forward scattered photons that retain

the coherence, polarization, and directionality properties of the incident beam. Ballistic photons travel the shortest path within the turbid medium, arrive early in time and can form direct 'shadow' images of a target whose optical properties, such as index of refraction, scattering coefficient, absorption coefficient, and transport length, differ from that of the intervening medium [5,6]. The diffusive component comprises photons that suffer multiple scattering events, traverse long path lengths within the medium, arrive late, and lose the coherence and polarization memory. Diffusive photons do not form a direct image, but carry useful information about the turbid medium that need to be sorted out. The snake photons undergo fewer scattering events, and are paraxially forward scattered. The snake photons arrive after the ballistic photons, retain some of the characteristics of the incident light beam, and can form direct images whose quality depends on the time window of their arrival. An earlier-arriving fraction of snake photons forms a better-resolved image than a late-arriving fraction. However, for a highly scattering and thick medium, such as full-size human breast, the ballistic and early-snake components are too weak to form a direct shadow image [5-9]. One then resorts to inverse image reconstruction approaches that make use of the scattered light intensity pattern measured around the medium boundary, knowledge of the incident beam characteristics and average optical properties of the medium, a mathematical model for description of light propagation through turbid media, and numerical algorithm for reconstruction of an interior map of the medium [9,10].

The efforts to realize the potential of optical imaging have led to the development of a variety of experimental, analytical, and numerical techniques [2-20]. A major thrust was to circumvent the deleterious effect of light scattering by biological tissues on the

contrast of direct image [2,5,6]. The realization that paucity of ballistic photons would make direct imaging of breast interior impractical led to the development of image reconstruction approaches to extract information contained in the snake and multiple scattered light [9-13]. The key optical parameters that one attempts to map in optical mammography include the scattering coefficient ($\mu_s$), reduced scattering coefficient ($\mu_s' = (1-g)\mu_s$) or the transport length ($l_t = 1/\mu_s'$), and absorption coefficient ($\mu_a$) that depend on the wavelength, $\lambda$ of light.

The concepts, techniques, components, and algorithms have developed sufficiently to enable design and testing of some optical mammography systems [14-20]. These systems use either frequency domain or time resolved optical approaches in an attempt to obtain two-dimensional (2D) projection images, or three-dimensional (3D) tomographic images of the breast. While the results are promising, the ultimate goal of high spatial resolution and genuine diagnostic ability remains elusive. The time-resolved approach has higher potential to enhance resolution since time-resolved measurements provide data over a multitude of frequencies that is essential for high-resolution image reconstruction. However, it is the diagnostic potential that makes optical mammography attractive over x-ray mammography that provides the best spatial resolution compared to other modalities. Spectroscopic imaging offers that diagnostic potential, since the wavelength of light can be tuned to molecular changes in tissue constituents that are associated with cancer. The key is to identify those changes, and the wavelengths needed to interrogate the effects of those changes.

In Chapter 2, we present results of time-resolved and spectroscopic imaging measurements on *ex vivo* normal and cancerous human breast tissues to demonstrate the

potential of these methods. We have developed a fast, time-resolved imaging approach [12, 22, 23] that makes use of the transmitted ultrashort NIR light pulses and a 80 ps resolution time gate to provide a sequence of direct 2D images. As the time gate selects out different 80 ps duration slices of the transmitted light pulse to form 2D images, we refer to this embodiment of time-resolved imaging as "time-sliced" imaging. It is an extension of the idea of time-gated imaging using early light [5, 6], whereby temporal slices (or windows) of the entire transmitted pulse are used for recording a sequence of 2D images, not just an image with the earliest arriving light. Different temporal slices correspond to different sets of photon paths within the tissue, and carry complementary sets of information.

The time-resolved approach that we use differs from that used by other groups in the use of detector and mode of data acquisition. We illuminate the sample using an expanded ultrafast beam, and use a gated imaging system to obtain time-resolved 2D transillumination images with a temporal resolution of 80 ps. Other groups use optical fiber-based delivery of ultrashort light pulses for sample illumination and multi-channel optical fiber-based signal acquisition at a number of positions over the sample surface, or, scan the source and detector fibers in tandem over the opposite sides of a compressed sample. They use fast photodiodes, photo-multiplier tubes, or streak camera to obtain temporal profiles of the diffusely transmitted light and generate images through further processing of those temporal profiles, and use of image reconstruction schemes [15,18,24].

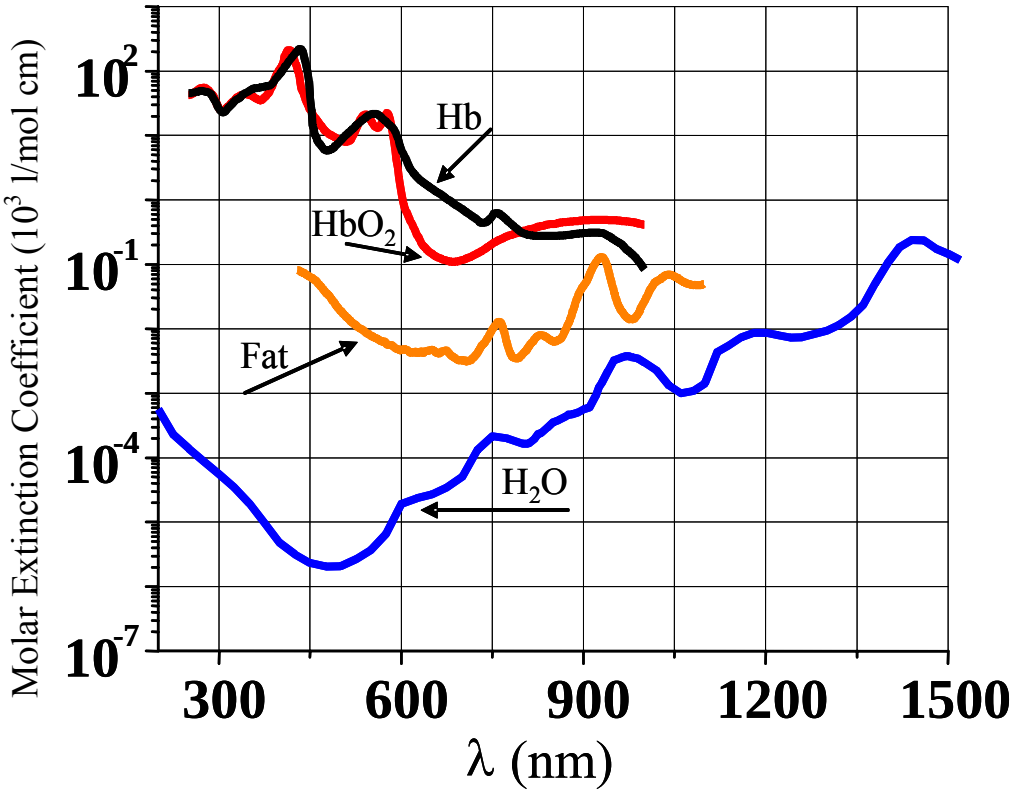


Figure 2.1: Absorption spectrum of organic species: oxy-hemoglobin ($HbO_2$) deoxy-hemoglobin (Hb), fat , and water ($H_20$) (after Reference 40)

We complement the time-sliced imaging measurements with spectroscopic imaging that uses NIR light in the wavelength range of 1225-1300 nm to explore the diagnostic potential of optical imaging approach [25, 26]. Multi-spectral imaging of breast tissues to date has focused on 2 to 4 wavelengths in 680-975 nm range [18, 20] and mainly interrogates the oxy-hemoglobin and deoxy-hemoglobin absorption, and blood volume as shown in Figure 2.1. The 1000-1350 nm spectral window has not been used much for breast tissue imaging, and can provide useful information associated with absorption by adipose tissue and water [25,26], as can be seen from the transmission spectrum of human breast tissue in Figure 2.2. The spectrum shows that although the transmittance through breast tissue drops significantly at the adipose absorption peak of 1203 nm compared to that in the 700-900 nm range, depending on the sample thickness

appropriate near-resonant wavelengths can be chosen within 1150-1275 nm range to exploit the adipose absorption while maintaining reasonable transmission.

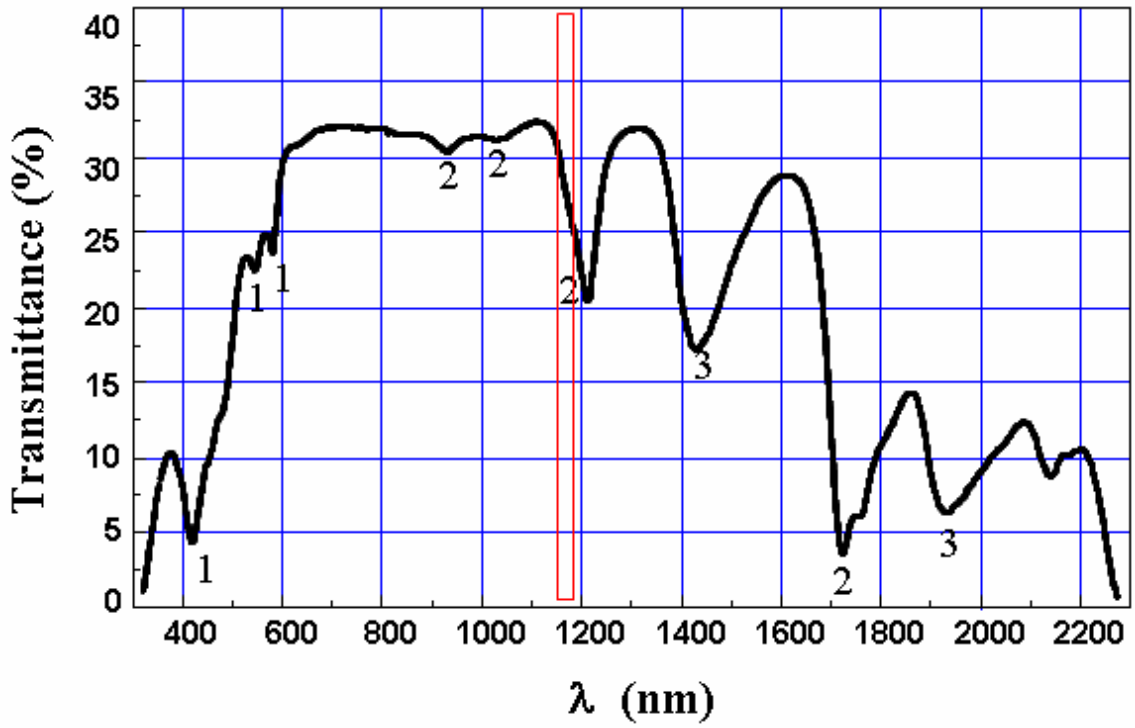


Figure 2.2: Transmission spectrum of a 3 mm thick normal breast tissue sample showing absorption resonances of oxy-hemoglobin (1), fat (2), and water (3) superimposed on the losses due to scattering (after Reference 33)

The use of *ex vivo* breast tissue specimens helps obtain useful information about light transport and optical characteristics of breast tissues that are necessary for use of the approach for *in vivo* imaging. We explore the efficacy of the 1225-1300 nm NIR window for transillumination breast imaging. *In vivo* tissues are characterized by higher blood volume than *ex vivo* samples. Since oxy-hemoglobin and deoxy-hemoglobin do not absorb light in this wavelength range, the information obtained from the study of *ex vivo* tissues in this wavelength range may better reflect the behavior of *in vivo* tissues than measurements at NIR wavelengths of 700-1000 nm that resonates with changes in light absorption by hemoglobins.

## 2.2 Materials and Methods

### 2.2.1 Excised Breast Tissue Specimens

The *ex vivo* breast tissue samples used in the study were obtained from National Disease Research Interchange (NDRI) or Memorial Sloan Kettering Cancer Center (MSKCC) under an Internal Review Board (IRB) approval at the City College of New York. The samples with tumor were obtained following surgery to remove the tumor. These samples contained both normal and cancerous tissues, and were used to test if the optical imaging experiments could distinguish between the two. Some normal breast tissue samples were obtained following reduction mammoplasty. The ages of the female patients donating the specimens varied from 27 years to 79 years.

Overall, 11 different breast tissue specimens from different patients were investigated, of which nine samples had both normal and cancerous parts, and 2 samples were normal with different types of tissues. The types of tumors included infiltrating (or invasive) ductal carcinoma (8 samples), poorly differentiated carcinoma with sarcomatoid features (1 sample), and benign tumor (1 sample). The two normal samples comprised adipose tissues, as well as ducts and lobules supported by fibrous tissues, which together will be referred to as glandular tissues. The lower end of the 1204-1300 nm NIR range used in the spectroscopic study is near resonant with the adipose absorption resonance centered at 1203 nm. The absorption of light around 1203 nm and time-dependent NIR light transmission are significantly different for adipose tissue and non-adipose tissues (lobules, blood vessels, ducts, and fibrous tissues). In a subsequent discussion of normal breast tissue, images and light transmission characteristics of adipose tissues and

glandular tissues will be compared. Both NDRI and MSKCC provided us with surgical pathology reports of the specimens. The providers removed the patient identifiers.

Each sample was received on dry ice in an insulated Styrofoam box. The samples were stored in a refrigerator, and brought to room temperature before carrying out imaging experiments. The samples were cut to 5 mm or 10 mm thick slabs, with lateral dimensions in the 15 – 30 mm range. Each sample was placed between two glass plates, and slightly compressed in an attempt to provide uniform thickness and good physical contact between adjacent pieces of tissues, and to avoid any void in the specimen.

Table 2.1: Characteristics of ex vivo breast tissue samples

| Sample Number | Age (Years) | Sample Characteristics | Dimensions |
|---|---|---|---|
| 1 | 38 | Infiltrating ductal carcinoma, and normal adipose tissue | 25 mm x 10 mm x 5 mm |
| 2 | 30 | Poorly differentiated carcinoma with sarcomatoid features, and normal tissue | 30 mm x 10 mm x 5 mm |
| 3 | 38 | Benign tumor and non-adipose tissues | 25 mm x 25 mm x 10 mm |
| 4 | 33 | Invasive (or, infiltrating) ductal carcinoma | 25 mm x 25 mm x 5 mm |
| 5 | 61 | Invasive (or, infiltrating) ductal carcinoma | 25 mm x 25 mm x 10 mm |
| 6 | 53 | Invasive (or, infiltrating) ductal carcinoma | 10 mm x 10 mm x 5 mm |
| 7 | 41 | Invasive (or, infiltrating) ductal carcinoma | 25 mm x 25 mm x 10 mm |
| 8 | 79 | Invasive (or, infiltrating) ductal carcinoma | 25 mm x 25 mm x 10 mm |
| 9 | 27 | Normal of glandular and adipose tissue | 25 mm x 10 mm x 5 mm |
| 10 | 63 | Invasive (or, infiltrating) ductal carcinoma | 20 mm diameter .x 5 mm |

Results of measurements on 9 different samples, 7 with invasive (or infiltrating) ductal carcinoma (IDC), 1 with sarcomatoid carcinoma, and one comprising benign

tumor and normal tissues are presented in detail as these are representative of the breast tissue samples investigated in the study. Characteristics of these nine samples are summarized in Table 2.1. Results of measurements on other IDC samples that included cancerous parts (summarized in Table 2.2) were similar to those observed in the two IDC samples mentioned above.

### 2.2.2 Time-gated Imaging

The experimental arrangement for time-sliced imaging, displayed schematically in Figure 2.(a), made use of light pulses form a Ti-sapphire laser and amplifier (Quantronix Titan) system.[Reference *Q. Fu et. al*. paper] The amplifier system consists of four key components: a pulse stretcher (PS), a regenerative amplifier (RGA), a multipass power amplifier (MPPA) and a pulse compressor (PC). The ultrashort light pulses to be amplified were derived from a self-mode-locked Ti:sapphire laser (Spectra-Physics Tsunami) that generated 100 fs pulses tunable over the 750–850 nm spectral range at an 82-MHz repetition rate. A (70/30) beam splitter was used to send approximately 400 mW of the oscillator output to the PS for pulses to be temporally stretched to 200 ps.

The output of PS is then sent to RGA that is pumped with 527 nm, 200 ns second-harmonic pulses of a Q-switched Nd:yttrium lithium fluoride (YLF) laser (Quantronix Model 527DP-H). The RGA is used for the first stage of amplification and stepping down the repetition rate form 82-MHz to 1-KHz. A Pockels cell pulse picker cleans any mini-pulses, resulting in an improvement in the pulse contrast ratio to $>10^3$.

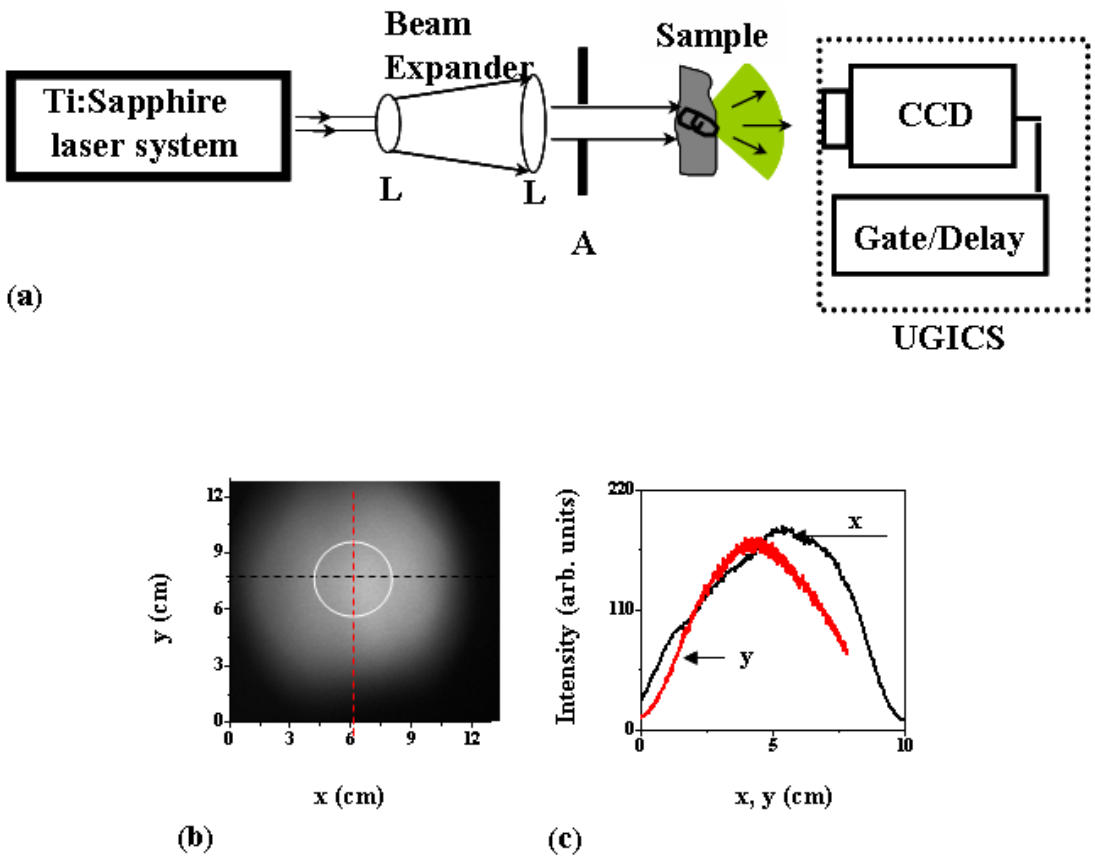


Figure 2.3: Schematic of apparatus: (a) time-sliced imaging, Key: A=aperature, L=lens, CCD=charge-coupled device, UGICS=ultrafast gated intensified camera system., (b) Photo of beam at expansion to 10 cm, (c) intensity profile in X (black) and Y (red) directions

The output pulse from the RGA is then sent to the MPPA pumped by two Nd:YLF lasers, for four pass amplification. The amplified pulse is then compressed back using the PC. The final output from the MPPA is 1-KHz repetition rate pulses of light at 800 nm with temporal width of 120 fs, and a maximum optical power of 3 W [27].

The average beam power used in the experiment was approximately 400 mW. The beam was expanded and collimated to a diameter of 10 cm. The beam image and profile are shown Figure 2.3 (b) and Figure 2.3 (c), respectively. A 3 cm-diameter central part of the beam (white circle in photograph) was selected out to illuminate the entire specimen. The expansion and selection of the central part of the beam ensured that

the light intensity is not too low at the sample margins compared to that at the center. The ratio of intensity at the margin to that at the center was approximately 0.75 along the horizontal direction, and 0.94 along the vertical direction. The average intensity of $5.3 \times 10^{-3}$ W/cm$^2$ and peak intensity of $3.4 \times 10^{7}$ W/cm$^2$ are well below the safe limits for *in vivo* human exposure [40-41].

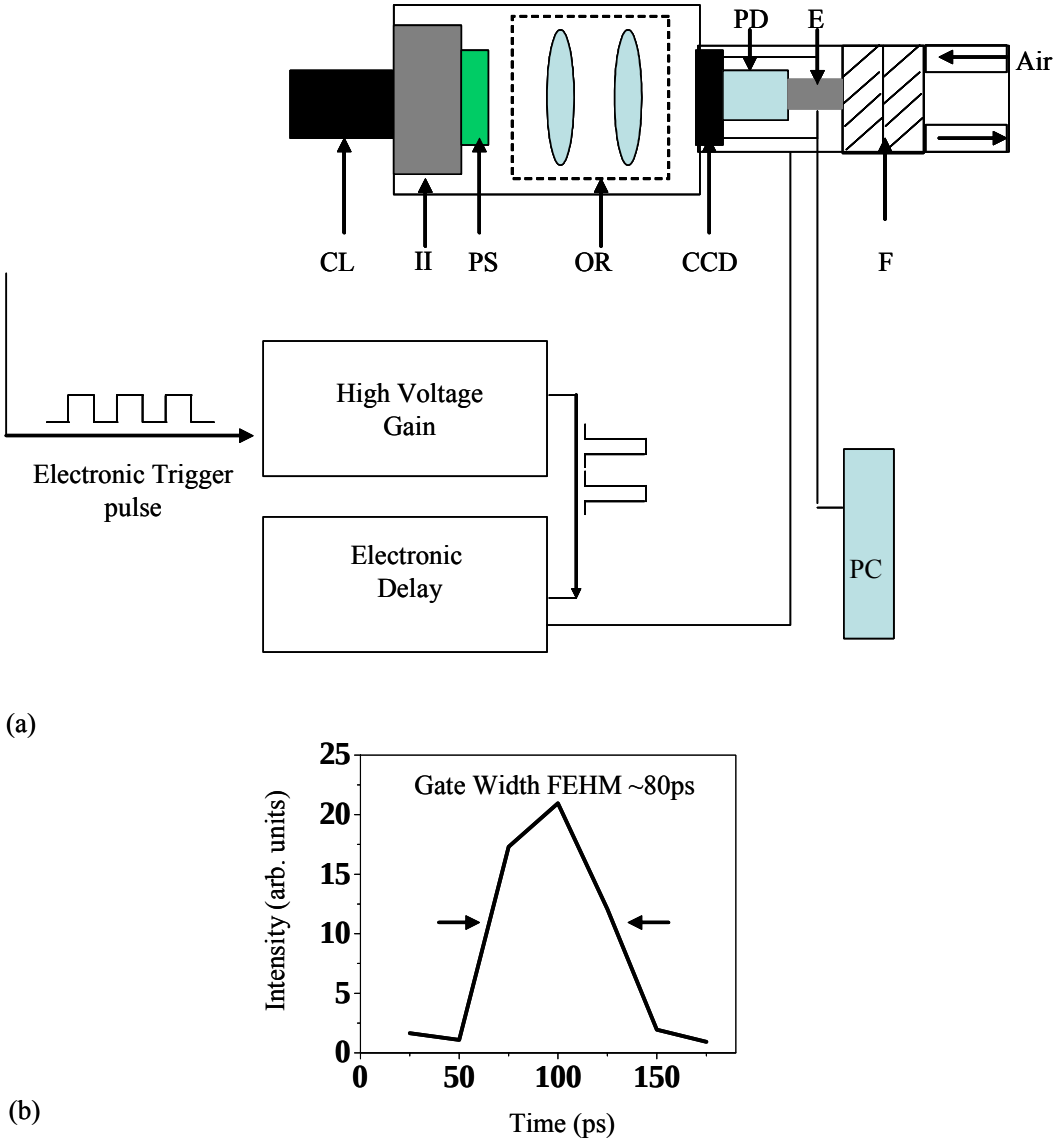


Figure 2.4: (a) Schematic of UGICS: CL= camera lens, II= image intensifier, PS= phosphor screen, OR= optical relay, CCD= charge coupled device, PD= Peltier device, E= electronics, F= fan, PC= computer (b) Temporal response of UGICS with gate with FWHM= 80 ps

The light transmitted through the sample was recorded using an ultrafast gated intensified camera system (UGICS) for recording 2D images. The UGICS, shown schematically Figure 2.4 (a), is a compact time-gated image intensifier unit that was optically coupled to a charge-coupled device (CCD) camera.

The operation for forming a time sliced 2D image starts with pre-trigger electronic (TTL + 5V) pulses (47 ns leading the optical pulse from the Pockels cell driver timer). These trigger the high voltage gain (HVG), in turn it sending out ~10 KV ($10^4$ V) electronic pulses that activate the image intensifier (II) composed of micro channel plate (MCP), that converts weak optical pulses into electron pulses. The electrons strike the phosphor screen (PS). The light emitted from the PS is optically relayed onto the CCD, and then the electronic data is sent to the computer for image developing. The UGICS provided an electronic gate pulse whose full-width-at-half-maximum (FWHM) duration could be adjusted to a minimum of 80 ps as displayed in Figure 2.4 (b).

The position of the time gate could be varied over a 20 ns range with a step size of 25 ps (or some integral multiple of it up to 2 ns). The signal recorded by the UGICS at a particular gate position $t_i$ was a two-dimensional (2D) image, that is, a 2D intensity distribution $I(x, y, t_i)$ formed by the convolution of the transmitted light pulse with the gate pulse centered on the gate position. A sequence of these 2D images for different gate positions were recorded and displayed on a personal computer, and stored for further analysis and processing.

The image acquisition and processing was carried out using WinSC 4.1 program provided by *LaVision*, the manufacturer of the UGICS system. The software was used to display the image profiles, integrate the intensity over any selected area of the recorded

image, compare the intensities of two images, or of the different areas of the same image. No further image processing was involved in the analysis of direct images [25]

### 2.2.3 Spectroscopic Imaging

The arrangement for NIR spectroscopic imaging is displayed in Figure 2.5 (a). The continuous-wave mode-locked output of a $Cr^{4+}$:forsterite laser pumped by a Coherent Antares 76-S laser operating in pulsed mode. The pump laser puts out up to 22 W of power in $TEM_{00}$ mode at 1064 nm at a repetition rate of 76.16 MHz, with each pulse being of 100 ps duration. The output of the $Cr^{4+}$:forsterite laser could be tuned from 1210 to 1325 nm using an intracavity birefringent plate. [In pulse mode operation $Cr4^{+}$:forsterite laser can produce a pulse width = 80 fs at repetition rate of 76 MHz] Appropriate neutral density filters were used to maintain the average optical power of the incident beam at approximately 35 mW for all the wavelengths used in the imaging experiment. The output wavelength was monitored with a spectrum analyzer. The beam was expanded and collimated to have a diameter of 75 mm and a 35 mm-diameter central part was selected for the imaging experiment (white circle in photograph).

Figure 2.5 (b)-(c) shows beam image and intensity profile. The ratio of intensity at the margin to that at the center was approximately 0.80 along the horizontal direction, and 0.76 along the vertical direction. The average intensity of $3.6 \times 10^{-3}$ W/cm$^2$ and peak intensity of $9.9 \times 10^{5}$ W/cm$^2$ are well below the safe limits for *in vivo* human exposure [40-41].

A Fourier space gate [28] selected out a fraction of the less scattered image-bearing photons. The Fourier space gate was realized by placing the sample at the back focal plane of a 225 mm focal-length lens and a variable-diameter aperture at the front

focal plane with the center of the aperture at the focus. A 50 mm focal-length camera lens was placed on the optical axis at a distance of 50 mm from the aperture on the opposite side of the sample. The camera lens collected and collimated the low-spatial-frequency light filtered by the aperture and directed it to the sensing element of an InGaAs NIR area cameras (Sensors Unlimited SU 128-1.7RT and SU 320 -1.7RT) placed at its front focal plane.

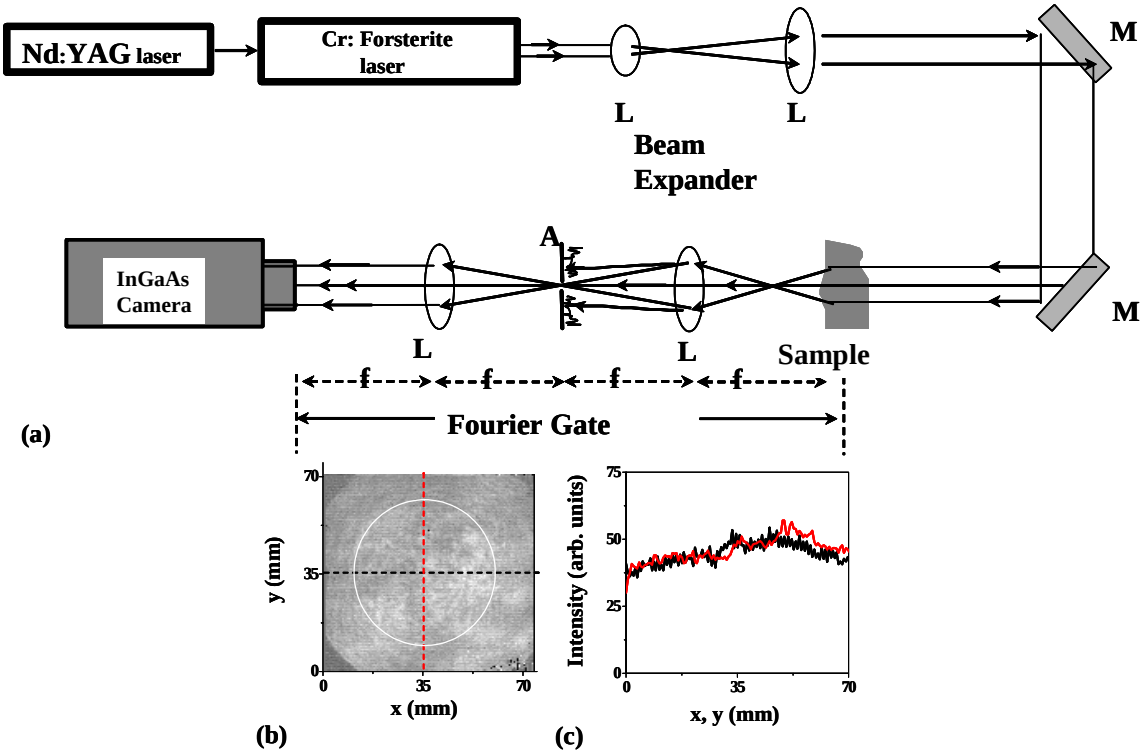


Figure 2.5: Schematic of experiment for (a) spectroscopic imaging, key: A=aperature, L=lens, M=mirror, CCD= charge coupled device, (b) photo of beam expanded to 75 mm, and (c) intensity profile in X (black) and Y (red) directions.

The SU 128-1.7RT and SU 320 -1.7RT cameras had a 128 x 128 and 320 x 240 pixel sensing element with a pixel size of 25 μm and 40 μm, respectively. The sensing area (chip) has a flat spectral response from 900 nm to 1700 nm with a quantum efficiency (electron / photons) of ~0.8. The resulting 2D images for different

wavelengths in the 1225 – 1300 nm range were recorded and displayed on a personal computer, and stored for further analysis and processing.

The image acquisition and processing used a software package (known as V for Windows) provided by CCD camera manufacturer Phototmetrics. As in the case of time-resolved images, the software was used to display the image profiles, obtain integrated intensity over any area of the image, and compare intensity distribution in images.

### 2.2.4 Validation of Optical Imaging Results

Validation of optical imaging results is an important consideration. Initial indication of the pathology of all the investigated samples was obtained from the surgical pathology report provided by the sample suppliers. Further validation schemes following optical imaging of the samples were pursued.

#### 2.2.4.1 Histopathology

Histopathological analysis is ideal for validation of measurements on *ex vivo* tissue specimens. The specimens were placed in formalin after optical measurements, and were transferred to our collaborators at the New York Eye and Ear Infirmary (NYEEI) for histological analysis. Histopathological evaluation of normal and malignant tissue samples was carried out on Hemotoxyline and Eosin (H-E) stained sections. The key features of malignancy are glandular hyperplasia with loss of glandular architecture, cellular atypia, increased mitotic figures, changes in the connective tissue matrix, tissue necrosis and increased blood vessel density. Salient feature of the normal breast tissue are glandular architecture, with adipose tissue [42].

### 2.2.4.2 Magnetic Resonance Imaging

Alternative validation scheme is needed for *in vivo* measurements. Magnetic resonance (MR) imaging carried out in coordination with the optical imaging measurements seems promising for validation of both *in vivo* and *ex vivo* measurements. While NIR optical spectroscopic imaging provides information about distribution of optical properties that depend on the distribution of chromophores in the breast, MR generates structural and contrast-enhanced images with a high resolution. Co-registration of optical and MR approaches holds the promise to enable monitoring of tumor growth, and changes in response to treatment at both structural and molecular levels [9, 29-31].

We wanted to test the correlation between NIR and MR imaging results on *ex vivo* specimens, and carried out MR measurements on two samples. The specimen was placed in a high grade Pyrex glass (suitable for both optical and NMR studies) container that slightly compressed and retained the tissue axial orientation. Following the optical imaging, the undisturbed sample cell was transported under ice in an insulated box to our collaborators at the Memorial Sloan Kettering Cancer Center and MR measurements were carried out the same day. Weighted T1 and T2 relaxation time MR images of the sample were recorded [32].

## 2.3 Results

### 2.3.1 Time-sliced imaging

*Sample 1*

Time-sliced 2D transillumination images of a 5 mm thick breast tissue sample (Sample 1 in Table 2.1) comprised of an adipose tissue in the middle, and cancerous (infiltrating ductal carcinoma) tissues in the two sides. For gate positions of 25, 75, 125, 175 and 225 ps are displayed in the left frames of Figure 2.6: The zero position was taken to be the time of arrival of a light pulse through a 5 mm thick quartz cell filled with water. The corresponding right frames present the spatial intensity profiles of the respective images integrated over the same horizontal area in all the images.

The salient feature of the images is the difference in time-dependent brightness of the normal and cancerous tissue regions in the sample. In the 25 ps image, the cancerous region is prominent at both edges. The corresponding horizontal spatial intensity profile exhibits peak in the cancerous region. At this early time, markedly more light was transmitted through the tumor than through the normal adipose tissue. With time both the normal and cancerous tissue regions in the image gained in brightness as shown in the 75-125 ps image, however the ratio of intensity at the cancerous region to that at the normal region decreased. The brightness is somewhat higher in the middle of image, where the adipose normal region compared to other sections of the tissue, but still substantially lower than cancerous region in the 75 ps image. At the sufficiently late time of 125-225 ps, the normal tissue was highlighted and very little light emerged through the cancerous region. The corresponding spatial intensity profile peaks in the normal tissue

position indicating higher light transmission through the normal region than the tumor. Similar time-dependent NIR light transmission behavior was observed in all the investigated breast tissue specimens with invasive ductal carcinoma.

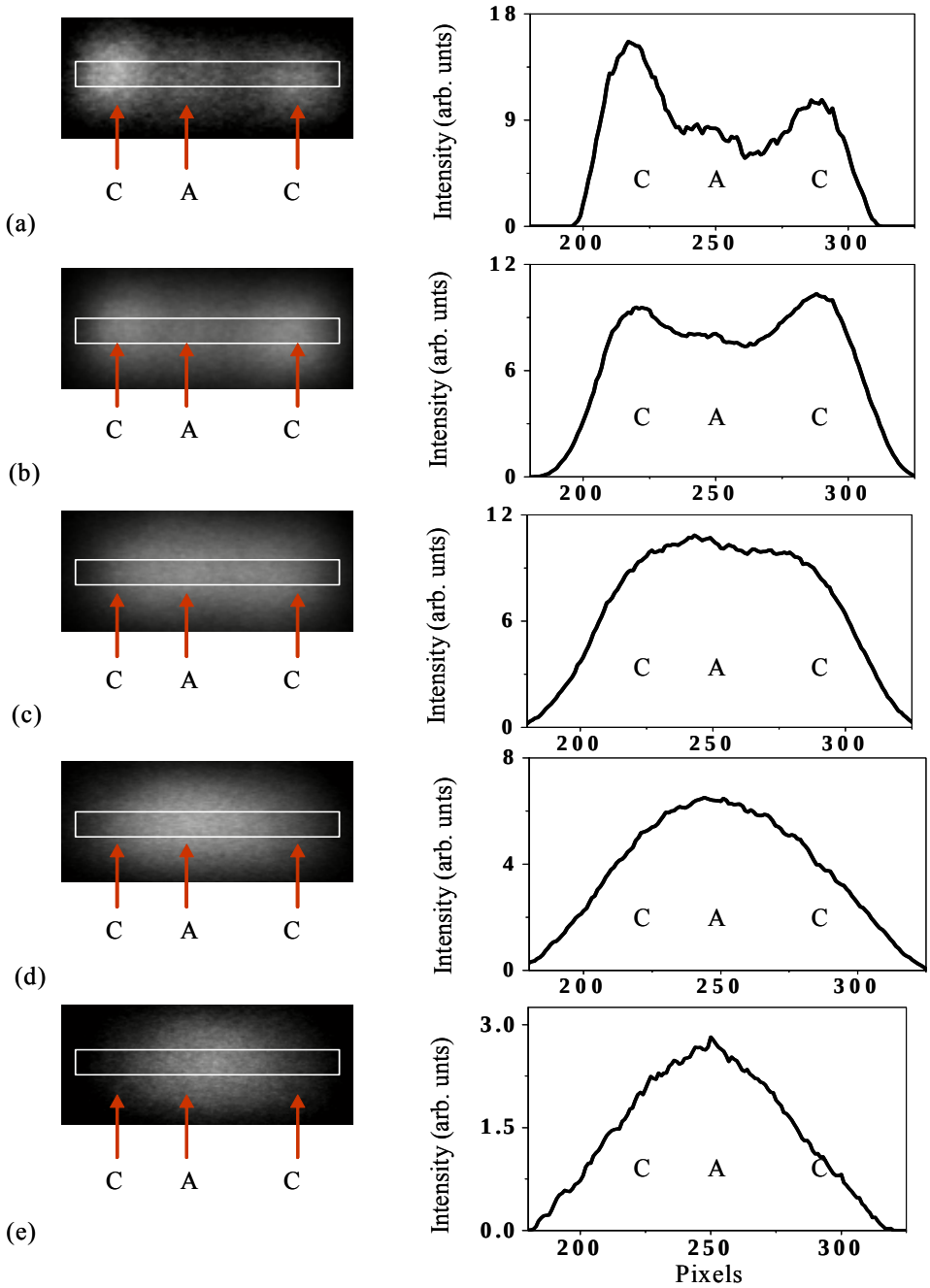


Figure 2.6: Time-sliced 2D images of breast tissue (Sample 1) for gate positions (a) 25 ps, (b) 75 ps, (c) 125 ps, (d) 175 ps, (e) 225 ps. Corresponding spatial intesity distributions integrated over the same horizontal area (white box) are shown on the right.

*Sample 2*

Figure 2.7 shows the results of investigation on a composite excised breast tissue sample (Sample #2 in Table 2.1) assembled from tissues obtained from NDRI following the modified radical mastectomy of a 30 year old patient (22). It comprised a lymph node (LN) with surrounding tissues, a piece of adipose (A) tissue, and a piece with normal (N) glandular and cancerous (C) tissue. Each of the pieces was approximately 5 mm thick, and was pressed into a 5 mm thick quartz cell to ensure uniform sample thickness and good optical contact between the adjacent pieces. According to an accompanying surgical pathology report, the cancer was a poorly differentiated carcinoma grade III with sarcomatoid features.

Figure 2.7: (a) shows a photograph of the exit face (the side that faces the camera in the experimental arrangements of Figure 2.7: (a)) of the sample wherein the locations of different types of tissues in the composite sample are tentatively labeled. Time-sliced transillumination images of the sample for gate positions of 100 ps and 350 ps are displayed in Figure 2.7 (b) and (c), respectively. The spatial intensity profiles of the images in Figure 2.7 (b) and (c) integrated over two 6 pixel wide horizontal areas around the white dashed lines are presented in Figure 2.7:(d) and (e), respectively.

The two areas were chosen such that one included the normal glandular tissue in the upper right part of the sample while the other included the cancerous tissue in the lower right part to enable close comparison. The time-sliced 100 ps image clearly highlights the lymph node, adipose, normal fibroglandular, and cancerous tissue regions. The contrast is the highest between the lymph node that appears the brightest and the adipose tissue that appears dark in the image in the 100 ps image. The spatial intensity

distributions of the 100 ps image, displayed in Figure 2.7 (d), show the highest peak in intensity values in the lymph-node region and a marked trough in the adipose tissue region indicating much higher light transmission through the lymph node and much lower transmission through the adipose tissue region at early time.

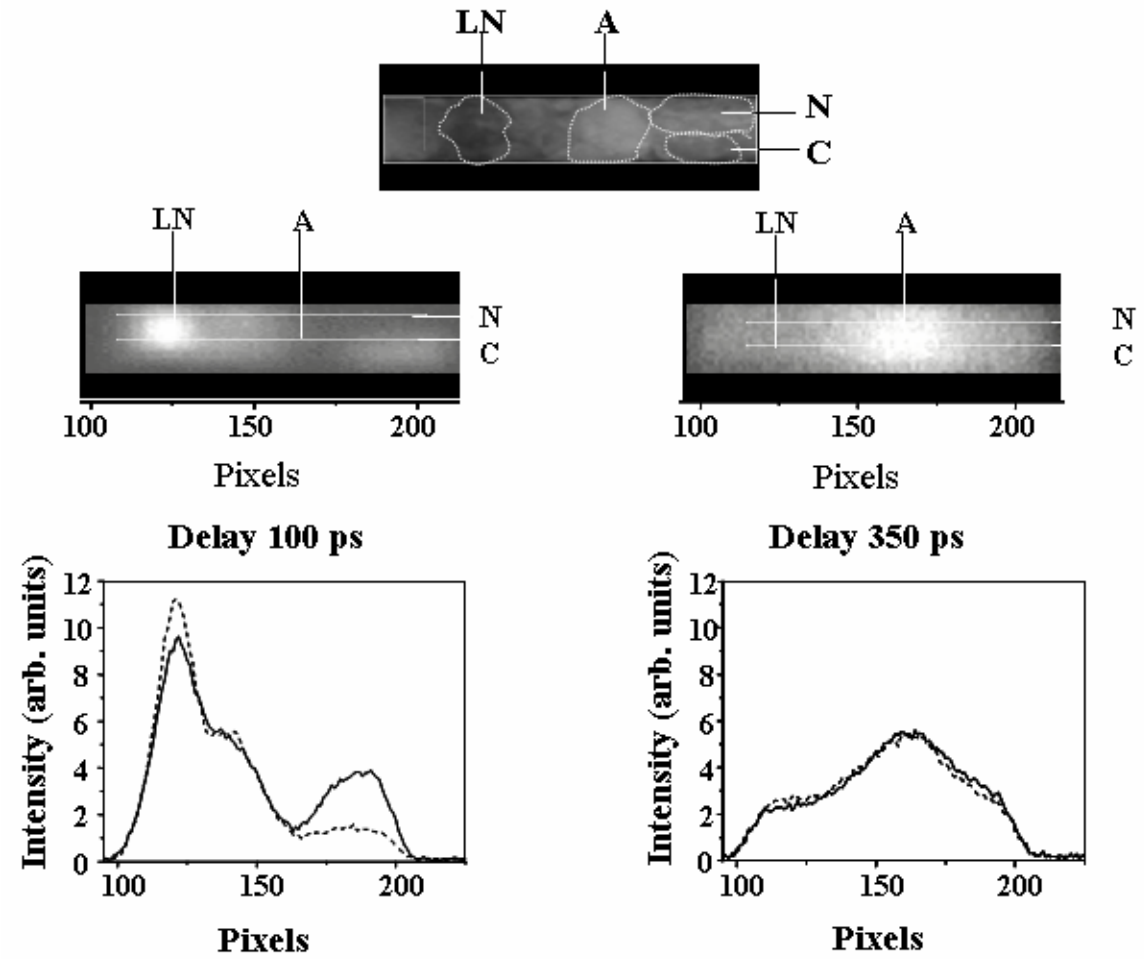


Figure 2.7: (a) exit face photo of 5 mm composite breast tissue (Sample #2). LN: lymph node A: adipose tissue, N: normal glandular tissue, C: cancerous tissue (poorly differ differentiated carcinoma with sarcomatoid features). Time sliced transillumination images of sample for gate delays of (b) 100 ps, and (c) 350 ps. Spatial profile of the integrated intensity distribution along a horizontal area of 6 pixel vertical width around the dashed white line that passes through the normal fibrous tissue (dashed line), or the cancerous tissue (solid line) for gate delays of (d) 100 ps, and (e) 350 ps.

More interesting is the contrast between the cancerous and normal tissues in the 100 ps image. As seen in the right side of the image and the spatial intensity profiles of Figure 2.7 (d), light transmission through the cancerous tissue is significantly higher than that through the normal tissue. A markedly different situation is observed in the 350 ps image of Figure 2.7 (c) and the corresponding spatial intensity profiles of Figure 2.7 (e). The adipose tissue region appears the brightest, and the spatial intensity profile peaks in the adipose tissue region indicating much higher light transmission through the adipose tissue compared to transmission through other tissues in the sample at this later time.

What is even more noteworthy, the difference in light transmission through the normal and cancerous regions that appeared so prominent in the profiles of Figure 2.7 (d) is not appreciable at this late time. It is reflected by the close overlapping of the two profiles in the regions of the normal and cancerous tissues in the profiles of Figure 2.7 (e). At intermediate times, (not shown in figures) relative light transmission through the lymph node and cancerous tissues decreased while that through adipose and normal fibroglandular tissues increased with time. Summarizing the time-dependent transit of light, we find that the light transits fastest through the lymph node, followed by that through cancerous tissue, non-adipose normal tissue, and the adipose tissue.

*Sample 3*

Time-sliced 2D transillumination images of a 10 mm thick breast tissue sample (Sample #3 in Table 2.1) comprised of a piece of normal tissue and a benign tumor for gate positions of 25, 75, 125, 375 and 475 ps are displayed in the left frames of Figure2.8. The zero position was taken to be the time of arrival of a light pulse through a 10 mm thick quartz cell filled with water. The corresponding right frames present the spatial

intensity profiles of the respective images integrated over the same horizontal area in all the images.

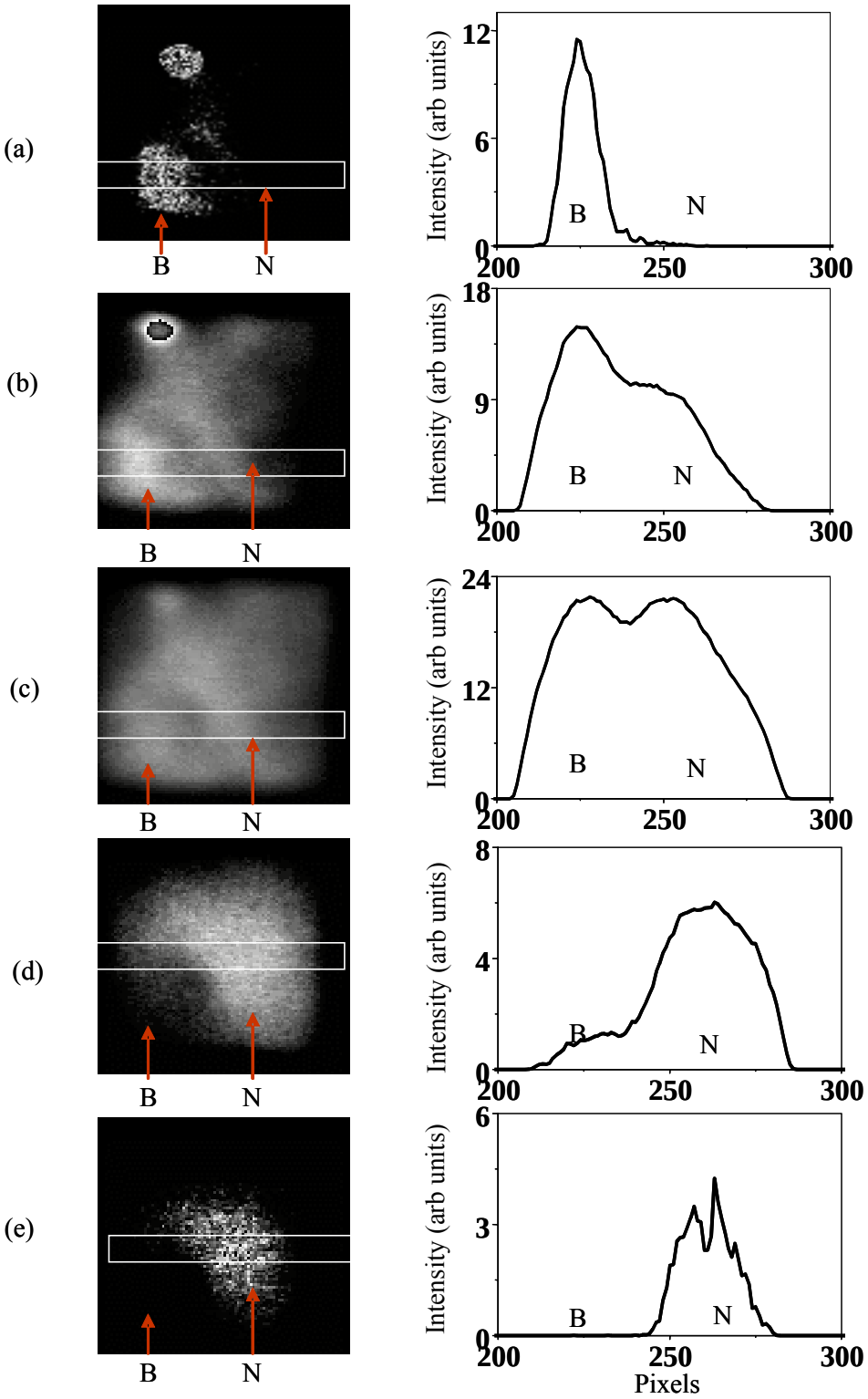


Figure 2.8: Time-sliced 2D images of breast tissue (Sample 3) for gate positions (a) 25 ps, (b) 75 ps, (c) 125 ps, (d) 375 ps, (e) 475 ps. Corresponding spatial intesity distributions integrated over the same horizontal area (white box) are shown on the right.

The salient feature of the images is the difference in time-dependent brightness of the normal and benign tumor tissue regions in the sample. In the 25 ps image, the benign tumor region is prominent in the left bottom and upper corner. The corresponding horizontal spatial intensity profile exhibits peak in the benign tumor region. At this early time, markedly more light was transmitted through the benign tumor than through the normal tissue. With time, both the normal and benign tumor regions in the image gained in brightness as shown in the 75-125 ps image, and the ratio of intensity at the benign tumor region to that at the normal region decreased. The brightness is shifting from left region of tissue to right side of the tissue, as displayed in the time series. At the sufficiently late time of 375 and 475 ps, the normal tissue was highlighted and very little light emerged through the benign tumor region. The corresponding spatial intensity profile peaks in the normal tissue position indicating higher light transmission through the normal region than the tumor.

*Sample 4*

Time-sliced 2D transillumination images of a 5 mm thick breast tissue sample (Sample #4 in Table 2.1) comprised of a piece of normal tissue and a cancerous piece with infiltrating ductal carcinoma for gate positions of 25, 75, 125, 175 and 225 ps are displayed in the left frames of Figure 2.9. Similar preparations were applied for the zero position (as were applied for previous samples). The corresponding right frames present the spatial intensity profiles of the respective images integrated over the same horizontal area in all the images.

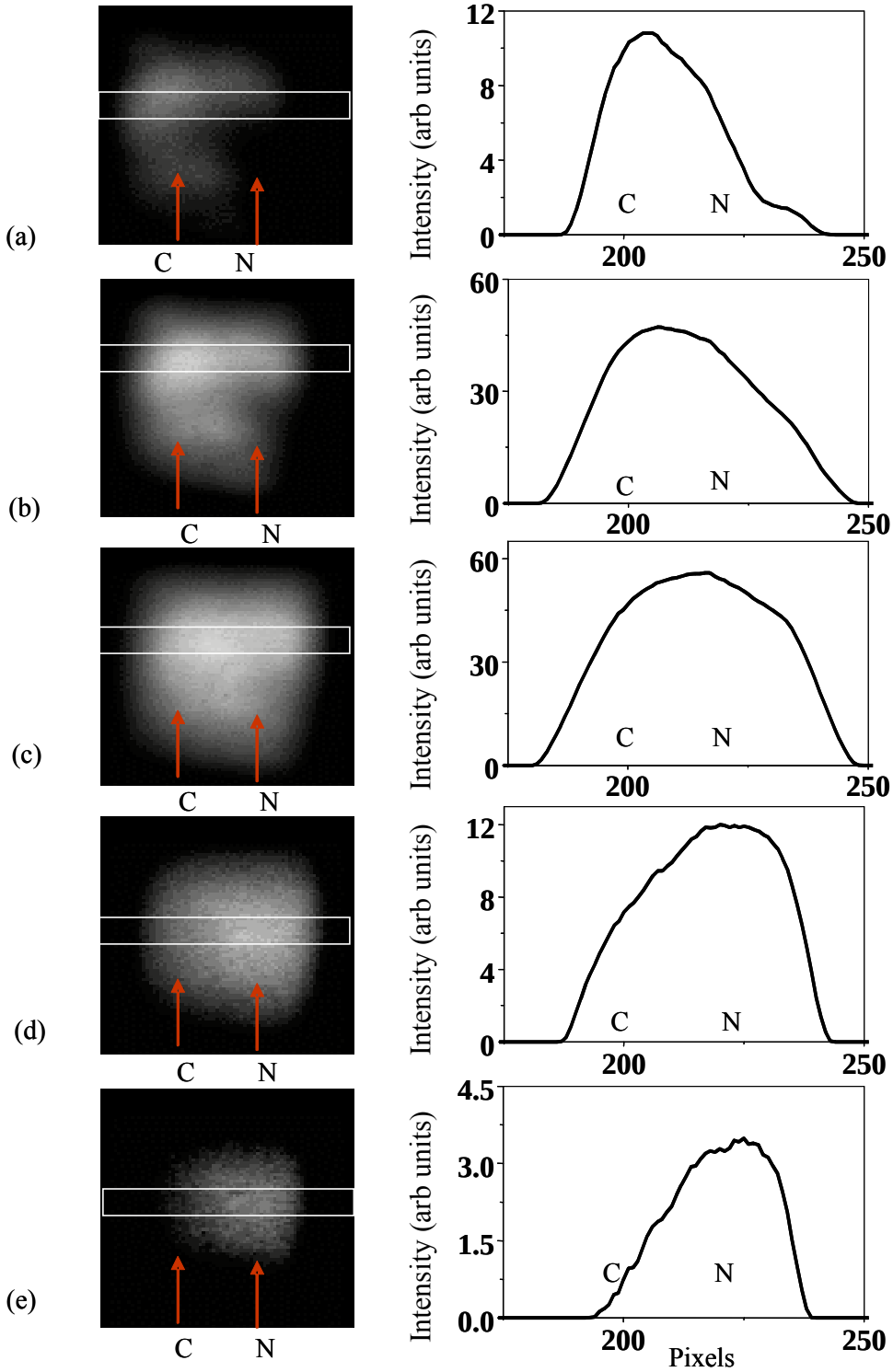


Figure 2.9: Time-sliced 2D images of breast tissue (Sample 4) for gate positions (a) 25 ps, (b) 75 ps, (c) 125 ps, (d) 175 ps, (e) 225 ps. Corresponding spatial intesity distributions integrated over the same horizontal area (white box) are shown on the right.

Once again, the salient features of the images are observed at the difference in time-dependent brightness of the normal and cancerous tissue regions in the sample. In the 25 ps image, the cancerous region is prominent at left side of the image. The corresponding horizontal spatial intensity profile exhibits peak in the cancerous region. At this early time, markedly more light was transmitted through the tumor than through the normal tissue. With time both the normal and cancerous tissue regions in the image gained in brightness as shown in the 75-125 ps image, however the ratio of intensity at the cancerous region to that at the normal region decreased. The brightness is somewhat higher in the left of the image, where the normal region compared to other sections of the tissue. At the sufficiently late time of 225 ps, the normal tissue was highlighted and very little light emerged through the cancerous region. The corresponding spatial intensity profile peaks in the normal tissue position indicating higher light transmission through the normal region than the tumor.

*Sample 5*

Time-sliced 2D transillumination images of a 10 mm thick breast tissue sample (Sample #5 in Table 2.1) comprised of a piece of normal-adipose tissue and a cancerous piece with invasive ductal carcinoma for gate positions of 25, 100, 200, 400 and 600 ps are displayed in the left frames of Figure 2.10. The corresponding right frames present the spatial intensity profiles of the respective images integrated over the same horizontal area in all the images.

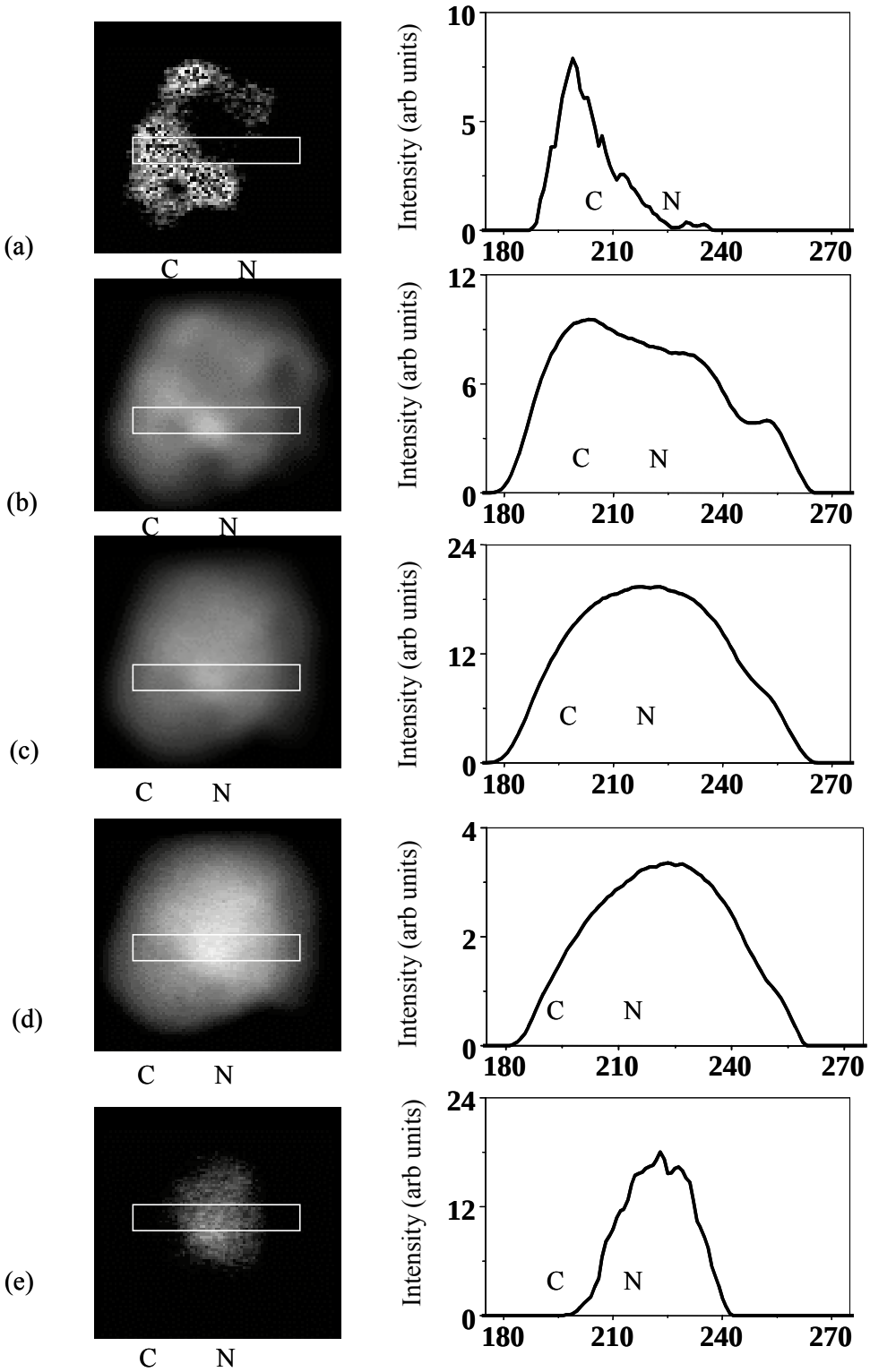


Figure 2.10: Time-sliced 2D images of breast tissue (Sample 5) for gate positions (a) 25 ps, (b) 100 ps, (c) 200 ps, (d) 400 ps, (e) 600 ps. Corresponding spatial intesity distributions integrated over the same horizontal area (white box) are shown on the right.

The key feature of the 25 ps image is that the cancerous region is prominent at left side of the image. The corresponding horizontal spatial intensity profile exhibits peak in the cancerous region. At this early time, markedly more light was transmitted through the tumor than through the normal tissue. As time progressed both the normal and cancerous tissue regions in the image gained in brightness as shown in the 100 ps through 400 ps images, however the ratio of intensity at the cancerous region to that at the normal region decreased and reached a minimum at the 600 ps image. The brightness is somewhat higher in the right and center of the image, where the normal-adipose region to other sections of the tissue. At the sufficiently late time of 600 ps, the normal-adipose tissue was highlighted and very little light emerged through the cancerous region. The corresponding spatial intensity profile peaks in the normal tissue position indicating higher light transmission through the normal-adipose region than the tumor.

*Sample 6*

Time-sliced 2D transillumination images of a 5 mm thick breast tissue sample (Sample #6 in Table 2.1) comprised of a piece of mostly cancerous (invasive ductal carcinoma) with small amount of normal tissue for gate positions of 25, 75, 175, 225 and 275 ps are displayed in the left frames of Figure 2.11. Similar time-dependent features are observed as described for other samples that had both normal and cancerous tissues

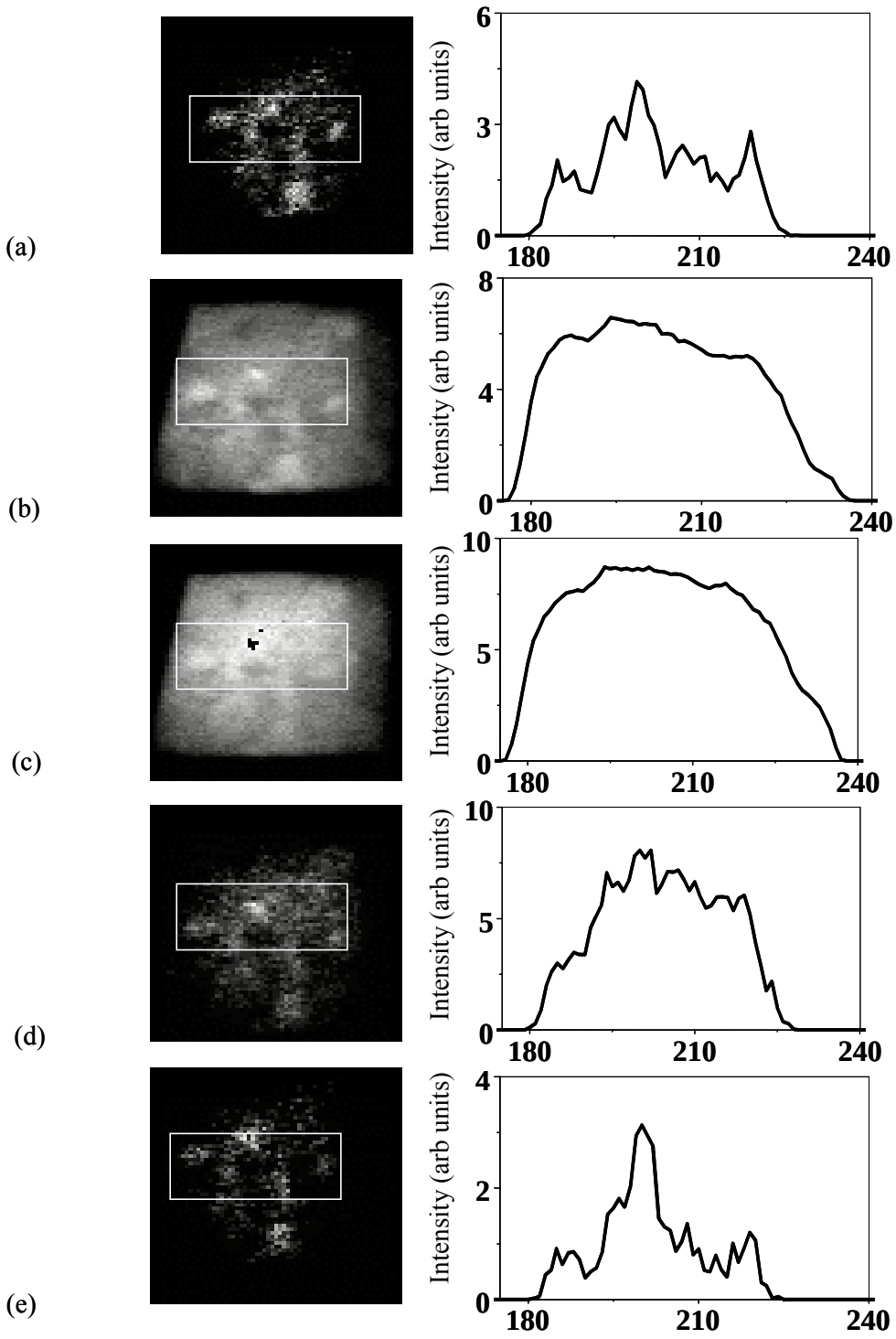


Figure 2.11: Time-sliced 2D images of breast tissue (Sample 6) for gate positions (a) 25 ps, (b) 75 ps, (c) 175 ps, (d) 225 ps, (e) 275 ps. Corresponding spatial intesity distributions integrated over the same horizontal area (white box) are shown on the right.

*Sample 8*

Time-sliced 2D transillumination images of a 10 mm thick breast tissue sample (Sample #8 in Table 2.1) comprising a piece of mostly cancerous (invasive ductal carcinoma) with small amount of normal tissue for gate positions of 25, 50, 350, and 625 ps are displayed in the left frames of Figure 2.12. Again the ratio of transmitted light intensity through the cancerous part to that through the normal part decreased with time up to 350 ps, as in other samples. However, in the 675 ps image there seemed to be an increase in ratio, which is a typical.

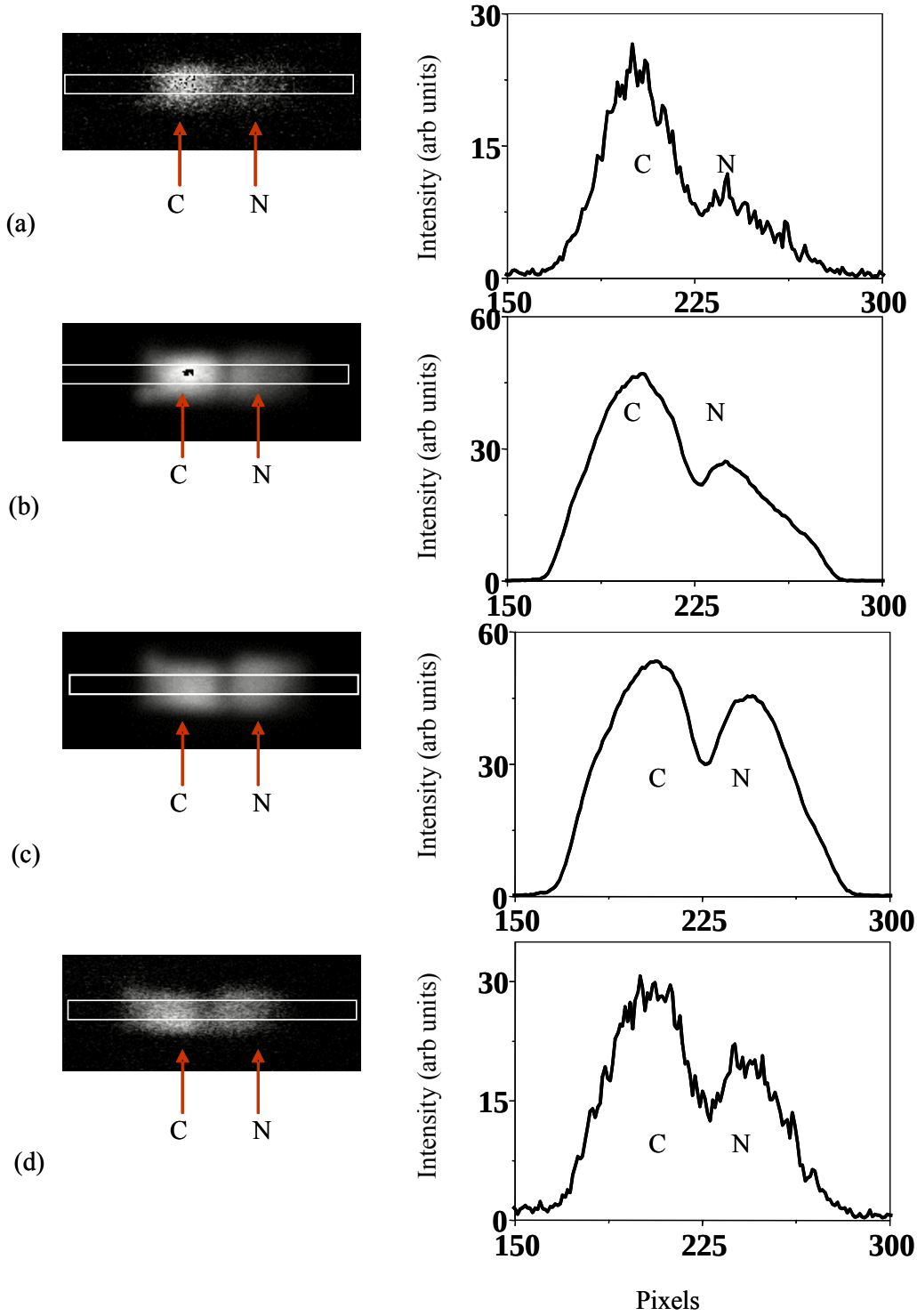


Figure 2.12: Time-sliced 2D images of breast tissue (Sample 8) for gate positions (a) 25 ps, (b) 50 ps, (c) 350 ps, (d) 625 ps. Corresponding spatial intesity distributions integrated over the same horizontal area (white box) are shown on the right.

*Sample 9*

Time-sliced 2D transillumination images of a 5 mm thick breast tissue sample (Sample #9 in Table 2.1) comprising a piece adipose tissue sandwich (side by side) between glandular tissue of normal breast tissue, for gate positions of 25, 75, 125, 175 and 225 ps are displayed in the left frames of Figure 2.13. The prominent features of the images are observed at the early times of 25-75 ps, which show higher light intensity at the glandular (left and right edge) region than adipose region (middle part). The corresponding horizontal spatial intensity profile exhibits peak in the glandular region, and dip in the adipose region. Ratio of glandular to adipose region exhibits a decline in intensity as time steps forward.

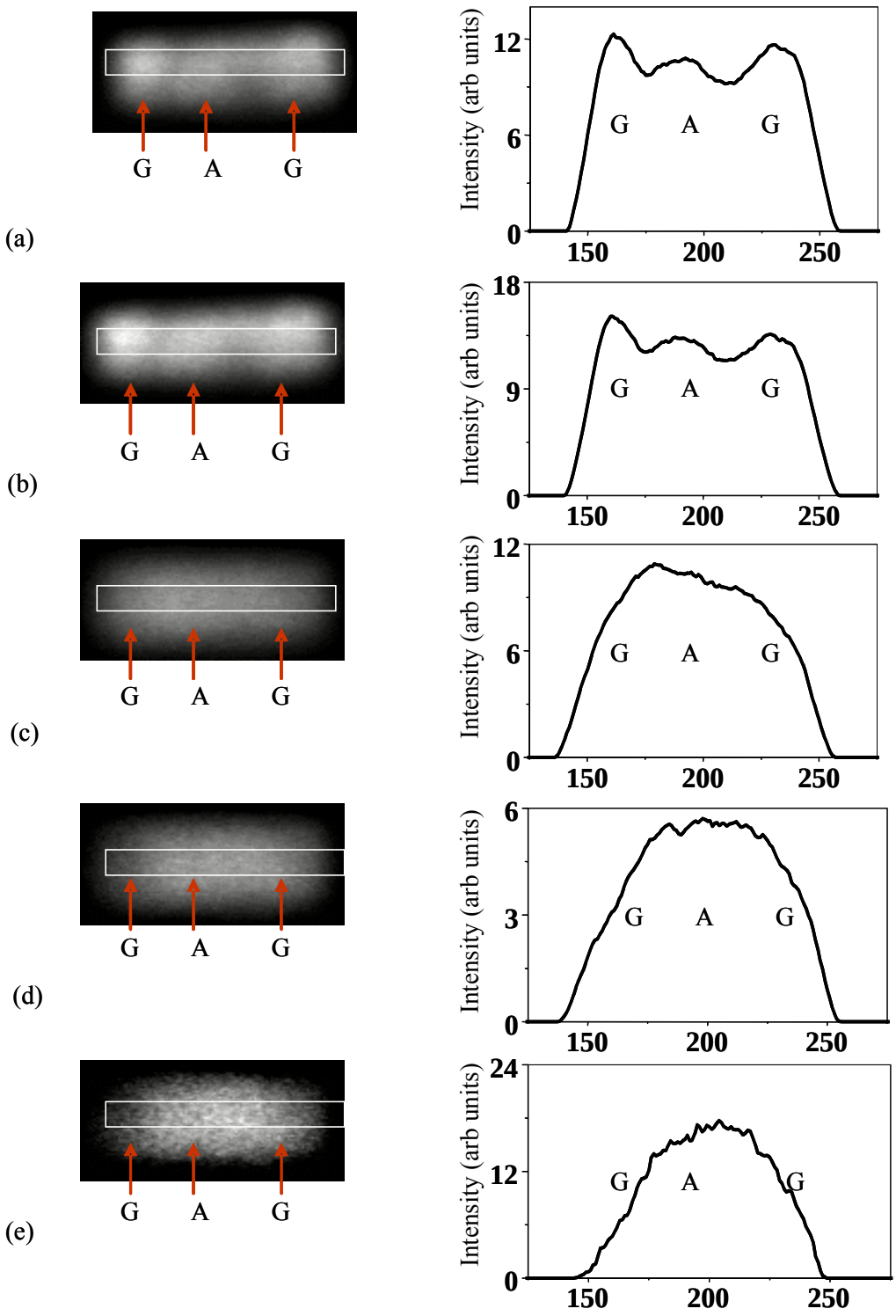


Figure 2.13 Time-sliced 2D images of breast tissue (Sample 9) for gate positions (a) 25 ps, (b) 75 ps, (c) 125 ps, (d) 175 ps, (e) 225 ps. Corresponding spatial intesity distributions integrated over the same horizontal area (white box) are shown on the right.

These results demonstrate that time-sliced imaging can highlight different types of tissues in a sample. What is even more important, it can highlight normal fibroglandular tissues from poorly differentiated carcinoma (grade III) with sarcomatoid features, and from IDC tumors. It should be noted that the difference in time-dependent light transmission characteristics between normal and cancerous regions in sample with sercomatoid features is not as pronounced as that observed in the sample with infiltrating ductal carcinoma (Sample #2) presented in Figure 2.7. This in turn indicates that light transport characteristics will vary between tissues with different types of carcinoma, as well as between normal and cancerous tissues.

In order to provide a comparison between different samples in terms of a normalized parameter, we estimated the time-dependent contrast, $C(t) = (I_c - I_n)/(I_c + I_n)$, where $I_c(t)$ and $I_n(t)$ are the intensity values in the middle of the cancerous and normal regions, respectively, of the image recorded at time t. In practice, $I_c(t)$ and $I_n(t)$ values were obtained from the average number of counts around the center positions of the cancerous and normal segments of the spatial profile (such as those shown in the right frames) of the images.

The values of contrast, $C(t)$ for different cancerous samples at an early time and a late time are presented in Table 2.2. For comparison, it should be noted that the value of $C(t)$ for Sample #1 is 0.33 at 25 ps, and -0.33 at 225 ps, which are similar to the values of contrast for other IDC samples listed in Table 2.2. The negative values of contrast emphasize the fact that at the early time $I_c(t)$ is much larger than $I_n(t)$, but can be much lower than $I_n(t)$ at the late time. While the values of C(t) show variations from sample to

sample, the early-time value is consistently higher than the late time value for all the samples.

### 2.3.2 Spectroscopic imaging

A proof-of-the-principle experiment was first carried out to test if a spectroscopic difference between tissues in a specimen would provide any distinguishable salient signatures in the transillumination image [25]. The optical absorption characteristics of adipose tissues around 1203 nm were selected as a spectral fingerprint. Marks [33] demonstrated that optical transmittance spectrum of a 3 mm thick normal human breast tissue sample, displayed in Figure , in the 1190-1330 nm range was composed of an absorption resonance by adipose tissues at 1203 nm, superimposed on a smoothly varying background caused by light scattering.

*Sample 4*

The normal human breast tissue specimen (Sample #4 in Table 2.1) used in the experiment was rotated such that the piece in the top was predominantly composed of normal (adipose) tissues, and pieces on the bottom cancerous tissues. Two-dimensional transillumination images were recorded using light in the 1204 to 1300 nm wavelength range. Some of the wavelengths used were near resonant with the adipose tissue absorption at 1203 nm, while the other wavelengths were far removed from that resonance. The left frames of Figure 2.14 present the 2D transillumination images recorded using the near-resonant wavelength of 1204 nm, the off-resonance wavelength of 1300 nm, and an intermediate wavelength of 1250 nm. Corresponding spatial intensity

profiles of the images obtained by integrating over the same vertical area outlined by the white box for all the images are shown in the right frames.

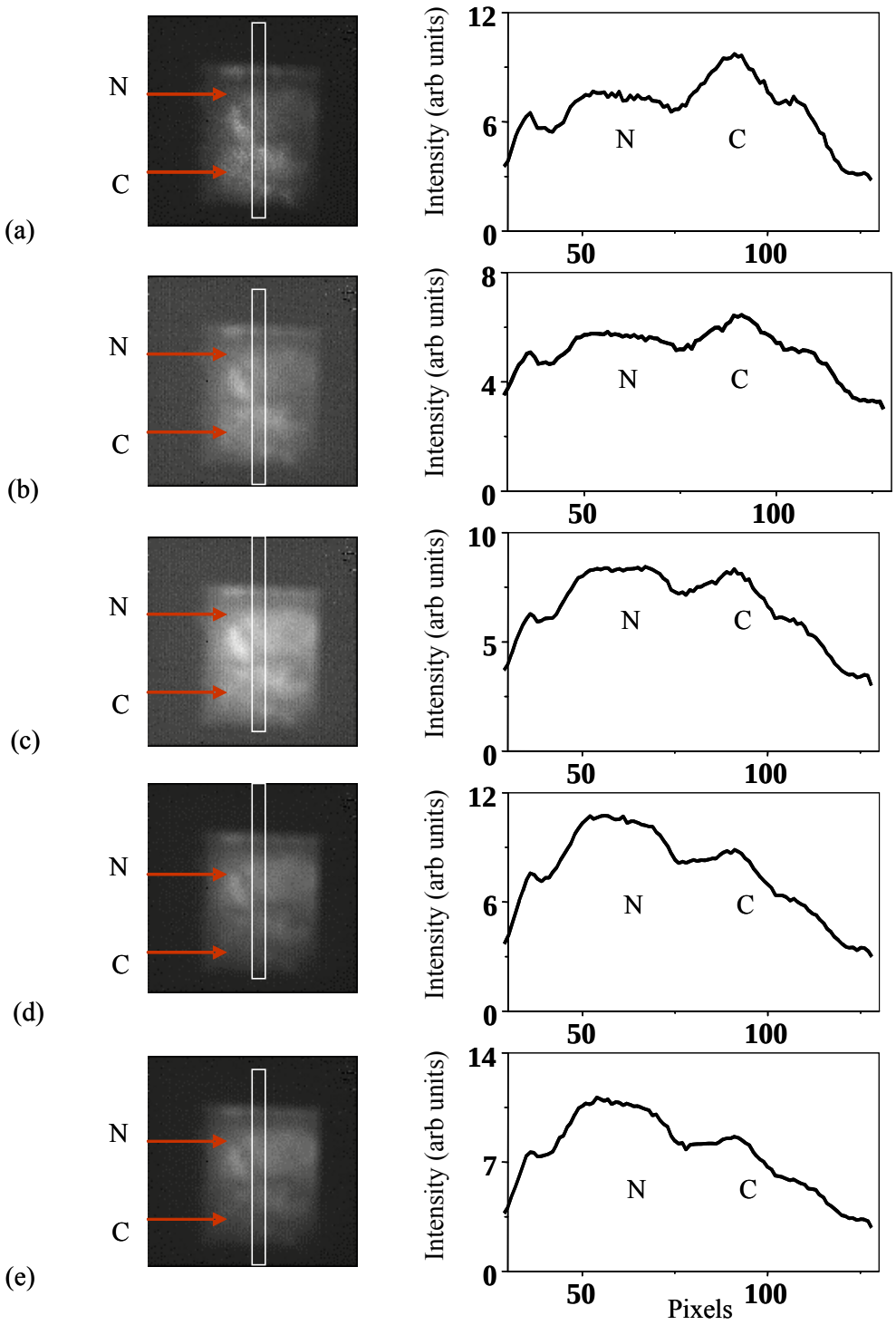


Figure 2.14: Spectroscopic 2D images of breast tissue (Sample 4) for wavelengths (a) 1204 nm, (b) 1225 nm, (c) 1250 nm, (d) 1285 nm, and (e) 1300 nm. Corresponding spatial intesity distributions integrated over the same vertical area (white box) are shown on the right.

The salient feature of the images is that the adipose tissue region appears much darker (less light transmission) than the cancerous tissue in the near-resonant 1204 nm and 1225 nm images, and appears as a trough in the resonant 1204-1225 nm profile. As the laser wavelength was tuned out of the adipose absorption resonance, the contrast between the adipose and cancerous tissue regions in the image decreased, as can be seen from the 1250-1300 nm images. At the non-resonant wavelength of 1300 nm, no appreciable distinction was observed between the adipose and the glandular regions, and the spatial profile followed the intensity distribution of the probing laser beam.

*Sample 2*

The spectroscopic imaging measurements were then extended to Sample #2, the *ex vivo* breast tissue specimen with poorly differentiated carcinoma grade III with sarcomatoid features [22]. Figure 2.15 (a) shows a photograph of the exit face of the sample that is imaged. Figure 2.15 (b) and (c) show a 'near-resonant image' recorded with 1225 nm light, and a typical 'non-resonant image' recorded with 1300 nm light, respectively. Figure 2.15 (d) and (e) display the corresponding spatial intensity profiles. The solid line in each figure shows the profile integrated over a 6 pixel wide area around the long dashed line that runs the entire length of the corresponding image and includes the cancerous tissue region in the lower right part of the image. The dashed curve superimposed on the solid curve shows the profile integrated over a 6 pixel wide normal glandular tissue area around the short dashed line in the corresponding image. The solid and the dashed curves in the right side of the profiles thus enable comparison of light transport characteristics through normal and cancerous tissues in the specimen.

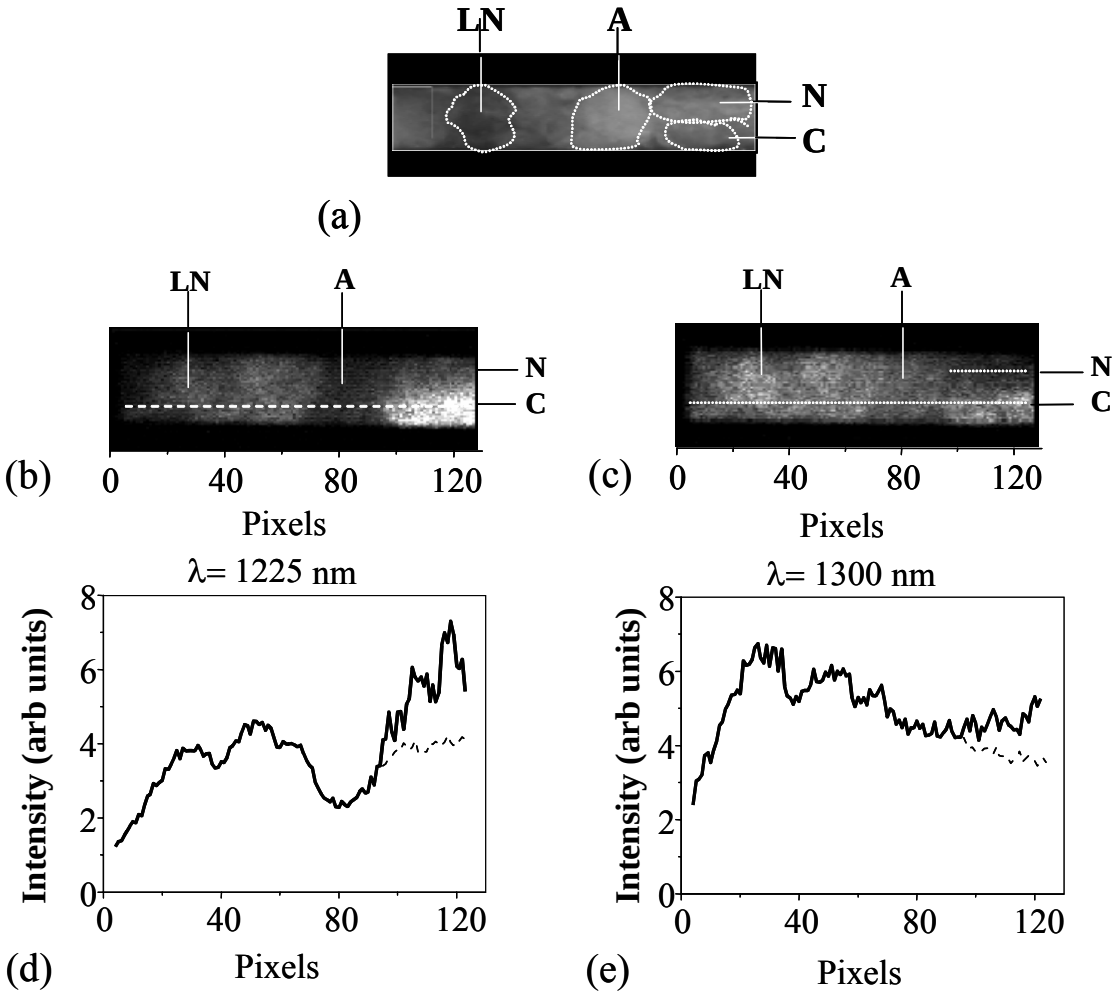


Figure 2.15: (a) Exit face photo of 5 mm thick composite breast tissue (Sample 2). LN: lymph node A: adipose tissue, N: normal glandular tissue, C: cancerous tissue (poorly differentiated carcinoma with sarcomatoid features). Spectroscopic 2D transillumination images of sample for wavelengths (b) 1225 nm and (c) 1300 nm. Spatial profile of the integrated intensity distribution along a horizontal area of 6 pixel vertical width around the dashed white line covering the entire length of the sample including the cancerous tissue region (solid line in the profiles) and that around the small dashed line denoting the normal tissue region (broken line in the profiles).

*Sample 6*

Spectroscopic imaging measurements were carried out on Sample #6, the ex vivo breast tissue specimen composed of (right) normal part next to an invasive ductal carcinoma (left) tissue. Figure 2.16 (a)-(d) show a 'near-resonant image' recorded with 1225 nm light, to a 'non-resonant image' recorded with 1300 nm light, respectively. Corresponding spatial intensity profiles are displayed to the right of the images, the

intensity profile were generated by integrating the solid white rectangle. Both images and profiles show the behavior of light intensity characteristics depend on tuning wavelength through normal and cancerous tissues in the specimen.

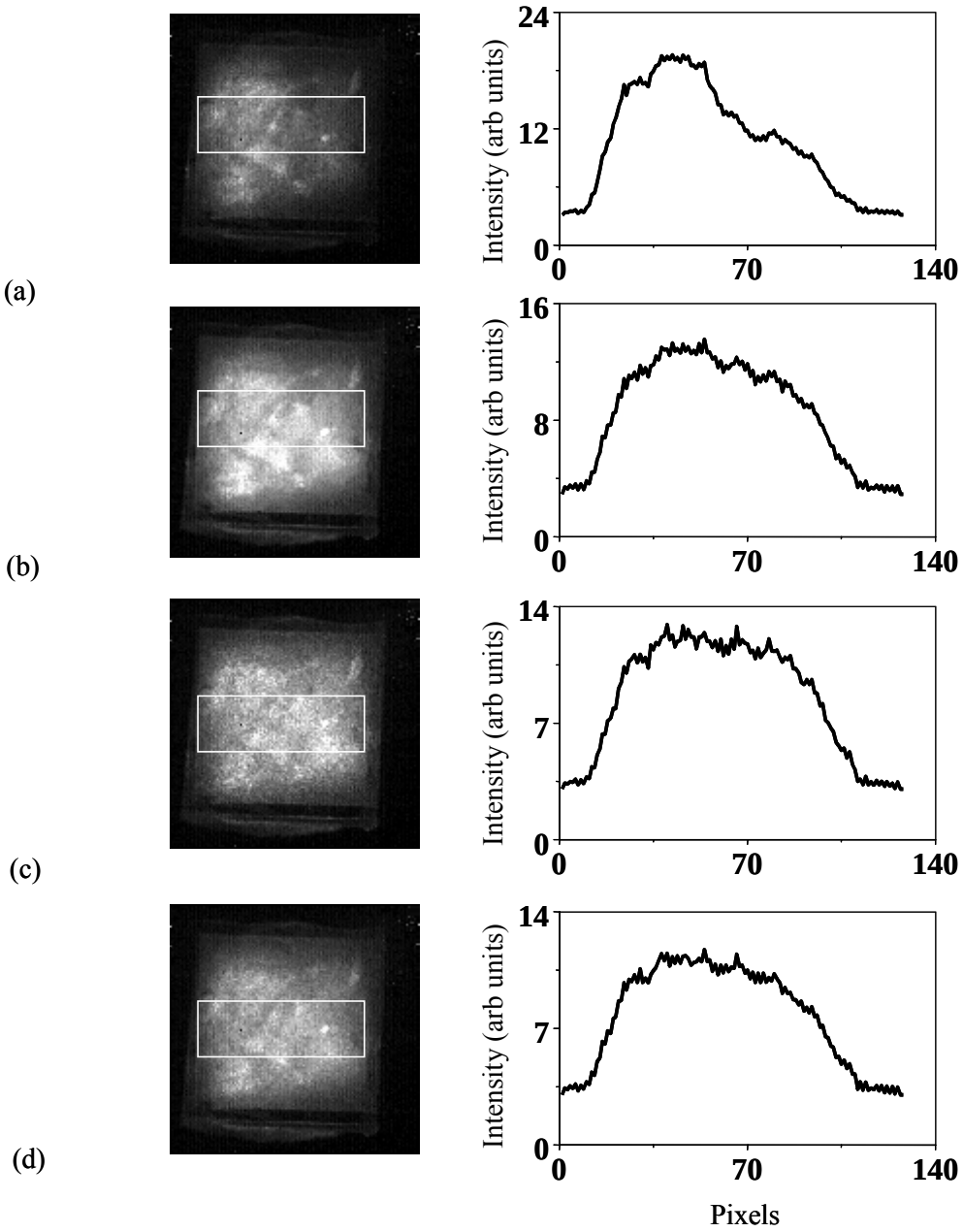


Figure 2.16: Spectroscopic 2D images of breast tissue (Sample 6) for wavelengths (a) 1225 nm, (b) 1250 nm, (c) 1285 nm, and (d) 1300 nm. Corresponding spatial intesity distributions integrated over the same horizontal area (white box) are shown on the right.

The salient features of the spectroscopic images and corresponding profiles are: (a) the normal tissues appear much darker (less light transmission) than other cancerous tissues in the near-resonant 1225 nm image as compared to that in the off-resonance 1300 nm image; (b) cancerous tissues appear brighter (higher light transmission) or same than the normal tissues in wavelengths 1225-1300 nm images.

*Sample 7*

Spectroscopic imaging measurements were carried out on Sample #7, the *ex vivo* breast tissue specimen composed of invasive ductal carcinoma (left) tissue and normal part (right) as shown Figure 2.17 (a)-(d). Figure 2.17 (a) shows a 'near-resonant image' recorded with 1225 nm light, while in Figure 2.1 (d) a 'non-resonant image' recorded with 1300 nm light. The intensity profiles were generated by integrating the solid white rectangle. Both images and profiles show the behavior of light intensity characteristics depend on tuning wavelength through normal and cancerous tissues in the specimen. The images show more light transmitted through cancerous part than normal part.

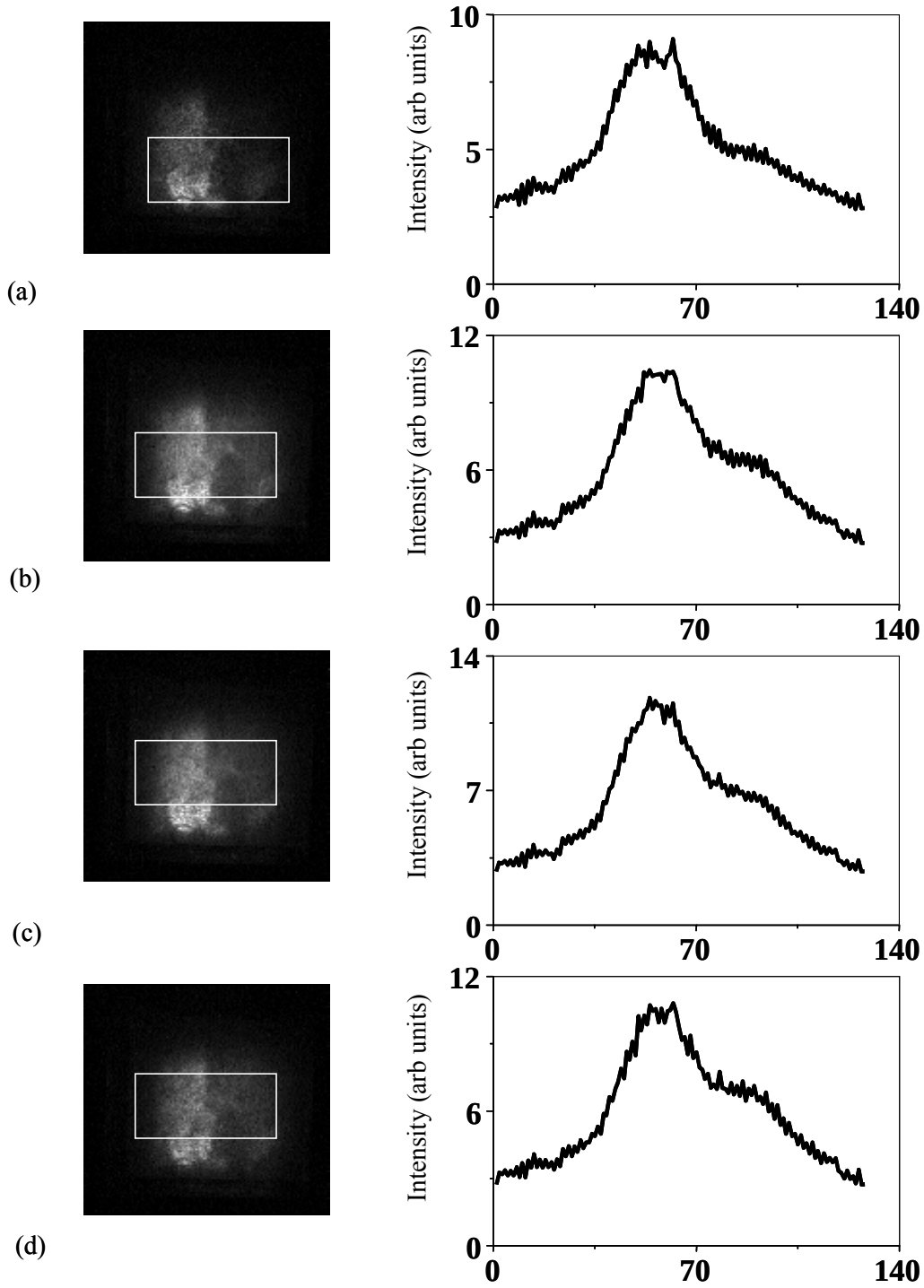


Figure 2.17 Spectroscopic 2D images of breast tissue (Sample 7) for wavelengths (a) 1225 nm, (b) 1250 nm, (c) 1285 nm, and (d) 1300 nm. Corresponding spatial intesity distributions integrated over the same horizontal area (white box) are shown on the right.

*Sample 8*

Spectroscopic imaging measurements were carried out on Sample #8, the *ex vivo* breast tissue specimen composed of normal part next to an invasive ductal carcinoma tissue. Figure 2.18 (a)-(e) show a set of images starting with the 'near-resonant image' recorded with 1223 nm light, progressing through images recorded with light of wavelengths that gradually move away from that resonance to a 'non-resonant image' recorded with 1300 nm light, respectively. Corresponding spatial intensity profiles are displayed to right of the images, the intensity profiles were generated by integrating the same area on all the images highlighted by the solid white rectangle. The images show that at 1223 nm to 1250 nm more light is transmitted through the cancerous part than the normal part as displayed in Figure 2.18 (a) and (b). In Figure 2.18 (c) the intensity of light for normal and cancer are the same. At wavelength above 1270 nm the intensity of light is more in normal part than the cancerous as shown in Figure 2.18 (d) and Figure 2.18 (e).

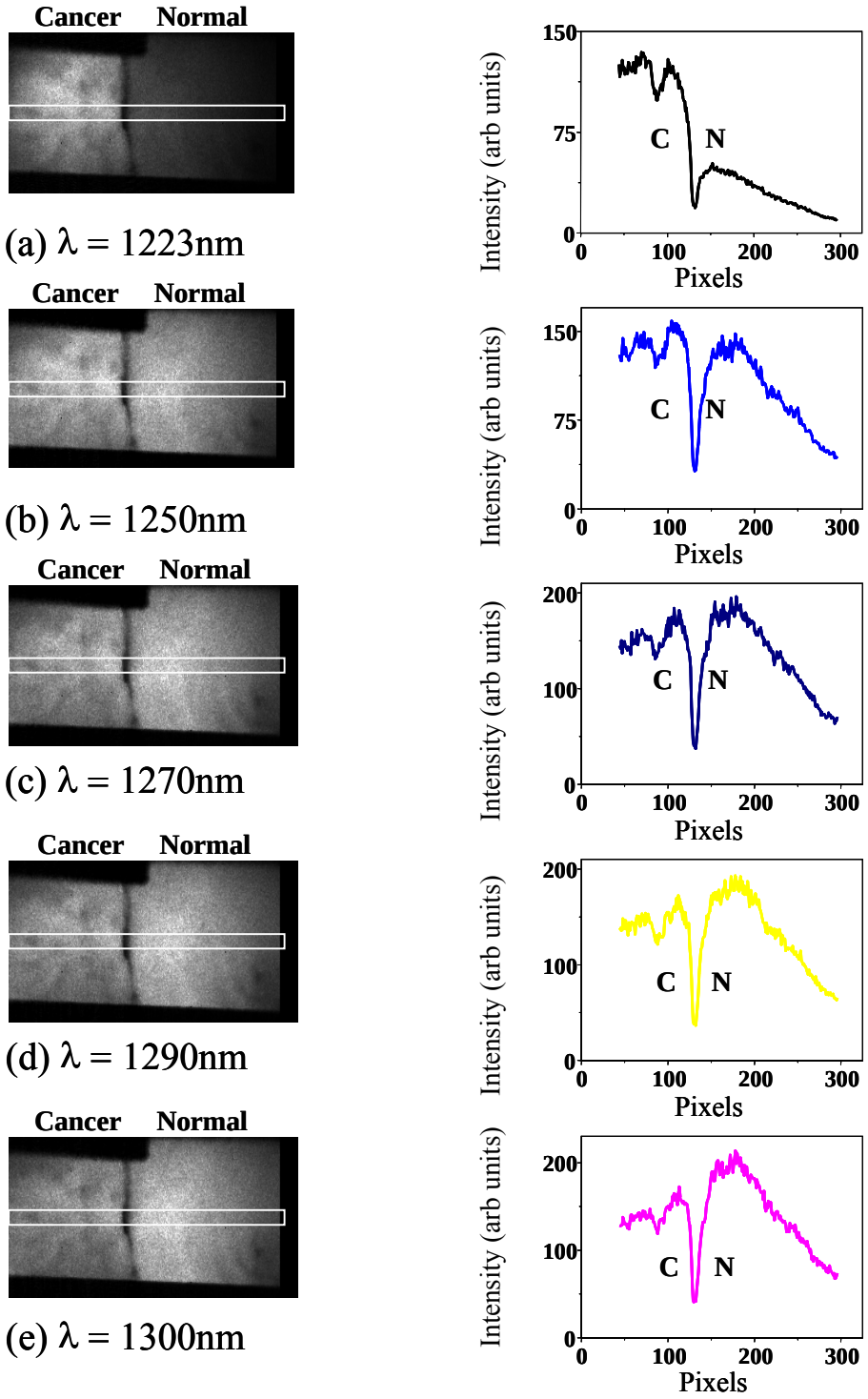


Figure 2.18: Spectroscopic 2D transillumination images of Sample 8 for wavelengths (a) 1223 nm, (b) 1250 nm, (c) 1270 nm, (d) 1290 nm, and (e) 1300 nm. Corresponding spatial intesity distributions integrated over the same horizontal area (white box) are shown on the right. The tissue is composed of invasive ductal carcinoma (C) and normal tissue (N). A black tape was attached at exit surface of the sample to prevent the camera of recording light leakage.

For a more quantitative description of the observed behavior, we monitored the wavelength-dependent image ration of cancer to normal intensity, $R_{CN}(\lambda)=I_C(\lambda)/I_N(\lambda)$ and contrast, $C(\lambda) = (I_C - I_N)/(I_C + I_N)$, where $I_N(\lambda)$ is the optimal intensity value at wavelength $\lambda$ on the spatial profile of the image at the normal tissue location, and $I_C(\lambda)$ is the corresponding intensity in the immediate cancerous tissue region. The ration/contrast varied from 3/0.5 at 1223 nm through 1.06/0.03 at 1250 nm to 0.7/–0.18 at 1300 nm for sample #8. The negative value of the contrast at 1300 nm indicates higher brightness at the adipose tissue region than at cancer tissue regions at this wavelength. [25]

The salient features of the spectroscopic images and corresponding profiles are: (a) the adipose tissues appear much darker (less light transmission) than other tissues in the near-resonant 1225 nm image as compared to that in the off-resonance 1300 nm image; (b) cancerous tissues appear brighter (higher light transmission) than the normal tissues in both the images; (c) while the overall light transmission through the normal region remains approximately at the same level, that through the cancerous region is significantly higher at 1225 nm than at 1300 nm; (d) transmission through the lymph node exhibits a wavelength-dependent variation as well, being higher at 1225 nm than at 1300 nm. The change in image contrast was the maximum for the adipose tissue as the wavelength of imaging light was changed from 1225 to 1300 nm. Adipose tissue region appeared as a much deeper trough in the spatial intensity profile of the 1225 nm image compared to that for the 1300 nm image. As the laser output was tuned away from 1225 nm to off-resonance wavelengths, the contrast between the adipose and glandular regions in the images decreased from a maximum of 0.27 at 1225 nm towards 0.10 at 1300 nm.

These results clearly demonstrate that an appreciable spectroscopic difference may significantly enhance the contrast between different types of breast tissues in a transillumination image, and is consistent with the results obtained from adipose (normal) glandular, and cancerous human breast tissues.

Table 2.2 summarizes the values of $R_{CN}(\lambda)=I_C(\lambda)/I_N(\lambda)$ for other samples with tumor used in the study. Data for the sarcomatoid carcinoma sample is included in Table 2.2 for comparison with the samples with IDC. While the ratio values exhibit sample-dependent variation, the trend toward higher value of the ratio at 1225 nm compared to that at 1300 nm is consistent for all the samples.

Table 2.2: Values of time-dependent contrast C(t) and wavelength-dependent intensity ratio $R_{CN}$ (λ) for different ex vivo cancerous tissue specimens

| Thickness (mm) | Age (y) | Cancer Type | $C(t)$ Early time | $C(t)$ Late time | $R_{CN}$ @ 1225 nm | $R_{CN}$ @ 1300 nm |
|---|---|---|---|---|---|---|
| 5 | 38 | IDC | 0.33 | -0.34 | 1.4 | 1.3 |
| 5 | 33 | IDC | 0.98 | -0.45 | 1.8 | 1.1 |
| 5 | 63 | IDC | 0.46 | -1.0 | 2.2 | 1.5 |
| 5 | 53 | IDC | 0.56 | -0.17 | 2.1 | 1.2 |
| 10 | 41 | IDC | 0.32 | -0.38 | 1.7 | 1.2 |
| 10 | 61 | IDC | 1.00 | -0.03 | 1.7 | 1.1 |
| 10 | 79 | IDC | 0.42 | 0.01 | 2.5 | 0.9 |
| 5 | 30 | SC | 0.58 | 0.13 | 1.5 | 1.2 |

IDC = Invasive (or infiltrating) ductal carcinoma, SC = Sarcomatoid carcinoma

Early time = 25 ps for all samples

Late time = 225 ps for 5 mm thick samples, and 500 ps for 10 mm thick samples

### 2.3.3 Coordinated time-resolved and spectroscopic imaging with validation

Time-resolved 2D imaging and spectroscopic 2D imaging with validation using magnetic resonance imaging, and/or, histological micrographs provide a complete set of measurements for evaluation of the efficacy of the optical imaging approach. Results of

such a set of coordinated measurements on a typical *ex vivo* breast tissue specimen is presented in this section.

The 5 mm thick sample (Sample #10 in Table 2.1) was obtained following a modified radical mastectomy and lymph node dissection of the left breast of a 63 year old female at the Memorial Sloan-Kettering Cancer Center. The clinical diagnosis revealed an invasive ductal carcinoma with poorly differentiated histological grade III/III and nuclear grade III/III. The specimen was placed in a high grade Pyrex glass (suitable for both optical and NMR studies) container that slightly compressed to retain the tissue axial orientation.

Time-sliced 2D transillumination images of Sample #10 for gate positions of 25 ps, 125 ps, and to 225 ps are displayed in the top frames of Figure 2.19 (a), 2.19 (b), and 2.19 (c), respectively. The corresponding bottom frames present the spatial intensity profiles of the respective images integrated over the same horizontal area in the images. Again, the salient feature of the images is the difference in time-dependent brightness of the normal tissue (N) and cancerous (C) regions in the sample. In the 25 ps image of Figure 2.2 (a) the cancer region (C) is prominent. The corresponding horizontal spatial intensity profile exhibits a peak in the cancer (C) region. At this early time, markedly more light is transmitted through the tumor than through the normal tissue. As time evolve around 125 ps of Figure 2.19 (b), the contrast diminished between cancerous (C) and normal (N) tissues. With time the normal tissue image gain in brightness as shown in the 225 ps image of Figure 2.19 (c). The corresponding spatial intensity profile peaks in the normal (N) position indicating higher light transmission through the normal region than the tumor.

Spectroscopic transillumination images of Sample #10 recorded using light of wavelength 1225 nm through 1300 nm appear in the upper frames of Figure 2.20 (a), (b), and (c), respectively. Corresponding spatial profiles integrated over the same horizontal region for both normal (N) and cancerous (C) regions are shown in the respective lower frames. This indicates higher overall light transmission through the tumor than through normal tissue. The value of $R_{TN}(\lambda)$, the tumor-to-normal intensity ratio introduced earlier, is approximately 2.2 at 1225 nm and 1.5 at 1300 nm, a notable difference.

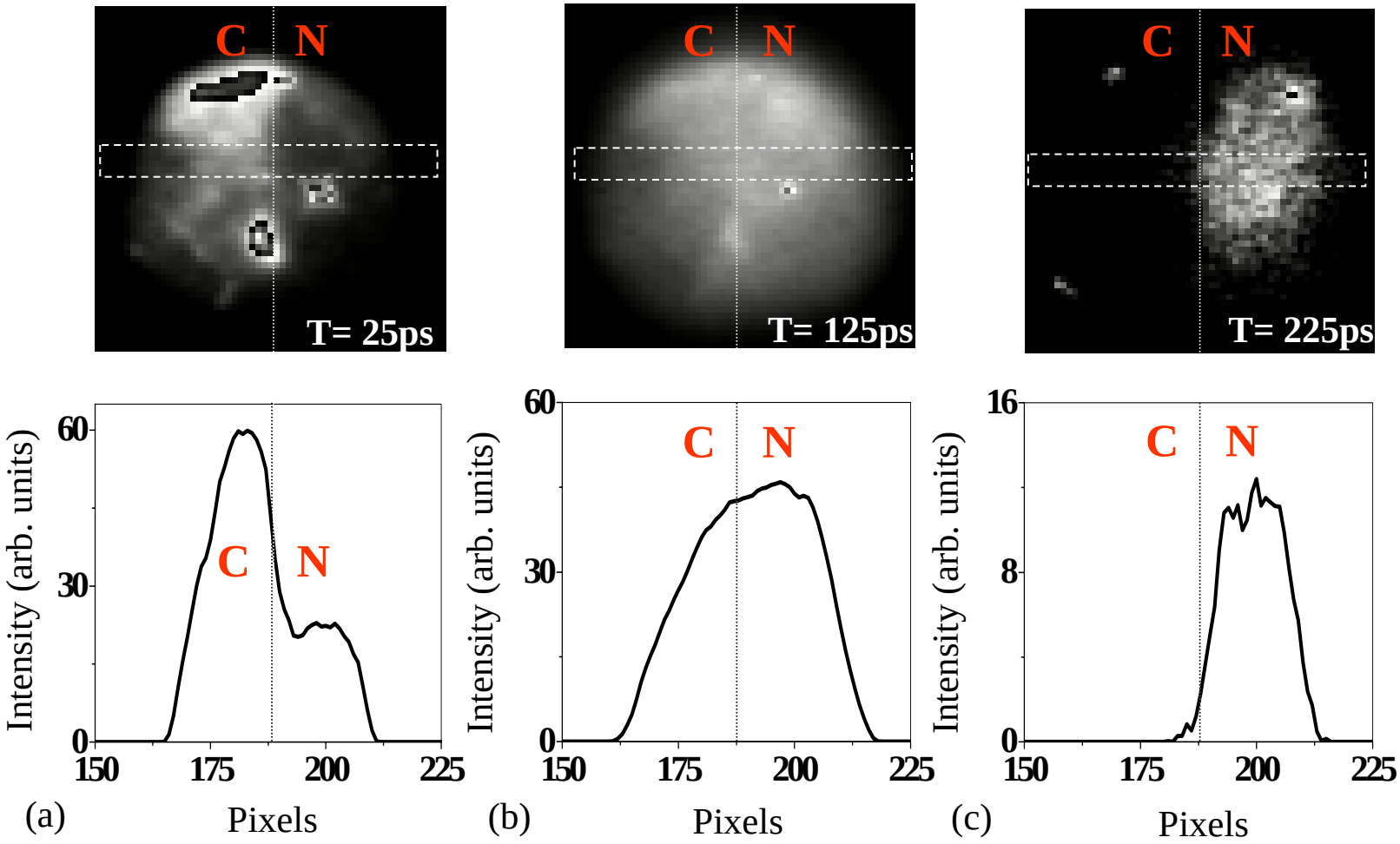


Fig. 2.19: (Upper frames) Time-sliced transillumination images of 5 mm thick Sample #10 comprising normal and cancerous (invasive ductal carcinoma) tissues at the time gate position of (a) 25 ps, (b) 125 ps, and (c) 225 ps. (Lower frames) Corresponding spatial intensity distribution integrated over the pixels enclosed by the white dashed boxes.

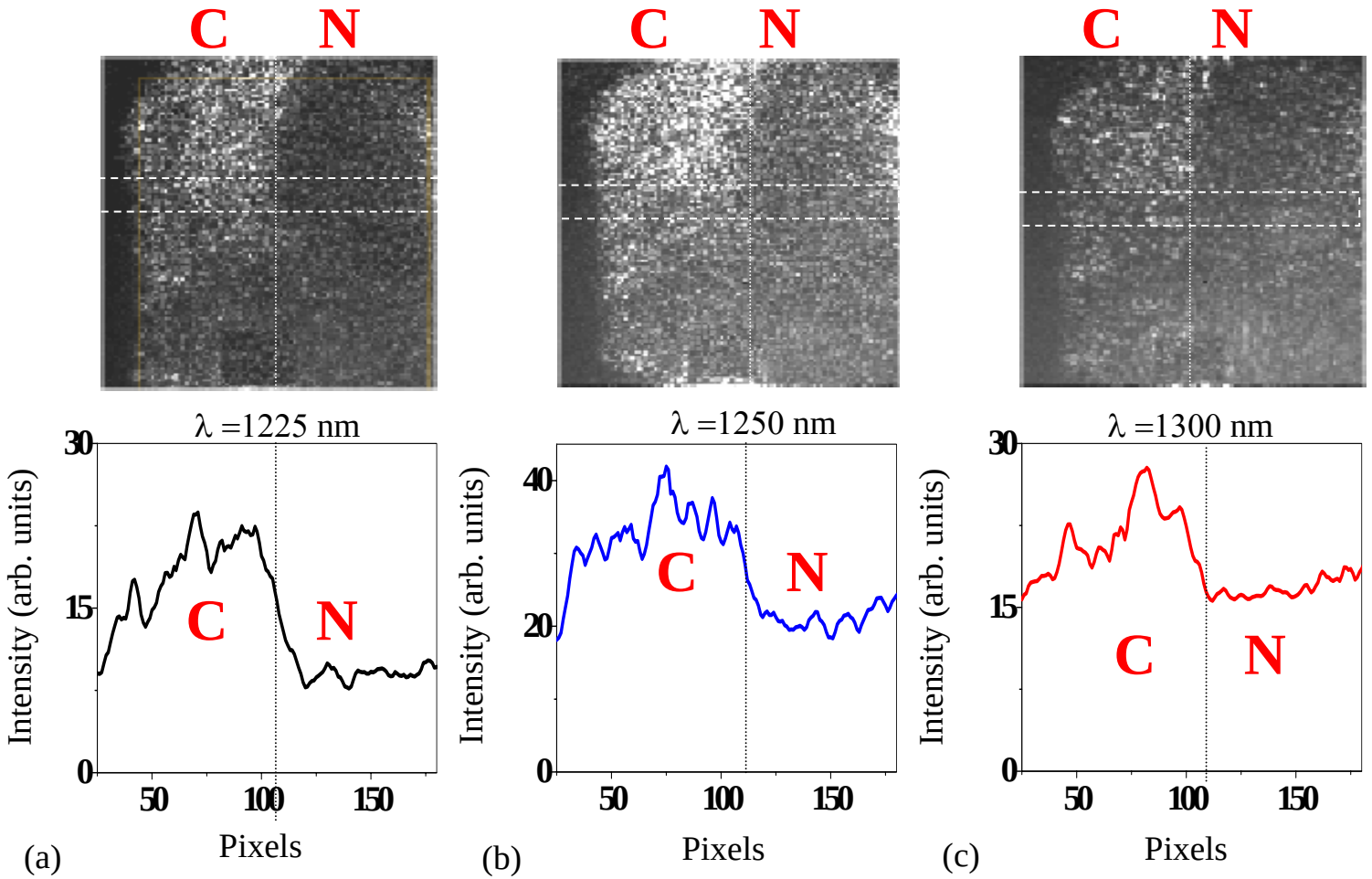


Fig. 2.20. (Upper frames) Spectroscopic transillumination images of 5 mm thick Sample #10 comprising normal and cancerous (invasive ductal carcinoma) tissues recorded using light of wavelength (a) 1225 nm, (b) 1250 nm, and (c) 1300 nm (Lower frames) Corresponding spatial intensity distribution integrated over the pixels enclosed by the white dashed boxes.

Magnetic resonance T1 and T2-weighted images of the front and the back 2.5 mm axial sections of Sample #10 are shown in Figure 2.21 (a)-(b) and (c)-(d), respectively. Repetition time for obtaining these images was 500 ms, which is greater than the lower limit of 300 ms required for good contrast/noise ratio [32]. Echo time was 16 ms (much shorter than 80 ms) that also implies a good effective-contrast [32]. The T2-weighted images (Figure 2.21 (c) and (d)) showed no further improvements in image contrast. The magnetic resonance images of the sample correlate well with the optical time-resolved and spectroscopic images.

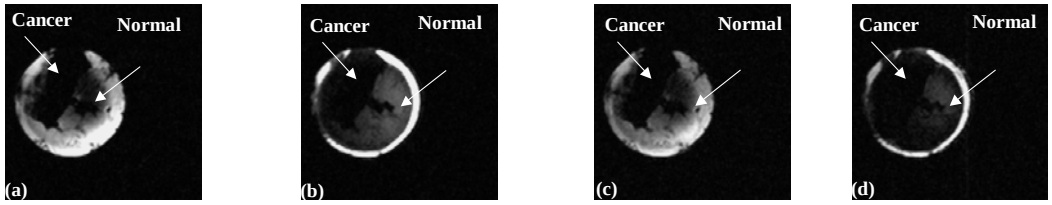


Figure 2.21: Magnetic resonance images of (a) T1-weighted first 2.5 mm axial section, and (b) T1- weighted second 2.5 mm axial section. (c) T2 -weighted first 2.5 mm axial, and (d) T2-weighted second 2.5 mm axial section, of Sample #10 which is 5 mm thick and comprises normal and cancerous (invasive ductal carcinoma) tissues.

Figure 2.22 (a) and (b) show a photograph and histological micrograph of a section of Sample #10. The upper left part of Figure 2.22 (b) that appears much denser than the rest of the micrograph has an abundance of cancer cells (C), the lower left part has extra-cellular collagen matrix with some interspersed cells, and the much lighter upper right part is rich in normal adipose (NA) tissues. The histology results are consistent with the optical imaging and MR imaging results.

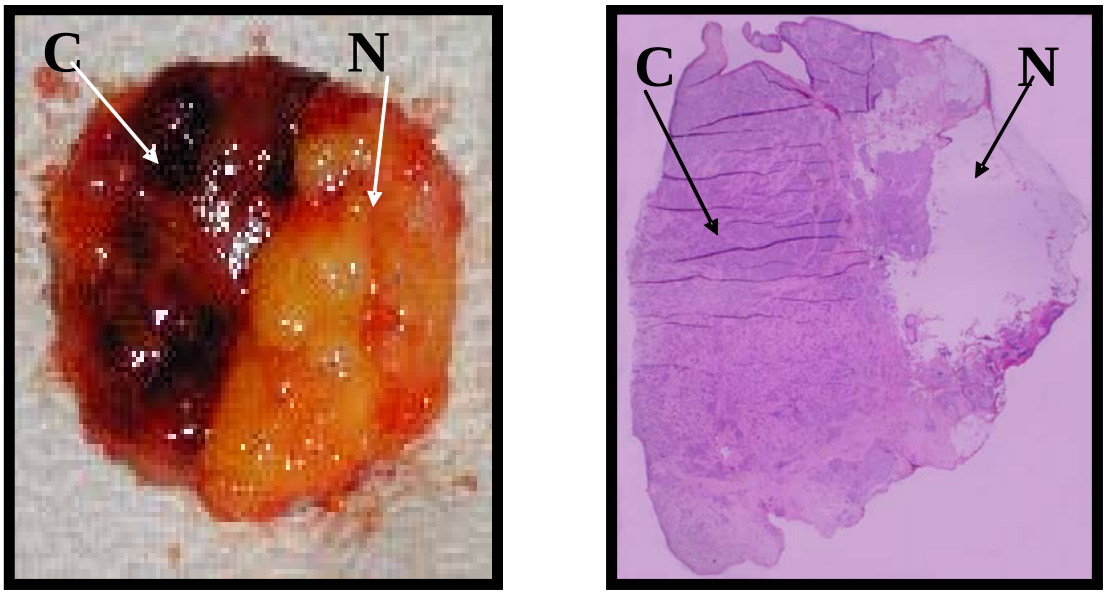


Figure 2.22: (a) Exit face photo of 5 mm composite breast tissue (Sample #10). N: normal glandular tissue, C: cancerous tissue (invasive ductal carcinoma). (b) Histological micrograph of a representative section from the sample showing an abundance of cancer cells in the upper left, and normal cells on the upper right.

## 2.4 Discussion

The experimental results on all the breast tissue specimens presented in this article show the ability of the optical imaging methods to select key spectral and temporal differences between the tumor and normal tissues. Images recorded with the earlier arriving light highlighted the tumor, while those recorded with later arriving light accentuated the normal region. Our observation is that for the same thickness of tissues, light arrives earliest through the cancerous tissue, next through normal glandular tissues and latest through the adipose tissues in a breast tissue specimen. Early-time images carry information about cancerous regions. Even within the cancerous tissues there appears to be a time-dependent transmission of light. Among the cancerous samples investigated, light transmission seemed to be the faster through the infiltrating (or invasive) ductal carcinoma samples than through the sample with poorly differentiated carcinoma with sarcomatoid features. Smaller but noticeable time-dependent variations in light transmission through different IDC samples were observed, which might be related to the level of growth of the tumor. Careful measurements on more IDC samples with different levels of tumor progression will be needed to establish a quantitative correlation. These results show the importance of time-resolved imaging on the picosecond time scale.

Probable reasons for the observed difference in time-dependent light transmission through the normal and cancerous tissues may be: (a) lower overall light scattering, (b) higher forward scattering of light, and (c) higher absorption of light in the cancerous tissue compared with the normal tissue. Cell nuclei are prominent among the cell organelles that scatter light. The size of nuclei (5-10 μm) in normal cell is appreciably

larger than the wavelength of light 0.8 μm used in time-resolved imaging experiments. Light is strongly forward scattered by these nuclei. The size of nuclei increases as the cells make transition through the pre-cancerous stage to cancerous stages, and a much wider variation of nuclear size and shape in malignant cells replace the nearly uniform size distribution of normal cells. Consequently, light in cancerous tissues is expected to be more forward scattered than that in the normal tissue. The extent of forward scattering will be higher in advanced stages of cancers than in the normal and earlier cancerous stages. Light scattering spectroscopy experiments with normal and malignant cells have lent credence to this line of reasoning [35,36]. Higher forward scattering of light in cancerous tissue is then a major reason for observed time-dependent transmission. Polarized backscattered light has been shown to provide important histological information [36]. Polarization memory combined with spectroscopic and time-resolved approaches may play an important role in backscattering optical mammography.

Normal breast tissues do not absorb 800 nm light appreciably. However, the growth of tumor is accompanied by an increase in blood volume. Consequently somewhat higher absorption of light may be expected in tumors, and more so in advanced tumors. It will also account in part for the observed behavior in time-sliced images.

Spectroscopic images are formed by the entirety of the transmitted light that passed through the Fourier gate, as no time gating was involved. Images recorded at all the wavelengths exhibited a higher level of light transmission through the cancerous tissue regions, as those regions appeared brighter in the images. We attribute this overall higher light transmission through the cancerous regions to the higher forward scattering of light in cancerous tissues than in normal tissues, as described above.

Normal tissue regions appeared darker in the 1225 nm images than in the 1300 nm images, as compared to the appearance of the cancerous tissues. Since 1225 nm is closer to the absorption resonance of adipose tissues centered at 1203 nm [33], the observed behavior may be attributed to relatively higher abundance of adipose cells in the normal tissue region than in the cancerous tissue region [37]. The absorbing species is presumed to be the $CH_2$ groups in fat molecules, with the transition corresponding to the second overtone of C-H symmetric stretching mode [38]. In particular, the regions dominated by the adipose tissues always appeared much darker than normal glandular and cancerous tissues in the transillumination spectroscopic images. These results indicate that the wavelengths of light absorbed by adipose tissues could be used as an indicator of pathology. However, it has to be corroborated with measurements at other wavelengths tuned to other chromophores, such as oxy-hemoglobin, deoxy-hemoglobin, water, and lipids. These results further indicate the usefulness of 1200 – 1300 nm wavelength range in optical mammography. So far, this wavelength range has not been substantially exploited for breast imaging [25,26]. The reasons may be somewhat higher absorption of light and paucity of commercially available tunable lasers in this spectral range. However, it has been shown that a small absorption helps improve image contrast [39], and depending on the sample thickness the wavelength can be tuned away from the absorption maximum to the wing of the adipose absorption band to allow adequate transmission, and still derive the benefit of contrast enhancement. The wavelength range is well suited for application involving on site evaluation of breast tissue specimens removed during lumpectomy, the breast-conserving surgery.

Spectroscopic imaging results are encouraging and may be useful in obtaining diagnostic information. In particular, the wavelength-dependent tumor-to-normal transmitted intensity ratio $R_{CN}(\lambda)$ seemed to depend on the cancer type. More extensive measurements involving normal tissues and tissues with different types and stages of cancers will be needed to explore if this ratio can be a useful parameter in tumor identification.

The optical imaging results corresponded well with pathology and MR results. While pathology is the 'gold standard' for *ex vivo* measurements, co-registration with MR measurements will be valuable for validation of *in vivo* optical measurements in the development stages of optical mammography.

Although the measurements presented in this chapter were carried out on *ex vivo* breast tissue specimens, the results have important implication for *in vivo* imaging of breast. The time-sliced imaging approach presented here is intuitively simple, fast, and provides ample data over a wide range of frequencies that is necessary for 3D image reconstruction [12]. A combined time-resolved and spectroscopic 3D inverse imaging approach with polarization sensitivity will be pursued to realize the potential of optical mammography as a modality for monitoring women's health.

## 2.5 References


1. Cutler, M., "Transillumination as an aid in the diagnosis of breast lesion", Surg. Gynecol. Obstet. **48**, 721-730 (1929).
2. For a brief review of different optical imaging techniques for biomedical applications see, Gayen, S. K., and Alfano, R. R. "Emerging optical biomedical imaging techniques". Opt. Photon. News **7(3)**, 17-22 (1996) and references therein.
3. Alfano, R. R., Gayen, S. K., and Zevallos, M. E. "Spectroscopic and time-resolved optical methods and apparatus for imaging objects in turbid media". U. S. Patent Number: 6,665,557 B1 awarded December 16, 2003.
4. Patterson, M. S., Chance, B., and Wilson, B. C. "Time-resolved reflectance and transmittance for the noninvasive measurement of tissue optical properties". Appl. Opt. **28**, 2331-2336 (1989).
5. Yoo, K. M. and Alfano, R. R. "Time-resolved coherent and incoherent components of forward light scattering in random media". Opt. Lett. **15**, 320 – 322 (1990).
6. Wang, L., Ho, P. P., Liu, C., Zhang, G., and Alfano, R. R. "Ballistic 2D imaging through scattering wall using an ultrafast Kerr gate". Science **253**, 769-771 (1991).
7. O'Leary M. A., Boas, D.A., Chance, B., and Yodh, A. G. "Experimental images of heterogeneous turbid media by frequency-domain diffusing-photon tomography". Opt. Lett. **20**, 426-428 (1995).

8. Hebden, J. C., Arridge, S. R. and Deply, D. T. “Optical imaging in medicine: I. Experimental Techniques”. Phys. Med. Biol. **42**, 825-840 (1997).
9. Arridge, S. R., and Hebden, J. C. “Optical imaging in medicine: II. Modeling and reconstruction”. Phys. Med. Biol. **42**, 841-853 (1997).
10. Arridge, S. R. “Optical tomography in medical imaging”. Inverse Probl. **15**, R41–R93 (1999).
11. Cai, W., Das, B. B., Liu, F., Zevallos, M., Lax, M., and. Alfano, R. R. “Time-resolved optical diffusion tomographic image reconstruction in highly scattering turbid media”. Proc. Natl. Acad. Sci. USA **93**, 13561-13563 (1996).
12. Cai, W., Gayen, S. K., Xu, M., Zevallos, M., Alrubaiee, M., Lax, M., and Alfano, R. R. “Optical tomographic image reconstruction from ultrafast time-sliced transmission measurements,” Appl. Opt. **38**, 4237-4246 (1999).
13. Markel, V. A., Schotland, J. C. “Scanning paraxial optical tomography”. Opt. Lett. **27**, 1123 – 1125 (2002).
14. Ntziachristos, V., Yodh, A., Schnall, M., and Chance, B. “MRI-guided diffuse optical spectroscopy of malignant and benign breast lesions”. Neoplasia **4**, 347-354 (2002).
15. Grosenick, D., Moesta, K.T., Wabnitz, H., Mucke, J., Stroszczynski, C., Macdonald, R., Schlag, P. M., and Rinneberg. H. “Time-domain optical mammography: Initial clinical results on detection and characterization of breast tumors”. Appl. Opt. **42**, 3170-3186, (2003).

16. Dehgani, H., Pouge, B. W., Poplack, S. P., Paulsen, K. D. "Multiwavelength three-dimensional near-infrared tomography of the breast: initial simulation, phantom, and clinical results". Appl. Opt. **42**, 135-145 (2003).
17. Colak, S. B., van der Mark, M. B., 't Hooft, G. W., Hoogenraad, J. H., van der Linden, E. S., and Kuijpers, F. A."Clinical optical tomography and NIR spectroscopy for breast cancer detection". IEEE J. Select. Topics Quantum Electron. **5**, 1143-1158 (1999).
18. Taroni, P., Danesini, G., Torricelli, A., Pifferi, A., Spinelli, L., Cubeddu, R. "Clinical trial of time-resolved scanning optical mammography at 4 wavelengths between 683 and 975 nm". J. Biomed. Opt. **9**, 464-473 (2004).
19. Franceschini, M. A., Moesta, K. T., Fantini, S., Gaida, G., Gratton, E., Jess, H., Mantulin, W. W., Seeber, M., Schlag, P. M., and Kaschke, M. "Frequency-domain techniques enhance optical mammography: initial clinical results". Proc. Natl. Acad. Sci. USA **94**, 6468-6473 (1997).
20. Cheng, X., Mao, J. M., Bush, R., Kopans, D. B., Moore, R. H., Chorlton, M. "Breast cancer detection by mapping hemoglobin concentration and oxygen saturation". Appl. Opt. **42**, 6412-6421 (2003).
21. Webb, S. "The Physics of Medical Imaging". Bristol: Institute of Physics Publishing (1988).
22. Gayen, S. K., Alrubaiee, M., Zevallos, M. E., and Alfano, R. R. "Temporally and spectrally resolved optical imaging of normal and cancerous human breast tissues". Proceedings of Inter-Institute Workshop on In Vivo Optical Imaging

at the NIH, Amir H. Gandjebakhche, ed. (Optical Society of America, Washington, DC, 2000), pp. 142-147.

23. Gayen, S. K., Alrubaiee, M., Savage, H.E., Schantz, S. P., and Alfano, R. R. "Parotid gland tissues investigated by picosecond time-gated and optical spectroscopic imaging techniques". IEEE J. Select. Top. Quantum Electron. **7**, 906-911 (2001).
24. Schmidt, F. E. W., Fry, M. E., Hillman, E. M. C., Hebden, J. C., and Deply, D. T. "A 32-channel time-resolved instrument for medical optical tomography". Rev. Sci. Instrum. **71**, 256-265 (2000).
25. Gayen, S. K., Zevallos, M. E., Alrubaiee, M., and Alfano, R. R. "Near-infrared laser spectroscopic imaging: a step towards diagnostic optical imaging of human tissues". Laser Life Sci. **8**, 187-198 (1999).
26. Gayen, S. K. and Alfano, R. R. "Sensing lesions in tissues with light". Opt. Express **4**, 475-480 (1999).
27. Fu, Q, Seier, F., Gayen S. K., and Alfano, R. R. "High-average-power kilohertz-repetition-rate sub-100 fs Ti:sapphire amplifier system". Opt. Lett. **22**, 712-714 (1997).
28. Dolne, J. J., Yoo, K. M., Liu, F., and Alfano, R. R. "IR Fourier space gate and absorption imaging through random media". Laser Life Sci. **6**, 131-141 (1994).
29. Ntziachristos, V., Yodh, A., Schnall, M., and Chance, B. "Concurrent MRI and diffuse optical tomography of breast after indocyanine green enhancement". PNAS **97**, 2767-2772 (2000).

30. Merritt S, Bevilacqua, F., Durkin, A. J., Cuccia, D. J., Lanning, R., Tromberg, B. J., Gulsen, G., Yu, H., Wang, J., Nalcioglu, O. "Coregistration of diffuse optical spectroscopy and magnetic resonance imaging in arat tumor model". Appl. Opt. **42**, 2951-2959 (2003).

31. Bremer, C., Ntziachristos, V., Weitkamp, B, Theilmeier, G., Heindel, W., Weissleder, R. "Optical imaging of spontaneous breast tumors using protease sensing 'smart' optical probes". Investigative Radiology **40**, 321-327 (2005).

32. For details on the MR experimental arrangement, see Koutcher, Jason A., Motwani, M., Zakian, Kristen L., Li, Xiao-Kui, Matei, C., Dyke, Jonathan P., Ballon, D., He Yoo H., and Schwartz, Gary K. "The *in vivo* effect of bryostatin-1 on paclitaxel-induced tumor growth, mitotic entry, and blood flow". Clin. Cancer Res. **6**, 1498-1507 (2000).

33. Marks, F. A. "Optical determination of the hemoglobin oxygenation state of breast biopsies and human breast cancer xenografts in nude mice". SPIE **1641**, 227-237 (1992).

34. A 5-point smoothed average of intensity values around pixel #110 was used to reduce the effect of noise in determining the ratio.

35. Perelman, L. T., Backman, V., Wallace, M., Zonios, G., Manoharan, R., Nusrat, A., Shields, S., Seiler, M., Lima, C., Hamano, T., Itzkan, I., Van Dam, J., Crawford, J. M., and Feld, M. S. "Observation of periodic fine structure in reflectance from biological tissue: a new technique for measuring nuclear size distribution". Phys. Rev. Lett. **80**, 627-630 (1998).

36. Backman, V., Gurjar, R., Badizadegan, K., Itzkan, I., Dasari, R. R., Perelman, L. T., and Feld, M. S. Polarized light scattering spectroscopy for quantitative measurement of epithelial cellular structures *in situ*. IEEE J. Select. Top. Quantum Electron. **5**, 1019-1026 (1999).

37. Jakubowski, D. B., Cerussi, A. E., Bevilacqua, F., Shah, N., Hsiang, D., Butler, J., and Tromberg, B. J. "Monitoring neoadjuvant chemotherapy in breast cancer using quantitative diffuse optical spectroscopy: a case study". J. Biomed. Opt. **9**, 230-238 (2004).

38. Osborne, B. G., Fearn T., P. H. Hindle. "Near Infrared Spectroscopy in Food Analysis". 2nd Edition, Longman Group UK Limited, 1993, pp. 13-33.

39. Yoo, K. M., Liu, F., and Alfano, R. R. "Imaging through a scattering wall using absorption". Opt. Lett. **16**, 1068 – 1070 (1991).

40. Ralph Weissleder, "A clearer vision for in vivo imaging, Nature Biotechnology" **19**, 316 - 317 (2001).

41. Ntziachristos, V., Yodh, A. G., Schnall, Mitchell, Chance, "Concurrent MRI and diffuse optical tomography of breast after indocyanine green enhancement" Proc. Natl. Acad. Sci. USA 97, 2767–2772 (2000).

42. Kristen L Murphy, and Jeffrey M Rosen, "Mutant p53 and genomic instability in a transgenic mouse model of breast cancer", Oncogene **19**, 1045-1051, (2000)

# Chapter 3
# Optical Tomography using Independent Component Analysis for Detection and Localization of Targets in Homogenous Turbid Media

## 3.1 Introduction

Direct optical imaging of highly scattering, optically thick samples is not practical, so researchers are pursuing optical tomography or inverse image reconstruction approaches [1-25]. These use a forward model for light propagation, the measured light intensity distribution on the boundary of the turbid medium, and an inversion algorithm to generate a map of the optical properties, such as the absorption coefficient ($\mu_a$) and the scattering coefficient ($\mu_s$), of the medium and the embedded objects. The objects are desired to appear as localized inhomogeneities in the spatial distribution of these optical coefficients. Determination of the three dimensional (3D) location of target(s) is another important issue.

In this chapter a novel and fast approach for target detection and 3D localization is presented. It employs continuous-wave transillumination measurements and a novel algorithm based on independent component analysis (ICA) [26,27] from information theory to locate inhomogeneities embedded in turbid media. ICA has been successfully applied in a variety of other applications, such as, electroencephalography (EEG), functional Magnetic Resonance Imaging (fMRI), Electrocardiogram (EKG), telecommunication, and geological signals [27–30].

The remainder of Chapter 3 is organized as follows: Section 3.2 presents the general theoretical framework for OPTICA and then discuss the specific case of a turbid

medium in the form of a slab. However, the approach can be adapted to any arbitrary geometry. Scattering absorbing, and fluorescent objects are considered separately. Sections 3.3 and 3.4 present the experimental methods, materials, parameters, and algorithm; results are presented in Section 3.5. Finally, the implications of these results and the scope of OPTICA are discussed in Section 3.6.

### 3.2 Theoretical Formalism

In the linearized scheme of inversion, the perturbation of the detected light intensities on the boundaries of the medium (the scattered wave field due to absorptive and scattering objects (inhomogeneities) is given by [3,13]

$$\phi_{sca}(\mathbf{r}_d,\mathbf{r}_s) = -\int G(\mathbf{r}_d,\mathbf{r})\delta\mu_a c G(\mathbf{r},\mathbf{r}_s) d^3 r \\ -\int d^3 r \delta D(\mathbf{r}) c \nabla_r G(\mathbf{r}_d,\mathbf{r}) \cdot \nabla_r G(\mathbf{r},\mathbf{r}_s) \quad (3.1)$$

in the Diffusion Approximation (DA) of the Radiative transfer equation (RTE) [31] when illuminated by a unit point source, where $\mathbf{r_s}$, $\mathbf{r}$ and $\mathbf{r_d}$ are the positions of the source, the inhomogeneity, and the detector, respectively, $\delta\mu_a = \mu_{a,\,obj} - \mu_a$ and $\delta D = D_{obj} - D$ are the differences in the absorption coefficient and the diffusion coefficient, respectively, between the inhomogeneity and the background, $c$ is the speed of light in the medium and $G(\mathbf{r}, \mathbf{r'})$ is the Green's function describing light propagation from $\mathbf{r'}$ to $\mathbf{r}$ inside the background turbid medium with absorption coefficient $\mu_a$ and diffusion coefficients $D$. We do not explicitly include the modulation frequency of the incident wave in the arguments of Eq. (3.1) for clarity. The following formalism can be applied to continuous-wave, frequency-domain, and time-resolved measurements. The time-domain measurement is first Fourier transformed over time to obtain data over many different frequencies. Although Eq.(3.1) starts with DA, it should be emphasized that the formalism is not limited to DA, but can be used with other models of light propagation in turbid media, such as the cumulant approximation [20,22,32], the random-walk model [10,24], and radiative transfer [17,33] when they are linearized.

The Green's function G for slab geometry in the diffusion approximation is given by:

$$G(r,r') \equiv G(\rho,z,z') = \frac{1}{4\pi D}\sum_{k=-\infty}^{\infty}\left[\frac{\exp(-\kappa r_k^+)}{r_k^+} - \frac{\exp(-\kappa r_k^-)}{r_k^-}\right] \qquad (3.2)$$
$$r_k^{\pm} = \sqrt{\rho^2 + (z \mp z' \pm 2kd)}$$

for an incident amplitude-modulated wave of modulation frequency ω, where k = ±1, ±2, ..., $\rho = \sqrt{(x-x')^2 + (y-y')^2}$ is the distance between the two points r = (x,y,z) and r' = (x',y',z'), projected onto the *xy*-plane, $\kappa = \sqrt{(\mu_a - i\omega/c)/D}$ chosen to have a nonnegative real part. The extrapolated boundaries of the slab are located at $z = 0$ and $z = d = L_z + 2z_e$, respectively, where $L_z$ is the physical thickness of the slab and the extrapolation length $z_e$ should be determined from the boundary condition of the slab [34–36]. Equation (3.2) serves as the model Green's function for the uniform background medium of a slab geometry.

The modulation frequency $\omega = 0$ for continuous-wave light. In practice, the projections of the Green's function on the source and detector planes are determined from the measured perturbations in the light intensity distribution through independent component analysis. The comparison with the Green's function computed with Eq. (3.2) is then used to locate and characterize the inhomogeneities. We develop the formalism for absorptive and scattering inhomogeneities in the Subsections 3.2.1, 3.2.2, and 3.2.3 respectively.

Independent Component Analysis, Blind source separation is a class of problem of general interest that consists of recovering unobserved signals or virtual sources from several observed mixtures. Typically the observations are the output of a set of sensors, where each sensor receives a different combination of the source signals. Prior knowledge about the mixture in such problems is usually not available. The lack of prior

knowledge is compensated by a statistically strong but often physically plausible assumption of independence between the source signals. Over the last decade, ICA has been proposed as a solution to the blind source separation problem and has emerged as a new paradigm in signal processing and data analysis [22-25].

The simplest ICA model, an instantaneous linear mixture model [25] assumes the existence of $n$ independent signals $s_i(t)$ ($i$ =1,2, ... , $n$) and the observation of at least as many mixtures $x_i(t)$ ($i$ =1,2, ... , $m$) by $m \geq n$ sensors, these mixtures being linear and instantaneous, i.e., $x_i(t) = \sum_{j=1}^{n} a_{ij} s_j(t)$ for each $i$ at a sequence of time t. In a matrix notation,

$$x(t) = \mathbf{A}s(t), \quad \mathbf{A} \in \mathrm{R}^{m \times n} \tag{3.3}$$

where **A** is the mixing matrix. The $j^{th}$ column of **A** gives the mixing vector for the $j^{th}$ virtual source. ICA can be formulated as the computation of an $n \times m$ separating matrix **B** whose output

$$y(t) = \mathbf{B}s(t) = \mathbf{C}s(t), \quad \mathbf{B} \in \mathrm{R}^{n \times m}, \quad \mathbf{C} = \mathbf{BA} \in \mathrm{R}^{n \times n}, \tag{3.4}$$

is an estimate of the vector $s(t)$ of the source signals.

The basic principle of ICA can be understood in the following way. The central limit theorem in probability theory tells us that the distribution of independent random variables tends toward a Gaussian distribution under certain conditions. Thus, a sum of multiple independent random variables usually has a distribution that is closer to Gaussian than any of the original random variables. In Eq (3.4) $y_i(t) = \sum_j C_{ij} s_j(t)$, as a summation of independent random variables $s_j(t)$, is usually more Gaussian than $s_j(t)$, while $y_i(t)$ becomes least Gaussian when it in fact equals one of the $s_j(t)$. This heuristic

argument shows that ICA can be intuitively regarded as a statistical approach to find the separating matrix **B** such that $y_i(t)$ is least Gaussian. This can be achieved by maximizing some measure of non-Gaussianity, such as maximizing kurtosis [25, 26] (the fourth-order cumulate), of $y_i(t)$.

ICA separates independent sources from linear instantaneous or convolutive mixtures of independent signals without relying on any specific knowledge of the sources except that they are independent. The sources are recovered by a maximization of a measure of independence (or, a minimization of a measure of dependence), such as non-Gaussianity and mutual information between the reconstructed sources. [24,25] The recovered virtual sources and mixing vectors from ICA are unique up to permutation and scaling. [24,25].

### 3.2.1 Absorptive Inhomogeneity

The assumption that absorptive inhomogeneities are localized [that is, the $j^{th}$ one is contained in volume $V_j$ centered at $\mathbf{r}_j$ (1< j < J)] enables one to rewrite the scattered wave field in Eq. (3.1) as:

$$-\phi_{sca}(\mathbf{r}_d, \mathbf{r}_s) = \sum_{j=1}^{J} G(\mathbf{r}_d, \mathbf{r}_j) q_j G(\mathbf{r}_j, \mathbf{r}_s) \qquad (3.5)$$

where $q_j = \delta D(\mathbf{r}_j) c V_j$ is the absorption strength of the j[th] inhomogeneity. The scattered wave may be interpreted as an instantaneous linear mixture [37]

$$x(r_s) = As(r_s) \qquad (3.6)$$

Here $s(r_s) = [q_1 G(r_1, r_s), ..., q_J G(r_J, r_s)]^T$ represents the J virtual sources, i.e. the J inhomogeneities illuminated by the incident wave. A is the mixing matrix given by

$$A=\begin{pmatrix} G(r_{d_1},r_1) & G(r_{d_1},r_2) & \cdots & G(r_{d_1},r_J) \\ G(r_{d_2},r_1) & G(r_{d_2},r_2) & \cdots & G(r_{d_2},r_J) \\ \vdots & \vdots & \ddots & \vdots \\ G(r_{d_m},r_1) & G(r_{d_m},r_2) & \cdots & G(r_{d_m},r_J) \end{pmatrix} \qquad (3.7)$$

whose $j^{th}$ column (mixing vector) provides the weight factors for the contributions from the $j^{th}$ inhomogeneity to the detectors, and $x(r_s)=[-\phi_{sca}(r_{d_1},r_s),...,-\phi_{sca}(r_{d_m},r_s)]^T$ is the observed light intensity change. The superscript *T* denotes transposition. The incident light source scans a total of *n* positions $r_{s_1},...,r_{s_m}$ sequentially. For each source position $r_{s_j}$, the observation is made over *m* positions $r_{d_1},...,r_{d_m}$. Each set of such measurement is considered data at one temporal sampling point, as used in the conventional instantaneous linear mixture model [38] The multisource, multidetector data set $x(r_s)$ thus describes signals observed in *m* channels (*m* detectors) from *J* virtual sources (or *J* inhomogeneities) simultaneously over n discrete temporal points (n spatial scanning points). One absorptive inhomogeneity is represented by one virtual source $q_jG(r_j,r_s)$. The virtual source $q_jG(r_j,r_s)$ represents the individual inhomogeneity illuminated by the incident wave and is similar to the concept of the secondary source in Huygens's principle.[39] The role of detectors and sources can be interchanged owing to the reciprocal property of light propagation.

The principal assumption of this formalism is that the virtual source $q_jG(r_j,r_s)$ at the $j^{th}$ inhomogeneity is independent of the virtual sources at other locations. Under this assumption, ICA can be used with the observations from the light source scanned

at $n >> J$ positions to separate out both virtual sources $\mathbf{s}(\mathbf{r}_s)$ and the mixing matrix $\mathbf{A}$ [26,37].

ICA is a statistical approach to separate independent sources from linear instantaneous or convolutive mixtures of independent signals without relying on any specific knowledge of the sources except that they are independent. The sources are recovered by a minimization of a measure of dependence, such as mutual information, [26,27] between the reconstructed sources [30,37]. The recovered virtual sources and mixing vectors from ICA are unique up to permutation and scaling [30,37].

The two Green's functions describing light propagating from the source to the inhomogeneity and from the inhomogeneity to the detector are retrieved from the separated virtual sources $\mathbf{s}(\mathbf{r}_s)$ and the mixing matrix $\mathbf{A}$. The $j^{th}$ element $s_j(\mathbf{r}_s)$ of the virtual source array and the $j^{th}$ column $\mathbf{a}_j$ (mixing vector) of the mixing matrix $\mathbf{A}$ provide the scaled projections of the Green's function on the source and detector planes, $G(\mathbf{r}_j,\mathbf{r}_s)$ and $G(\mathbf{r}_d,\mathbf{r}_j)$, respectively. We can write

$$\begin{aligned} s(\mathbf{r}_s) &= \boldsymbol{\alpha}_j G(\mathbf{r}_j,\mathbf{r}_s) \\ a(\mathbf{r}_s) &= \boldsymbol{\beta}_j G(\mathbf{r}_d,\mathbf{r}_j) \end{aligned} \qquad (3.8)$$

where $\alpha_j$ and $\beta_j$ are scaling constants for the $j^{th}$ inhomogeneity. Both the location and the strength of the $j^{th}$ object can be computed by a simple fitting procedure by use of Eq. (3.8). We adopted a least-square fitting procedure given by

$$\min_{r_j,\alpha_j,\beta_j} \left\{ \sum_{r_s} \left[ \alpha_j^{-1} s_j(\mathbf{r_s}) - G_x(\mathbf{r_j},\mathbf{r_s}) \right]^2 + \sum_{r_d} \left[ \beta_j^{-1} a_j(\mathbf{r_d}) - G_m(\mathbf{r_d},\mathbf{r_j}) \right]^2 \right\} \quad (3.9)$$

The fitting yields the location $r_j$ of and the two scaling constants $\alpha_j$ and $\beta_j$ for the $j^{th}$ inhomogeneity, whose absorption strength is then given by $q_j = \alpha_j\beta_j$.

### 3.2.2 Scattering Inhomogeneity

For scattering inhomogeneities, under the assumption that the inhomogeneities are localized in a few regions, the same analysis can be carried out as that for absorptive inhomogeneities. The only modification is that up to three virtual sources may appear for one scattering inhomogeneity corresponding to the *x,y,z* components in the dot product $\nabla_{\mathbf{r}} G(\mathbf{r}_d,\mathbf{r})\cdot\nabla_{\mathbf{r}} G(\mathbf{r},\mathbf{r}_s) = \partial_x G(\mathbf{r}_d,\mathbf{r})\partial_x G(\mathbf{r},\mathbf{r}_s) + \partial_y G(\mathbf{r}_d,\mathbf{r})\partial_y G(\mathbf{r},\mathbf{r}_s) + \partial_z G(\mathbf{r}_d,\mathbf{r})\partial_z G(\mathbf{r},\mathbf{r}_s)$ in Eq. (0.1). Introducing two auxiliary functions

$$g_\perp(r,r_d) = = \frac{1}{4\pi D}\sum_{k=-\infty}^{\infty}\left[(\kappa r_k^+ + 1)\frac{\exp(-\kappa r_k^+)}{(r_k^+)^2} - (\kappa r_k^- + 1)\frac{\exp(-\kappa r_k^-)}{(r_k^-)^2}\right] \tag{3.10}$$

$$g_\perp(r,r_d) = = \frac{1}{4\pi D}\sum_{k=-\infty}^{\infty}\left[(z-z'+2kd)(\kappa r_k^+ + 1)\frac{\exp(-\kappa r_k^+)}{(r_k^+)^2} - (z+z'-2kd)(\kappa r_k^- + 1)\frac{\exp(-\kappa r_k^-)}{(r_k^-)^2}\right] \tag{3.11}$$

and the scattered wave due to scattering inhomogeneities can be rewritten as

$$\phi_{sca}(r_d,r_s) = -\int d^3 r\,\delta D(r) c \times \left\{\left[(x-x_d)(x-x_s)+(y-y_d)(y-y_s)\right] g_\perp(r,r_d) g_\perp(r,r_s) + g_z(r,r_d) g_z(r,r_s)\right\} \tag{3.12}$$

Denoting the scattering inhomogeneities as $q_j' = \delta D(r_j) c V_j$, where *c* is the speed of light in the medium, and $V_j$ is the volume of the j$^{th}$ scattering inhomogeneity, the scattered wave field can be transformed to

$$\begin{aligned} -\phi_{sca}(r_d,r_s) = & \sum_{j=1}^{n'} g_z(r_j,r_d) q'_j\, g_z(r_j,r_s) \\ & + \sum_{j=1}^{n'} \rho_{dj}\cos\theta_d\, g_\perp(r_j,r_d) q'_j\, \rho_{sj}\cos\theta_s\, g_\perp(r_j,r_s) \\ & + \sum_{j=1}^{n'} \rho_{dj}\sin\theta_d\, g_\perp(r_j,r_d) q'_j\, \rho_{sj}\sin\theta_s\, g_\perp(r_j,r_s) \end{aligned} \tag{3.13}$$

where $\rho_{dj} = \sqrt{(x_d - x_j)^2 + (y_d - y_j)^2}$, $\rho_{sj} = \sqrt{(x_s - x_j)^2 + (y_s - y_j)^2}$, and $\theta_d$ and $\theta_s$ are the azimuthal angles of $\mathbf{r}_d$-$\mathbf{r}_j$ and , respectively. This scattered wave can be regarded as a mixture of contributions from $(3J')$ virtual sources:

$$q'_j\, g_z(r_j,r_s),\ q'_j \rho_{sj} \cos\theta_s g_\perp(r_j,r_s),\ q'_j \rho_{sj} \sin\theta_s g_\perp(r_j,r_s)) \qquad (3.14)$$

with mixing vectors

$$g_z(r_j,r_d),\ \rho_{dj} \cos\theta_d g_\perp(r_j,r_d),\ \rho_{dj} \sin\theta_d g_\perp(r_j,r_d) \qquad (3.15)$$

where ($1< j < J'$), respectively. There are in general three virtual sources of specific patterns **(***one centrosymmetric* and two *dumbbell shaped*) associated with one scattering inhomogeneity, whereas only one centrosymmetric virtual source is associated with one absorptive inhomogeneity. This difference may be used to discriminate absorptive inhomogeneities from scattering inhomogeneities. However, for scattering inhomogeneities deep within turbid media, only the $q_j' g_z(r_j,r_s)$ virtual source remains significant and the other two are much diminished. In such a situation, other corroborative evidence, such as multiwavelength measurements, are required to determine the nature of inhomogeneities. Both the location and the strength of the *jth* scattering object are computed by fitting the retrieved virtual sources and mixing vectors to expressions (3.12) and (3.13), respectively.

When the noise level is high or systematic errors are present, extra independent components may appear. Only the leading independent components need to be analyzed to detect and characterize the inhomogeneities of interest, and other components can be discarded.

### 3.2.3 Fluorescent Inhomogeneity

The formalism for fluorescence OPTICA is based on the premise that the spatial distribution of the light intensity at the exit boundary of the medium is a weighted mixture of signals arriving from the fluorescent targets (‘sources’) embedded in the medium:

$$\boldsymbol{x}(\mathrm{r}_{\boldsymbol{d}},\mathrm{r}_{\boldsymbol{s}}) = \Sigma_{\boldsymbol{j}}\, \boldsymbol{a}_{\boldsymbol{j}}(\mathrm{r}_{\boldsymbol{d}})\boldsymbol{s}_{\boldsymbol{j}}(\mathrm{r}_{\boldsymbol{s}}) \qquad (3.16)$$

where $a_j(\mathbf{r}_d)$ is the mixing vector and $a_j(\mathbf{r}_d)s_j(\mathbf{r}_s)$ represents contribution of the $j^{\text{th}}$ target to the fluorescent signal at the detector plane for illumination of the source plane at $\mathbf{r}_s$. Independent component analysis assumes that these fluorescent sources are independent, treats the problem of detecting those as a source separation problem, and obtains $a_j$ and $s_j$ by seeking maximal mutual independence between $s_j$'s [14,12].

Light propagation in a highly scattering medium with an embedded fluorescent target excited by an external light source is approximately described by coupled diffusion equations at the excitation and emission wavelengths [16,17]. The fluorescence signal $U_m(\mathbf{r}_d,\mathbf{r}_s,\omega)$ can be expressed in terms of the two Green's functions $G_x(\mathbf{r},\mathbf{r}_s,\omega)$ and $G_m(\mathbf{r}_d,\mathbf{r},\omega)$ describing light propagation from the excitation source at $\mathbf{r}_s$ to the fluorescent target at $\mathbf{r}$ at the excitation wavelength $\lambda_x$, and the light propagation from the target to the detector at $\mathbf{r}_d$ at the emission wavelength $\lambda_m$. Again a slab sample is used with the corresponding Green's functions for slab geometry [18] under the diffusion approximation of the radiative transfer equation.

Assuming the $j^{\text{th}}$ fluorescent target is contained in volume $V_j$, centered at $\mathbf{r}_j$, the fluorescence signal under excitation by a unit point source at $\mathbf{r}_s$ is given by

$$U_m(\mathbf{r}_d,\mathbf{r}_s,\omega)=\sum_{j=1}^{J} G_m(\mathbf{r}_d,\mathbf{r}_j,\omega)f_j(\omega)G_x(\mathbf{r}_j,\mathbf{r}_s,\omega) \qquad (3.17)$$

where $f_j(\omega) = \gamma(\mathbf{r}_j)cV_j/[1-i\omega\tau(\mathbf{r}_j)]$ represents the fluorescence signal strength of the $j^{\text{th}}$ target, $\gamma$ is the fluorescent yield, $c$ is the speed of light in medium, $\tau$ is the fluorescence lifetime, and $\omega$ is the angular modulation frequency of the excitation light intensity.

Both the location and the strength of the $j^{th}$ target can be computed by using a least square fitting procedure:

$$\min_{r_j,\alpha_j,\beta_j}\left\{\sum_{r_s}\left[\alpha_j^{-1}s_j(\mathbf{r}_s)-G_x(\mathbf{r}_j,\mathbf{r}_s)\right]^2+\sum_{r_d}\left[\beta_j^{-1}a_j(\mathbf{r}_d)-G_m(\mathbf{r}_d,\mathbf{r}_j)\right]^2\right\} \quad (3.18)$$

where $s_j(\mathbf{r}_s)\propto G_x(\mathbf{r}_j,\mathbf{r}_s,\omega)$ and $a_j(\mathbf{r}_d)\propto G_m(\mathbf{r}_d,\mathbf{r}_j,\boldsymbol{\omega})$. The fitting yields the location $\mathbf{r}_j$ of and the two scaling constants $\alpha_j$ and $\beta_j$ for the $j$-th target. The fluorescence strength then is, $f_j = \alpha_j\beta_j$.

## 3.3 Methods and Materials

The homogenous scattering media used in the experiments of this chapter are suspensions in water of Intralipid 10% fat emulsion (a product of Phamacia-Upjohn distributed by VWR Scientific Products). It has been widely used to simulate the optical absorption and scattering characteristics of human breast tissue. However, it does not simulate the non-homogeneous nature of breast tissue. van Staveren *et al* investigated the optical properties of Intralipid 10% over the wavelength range of 400-1100 nm, the results with 5% error shows that the anisotropy factor $\langle g \rangle$ is a linear function of the wavelength ($\lambda$ in units of microns):

$$g(\lambda) = 1.1 - 0.58\lambda(\mu m) \qquad (3.19)$$

The scattering coefficient ($\mu_s$) was interpolated empirically from the compiled data and shows a nonlinear relationship dependence on wavelength giving by

$$\mu_s(\lambda) = 0.016\lambda^{-2.4} \qquad (3.20)$$

where $\lambda$ is wavelength in $\mu$m, $\mu_s$ is the scattering coefficient in $mL^{-1}$ L $mm^{-1}$ [41].

### 3.3.1 Absorptive sample

The first set of absorptive targets, shown schematically in Figure 3.1, were two cylindrical glass tubes filled with an absorbing solution that were placed inside a 250 mm x 250 mm x 50 mm transparent plastic container filled with Intralipid-10% suspension in water. The concentration of Intralipid-10% was adjusted to provide a transport length $l_t$ = 1 mm and an absorption coefficient $\mu_a$ = 0.003 $mm^{-1}$ at 785 nm, emulating those of human breast tissue. The cylindrical glass tubes (outer diameter 8 mm, inner diameter

7 mm and length 250 mm) were filled with an Intralipid-10% suspension to provide the same scattering coefficient, but the absorption coefficient was changed to 0.023 $mm^{-1}$ by the addition of absorbing ink. The two absorptive tubes were placed at locations #1: ($x$,$z$) = (24,29) mm and #2: ($x$,$z$) = (47,33) mm, respectively, with the axes of cylindrical tubes along $y$-axis. For the long cylindrical tubes in absorption specimen 1, a line scan of 16 points with a step size of 2.5 mm along the $x$-axis was enough to obtain ($x$,$z$) the locations of the absorbing cylinders.

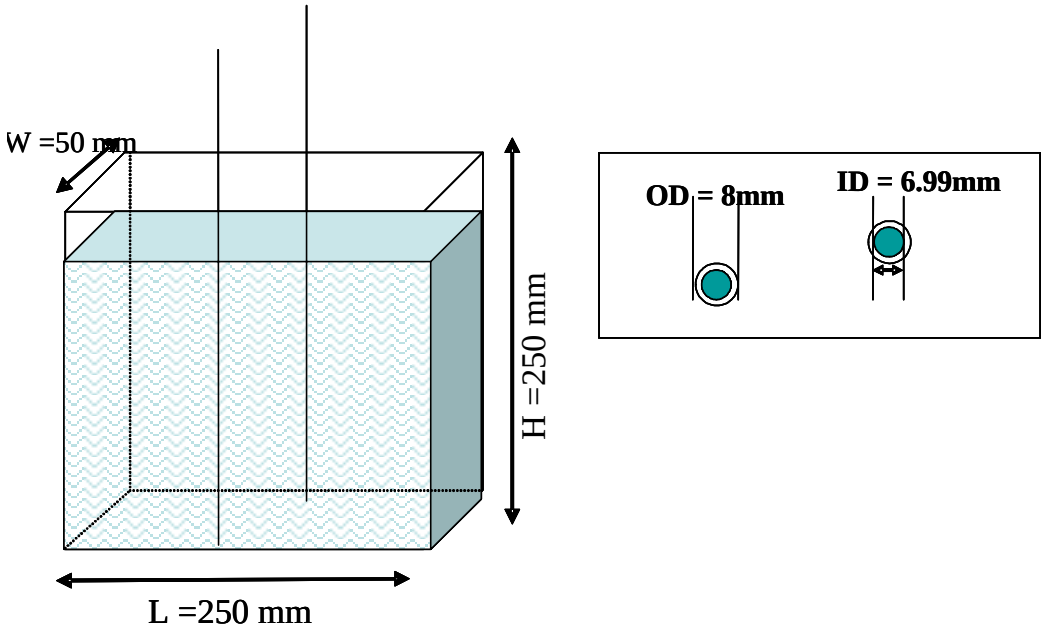


Figure 3.1: (a) Front view, and (b) top view of a250 mm x 250 mm x 50 mm transparent plastic container filled with Intralipid10% suspension in water. The concentration of Intralipid 10% was adjusted to provide a transport length $l_t$=1 mm and an absorption coefficient $\mu$ = 0.003 $mm^{-1}$ at 785 nm. Two cylindrical glass tubes of length = 250 mm, outer diameter OD= 8 mm and inner diameter ID= 6.98 mm were filled with an Intralipid 10% suspension to provide the same scattering coefficient, but the absorption coefficient was changed to 0.023 $mm^{-1}$ by the addition of absorbing ink.

### 3.3.2 Scattering sample

Two different scattering samples were used in the experiments reported here. The first single scattering target (SST) sample was a 250 mm x 250 mm x 50 mm transparent

plastic cell filled with Intralipid-10% suspension in water. The concentration of Intralipid-10% was adjusted to provide a transport length $l_t$ of ~2 mm at 785 nm. A ~9 mm diameter glass sphere filled with a suspension of 0.707μm diameter polystyrene spheres in water was the scattering target. The micro-spheres do not absorb 785 nm light, and their concentration was adjusted to provide a scattering length, $l_s$ of ~0.0188 mm, transport length $l_t$ of ~0.133 mm, and anisotropy factor, $\langle g \rangle$ ~0.858. The location of the center of the target was (25 mm, 25 mm, 21 mm) with respect to the front upper left corner of the sample cell see inset of Figure 3.2. This sample was used to test the predictions of the theoretical formalism.

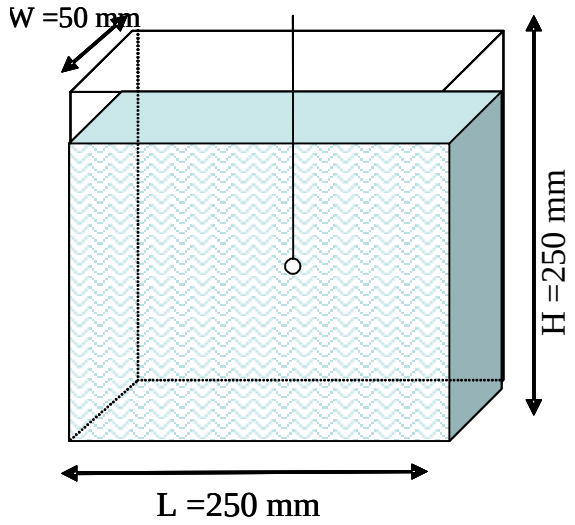


Figure 3.2: A 250 mm x250 mm x 50 mm transparent plastic container filled with Intralipid 10% suspension in water. The concentration of Intralipid 10% was adjusted to provide a transport length $l_t$ =2 mm and an absorption coefficient $\mu$ = 0.003 $mm^{-1}$ at 785 nm. A ~9 mm diameter glass sphere filled with a suspension of 0.707 μ**m** diameter polystyrene spheres in water was. The micro-sphere concentration was adjusted to provide a scattering length $l_s$ ~0.0188 mm, transport length $l_t$ ~0.133 mm, and anisotropy factor $\langle \mathbf{g} \rangle$ ~0.858.

Figure 3.3 shows the second sample multi-scattering target (MST) as a 166 mm long, 82 mm wide, and 55 mm thick scattering slab cast from a suspension of titanium dioxide particles and a near-infrared dye in epoxy resin containing 4 cylindrical scattering

targets [42]. The slab material had an optical transport length of ~1.1 mm, and absorption coefficient of 0.006 $mm^{-1}$. Each of the four cylinders had a length of 5 mm, a diameter of 5 mm, absorption coefficient equal to that of the slab material, and scattering coefficients 4, 2, 1.5, and 1.1 times higher than that of the slab. The first and the third cylinders, and the second and the fourth cylinders, are on two horizontal lines approximately 22 mm apart. The distance between neighboring cylinders is 11 mm. The center of each cylinder was located in the plane halfway between the front and back surfaces of the slab, and their known coordinates are presented in column 3 of Table 3.1. The second sample was used to test the efficacy of OPTICA on a breast-simulating specimen. Scattering sample 1 was scanned in an x-y array of 21 x 21 grid points with a step size of 2.5 mm across the laser beam, while scattering sample 2 was scanned in a 20 x 18 array of same step size.

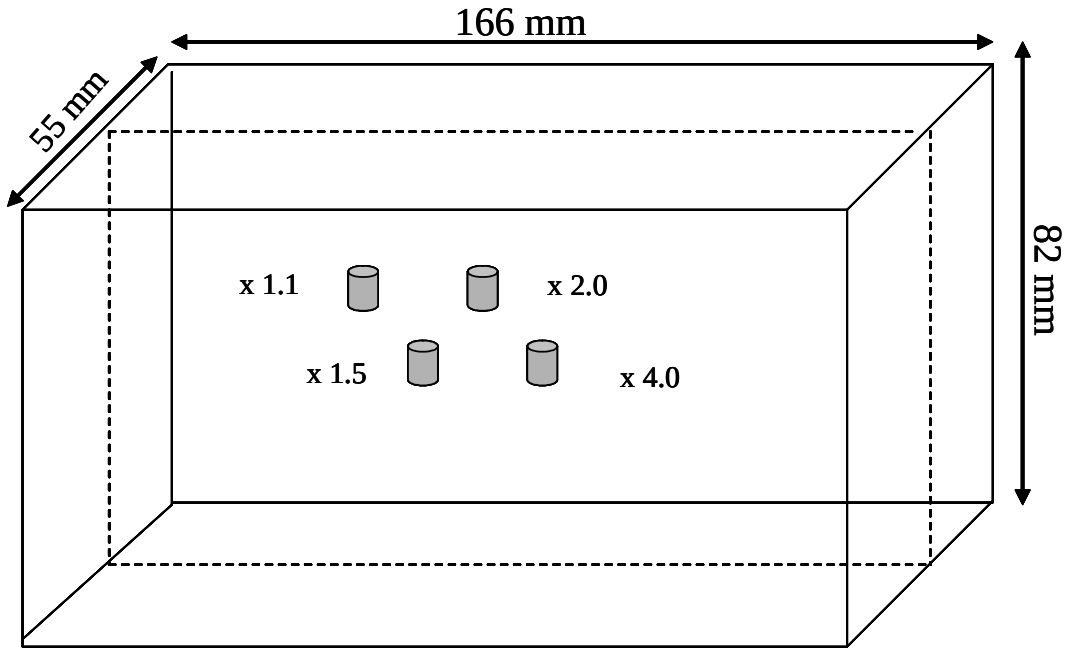


Figure 3.3: Schematic diagram of multi-scattering target (MST), a 166 mm long, 82 mm wide and 55 mm thick scattering slab containing four cylindrical scattering targets of dimension 5 mm long and 5 mm diameter. The axes of the four cylinder targets were vertically aligned on the mid plane of the slab.

### 3.3.3 Fluorescent sample

The fluorescent target was a glass sphere (outer diameter ~4 mm and inner diameter 3.2 mm) filled with a solution of indocyanine green (ICG) in water. The water solution of ICG had an absorption coefficient of 11.5 $cm^{-1}$ at 785 nm, and fluoresced over the 790-966 nm spectral range with a peak at 825 nm as displayed in Figure 3.4. In this experiment we test if the approach could locate a target inside an average-size human female breast, the sphere was placed inside a 250 mm x 250 mm x 50 mm transparent plastic cell filled with Intralipid 10% suspension in water as shown in Figure 3.5. The concentration of Intralipid-10% was adjusted to provide a transport length $l_t$ of ~1 mm at 785 nm, and 1.1 mm at 830 nm which is within the reported range of values for healthy human breast tissues [19].

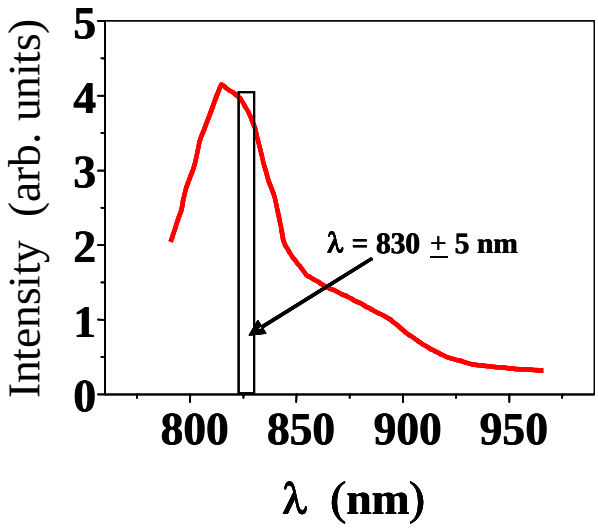


Figure 3.4: Fluorescent spectra of ICG in water solution. The black rectangle box spectral response of the narrow band filter used in the experiment

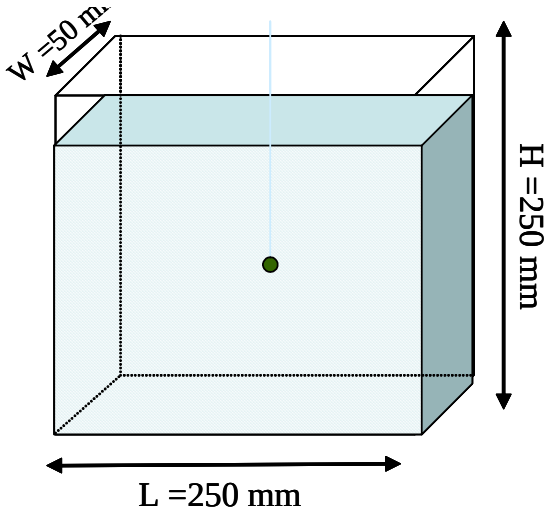


Figure 3.5: An L= 250 mm x H= 250 mm x W= 50 mm transparent plastic container filled with Intralipid 10% suspension in water. The concentration of Intralipid 10% was adjusted to provide a transport length $l_t$ =1 mm and an absorption coefficient $\mu_a$ = 0.003 $mm^{-1}$ at 785 nm. A ~4 mm diameter glass sphere filled with an ICG in water solution.

### 3.3.4 Experimental setup

The experimental arrangement for demonstrating the efficacy of OPTICA is shown schematically in Figure 3.6. Continuous wave 785 nm radiation from a diode laser (Ocean Optics R-2000) delivered by a 200-μm optical fiber was used for illuminating the entrance face (henceforth referred to as the 'source plane') of the slab sample. Multiple source illumination was realized in practice by step scanning the slab sample along the horizontal (*x*) and vertical (*y*) directions across the laser beam using xy-computer control stage. A camera lens of focal length (*f* = 50 mm) collected the diffusely transmitted light on the opposite face of the slab (henceforth referred to as the 'detection plane') sample and projected it onto the sensing element of a liquid cooled (-40° Celsius) charged couple device (CCD) camera (photometric model CH-350). Each illuminated pixel of the 1024x1024 pixels of the CCD camera could be regarded as a detector. For illumination of every scanned point on the source plane, the CCD camera recorded the diffusely transmitted intensity pattern on the detection plane.

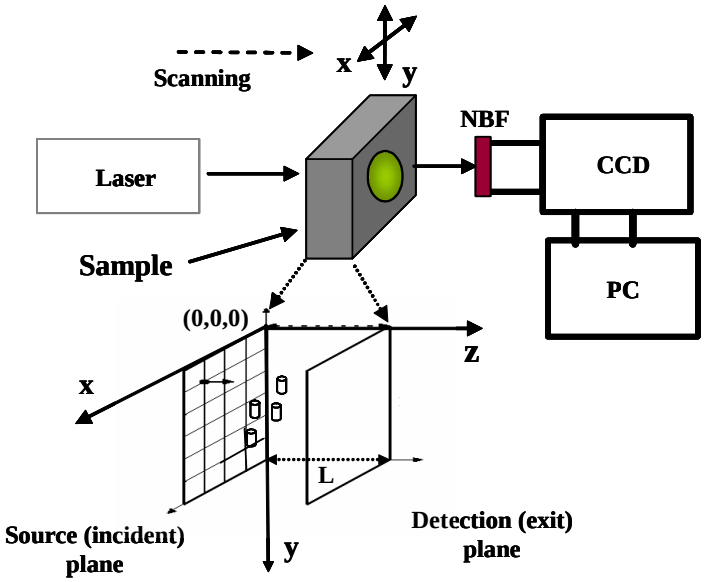


Figure 3.6: Schematic diagram of the experimental arrangement. Inset shows a 2-D array of horizontal and verical points in the input plane that are scanned across the laser beam. Key: PC= computer, CCD= charge coupled device and NBF= narrow band filter.

## 3.4 Algorithm

A schematic diagram of OPTICA algorithm is shown in Figure 3.7. A series of images corresponding to the scanned points of sample were fed into the first phase of the program. Each image was filtered for hot spots (i.e. pixels whose value is saturated), replacing those pixels by a neighborhood average. For example, a 16-bit CCD camera will have maximum intensity value per pixel $2^{16}$-1 = 65535. The program then cropped each image, removing the dark region (no information) from the lighted region, as demonstrated in Figure 3.8 (a).

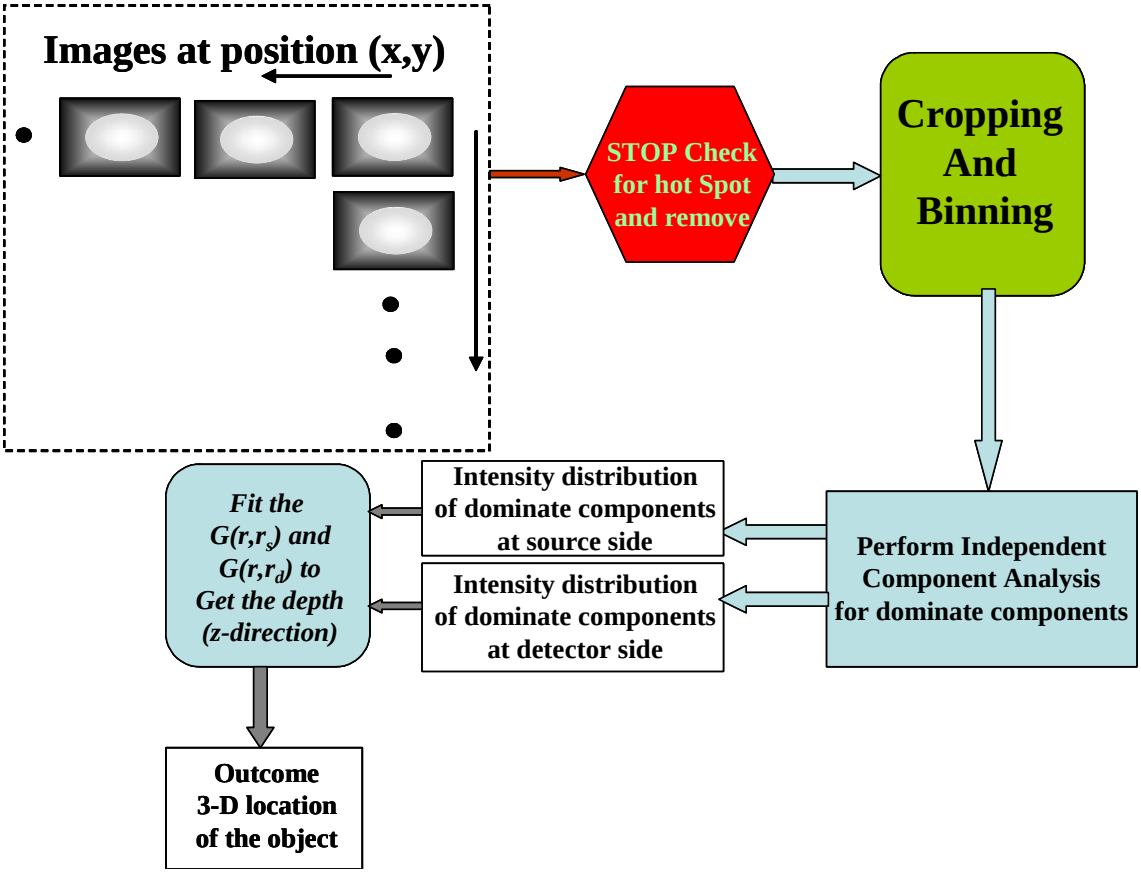


Figure 3.7: Schematic of OPTICA algorithm

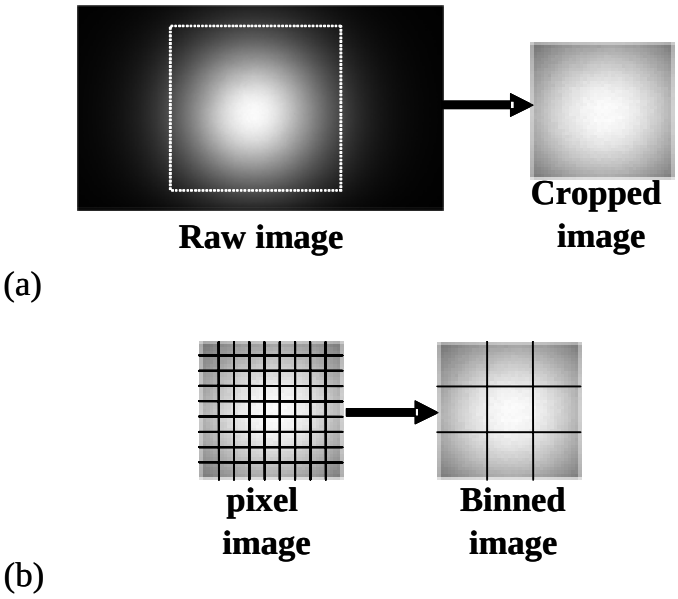


Figure 3.8: (a) typical raw image recorded by the CCD, and how it is cropped (b) Cropped image being binned for analysis

After the cropping process, the image underwent binning, which means adding an area of $n \times n$ pixels to make a super-pixel as shown in Figure 3.8 (b). The binning process improves the image quality by lowering the pixel-to-pixel intensity fluctuation and compresses the image matrix size, which help reduce computational time. After this initial cosmetic image processing the image series undergoes the independent components analysis (ICA) and generate the components at both detector and source plane (see Appendix A). The contribution of each target to $\phi_{sca}$ on the detection plane (and also on the source plane) can be obtained as a two-dimensional (2D) independent intensity distribution (IID). IID due to a target may be looked upon as the light intensity pattern that a source located at the target position would generate on the detection (or source) plane. The 3-D location of the target relative to sample boundaries is estimated from fits of these OPTICA generated IID to the model Green's functions.

## 3.5 Experimental Results

ICA of the perturbations in the spatial intensity distributions provided the corresponding independent intensity distributions (IID) on the source and detector planes.

### 3.5.1 Absorptive target

Figure 3.9 shows the results for the two absorbing cylinders. The locations of the absorbing cylinders are obtained from fitting these independent component intensity distributions to those of the DA in a slab [Eq. 3.2]. The first cylinder is found at $x$ = 24 mm, 29 mm away from the source plane and 21 mm away from the detector plane. The second cylinder is found at $x$ = 47 mm, 33 mm away from the source plane and 17 mm away from the detector plane. The ($x$,$z$) coordinates of both the cylinders agree to within 0.5 mm of their known locations. The absorption strengths of the two rods are estimated by use of a least-square fitting procedure [Eq. 3.7].

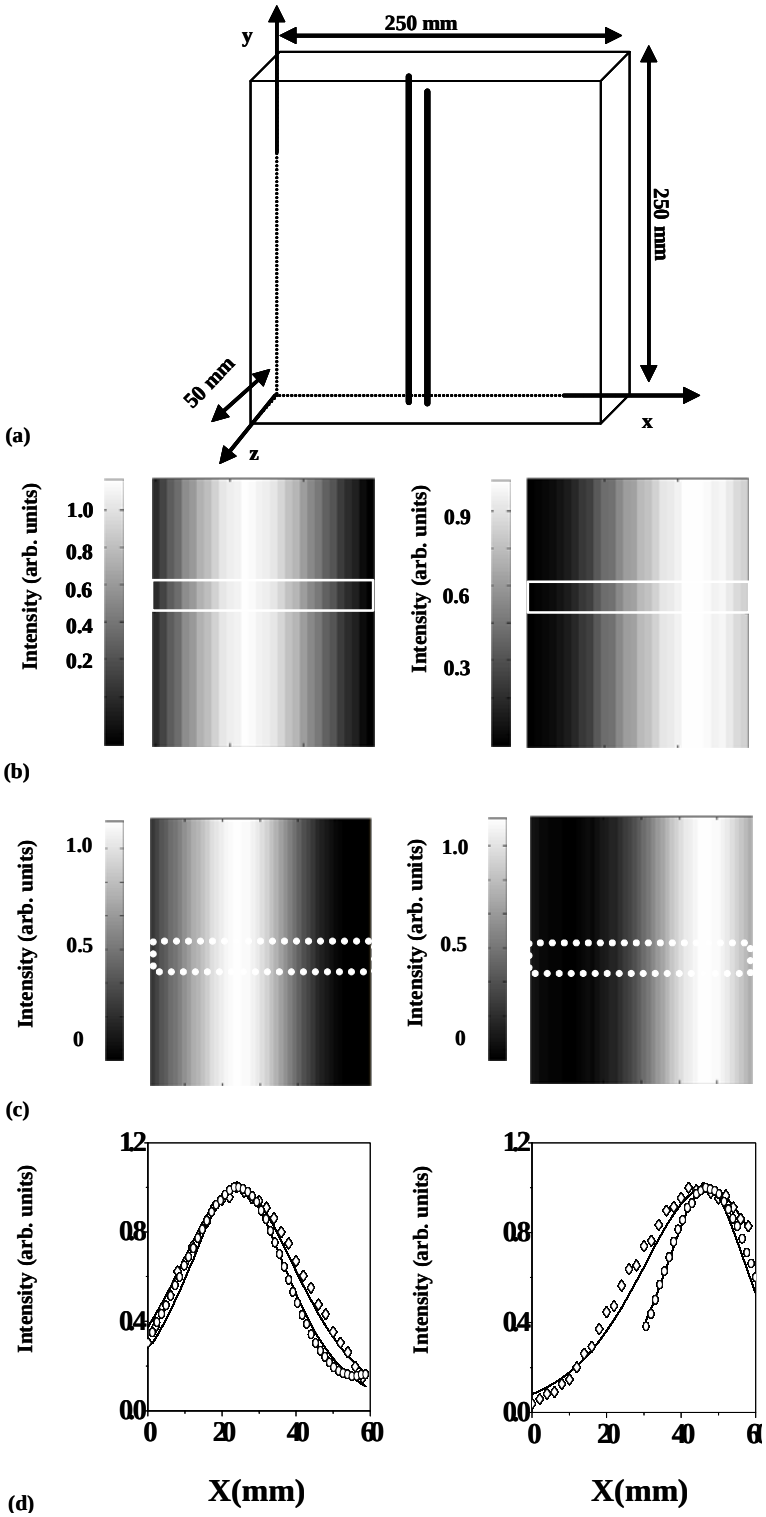


Figure 3.9: Schematic showing the positions of the absorbing cylindrical tubes in the Intralipid 10% suspension (Specimen 1). Independent spatial intensity distributions (independent components) in th (b) input plane and (c) exit plane of the specimen. (d) Green function obtained using these independent components provide the locations of the two absorbing inhomogeneities.

### 3.5.2 Scattering target

OPTICA generated 2-D independent intensity distributions (IIDs) at the detection plane for the single scattering target (SST) are presented in the upper frames of Figure 3.10 (a)–(c). The corresponding spatial intensity profiles integrated over the areas enclosed by white dashed boxes appear in the lower frames. As predicted by the theoretical formalism, three intensity distributions from three virtual sources corresponding to the single scattering target are observed. The spatial intensity profile of Figure 3.10 (a) is symmetric about the vertical centerline (centrosymmetric), the profile of Figure 3.10 (b) has a peak followed by a dip, and that of Figure 3.10 (c) has a dip followed by a peak, and resembles the predicted dumbbell shape. The location of the target determined by the Green's function fit of the intensity distribution was (23 mm, 25 mm, 22 mm), which agrees well with the known position of (25 mm, 25 mm, 21 mm). The relative peak intensity of the centrosymmetric component is approximately 3x larger than that of the dumbbells. For more highly scattering samples and with decrease of the signal-to-noise ratio, the dumbbell-shaped components get much reduced in intensity, and may not be observable. It should be mentioned that an absorptive target generates only a centrosymmetric IID.

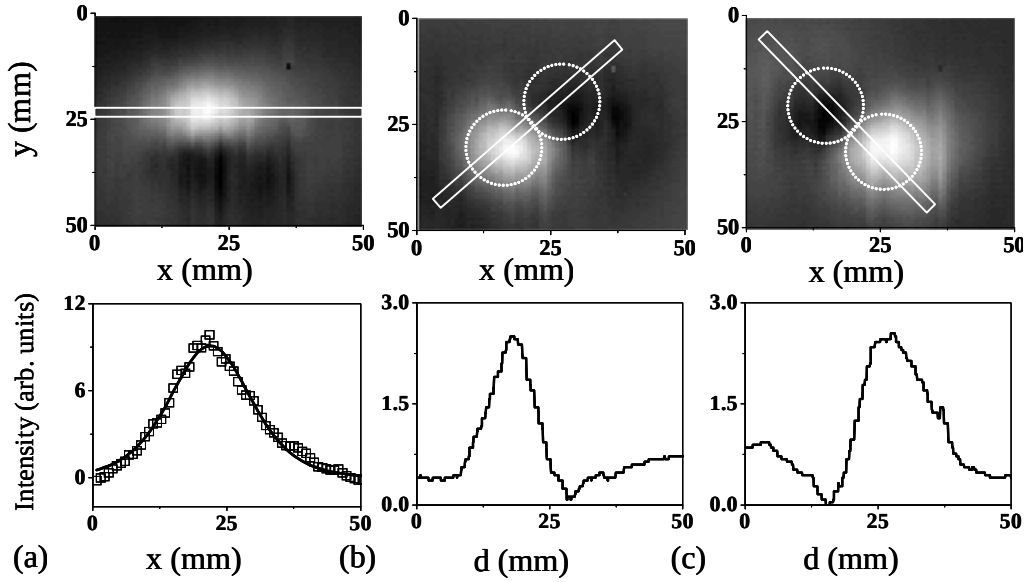


Figure 3.10: Independent 2-D spatial intensity distributions at the detection plane of the scattering sphere in single scattering target (SST) generated by OPTICA: (a) the centrosymmetric component, (b) and (c) the dumbbell shaped components. The white dotted circles in the images presented in (b) and (c) are provided as a guide for the eye to show the high intensity and low intensity areas of the dumbbell. The white rectangles in the images are the regions that are integrated over to generate the spatial profiles.

### 3.5.3 Multiple scattering targets

The independent intensity distributions at the detector plane corresponding to multiple scattering targets, for the four scattering inhomogeneities in MST specimen are displayed in Figure 3.11 (a)–(d). These independent components are then used to obtain the projections of the inhomogeneity detector Green's function, $G(r_d, r_j)$, j = 1, 2, 3, 4, on the detector plane for the four small cylindrical scattering inhomogeneities embedded in MST specimen . The locations of the inhomogeneities are determined by fitting the projections to those of the model Green's function as shown in Figure 3.11 (e)–(h). The locations of all four inhomogeneities were found.

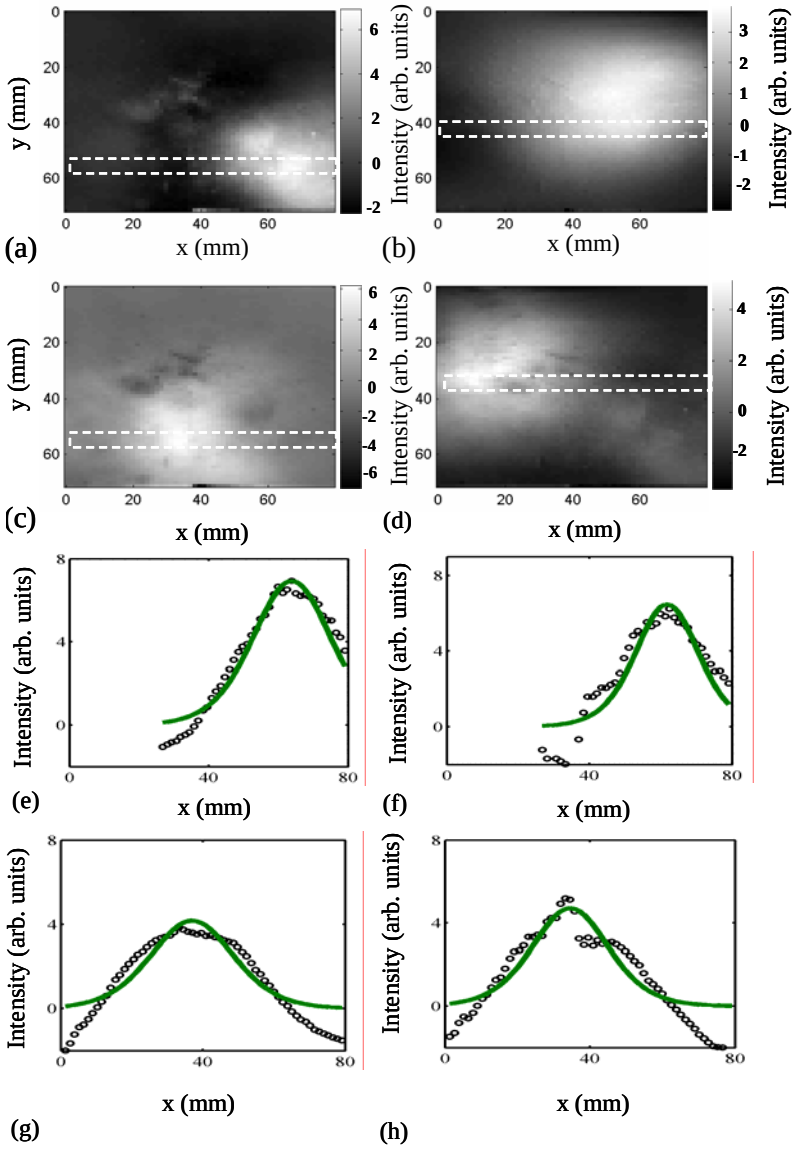


Figure 3.11: OPTICA generated independent intensity distributions (upper frames) on the detection plane for the target with scattering coefficients (a) 4x, (b) 2x, (c) 1.5x and (d) 1.1x that of the slab material. (e)-(h) Corresponding horizontal profiles of intensity distributions are shown by circles in the corresponding lower frames, while the solid green lines represent the Green function fit for extracting target locations.

Even the weakest scatterer, with a scattering coefficient just 1.1 times the background and hence considered to be rather unlikely to be found, [42] was detected. Positions of the cylinders along the *z*-axis (depth) were found to be at 28.1 mm, 27.9 mm, 27.1 mm, and 32.6 mm. Except for the last cylinder, the depth of the cylinders agree well with their known center positions of 27.5 mm. The lateral positions are determined to be

(62, 63), (48, 33), (33, 62), and (18, 33) mm for the four scattering cylinders (see Table 3.1). The strongest and the third-strongest scatterers are on the same horizontal line y = 62 mm, whereas the second strongest and the weakest scatterers are on the horizontal line y = 33 mm with a spacing of 29 mm. The four scatterers are separated by equal spacing, ~14 mm in the horizontal direction. The lateral positions agree well with the known (x, y) coordinate values. The uncertainties in location and separation are not greater than 3 mm except for the weakest target.

Table 3.1: Comparison of Known and OPTICA-Determined Positions of the Four Targets

| Target | $\mu_{s,target}/\mu_{s,slab}$ | Known position (x, y, z) mm | Observed position (x, y, z) mm | Error ($\Delta$x, $\Delta$y, $\Delta$z) mm |
|---|---|---|---|---|
| #1 | 4 | (60, 60, 27.5) | (62, 63, 28.1) | (2, 3, 0.6) |
| #2 | 2 | (47, 30, 27.5) | (48, 33, 28.9) | (1, 3, 1.4) |
| #3 | 1.5 | (23, 30, 27.5) | (18, 33, 32.6) | (5, 3, 5.1) |
| #4 | 1.1 | (33, 60, 27.5) | (33, 62, 27.1) | (0, 2, 0.4) |

### 3.5.4 Fluorescent target

The fluorescent target (FT) in this case was the 4 mm diameter sphere. Independent components analysis used the set of 100 images to generate independent intensity distribution on source and detector planes, as shown in Figure 3.12 (a) and (b), respectively. The Green's function (solid line) fit to these intensity distributions represented by squares for the source plane and by circles for the detector plane are shown in Figure 3.12 (c) and (d), respectively. The x-y-z coordinates of the fluorescence target (FT) were estimated to be approximately, $x$ = 15 mm, $y$ = 15 mm, and $z$ = 16 mm,

which are in excellent agreement with the known location of $x$ = 15 mm, $y$ = 15 mm, and $z$ = 15 mm.

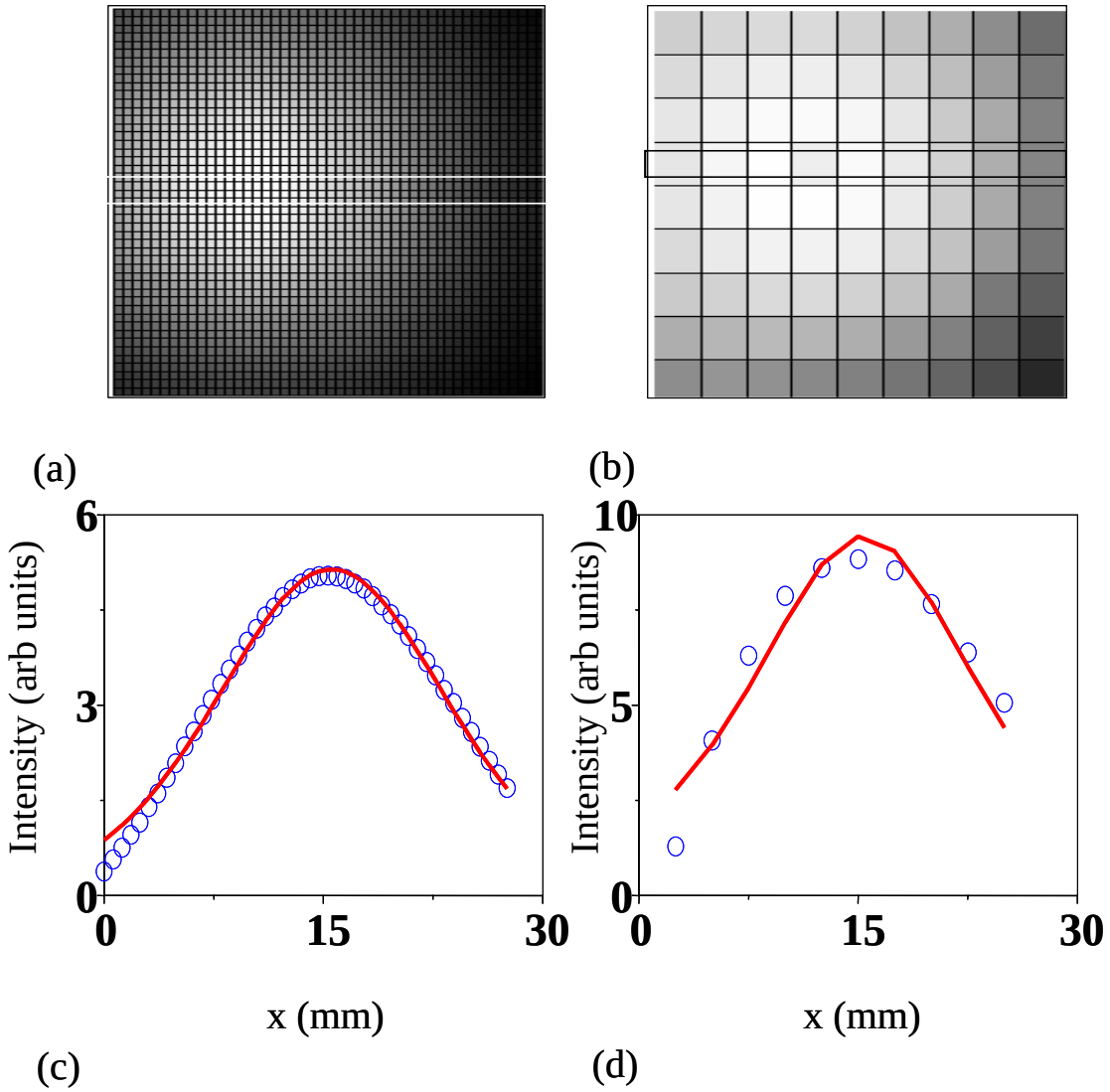


Figure 3.12: OPTICA generated independent intensity distributions (upper frames) on the (a) detection plane, and (b) source plane for the fluorescent target. (c) and (d) corresponding horizontal profiles of intensity distributions are shown by blue circles in the corresponding lower frames, while the solid red lines represent the Green's function fit for extracting target locations.

## 3.6 Conclusion

The OPTICA presented in Chapter 3 introduces the information theory technique of ICA to the problem of optical tomographic imaging of objects in homogenous turbid media. It is shown to provide object locations accurate to ~1 mm in human-breast-like turbid media. It uses multiple-source (realized in this case through scanning of the sample in the xy-plane across the incident beam propagating in the z-direction) illumination and a multiple-detector (each pixel on the CCD may be viewed as a detector) data-acquisition scheme. The resulting spatial diversity and multiple angular observations provide robust data for extracting 3-D location information about the embedded objects (inhomogeneities) in the medium. A salient feature of OPTICA is that ICA provides the independent components due to the inhomogeneities with errors in location no greater than 3 mm. Under the favorable conditions of low scattering by the medium and high signal-to-noise ratio, as for SST sample, all three virtual sources can be discerned, and the target can be identified as a scatterer. For highly scattering medium (such as, MST sample), additional information, such as, measurements at different wavelengths are needed for identification of the target as a scatterer or an absorber.

OPTICA can be used for locating absorptive and scattering targets as well [12]. The advantage for the fluorescent target (FT) is that the background light can be minimized by use of appropriate filters, making it a ‘zero-background’ measurement in principle, as opposed to the situations involving absorptive and scattering targets when changes in high light levels are measured. The 3-D localization of the object is achieved with a high accuracy, and shorter computation time compared to other commonly used methods.

Processing of the data does not have to resort to any specific light propagation model for obtaining this information. Specific light propagation models are needed only in the later stage to determine the location by curve fitting of the Green's functions. OPTICA is not model specific; any appropriate model for light propagation, including the DA and the cumulant solutions of the RTE, may be used. Although we used the slab geometry, the approach does not depend on any specific geometry. It may be used for other geometries or even an arbitrary-shaped boundary. The approach is fast and is expected to be amenable to near-real-time detection and localization of objects in a turbid medium, which is a key consideration for *in vivo* medical imaging. The approach is remarkably sensitive, considering that it could discern all four cylinders in MST specimen. The approach successfully detected even the lowest-contrast inhomogeneity of the four, which had a reduced scattering coefficient (only 10% higher than the surrounding medium), and was considered unlikely to be detected [42]. OPTICA obtains locations of the objects by fitting either or both of the Green's functions $G(\mathbf{r}, \mathbf{r}_s)$ and $G(\mathbf{r}_d, \mathbf{r})$, and is suited for physically small inhomogeneities. Given its capability of identifying low-contrast small objects, the approach is expected to be useful for detecting tumors at their early stages of growth, a coveted goal in medical imaging.

When both absorptive and scattering objects are present in the same turbid specimen, OPTICA can locate them, but their identification as absorbing or scattering entities becomes a more challenging task. Multiwavelength spectroscopic imaging measurements have the potential to provide diagnostic information, such as whether a tumor is malignant or benign.

In summary, OPTICA has the potential to emerge as a new versatile tool for locating targets in turbid media.

Detail of the programs that implemented the OPTICA program is presented in Appendix A. The programs was written in the MATLAB language (v. 6.5-7.01), which ran on Debian GNU/Linux platform (v 3.1)/ Microsoft window 2000. The computer processor used a Pentium4 (2.4 GHz). The computation time for each output file varies from sample to sample and on the average of < 1 minute.

## 3.7 References


1. G. Muller, R. R. Alfano, S. R. Arridge, J. Beuthan, E. Gratton, M. Kaschke, B. R. Masters, S. Svanberg, and P. van der Zee, eds., “Medical Optical Tomography: Functional Imaging and Monitoring”, Vol. **IS11** of SPIE Institute Series (SPIE, Bellingham, Wash., 1993).
2. A. Yodh and B. Chance, "Spectroscopy and imaging with diffusing light," Phys. Today **48**, 38-40 (1995).
3. M. A. O'Leary, D. A. Boas, B. Chance, and A. G. Yodh, "Experimental images of heterogeneous turbid media by frequency-domain diffusing-photon tomography," Opt. Lett. **20**, 426-428 (1995).
4. S. K. Gayen and R. R. Alfano, "Emerging optical biomedical imaging techniques," Opt. Photon. News **7**, 17-22 (1996).
5. J. C. Hebden, S. R. Arridge, and D. T. Delpy, "Optical imaging in medicine: I. Experimental techniques," Phys. Med. Biol. **42**, 825-840 (1997).
6. S. R. Arridge and J. C. Hebden, "Optical imaging in medicine: II. Modeling and reconstruction," Phys. Med. Biol. **42**, 841-853 (1997).
7. W. Cai, S. K. Gayen, M. Xu, M. Zevallos, M. Alrubaiee, M. Lax, and R. R. Alfano, "Optical tomographic image reconstruction from ultrafast time-sliced transmission measurements," Appl. Opt. **38**, 4237-4246 (1999).
8. S. R. Arridge, "Optical tomography in medical imaging," Inverse Probl. **15**, R41-R93 (1999).

9. D. Grosenick, H. Wabnitz, H. H. Rinneberg, K. T. Moesta, and P. M. Schlag, "Development of a time-domain optical mammograph and first in vivo applications," Appl. Opt. **38**, 2927-2943 (1999).
10. V. Chernomordik, D. Hattery, A. H. Gandjbakhche, A. Pifferi, P. Taroni, A. Torricelli, G. Valentini, and R. Cubeddu, "Quantification by random walk of the optical parameters of nonlocalized abnormalities embedded within tissuelike phantoms," Opt. Lett. **25**, 951-953 (2000).
11. V. A. Markel and J. C. Schotland, "Inverse scattering for the diffusion equation with general boundary conditions," Phys. Rev. E **64**, 035601 (2001).
12. A. H. Hielscher and S. Bartel, "Use of penalty terms in gradient-based iterative reconstruction schemes for optical tomography," J. Biomed. Opt. **6**, 183-192 (2001).
13. M. Xu, M. Lax, and R. R. Alfano, "Time-resolved Fourier optical diffuse tomography," J. Opt. Soc. Am. A **18**, 1535-1542 (2001).
14. B. A. Brooksby, H. Dehghani, B. W. Pogue, and K. D. Paulsen, "Near-infrared (NIR) tomography breast image reconstruction with a priori structural information from MRI: algorithm development for reconstructing heterogeneities," IEEE J. Sel. Top. Quantum Electron. **9**, 199-209 (2003).
15. H. Dehghani, B. W. Pogue, S. P. Poplack, and K. D. Paulsen, "Multiwavelength three-dimensional near-infrared tomography of the breast: initial simulation, phantom, and clinical results," Appl. Opt. **42**, 135-145 (2003).

16. J. C. Hebden, D. A. Boas, J. S. George, and A. J. Durkin, "Topics in biomedical optics: introduction," Appl. Opt. **42**, 2869-3329 (2003).
17. W. Cai, M. Xu, and R. R. Alfano, "Three dimensional radiative transfer tomography for turbid media," IEEE J. Sel. Top. Quantum Electron. **9**, 189-198 (2003).
18. L. Wang, P. P. Ho, C. Liu, G. Zhang, and R. R. Alfano, "Ballistic 2-D imaging through scattering walls using an ultrafast optical Kerr gate," Science **253**, 769-771 (1991).
19. R. R. Alfano, X. Liang, L. Wang, and P. Ho, "Time-resolved imaging of translucent droplets in highly scattering media," Science **264**, 1913-1914 (1994).
20. W. Cai, M. Lax, and R. R. Alfano, "Analytical solution of the elastic Boltzmann transport equation in an infinite uniform medium using cumulant expansion," J. Phys. Chem. B **104,** 3996-4000 (2000).
21. W. Cai, M. Lax, and R. R. Alfano, "Analytical solution of the polarized photon transport equation in an infinite uniform medium using cumulant expansion," Phys. Rev. E **63**, 016606 (2000).
22. M. Xu, W. Cai, M. Lax, and R. R. Alfano, "Photon migration in turbid media using a cumulant approximation to radiative transfer," Phys. Rev. E **65**, 066609 (2002).
23. F. Natterer, “The Mathematics of Computerized Tomography” Wiley, New York, (1986).

24. A. H. Gandjbakhche, G. H. Weiss, R. F. Bonner, and R. Nossal, "Photon path-length distributions for transmission through optically turbid slabs," Phys. Rev. E **48**, 810-818 (1993).

25. A. H. Gandjbakhche, V. Chernomordik, J. C. Hebden, and R. Nossal, "Time-dependent contrast functions for quantitative imaging in time-resolved transillumination experiments," Appl. Opt. **37**, 1973-1981 (1998).

26. P. Comon, "Independent component analysis - a new concept?" Signal Process. **36**, 287-314 (1994).

27. A. J. Bell, "Information theory, independent component analysis, and applications," in Unsupervised Adaptive Filtering, Vol. **I**, S. Haykin, pp. 237-264. ed. Wiley, New York, (2000).

28. D. Nuzillard and J.-M. Nuzillard, "Application of blind source separation to 1-D and 2-D nuclear magnetic resonance spectroscopy," IEEE Signal Process. Lett. **5**, 209-211 (1998).

29. R. Vigário, J. Särelä, V. Jousmäki, M. Hämäläinen, and E. Oja, "Independent component approach to the analysis of EEG and MEG recordings," IEEE Trans. Biomed. Eng. **47**, 589-593 (2000).

30. A. Hyvärinen, J. Karhunen, and E. Oja, “Independent Component Analysis” Wiley, New York, (2001).

31. P. M. Morse and H. Feshbach, “Methods of Theoretical Physics” McGraw-Hill, New York, (1953), Vols. **I** and **II**.

32. M. Xu, W. Cai, M. Lax, and R. R. Alfano, "A photon transport forward model for imaging in turbid media," Opt. Lett. **26**, 1066-1068 (2001).

33. S. Chandrasekhar, “Radiative Transfer” Dover, New York, (1960).

34. M. Lax, V. Nayaramamurti, and R. C. Fulton, "Classical diffusion photon transport in a slab," in Laser Optics of Condensed Matter, J. L. Birman, H. Z. Cummins, and A. A. Kaplyanskii, eds. (Plenum, New York, 1987), pp. 229-237.

35. J. X. Zhu, D. J. Pine, and D. A. Weitz, "Internal reflection of diffusive light in random media," Phys. Rev. A **44**, 3948-3959 (1991).

36. R. C. Haskell, L. O. Svaasand, T.-T. Tsay, T.-C. Feng, M. S. McAdams, and B. J. Tromber, "Boundary conditions for the diffusion equation in radiative transfer," J. Opt. Soc. Am. A **11**, 2727-2741 (1994).

37. S. Roberts and R. Everson, eds., “Independent Component Analysis: Principles and Practice” Cambridge U. Press, Cambridge, UK, (2001).

38. J.-F. Cardoso, "Blind signal separation: statistical principles," Proc. IEEE **86**, 2009-2025 (1998).

39. M. V. Klein, “Optics” Wiley, New York, (1970).

40. H. Heusmann, J. Kölzer, and G. Mitic, "Characterization of female breasts in vivo by time resolved and spectroscopic measurements in near infrared spectroscopy," J. Biomed. Opt. **1**, 425-434 (1996).

41. H. J. van Staveren, C. J. M. Moes, J. van Marle, S. A. Prahl, and M. J. C. van Gemert, "Light scattering in intralipid-10% in the wavelength range of 400-1100 nm," Appl. Opt. **30**, 4507-4514 (1991).

42. D. J. Hall, J. C. Hebden, and D. T. Delpy, "Imaging very-low-contrast objects in breastlike scattering media with a time-resolved method," Appl. Opt. **36**, 7270-7276 (1997).

43. Q. Fu, F. Seier, S. K. Gayen, and R. R. Alfano, "High-average-power kilohertz-repetition-rate sub-100-fs Ti:sapphire amplifier system," Opt. Lett. **22**, 712-714 (1997).

# Chapter 4
# Optical Tomography using Independent Component Analysis for Target Detection, Localization and cross section reconstruction in *ex vivo* human breast tissue

## 4.1 Introduction

Optical tomography using independent component analysis (OPTICA) was introduced in Chapter 3. Detection and localization of single to multiple targets (absorbing, scattering and fluorescent) embedded in homogenous scattering medium was presented. In this chapter the approach is extended to *ex vivo* normal and cancerous human breast tissue, unlike the model scattering medial presented in Chapter 3, the optical properties of biological tissues are not homogenously distributed, which makes the imaging problem more challenging. Furthermore, Chapter 4 will augment Chapter 3 by introducing the cross-section reconstruction of the target using a back-projection Fourier transform. [1-20]

Chapter 4 is organized as follows: Section 4.2 reviews the theoretical framework for cross-section reconstruction; Section 4.3 presents the experimental methods, materials, and parameters. The results are presented in Section 4.4. Finally, the implications of these results and the scope of OPTICA are discussed in Section 4.5.

## 4.2 Theoretical Formalism

### 4.2.1 Cross-section reconstruction

The size and shape of the $j^{th}$ target can be estimated from a back-projection of $U_{mj}(\mathbf{r}_d, \mathbf{r}_s, \omega)$ from the detection plane onto the 'target plane,' *i.e.*, $z = z_j$ plane. The fluorescence/virtual source signal from the $j^{th}$ target is approximated by [21]

$$U_{m_j}(\mathbf{r}_d, \mathbf{r}_s, \omega) = \int G_m(\boldsymbol{\rho}_d - \boldsymbol{\rho}, \omega) X_j(\boldsymbol{\rho}) G_x(\boldsymbol{\rho} - \boldsymbol{\rho}_s, \omega) d\boldsymbol{\rho}, \qquad (4.1)$$

where the integration is over the $z = z_j$ plane, and $\boldsymbol{\rho}_d$ and $\boldsymbol{\rho}_s$ are the lateral coordinates of the detector and the source, respectively. In the Fourier space, $X_j(\mathbf{q})$ can be obtained from Eq. (4.1) as

$$X_j(\mathbf{q}) = \frac{U_{m_j}(\mathbf{q}-\mathbf{q}_s, \mathbf{q}_s, \omega)}{G_m(\mathbf{q}-\mathbf{q}_s, \omega) G_x^*(\mathbf{q}_s, \omega)}, \qquad (4.2)$$

where $\mathbf{q}$ and $\mathbf{q}_s$ are the spatial frequency on the *x-y* plane, and $^*$ denotes complex conjugate.

The inverse Fourier transform of $X_j(\mathbf{q})$ yields the cross sectional image of the fluorescent target in the $z = z_j$ plane. The full width at half maximum (FWHM) of the cross sectional image provides an estimate of the real target size [6,7,9-11,13-15,21].. The cross sectional image is a 2-D projection of the fluorescent object at the target plane. While the optical properties of the intervening medium determine the point spread function (PSF), the back-projection deconvolutes the effect of PSF to provide an estimate of the target size. The method can be applied for (absorbing and scattering) targets, as well.

## 4.3 Materials and Methods

The breast tissue specimens consisted primarily of adipose / glandular tissue with small amount of skin and were provided to us by National Disease Research Interchange under an Internal Review Board approval at the City College of New York. Two experiments were performed using two different breast tissue samples, as detailed in Section 4.3.1 and Section 4.3.2.

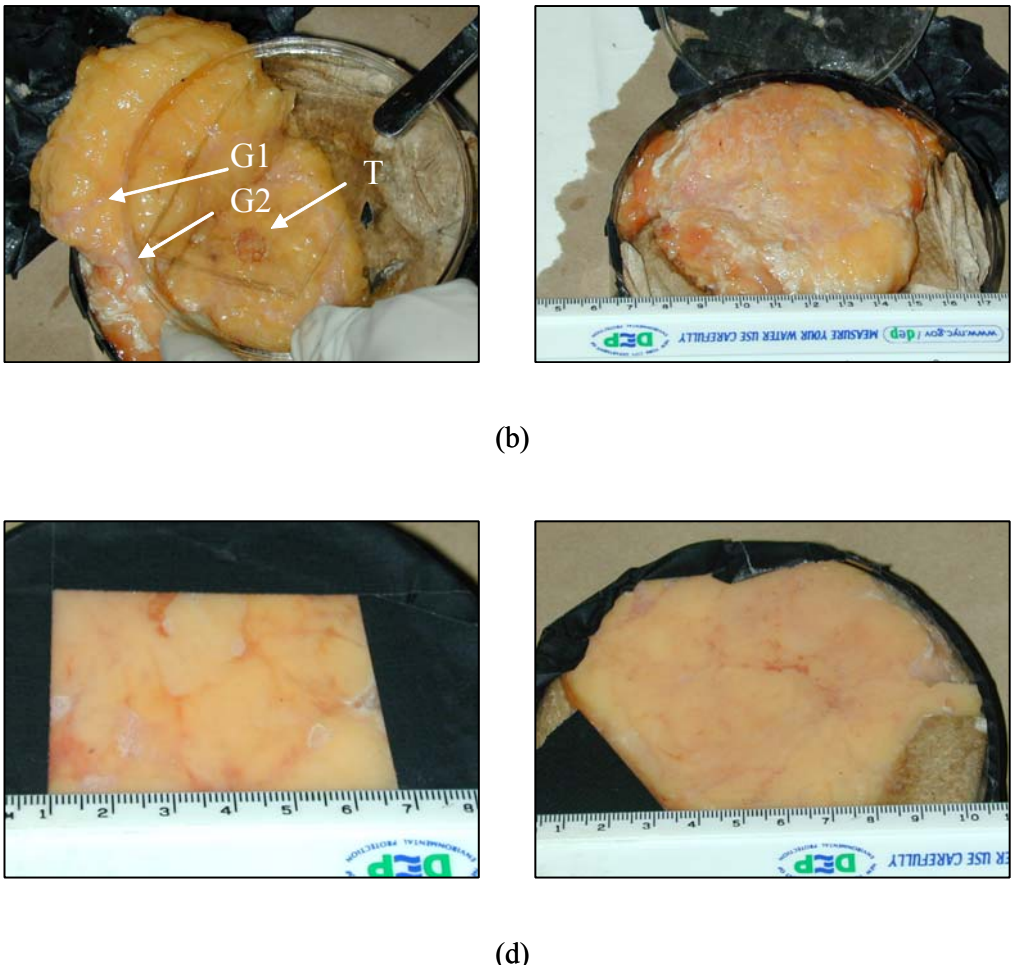


Figure 4.1: Photos of breast tissue with embedded tumor (T). (a) Location of tumor (T) and glandular (G1, G2) tissue. (b) Breast tissue compressed in clyindrical container. (c) Entrance (source) surface. (d) Exit (detector) surface.

### 4.3.1 Normal breast with cancerous tumor sample

The first sample was composed of a piece of normal breast tissue with a piece of malignant tumor embedded in it. Both, the pieces were obtained from NDRI under IRB approval from CCNY. The normal piece had an approximate dimension of 80 mm x 60 mm x 33 mm and the tumor had a dimension of 5 mm x 3 mm x 3 mm. An incision was made in the normal breast tissue and the tumor was inserted. The composite sample of normal and cancerous tissue was placed in a cylindrical transparent plastic container of diameter 100 mm, and thickness of 33 mm, as shown Figure 4.1 (a)-(b) and compressed slightly to maintain thickness uniformity. The container was black taped at one window (source side) in rectangular fashion, and the other window (detector side) in a manner to observe the entire tissue as displayed in Figure 4.1 (c)-(d).

### 4.3.2 Fluorescent target in normal breast sample

As in the case of section 3.3.3, the fluorescent target was a glass sphere (outer diameter ~4 mm and inner diameter 3.2 mm) filled with a solution of indocyanine green (ICG) in water. The water solution of ICG had an absorption coefficient of 11.5 $cm^{-1}$ at 784 nm, and fluoresced over the 790 nm – 966 nm spectral range with a peak at 825-nm. as displayed in Figure 4.2 (a). The sphere was placed inside a 100 mm X 100 mm X 26 mm slab of *ex vivo* female breast tissue specimen contained in a transparent plastic box. One of the sides of the box could be moved to uniformly compress and hold the tissue specimen in position as shown in Figure 4.2 (b). The breast specimen consisted primarily of adipose tissue with a small amount of skin,

and was provided by the National Disease Research Interchange under Internal Review Board approval at the City College of New York.

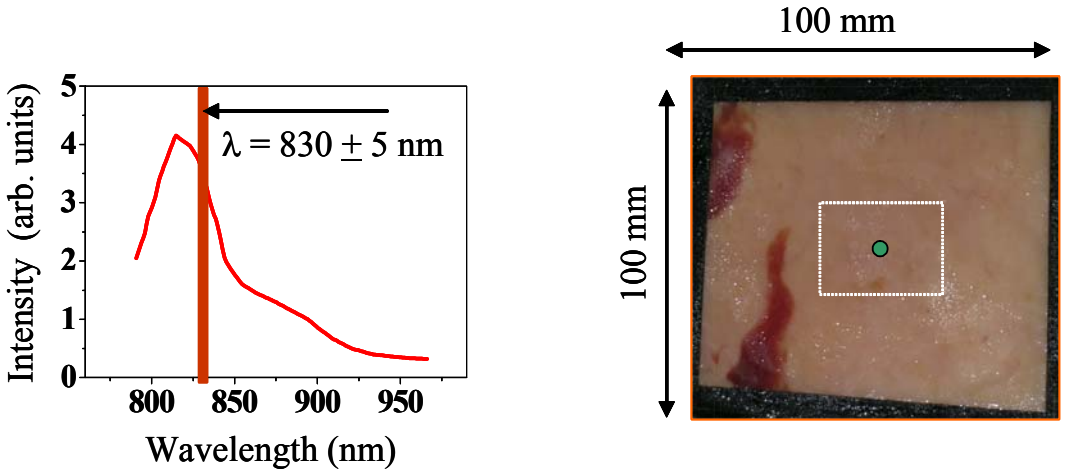


Figure 4.2: (a) Flourescent spectra of ICG when pumped at 784 nm. (b) Photograph of breast tissue embedded with ICG sphere at exit (detector) surface. The dashed white box shows the scanned region.

### 4.3.3 Experimental setup

The experimental arrangement for OPTICA is shown schematically in Figure 4.3. Continuous wave 784 nm radiation from a diode laser (Ocean Optics R-2000) delivered by a 200-μm optical fiber was used for illuminating the entrance face (henceforth referred to as the 'source plane') of the slab sample. Multiple source illumination was realized in practice by step scanning the slab sample along the horizontal ($x$) and vertical ($y$) directions across the laser beam using xy-computer control stage. A camera lens collected the diffusely transmitted light on the opposite face of the slab (henceforth referred to as the 'detection plane') sample and projected it onto the sensing element of a liquid cooled (-40 Celsius) charged couple device (CCD) camera (photometric model CH-350).

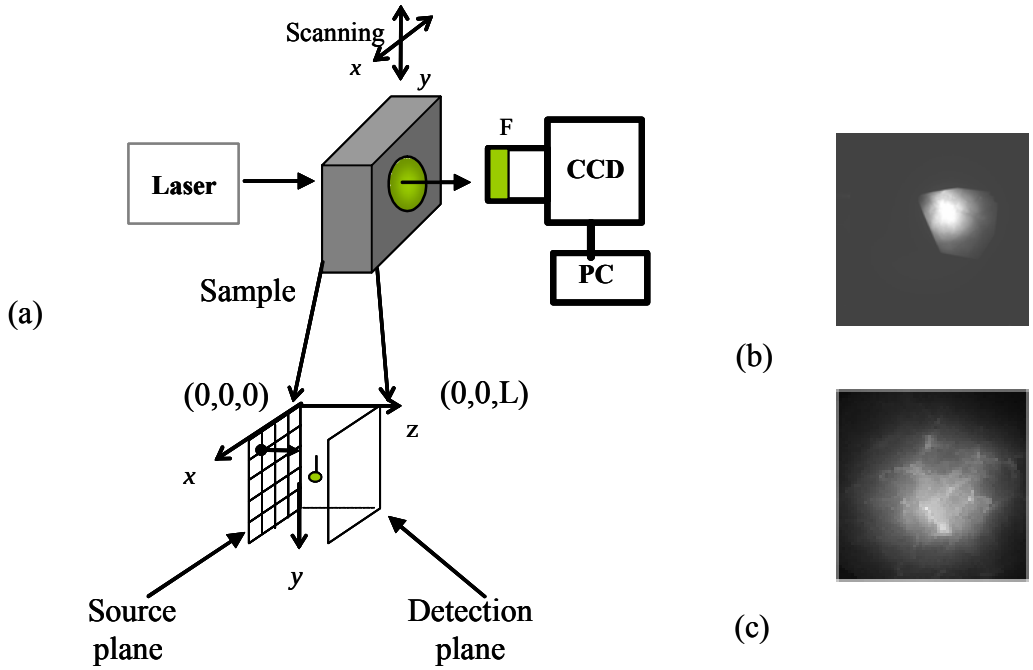


Figure 4.3: (a) Schematic diagram of the experimental arrangement, CCD= charge coupled device camera, F= filter, PC= computer. A typical raw CCD image of the detection plane of the sample described in (b) Section 4.3.1, and (c) Section 4.3.2

Each illuminated pixel of the 1024 x 1024 pixels of the CCD camera could be regarded as a detector. For illumination of every scanned point on the source plane, the CCD camera recorded the diffusely transmitted intensity pattern on the detection plane. In fluorescent case the light signal was passed through a narrow-band interference filter centered at 830 nm (FWHM ~ 10 nm, 50% transmission) to block the scattered 784 nm pump light. A second scan to estimate the average value of $\kappa = \sqrt{3\mu_a\mu_s'}$ (where $\mu_a$ and $\mu'_s$ are the absorption and scattering coefficients, respectively) of the background medium used a short-pass filter at 750 nm to block the fluorescent signal and admit a very small fraction of the transmitted excitation light. Table 4.1 provides the experimental requirement (step size, number of points.) for each tissue.

Table 4.1: Experimental Parameters

| Sample | Dimensions (mm) | Target | Dimension (mm) | Scan points matrix (n x m) | Step size (mm) |
|---|---|---|---|---|---|
| Normal breast with tumor | 100 mm dia. x 33 mm radius | tumor | 8 x 5 x 3 | 22 x 16 | 2 |
| Fluorescent target in normal breast | 100 x 100 x 26 | Fluore-scent sphere | Diameter = 4 | 18 x 15 | 2.5 |
| Intralipid 10% suspension | 250 x 250 x 50 | Fluore-scent sphere | Diameter = 4 | 10 x 10 | 2.5 |

## 4.4 Experimental Results

ICA of the perturbations in the spatial intensity distributions provided the corresponding independent intensity distributions (IID) on the source and detector planes. In addition, the cross-section size of each targets (tumors/fluorescent) are reconstructed using back-projection Fourier transform.

### 4.4.1 Tumor in normal breast tissue

The independent intensity distributions (IID) at the detector and source plane corresponding to the three scattering inhomogeneities (tumor, and two glandular) in breast tissue specimen are displayed in Figure 4.4 (a)-(f). These independent components are then used to obtain the projections of the inhomogeneity detector/source Green's function, $G(r_d, r_j)$, $G(r_j, r_s)$ j = 1, 2, 3 on the detector/source plane for the three scattering inhomogeneities entrenched in the breast specimen. The depth locations (z-direction) of the inhomogeneities are determined by fitting the projections to those of the model Green's function. The locations of all three inhomogeneities were obtained. The lateral ($x$,$y$) location was detected and can be read from the detector side of IID, the positions along the z-axis (depth) of the tumor and two glandular were found to be at 14.8, 14.6, and 2.5 mm from exit surface respectively (see Table 4.2).

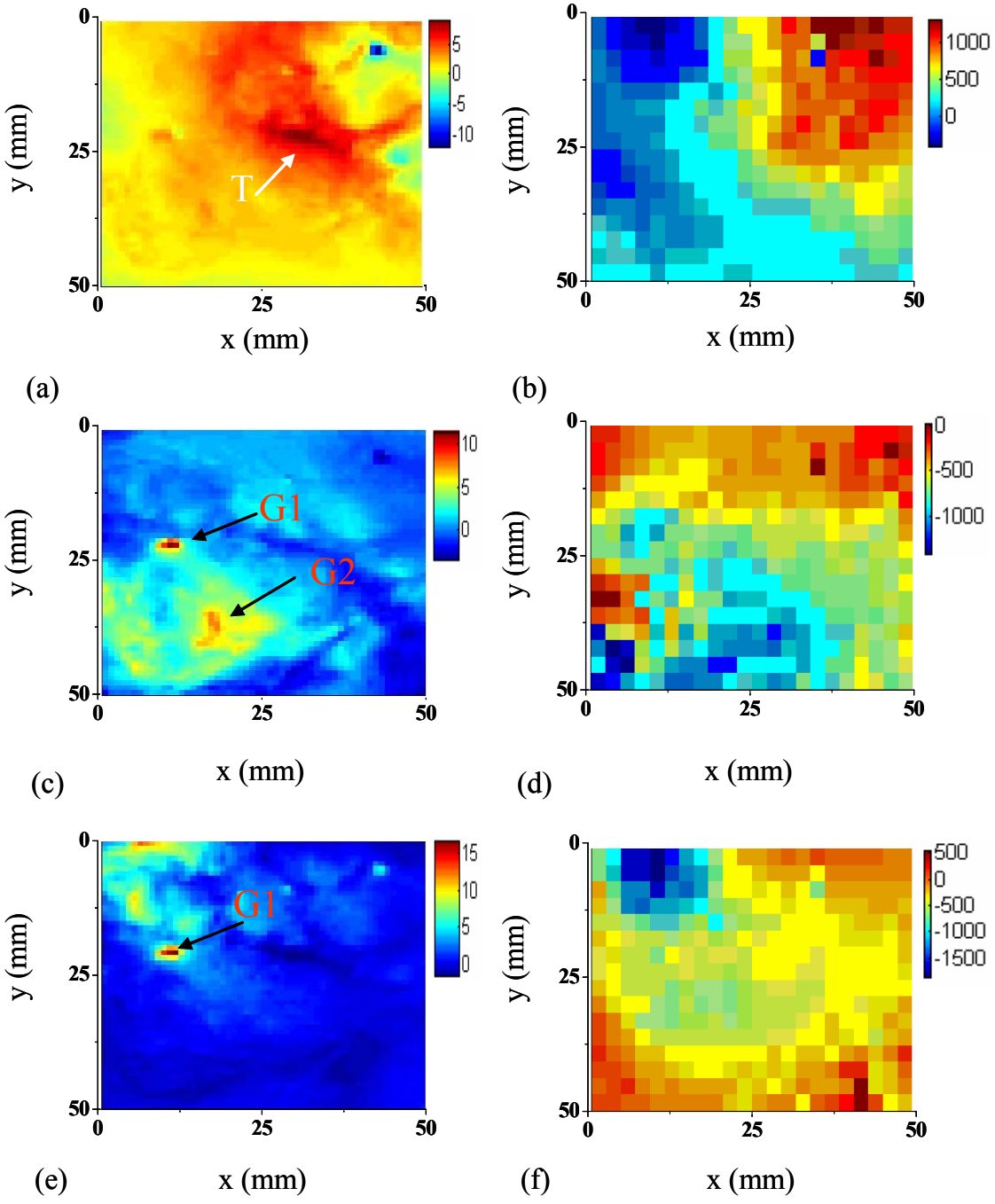


Figure 4.4: OPTICA generated independent intensity distributions on the detection plane (right frames), and source plane (left frames) for three targets (a,b) Tumor (T), (c,d) Glandular (1,2) G1 and G2, (e,f) Glandular 1 (G1)

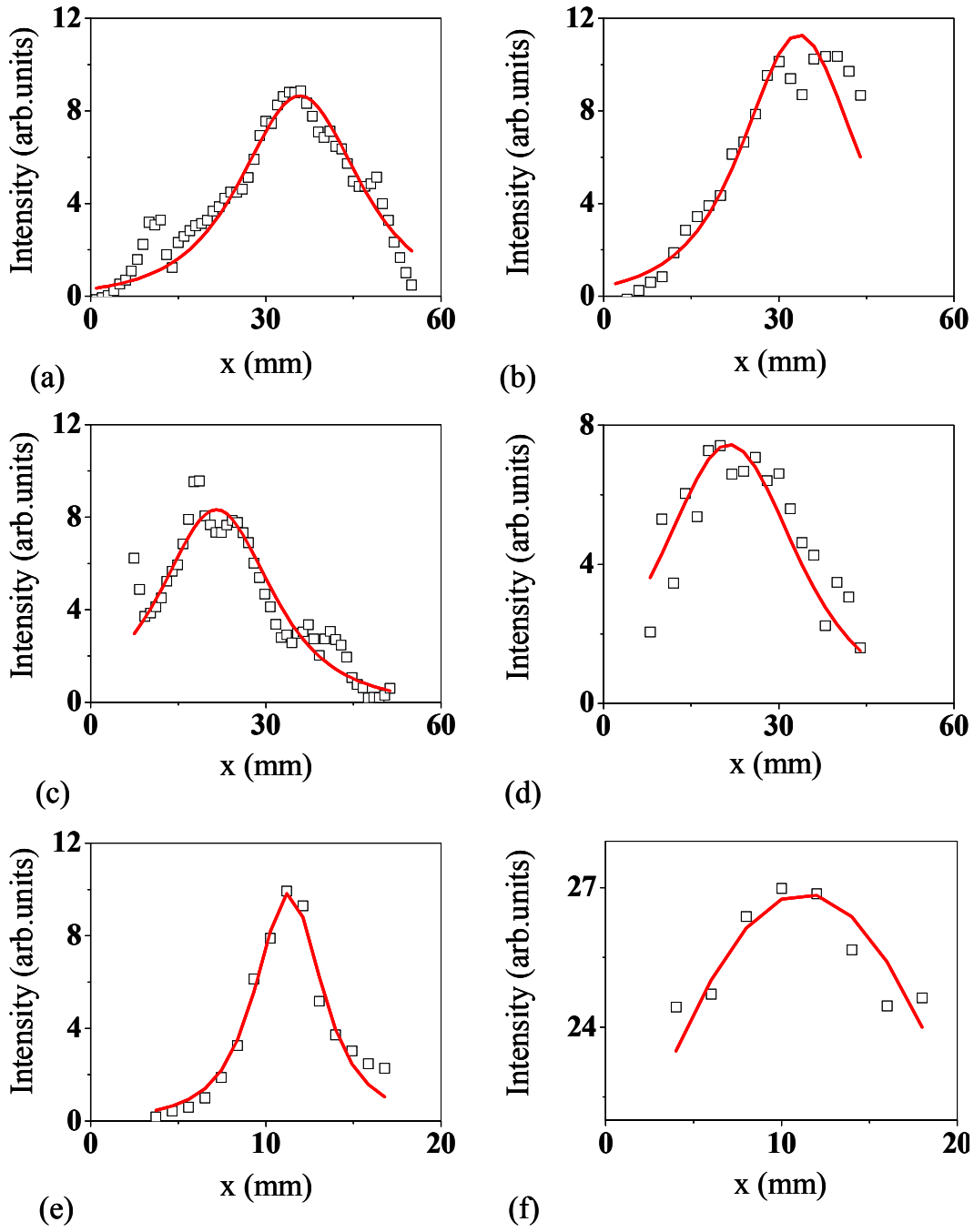


Figure 4.5: Green's function fit (red line) to the independent intensity distribution (hollow black square) on the detection plane (right frames), and source plane (left frames) for three targets (a) & (b) Tumor (T), (c) & (d) Glandular2 (G2), and (e) & (f) Glandular1 (G1) targets.

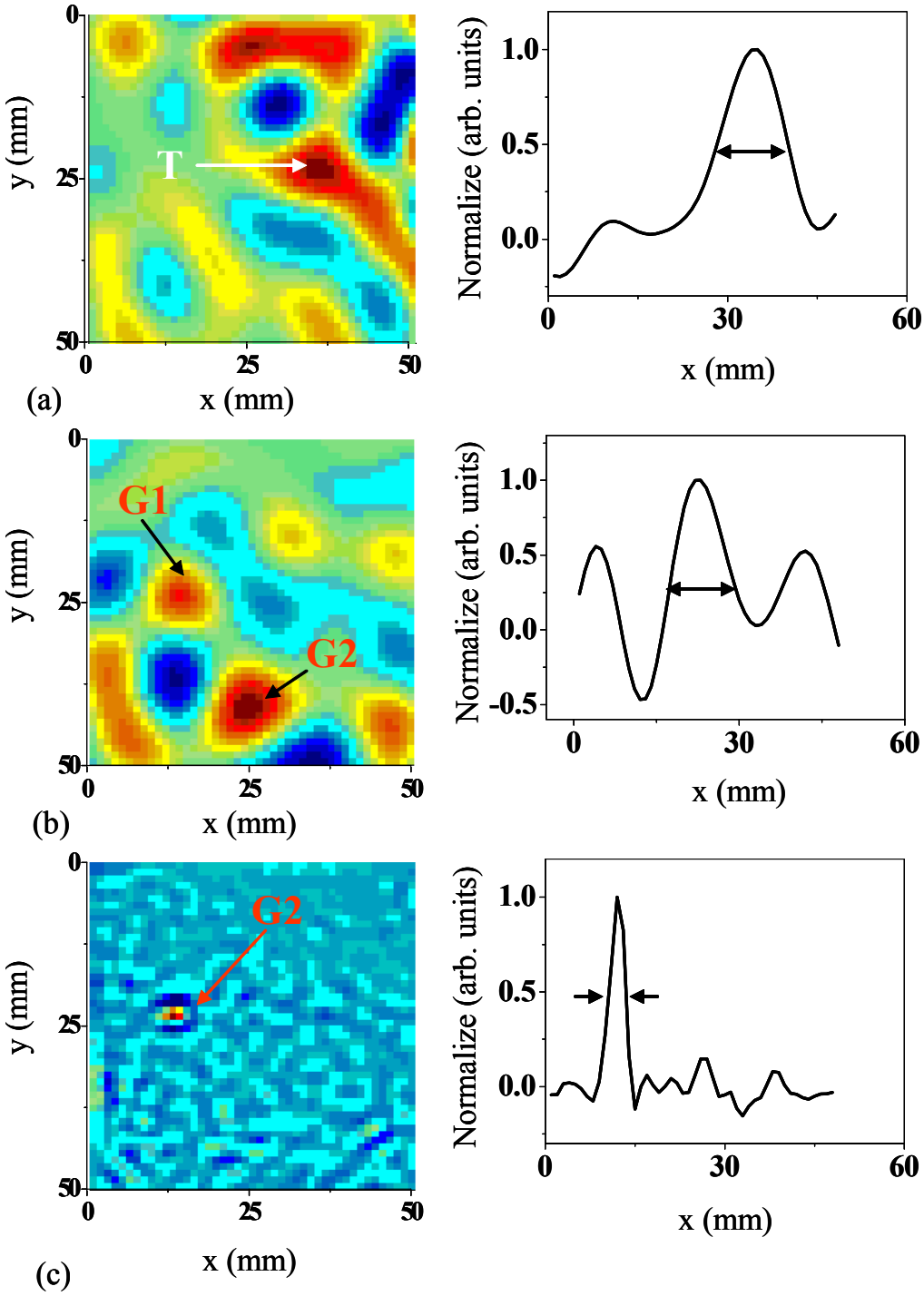


Figure 4.6: Two dimensional (2D) cross-section reconstructions with corresponding horizontal line profile of (a) Tumor (T) FWHM= 11 mm, (b) Glandular2 (G2) FWHM= 24.7 mm, and (c) Glandular1 (G1) FWHM= 2.5 mm.

The Green's function fit to IIDs for the tumor and two glandular tissues are shown in Figure 4.5 (a)-(f) . The depths of the tumor agree well with their known

depth positions of ~16.1 mm from the exit surface. The lateral positions are determined to be (21.5 mm, 33.3 mm), (18.7 mm, 37.3 mm), and (11.2 mm, 22.4 mm) for three inhomogeneities (see Table 4.2). The uncertainties in location and separation are not greater than 2 mm. The cross-section reconstructions are displayed in Figure 4.6 (a)-(c) with corresponding spatial profiles. The full width half maximum (FWHM) for tumor came out to be 11 mm, the two glandular $FWHM_1$ = 24.7 mm, and $FWHM_2$ = 2.7 mm (see Table 4.2).

Table 4.2: Known & OPTICA-predicted positions and sizes of the scattering target.

| Tissue Type | Known location (*x*, *y*, *z*) (mm) | Predicated location (*x*, *y*, *z*) (mm) | Cross-section (mm X mm) | Cross-section reconstruction FWHM (mm) |
|---|---|---|---|---|
| tumor | (21, 33, 16.9) | (21.5, 33.3, 18.2) | 8 x 5 | 11 |
| glandular1 | (11, 22, 30.5) | (11.2, 22.4, 30.5 ) | | 2.7 |
| glandular2 | (18, 37, 17) | (18.7, 37.3, 18.4) | | 24.7 |

### 4.4.2 Fluorescent glass sphere in normal breast tissue

Figure 4.7 (a) and (b) present the OPTICA generated intensity distributions on the detector and source planes, respectively of the fluorescent sphere in breast tissue sample. Corresponding Green's function fit to horizontal profile through the center of intensity distributions are shown in Figure 4.7 (c) and (d), respectively. The (*x*, *y*, *z*) location of the target center obtained from this analysis as presented in Table 4.3. The lateral positions (*x*, *y*) agree completely, and the axial position agrees within 1 mm of the known values. The cross sectional image, that is the projection of the fluorescent target onto the *x*-*y* plane using back-projection Fourier transforms, is shown in Figure 4.7 (e). Figure 4.7 (f) shows intensity profiles of the cross sectional image along the *x* and *y* directions shown by the white straight/ash lines in

Figure 4.7(e). The FWHM values of intensity profiles of the cross sectional image, presented in column 4 of Table 4.3, are in agreement with known outer diameter of the fluorescent sphere. It should be noted that multi-source measurements, though crucial for detection of multiple targets, might not in principle be needed for a small fluorescent target that was investigated experimentally, since the position of the target determines the normalized fluorescence intensity distribution. However, in reality multi-source measurements help reduce the deleterious effects of noise and inaccuracy in the estimation of optical properties of the medium, and provide better assessment of 3-*D* location even in the case of a single target.

The results of back-projection Fourier transform reconstruction on the same 4 mm diameter fluorescent sphere embedded in Intralipid-10% suspension in water are displayed in Figure 4.8 (a) and the corresponding lateral profile in Fig. 4.8(b), and key results and parameters are summarized in Table 4.3. Again, the lateral positions are in exact agreement, while the axial position agrees within 1 mm. However, the FWHM values of the intensity profiles of the cross sectional image are estimated to be 12 mm each, which is 3 times the known outer diameter of the sphere. FWHM values should be compared with the 3.2 mm inner diameter of the sphere.

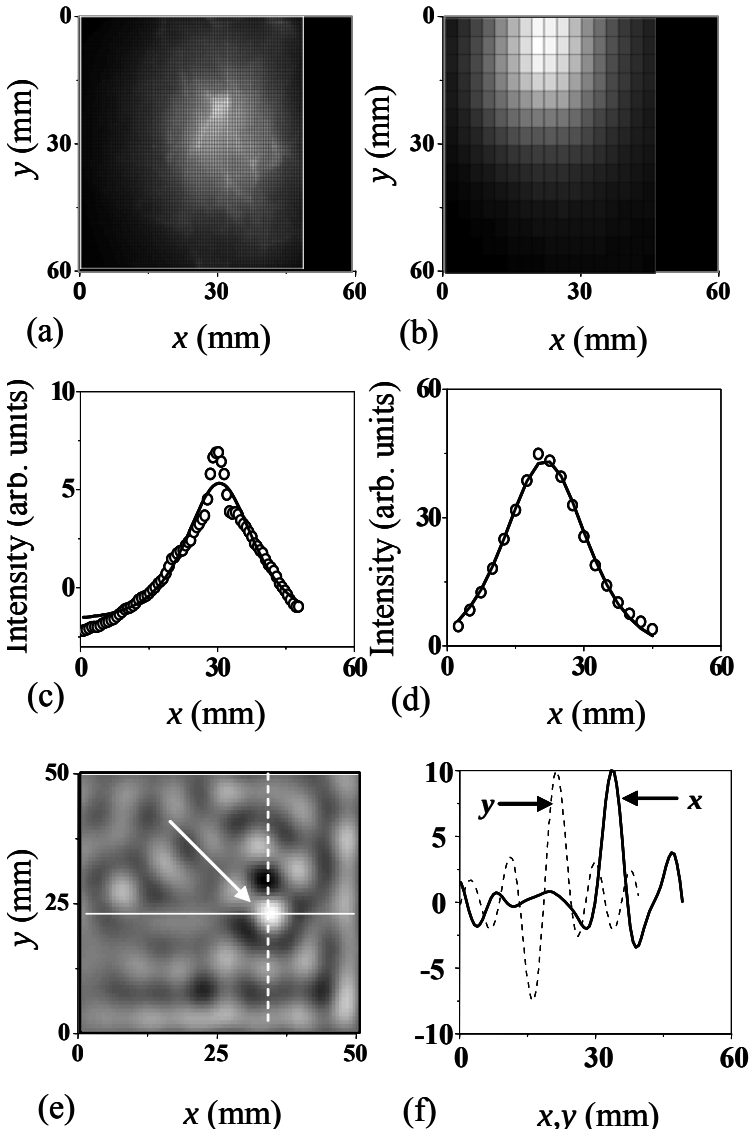


Figure 4.7: OPTICA generated fluorescence intensity distribution on the (a) detector and (b) source planes. (c) (d) Green's function fits to the horizontal spatial profiles through the centers of distributions in (a) and (b), respectively. (e) Cross sectional image at the $z = z_j$ plane. (f) Spatial profiles of the cross sectional image along the x and y directions shown by the white (solid/dashed) lines in (e).

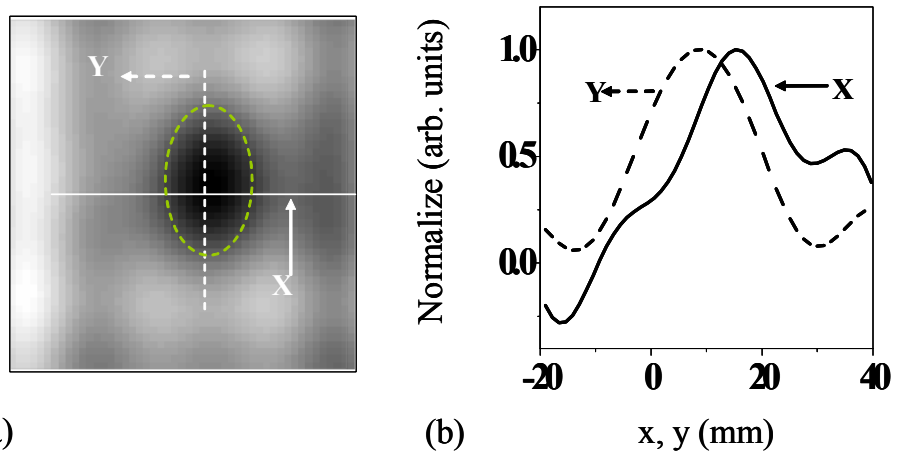


Figure 4.8: (a) Cross sectional image at the z= $z_j$ plane for Section 4.5.4. (b) Spatial profiles of the cross sectional image along the x and y direction directions shown by the white (solid/dashed) lines.

Table 4.3 Known & OPTICA-predicted positions and sizes of the fluorescent target.

| Samples | Known position ($x$, $y$, $z$) mm | Observed position ($x$, $y$, $z$) mm | Profile FWHM ($\Delta x$, $\Delta y$) mm |
|---|---|---|---|
| Breast tissue *ex vivo* | (30, 27, 15) | (30, 27, 16) | (4,4) |
| Intralipid-10% in water | (115, 115,15) | (115, 115,16) | (12,12) |

## 4.5 Discussion

OPTICA presented in Chapter 3 and applied to *ex vivo* human breast tissue, in Chapter 4 can detect and provide object locations accurate to ~1 mm. The uses of multiple-source illumination and multiple-detector data acquisition provide multiple angular observations and robust data for extracting 3-D location information. A salient feature of OPTICA is that ICA provides the independent components, which is directly related to the number of inhomogeneities with minimal errors in location. The cross-section shape reconstructions of the target (tumor) in breast tissue based on back-projection Fourier transforms produce the lateral size at the giving 3-D location.

For the fluorescent OPTICA the advantage is that the background light can be minimized by use of appropriate filters, making it a 'zero-background' measurement, as opposed to the situations involving absorptive and scattering targets when changes in high light levels are measured. The 3-D localization of the object is achieved with a high accuracy, and shorter computation time compared to other commonly used methods.

### 4.5.1 Tumor in normal breast tissue

OPTICA in the tumor case, detected and located the 8 mm x 5 mm x 3 mm cancerous tumor that was placed approximately in the mid-plane (z = ~16.1 mm from exit surface) of the breast slab. From the result of independent intensity distributions (IID) in Figure 4.4 (a) it can be shown that the (a) the tumor lateral size x = ~15 mm, and y = ~3 mm. (b) The relative intensity value of the tumor is 10 arb-units, which is more than the background value (see legend next to Figure 4.4 (a)).

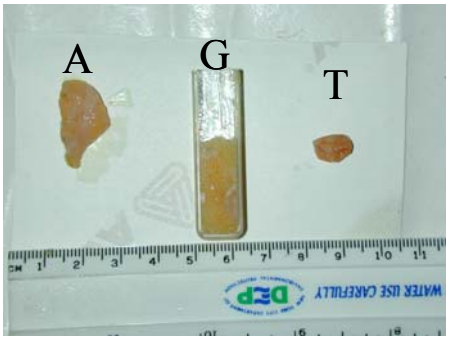


(a)

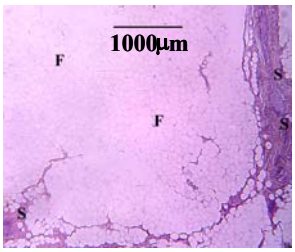


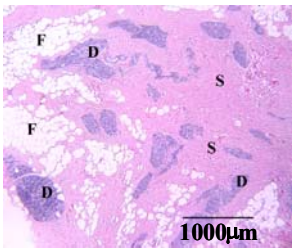


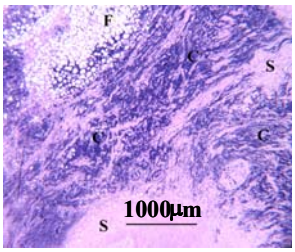


(b) (c) (d)

Figure 4.9: (a) Photograph of tissue samples sent for pathology histology (b) Adipose (A), (c) glandular (G) and (d) cancerous (tumor (T)) tissue

Clearly, it seems the tumor accentuated to the mostly adipose background, which what we have learn in chapter 2 and later chapter 5 that, the transport length ($l_t$) for cancerous is much larger than normal tissue, especially adipose tissue ($l_{tc} > l_{tn}$) [42]. The image cross-section reconstruction using back-projection Fourier transform, constructed the cross-section size of the tumor about ~1.4 of the full width at half maximum (FWHM) "real" size (see Figure 4.9 (a)). This have to do with function is known as the Radon transform (or sinogram) [6,43] of the 2D object. The projection-slice theorem [6,44] tells us that if we had an infinite number of one-dimensional projections of an object taken at an infinite number of angles, we could perfectly reconstruct the original object, $f(x,y)$ from equation 4.3.

$$p(r,\theta) = \int_{-\infty}^{\infty}\int_{-\infty}^{\infty} f(x,y)\delta(x\cos\theta + y\sin\theta - r)dxdy \qquad (4.3)$$

So to get *f(x,y)* back from the above equation means finding the inverse Radon transform. It is possible to find an explicit formula for the inverse Radon transform, however, the inverse Radon transform proves to be extremely unpredictable with respect to noisy data. In practice, a stabilized and discretized version of the inverse Radon transform is used, known as the filtered back-projection algorithm [43].

### 4.5.2 Fluorescent glass sphere in normal breast slab

The results of measurements on the same 4 mm diameter fluorescent sphere embedded in normal breast slab and Intralipid-10% suspension in water are summarized in Table 4.3. Again the lateral positions are in exact agreement, while the axial position agrees within ~1 mm. However, the FWHM values of the intensity profiles of the cross sectional image agrees with breast tissue slab FWHM = 3.2 mm, but not with Intralipid-10% suspension in water estimated to be FWHM = 12 mm, which is 3 times the known outer diameter of the sphere. We attribute this difference primarily to the much longer path length ($50l_t$) in Intralipid-10% sample than that in the tissue sample ($26l_t$). Since transport lengths ($l_t$) for both samples were comparable, the round trip path (transport of the fluorescence signal onto the detection plane, and back-projection from the detection plane onto the target location) in Intralipid 10% sample was approximately twice that in the tissue sample, and resulted in much more spreading of the thickness profile in the Intralipid 10% sample. As the incident beam power was limited to 300 mW for both the samples, higher optical thickness resulted in much lower fluorescence signal-to-noise ratio for the Intralipid-10% sample, which in turn contributed to a higher estimate of the target cross section. Substantial improvements in target size estimate are expected if an

intensified CCD camera for higher sensitivity, and more incident beam power are used. Although the simpler but important case involving a single target (e.g., a tumor in the breast) was chosen for this demonstration, the approach is applicable for multiple fluorescent targets and was demonstrated in computer simulation of three sphere target Figure 4.10 (a)-(c)

In summary, OPTICA has the potential to emerge as a new versatile tool for locating targets in turbid media, particularly in diagnostic medical imaging, in the case of tumor in breast our result was coordinated with histology of the tumor and other tissue as seen in Figure 4.9 (b)-(d).

Detail of the programs that implemented the detection / location (OPTICA) is presented in Appendix A. The programs was written in the MATLAB language (v. 6.5-7.01), which ran on Debian GNU/Linux platform (v 3.1)/ Microsoft Windows 2000. The computer processor used a Pentium 4 (2.4 GHz). The computation time for each output file varies from sample to sample and on the average of < 1 min.

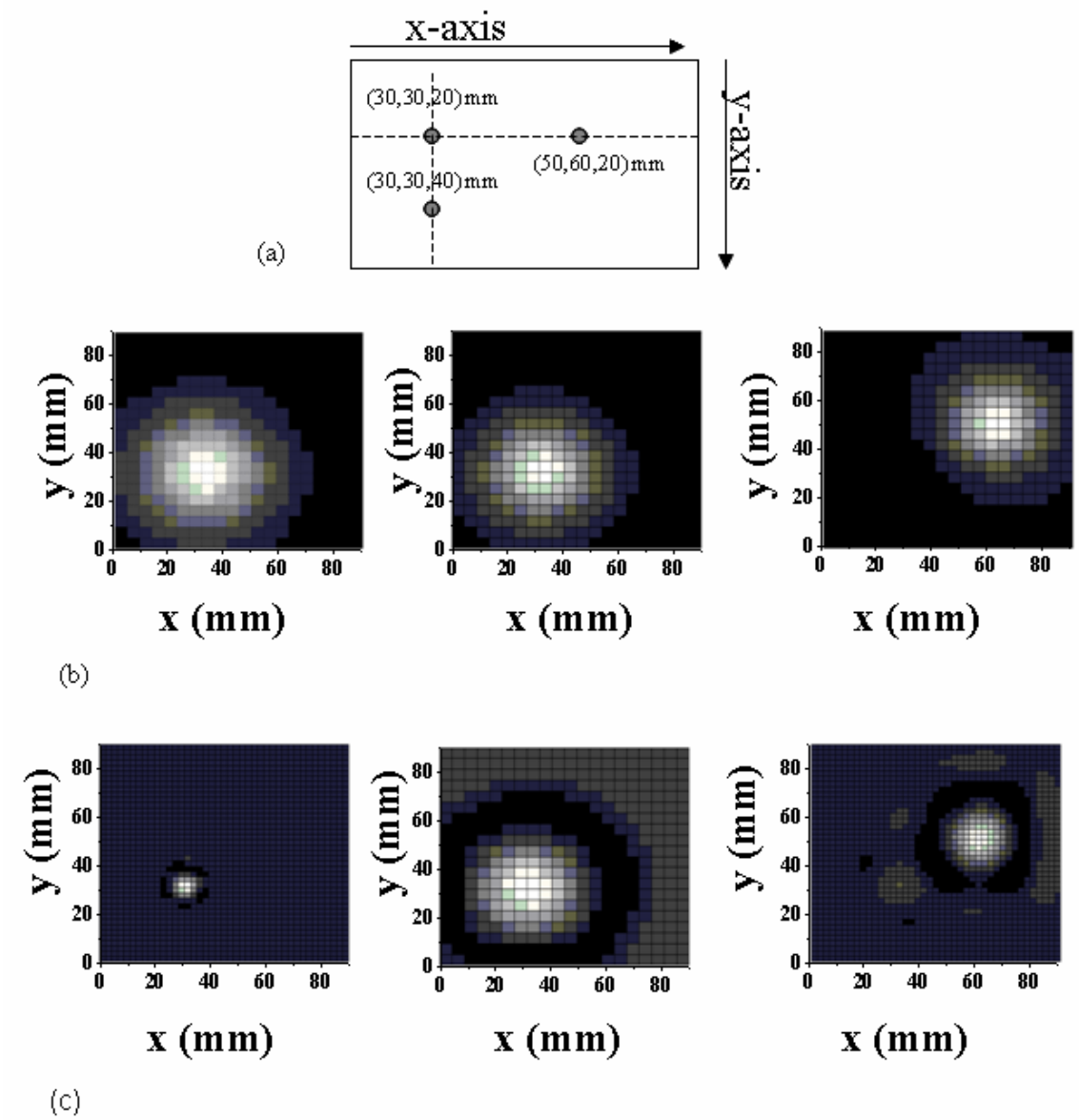


Figure 4.10: (a) Sphere xy coordinates. (b) Virtual souces calulated by OPTICA simulation. (c) Reconstructed 2-D cross-section images at the respective depths

## 4.6 References


1. B. Chance and R. R. Alfano, eds., "Optical Tomography and Spectroscopy of Tissue: Theory, Instrumentation, Model, and Human Studies", SPIE Proc. **2979**, The International Society for Optical Engineering, Bellingham, WA, (1997).
2. R. R. Alfano and J. G. Fujimoto, eds., "Advances in Optical Imaging and Photon Migrations, OSA Trends in Optics and Photonics Series", vol. **2**, Optical Society of America, Washington, DC, (1996).
3. B. Chance and R. R. Alfano, eds., "Optical Tomography Photon Migration and Spectroscopy of Tissue and Model Media: Theory, Human Studies, and Instrumentation", SPIE Proc. **2389**, Part 1 and 2, The International Society for Optical Engineering, Bellingham, WA, (1995).
4. A. Yodh , B. Chance, "Spectroscopy and Imaging with diffusing light", Physics Today **48**, pp. 34-40, (1995).
5. G. Müller, B. Chance, R. Alfano, S. Arridge, J. Beuthan, E. Gratton, M. Kaschke, B. Masters, S. Svanberg, P. van der Zee, "Medical Optical Tomography: Functional Imaging and Monitoring", SPIE Institutes for Advanced Optical Technologies Series, vol. IS11, Bellingham, WA, (1993).
6. William R. Hendee and E. Russell Ritenour, "Medical Imaging Physics" Wiley-Liss; 4$^{th}$ edition (2002)
7. A. Parker, "Image Reconstruction in Radiology", Boca Rato, FL: CRC Press, 1990.

8. D. A. Benaron, D. C. Ho, S. Spilman, J. P. van Houten, and D. K. Stevenson, "Non-recursive linear algorithms for optical imaging in diffusive media," Advances in Experimental Medicine & Biology: Oxygen Transport to Tissue **XVI**, Plenum Press, New York, pp. 215-222, (1994).
9. S. A. Walker, S. Fantini, and E. Gratton, "Image reconstruction by back-projection from frequency domain optical measurements in highly scattering media," Appl. Opt,**36**, pp. 170-179, (1997).
10. S. B. Colak, D. G. Papaioannou, G. W. 't Hooft, M. B. van der Mark, H. Schomberg, J. C. J. Paasschens, J. B. M. Melissen, and N. A. A. J. van Asten, "Tomographic image reconstruction from optical projections in light-diffusing media," Appl. Opt. **36**, pp. 180-213, 1997.
11. W. Cai, S. K. Gayen, M. Xu, M. Zevallos, M. Alrubaiee, M. Lax, R. R. Alfano "Optical tomographic image reconstruction from ultrafast time-sliced transmission measurements," Appl. Opt. **38**, 4237-4246 (1999).
12. Y. Q. Yao, Y. Wang, Y. L. Pei, W. W. Zhu, and R. L. Barbour, " Frequency-domain optical imaging of absorption and scattering distributions by Born iterative method," Journal of the Optical Society of America A, **14**, pp. 325-342, (1997).
13. K. D. Paulsen and H. Jiang, "Spatially varying optical property reconstruction using a finite element diffusion equation approximation," Med. Phys.. **22**, pp. 691-701, (1995).

14. H. Jiang, K.D. Paulsen, and U.L. Österberg, "Optical image reconstruction using DC data: simulations and experiments," Phys. Med. Biol., **41**, pp.1483-1498, (1996).

15. H. Jiang, K. D. Paulsen, U. L. Österberg, B. W. Pogue, M. S. Patterson, "Simultaneous reconstruction of optical absorption and scattering maps in turbid media from near-infrared frequency-domain data," Opt. Lett., **20**, pp. 2128-2130, (1995).

16. D. Y. Paithankar, A. U. Chen, B. W. Pogue, M. S. Patterson, and E. M. Sevick-Muraca, "Imaging of fluorescent yield and lifetime from multiply scattered light reemitted from random media," Appl. Opt., **36**, pp. 2260-2272, (1997).

17. T. R. Lucas, M. V. Klibanov, and R .M. Frank, "Imaging experimental data from optical tomography by the elliptic system method in Computational, Experimental, and Numerical Methods for Solving Ill-Posed Inverse Imaging Problems: Medical and Nonmedical Applications", R.L. Barbour, M.J. Carvlin, and M.A. Fiddy, eds., Proc. SPIE, **3171**, pp. 22-33, (1997) .

18. M. Xu, M. Alrubaiee, S. K. Gayen, and R. R. Alfano, "Three-dimensional localization and optical imaging of objects in turbid media with independent component analysis", Appl. Opt. **44**, 1889 (2005)

19. M. Xu, M. Alrubaiee, S. K. Gayen, and R. R. Alfano, "Optical imaging of turbid media using independent component analysis: theory and simulation", J. Biomed. Opt. **10**, 051705 (2005).

20. M. Alrubaiee, M. Xu, S. K. Gayen, M. Brito, and R. R. Alfano, “Three-dimensional optical tomographic imaging of scattering objects in tissue-simulating turbid media using independent component analysis”, Appl. Phys. Lett. **87**, 191112 (2005)
21. M. Alrubaiee, M. Xu, S. K. Gayen, and R. R. Alfano, “Localization and cross section reconstruction of fluorescent targets in ex vivo breast tissue using independent component analysis”, Appl. Phys. Lett. **89**, 133902 (2006)
22. P. Comon, "Independent component analysis—a new concept?” Signal Process. **36**, 287–314 (1994).
23. A.J. Bell, "Information theory, independent component analysis, and applications," in Unsupervised Adaptive Filtering, Vol. **I**, S. Haykin, Ed., pp. 237–264, Wiley, New York (2000).
24. A. Hyvärinen, J. Karhunen, and E. Oja, “Independent Component Analysis”, Wiley, New York (2001).
25. J.-F. Cardoso, "Blind signal separation: statistical principles," Proc. IEEE **86**, 2009–2025 (1998).
26. A. Hyvärinen and E. Oja, "Independent component analysis: algorithms and applications," Neural Networks **13**, 411–430 (2000).
27. S. Chandrasekhar, “Radiative Transfer”, Dover, New York (1960).
28. S. R. Arridge and J. C. Hebden, "Optical imaging in medicine: II. Modeling and reconstruction," Phys. Med. Biol. **42**, 841–853 (1997),

29. S. R. Arridge, "Optical tomography in medical imaging," Inverse Probl. **15**, R41–R93 (1999).

30. W. Cai, M. Lax, and R. R. Alfano, "Analytical solution of the elastic Boltzmann transport equation in an infinite uniform medium using cumulant expansion," J. Phys. Chem. B **104**, 3996–4000 (2000).

31. M. Xu, W. Cai, M. Lax, and R. R. Alfano, "Photon migration in turbid media using a cumulant approximation to radiative transfer," Phys. Rev. E **65**, 066609 (2002).

32. M. Xu, W. Cai, M. Lax, and R. R. Alfano, "A photon transport forward model for imaging in turbid media," Opt. Lett. **26**, 1066–1068 (2001).

33. V. Chernomordik, D. Hattery, A. H. Gandjbakhche, A. Pifferi, P. Taroni, A. Torricelli, G. Valentini, and R. Cubeddu, "Quantification by random walk of the optical parameters of nonlocalized abnormalities embedded within tissuelike phantoms," Opt. Lett. **25**, 951–953 (2000).

34. A. H. Gandjbakhche, G. H. Weiss, R. F. Bonner, and R. Nossal, "Photon path-length distributions for transmission through optically turbid slabs," Phys. Rev. E **48**, 810–818 (1993).

35. W. Cai, M. Xu, and R. R. Alfano, "Three dimensional radiative transfer tomography for turbid media," IEEE J. Sel. Top. Quantum Electron. **9**, 189–198 (2003).

36. P.M. Morse and H. Feshbach, “Method of Theoretical Physics”, Vols. **I** and **II**, McGraw-Hill, New York (1953).

37. S. R. Arridge, "Photon-measurement density functions. Part I: Analytic forms," Appl. Opt. **34**, 7395–7409 (1995).

38. S. R. Arridge and M. Schweiger, "Photon-measurement density functions. Part 2: Finite-element-method calculations," Appl. Opt. **34**, 8026–8037 (1995).

39. A. H. Hielscher and S. Bartel, "Use of penalty terms in gradient-based iterative reconstruction schemes for optical tomography, "J. Biomed. Opt. 6, 183–192 (2001).

40. B. A. Brooksby, H. Dehghani, B. W. Pogue, and K. D. Paulsen, "Near-infrared (NIR) tomography breast image reconstruction with a priori structural information from MRI: algorithm development for reconstructing heterogeneities," IEEE J. Sel. Top. Quantum Electron. **9**, 199–209 (2003).

41. Topics in Biomedical Optics, J. C. Hebden, D. A. Boas, J. S. George, and A. J. Durkin, Eds., pp. 2869–3329, a special issue of Appl. Opt.**42** (2003).

42. M. Alrubaiee, S. K. Gayen, J. A. Koutcher, and R. R. Alfano, “Spectral and Temporal Near-Infrared Imaging of Ex Vivo Cancerous and Normal Human Breast Tissues,” Technology in Cancer Research and Treatment **4** (2005).

43. Deans, Stanley R. “The Radon Transform and Some of Its Applications”. New York: John Wiley & Sons. (1983).

44. Bracewell, R.N. "Numerical Transforms". Science **248**: 697-704. (1990).

# Chapter 5

# Monte Carlo simulation investigation of tissue optical properties

## 5.1 Introduction

Monte Carlo simulation (MCS) of photon propagation in turbid media offers an approach toward understanding photon transport in tissue [1-12]. The method describes a photon's movement between two consecutive scattering events, and the angle of deflection in a photon's trajectory when a scattering event occurs [1, 2, 6-8]. Estimate of optical properties of the medium may be obtained using MCS [9, 14]. However, this method is statistical in nature, and it relies on large ensemble to generate a clear picture of the problem [10-12, 14]. The complexity and computation time, depends mainly on the physical problem and what question is being asked, the precision needed, acceptable noise level, and the spatial / temporal resolution desired [14].

In this chapter, MCS is used to obtain two key optical parameters transport length ($l_t$), and anisotropy parameter ($g$) from time-sliced two-dimensional (2-D) image sequences of *ex vivo* breast tumor and normal tissues that were presented in Chapter 2. The MCS will consider the propagation of a plane wave light pulse in thin breast tissue specimens ~5 mm thick on which experiments were carried out. The potential application for this technique is to merge the experimental benefit of time-sliced direct imaging with MCS to retrieve the optical parameters of breast tissues and to identify those as normal and cancerous for optical tomography and diagnosis (Chapters 3-4).

## 5.2 Regulations for photon propagation

MCS traces each individual photon as shown in Figure 5.1. Individual photons will be considered as packets that can receive a fractional weight to reduce the variance of the MCS. The initial weight of photon packet launched is equal to unity (w = 1). The initial position of the photon packet is denoted by *(x, y, z)* and its direction cosine $(\mu_x,\mu_y,\mu_z)$. propagation of the photon is simulated by a series of movement of random step size *s*.

$$\begin{aligned} x &\leftarrow x + \mu_x s \\ y &\leftarrow y + \mu_y s \\ z &\leftarrow z + \mu_z s \end{aligned} \tag{5.1}$$

For an absorption process step movements will get a **weight update** and for an scattering event a **direction cosine update**. The photon is terminated if one of the conditions is met: reflection or transmission outside of the medium, or the time frame is out side the interest of the problem (physically impossible). The system is constrained in that it must obey energy conservation (number of photons) without skewing the distribution of photon deposition at photon termination; hence, a roulette technique is used. The step size *s* of photon packet is chosen based on a sampling of the probability distribution for photon's free path $s \in (0,\infty)$. When entering a homogenous scattering medium the distribution of free path between successive scattering or absorption events is $e^{(-\mu_T s)} / \mu_T$ and can be sampled from

$$s = -\ln(\aleph) / \mu_T \tag{5.2}$$

where $\aleph$ is a uniform random number on (0,1) and $\mu_T = \mu_a + \mu_s$ is the total interaction coefficient. If the medium is inhomogeneous, the distribution of free path obeys:

$$\sum_i \mu_{\mathrm{Ti}} s_i = -\ln(\aleph) \tag{5.3}$$

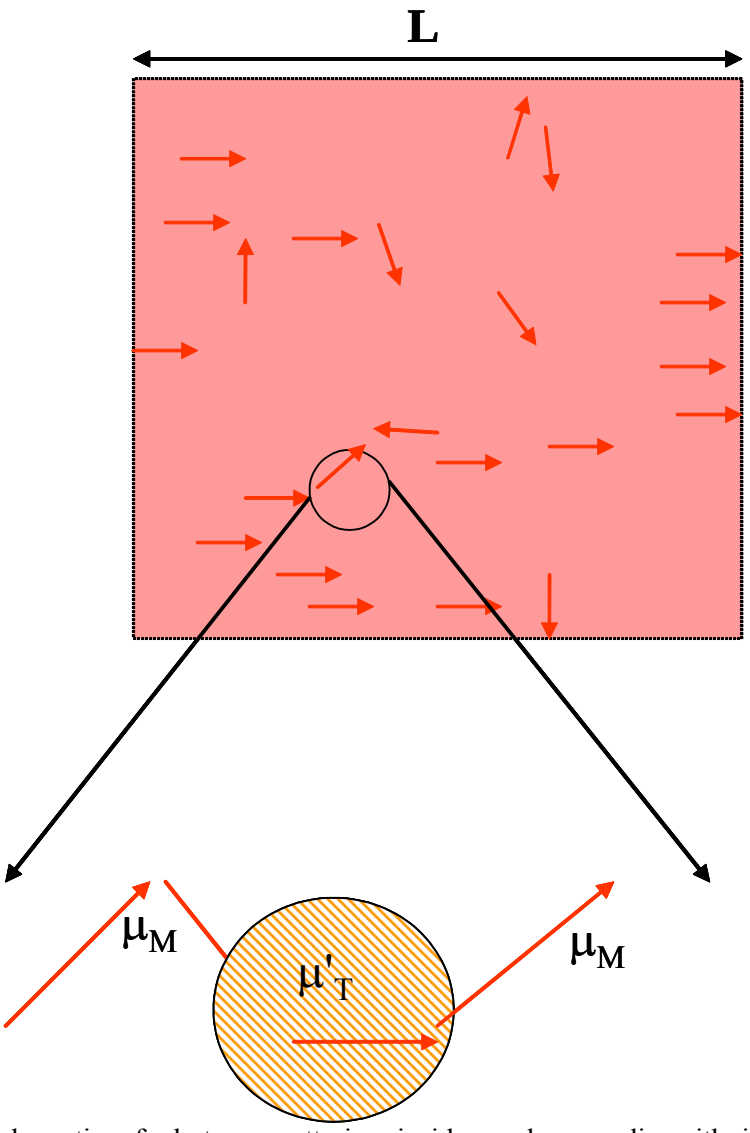


Figure 5.1: Schematic of photons scattering inside random media with inhomogeneous target. $\mu_M$= total interaction coefficient of the medium and $\mu'_T$= total interaction coefficient of targets optical properties

Figure 5.1, is the schematic diagram for a photon interacting with inhomogeneous targets of total interaction coefficient $\mu'_T$ embedded in homogenous medium with total interaction coefficient ($\mu_M$).

Absorption affect a photon step by updating fraction of its weight (w), the value is equal to:

$$\Delta w = w\frac{\mu_a}{\mu_T} \tag{5.4}$$

and the weight of the photon packet is updated as:

$$w \leftarrow w - \Delta w \tag{5.5}$$

The scattering events take on simple form in the coordinate system $\left(\frac{m-(n\cdot m)n}{|n\times m|}, \frac{n\times m}{|n\times m|}, n\right)$ attached to the moving photon, where $n = (\mu_x, \mu_y, \mu_z)$ the propagation direction of the photon prior to scattering and **m** is an arbitrary unit vector. The deflection angle $\theta \in [0, \pi]$ is distributed according to the phase function *P(coθ)*, and the azimuthal angle $\phi$ is a uniform random variable over [0,2π]. For specific scattering angle *(θ, ϕ)* the outgoing direction of the photon will be:

$$n' = \frac{m-(n\cdot m)n}{|n\times m|}\sin\theta\cos\varphi + \frac{n\times m}{|n\times m|}\sin\theta\sin\varphi + n\cos\theta \tag{5.6}$$

Any choice of the unit vector **m** is tolerable. Take m = (0,0,1):

$$\begin{aligned}
\mu_x' &= -\frac{\sin\theta}{\sqrt{1-\mu_z^2}}(\mu_x\mu_z\cos\varphi - \mu_y\sin\varphi) + \mu_x\cos\theta \\
\mu_y' &= -\frac{\sin\theta}{\sqrt{1-\mu_z^2}}(\mu_y\mu_z\cos\varphi + \mu_x\sin\varphi) + \mu_y\cos\theta \qquad (5.7) \\
\mu_z' &= \sqrt{1-\mu_z^2}\sin\theta\cos\varphi + \mu_z\cos\theta
\end{aligned}$$

If $|\mu_z| \to\sim 1$, then we can chose an alternative **m** = (0,1,0) and obtain:

$$\begin{aligned}
\mu_x' &= -\frac{\sin\theta}{\sqrt{1-\mu_z^2}}(\mu_x\mu_y\cos\varphi+\mu_z\sin\varphi)+\mu_x\cos\theta \\
\mu_y' &= \sqrt{1-\mu_y^2}\sin\theta\cos\varphi+\mu_y\cos\theta \qquad (5.8) \\
\mu_z' &= -\frac{\sin\theta}{\sqrt{1-\mu_y^2}}(\mu_y\mu_z\cos\varphi-\mu_x\sin\varphi)+\mu_z\cos\theta
\end{aligned}$$

In regard to the phase function, the simulation applies the common form Henyey-Greenstein (HG) phase function [13,14]:

$$p(\cos\theta) = \frac{1-g^2}{\left(1+g^2-2g\cos\theta\right)^{3/2}} \qquad (5.9)$$

where $\int_{-1}^{1} p(u)du = 2$, and the only variant is the anisotropy of the medium $g = \langle\cos\theta\rangle$. Using the inversion techniques [13, 14], the medium variable *cos θ* can be generated easily in simulation from:

$$\cos\theta = \frac{1}{2g}\left\{1+g^2-\left[\frac{1-g^2}{1-g+2g\aleph}\right]^2\right\} \qquad (5.10)$$

where $\aleph$ is a uniform random variable (0,1). Furthermore, the Henyey-Greenstein (HG) phase function has a simple expansion form in Legendre-polynomials:

$$p(\cos\theta) = \sum_{n=0}^{\infty} (2n+1) g^n P_n(\cos\theta) \qquad (5.11)$$

The Henyey-Greenstein (HG) phase function is widely adopted as an approximate phase function for the atmosphere and tissue due to its properties [13].

## 5.3 Implementing simulation

In implementing the Monte Carlo simulation for light transmitted through an *ex vivo* tissue sample, the spatial intensity data from the time-sliced two-dimensional (2D) images is extracted and plotted as a function of time. We fit the measured time-resolved light transmission profile to a Monte Carlo model of light propagation in turbid media. The Monte Carlo simulation (MCS) assumed a Henyey-Greenstein phase function and ran on all possible range of value of anisotropy **(*g*),** and transport length ($l_t$) for the samples investigated. The MCS follows a random walk of $10^4$ photons, chosen as a compromise between CPU time and acceptable least error. The fitting procedure scanned $l_t$ through a wide range (i.e. 0.4 mm to 1.4 mm), varying the anisotropy **(*g*)** from 0.8 to 0.975 until a minimum fitting error for both $l_t$ and $g$ is reached. The accuracy of fitted $l_t$ and $g$ is set to the desire step size (see Appendix A for program details).

### 5.3.1 Construction of temporal profiles from time-sliced images

A typical time-sliced image sequence is shown in Figure 5.2. Each 2-D image possesses the spatial information at a specific temporal window position. Figure 5.3 (a) is schematic diagram showing how time profile of photons emerging from the center of highlighted region of each image is used (dash red box). To generate the temporal profile the same constant region is chosen from all the images. The intensity distribution is integrated over the area to obtain a number that is proportional to number of photons.

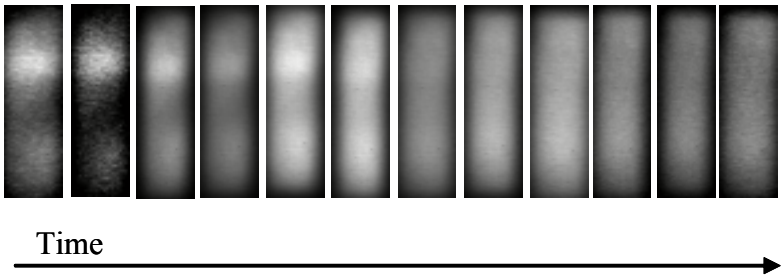


Figure 5.2: Typical time sliced image series. Each 2D image taken at a certain time window.

This number is then plotted as a function of the time delay that corresponds to the image. The overall temporal profile is a plot of these numbers against corresponding time. Figure 5.3 (b) shows a temporal profile thus generated.

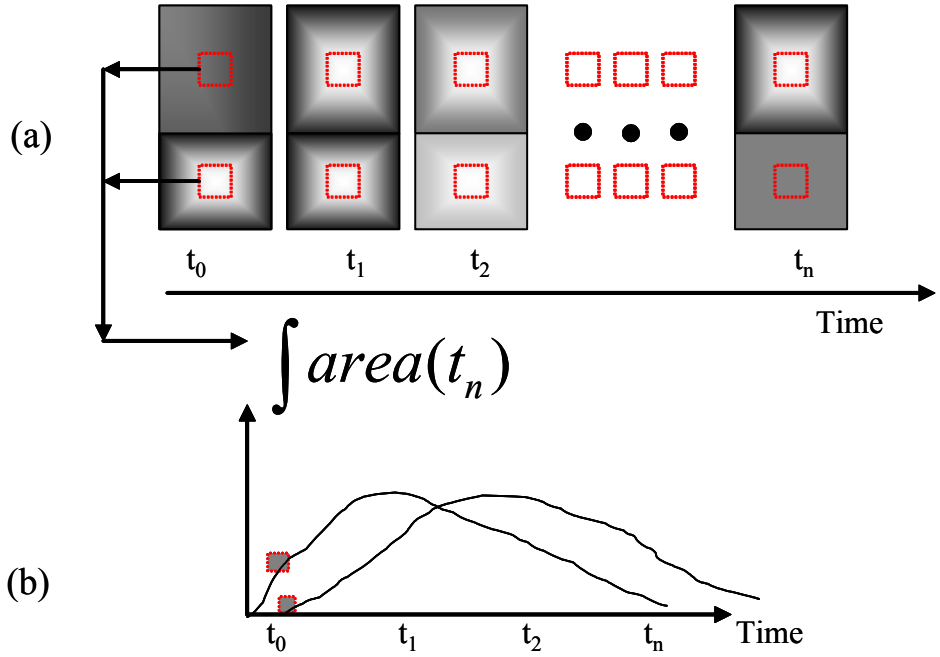


Figure 5.3: Schematic shows how to (a) extract and integrate (red dashed box) spatial intensity. (b) Plotting the intensity to form a temporal profile.

### 5.3.2 Monte Carlo simulation convolve to the gate width

In order to generate an accurate Monte Carlo simulation (MCS) we must take into account the history of the photon; the photon interaction with the media, and finally when the output photons interact with detector a flow chart in Figure 5.4 (a) show the stages for the simulation.

The MCS starts by inputting tissue optical parameters, tissue thickness, educated guess for the ballistic time (light arriving at the entrance  exit surface of sample "shine time") ($t_0$), tissue absorption coefficient ($\mu_a$) at the given wavelength ($\lambda$= 800 nm), the index of refraction of the tissue (using water) at given wavelength ($\lambda$= 800 nm), the range of anisotropy factor $g$ = 0.8 to 0.975, the number of photons for the simulation ($10^4$), and finally the initial estimate start-end for the transport length ($l_t$). $\boldsymbol{l_t}$ = 0.5 mm to 2 mm.

The result of MCS is shown in Figure 5.4 (b), the result is then convolved with the intensity temporal profile of the gate width of the detector as the result shown in Figure 5.4 (c).  Then the convolved MCS-gate-width is then fitted to the temporal profile of the tissue using Nelder and Mead 1965 [19-20].  The fitted results giving at a specified $l_t$ *and* $g$, gives the least error of the fitting parameters and, improved ballistic time $t_0$.  The process continues until the range of $l_t$ *and* $g$ is over.

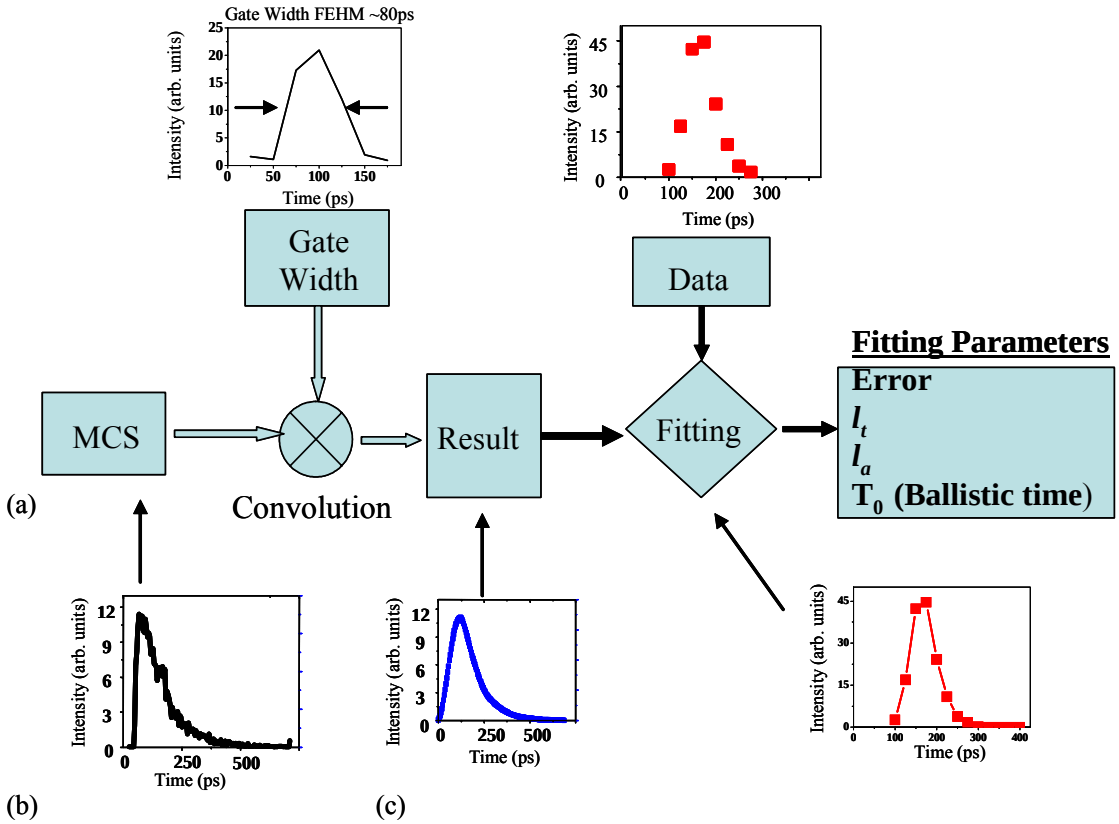


Figure 5.4: (a) Stages of simulation. (b) Monte Carlo simulation (MCS). (c) MCS convolved with gate width.

## 5.4 Samples

MCS was tested on data from Chapter 2 with tissue thickness of 5 mm. Table 5.1 presents key tissue with invasive ductal carcinoma (IDC) and normal tissue.

Table 5.1: Characteristics of *ex vivo* breast tissue samples

| Sample Number | Age (Years) | Sample Characteristics | Dimensions (mm) |
|---|---|---|---|
| 1 | 38 | Infiltrating ductal carcinoma, and normal tissue | 20 (diameter) X 5 |
| 2 | 30 | Invasive (or, infiltrating) ductal carcinoma | 30 x 10 x 5 |
| 3 | 28 | Poorly differentiated carcinoma with sarcomatoid features, and normal tissue | 30 x 14 x 5 |
| 4 | 57 | Invasive (or, infiltrating) ductal carcinoma | 20 x 20 x 5 |
| 5 | 63 | Invasive (or, infiltrating) ductal carcinoma | 20 x 10 x 5 |

## 5.5 Results

### 5.5.1 Invasive ductal carcinoma

A sequence of time-sliced 2-D images of sample #1 is shown in left frame of Figure 5.5 (a). The same normal and cancerous region of each time-sliced image was integrated and intensity versus time was plotted to generate respective temporal profiles as shown in Figure 5.5 (b). The extracted temporal profile (integrated over the white box) results for different section of each samples is displayed in the bottom frame of Figure 5.5.

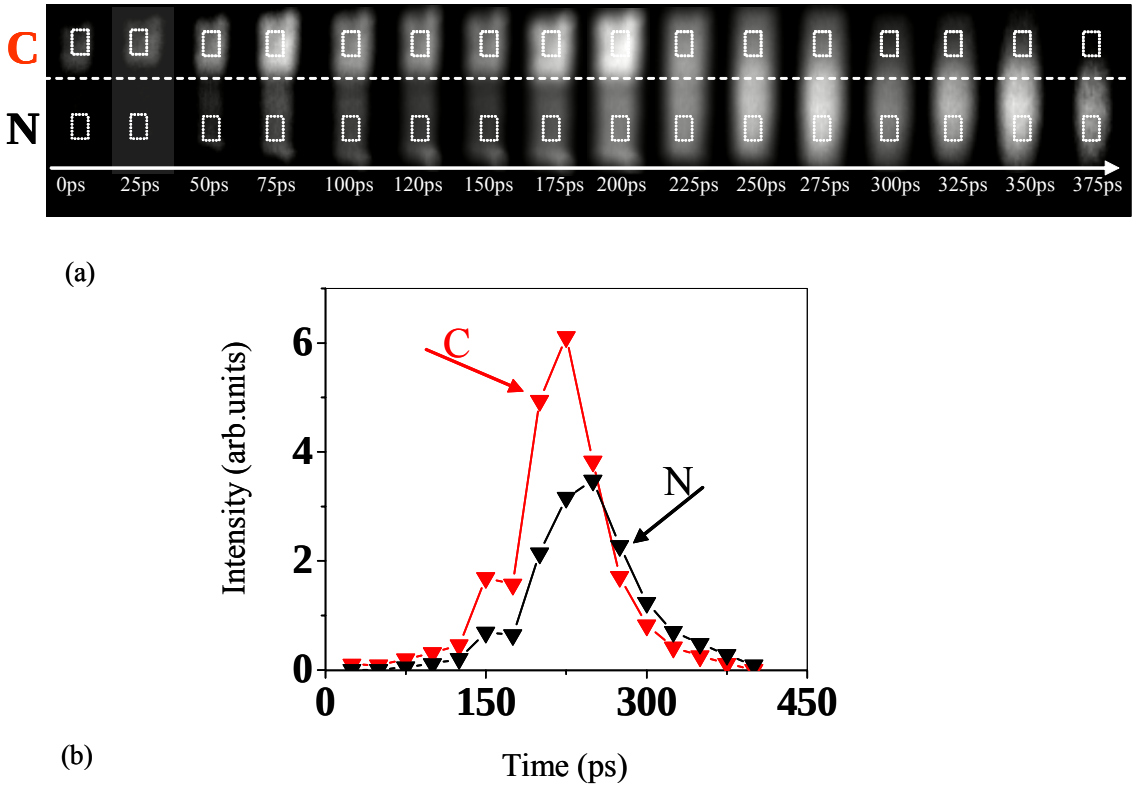


Figure 5.5: (a) Time sliced series images of Sample 1. (b) Cancer (C) region in red profile and normal (N) region in black profile.

The MCS fitting procedure results for sample #1 are shown in Figure 5.6 (a)-(d) for cancer part and Figure 5.6 (e)-(h) normal part. Figure 5.6 (a) and (e) show a

typical MCS profiles (black) at a given g and $l_t$ and the temporal profile convolved with temporal gate width (blue profile). Figure 5.6 (b)-(c) and (f)-(g) shows the output of all trials of g, and $l_t$. of the cancerous and normal part respectively. The result shows the trial of g, and $l_t$ reaches a minimum fitting error. At the minimum fitting error in both Figure 5.6 (b)-(c) g, and $l_t$ for cancerous part of tissue tell different value for $g_{\text{cancerous}} = 0.925$ and $l_{t\ cancerous} = 1.6$ mm. For normal part tissue Figure 5.6 (f)-(g) tells that the minimum value $g_{\text{normal}} = 0.95$ and $l_{t\ normal} = 1.1$ mm. finally the fitting the MCS profile to data of both part of the tissue is shown in Figure 5.6 (d) and (h) cancerous and normal part respectively.

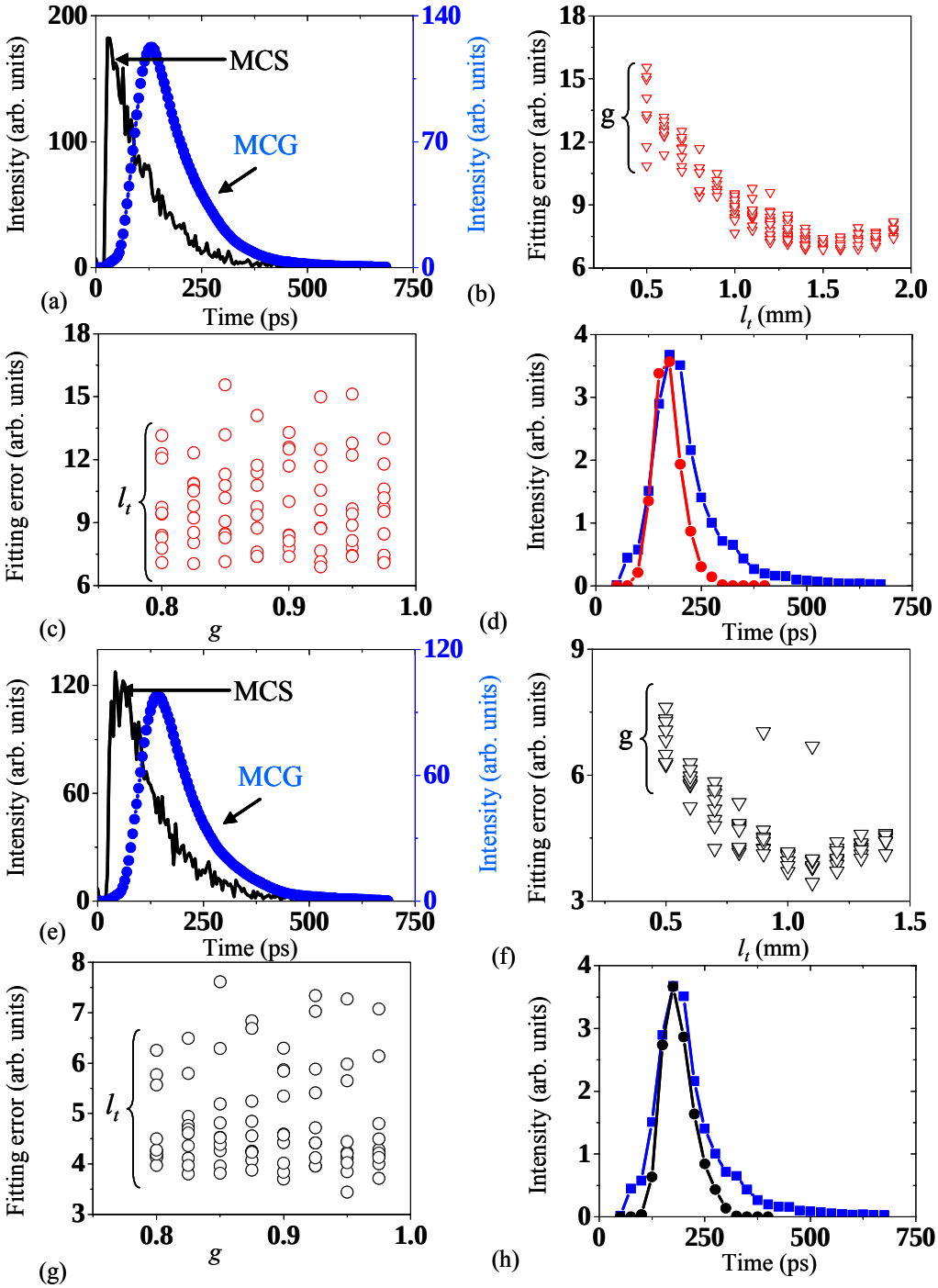


Figure 5.6: (a) and (e) Monte Carlo simulation (MCS black) and convolution with gate (MCG blue) of Sample 1. (b) Cancer (red) and (f) normal (black). MCS fitting error for various ranges of $l_t$. (c) Cancer and (g) normal MCS fitting error for various ranges of $g$. (d) Cancer and (h) normal fitting time data to MCG.

The same process was applied to sample #2. Figure 5.7 (a) shows a sequence of time-sliced 2-D images. The early-light images highlight cancerous regions, while

image recorded with late arriving light accentuate normal regions. A selected equal area (box) from the cancerous region and normal region were integrated of each time-sliced image and plotted this intensity versus time to generate respective temporal profiles as shown in Figure 5.7 (b). MCS was performed for the known thickness (~5 mm), $g$ = **0.8 to 0.975,** $l_t$ **= 0.5 mm to 2 mm** and an input of $10^4$ photons.

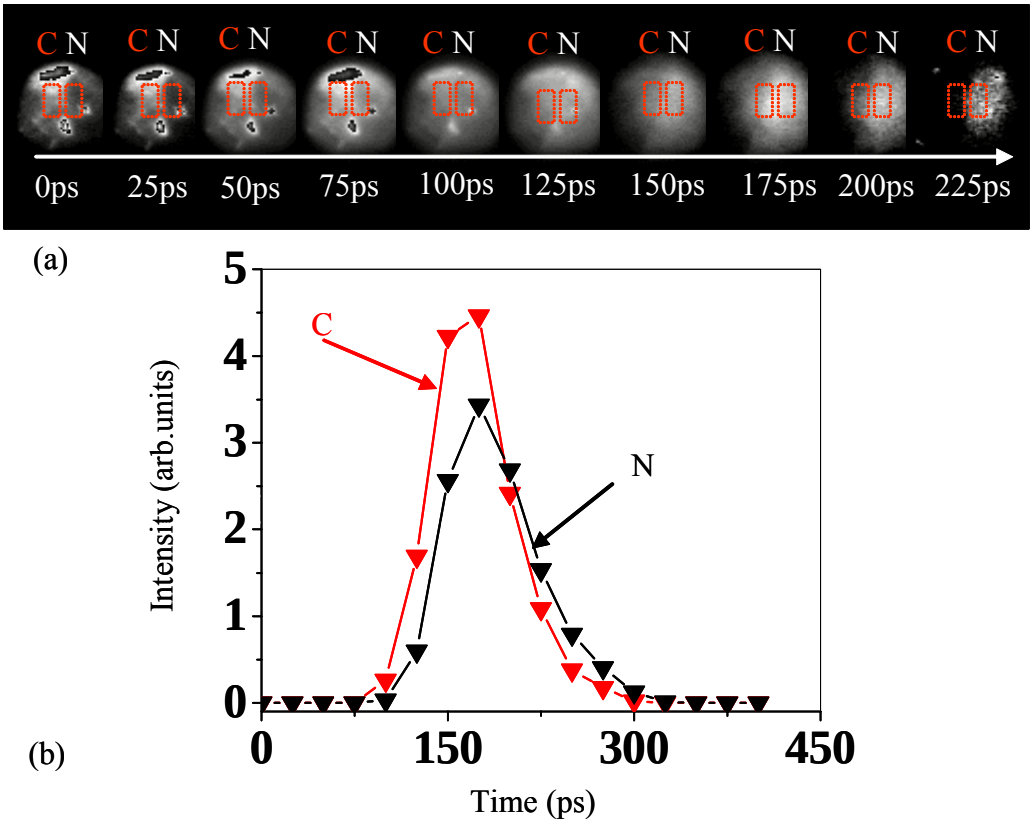


Figure 5.7: (a) Time sliced series images of Sample 2. (b) Cancer (C) region in red profile and normal (N) region in black profile

The MCS fitting results for sample #2 are shown in Figure 5.8 (a)-(d) for cancerous part and Figure 5.8 (e)-(h) normal part. Figure 5.8 (a) and (e) show a typical MCS profiles (black) at a given g and $l_t$ and of the temporal profile convolved with temporal gate width (blue profile). Figure 5.8 (b)-(c) and (f)-(g) shows the output of all trials of g, and $l_t$ of the cancerous and normal part respectively.

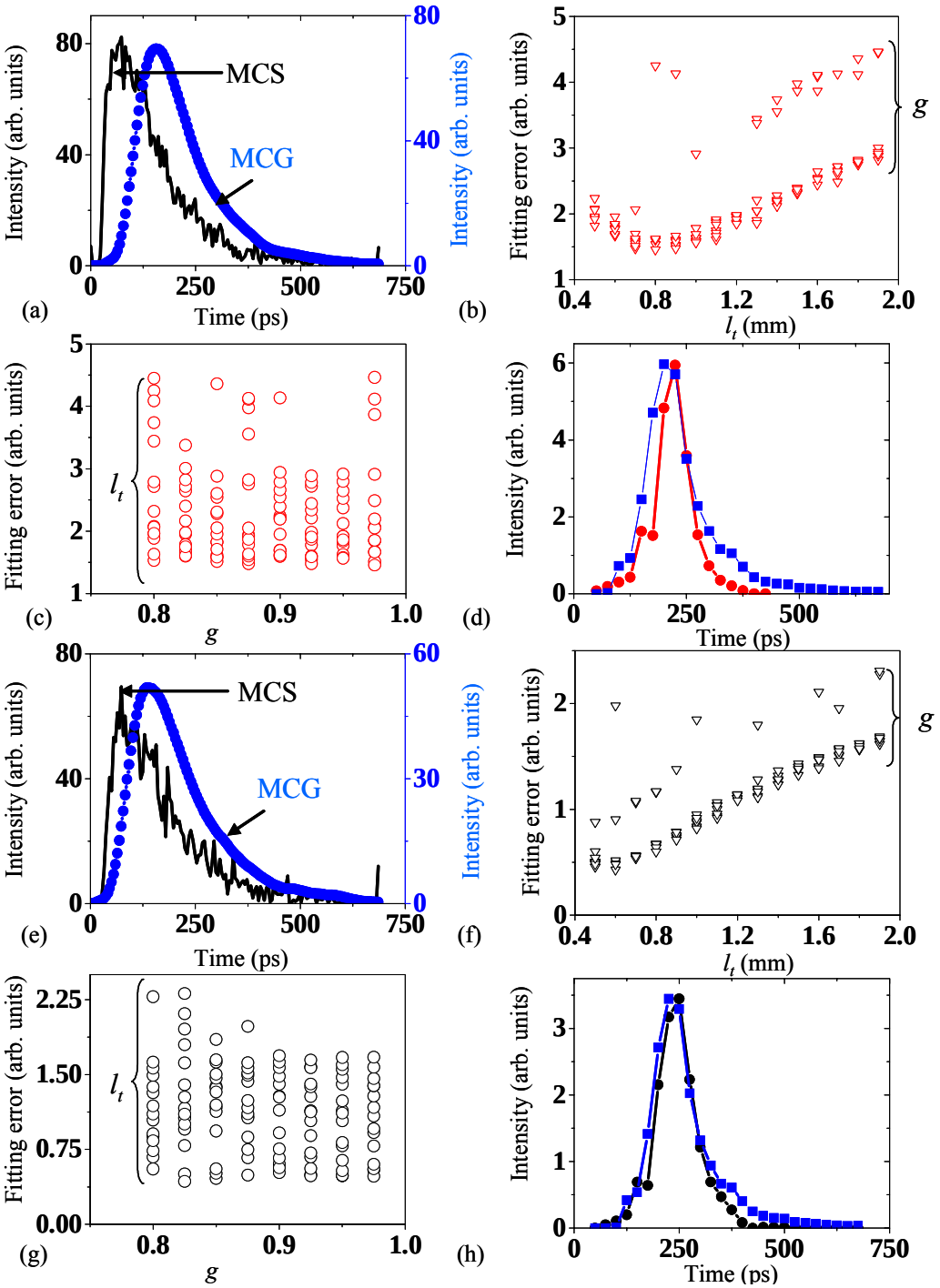


Figure 5.8: (a) and (e) Monte Carlo simulation (MCS black) and convolution with gate (MCG blue) of Sample 2. (b) Cancer (red) and (f) normal (black). MCS fitting error for various ranges of $l_t$. (c) Cancer and (g) normal MCS fitting error for various ranges of $g$. (d) Cancer and (h) normal fitting time data to MCG.

The result shows the trial of g, and $l_t$ reaches a minimum fitting least fitting error. At the minimum fitting error in both Figure 5.8 (b)-(c) g, and $l_t$ for cancerous

part of tissue tell different value for g $_{\text{cancerous}}$ = **0.975** and $l_{t\ cancerous}$ = **0.8 mm**. For normal part tissue Figure 5.8 (f)-(g) tells that the minimum value g $_{\text{normal}}$ = **0.825** and $l_{t\ normal}$ = **0.6 mm**. finally the fitting the MCS profile to data of both part of the tissue is shown in Figure 5.8 (d) and (h) cancerous and normal part respectively.

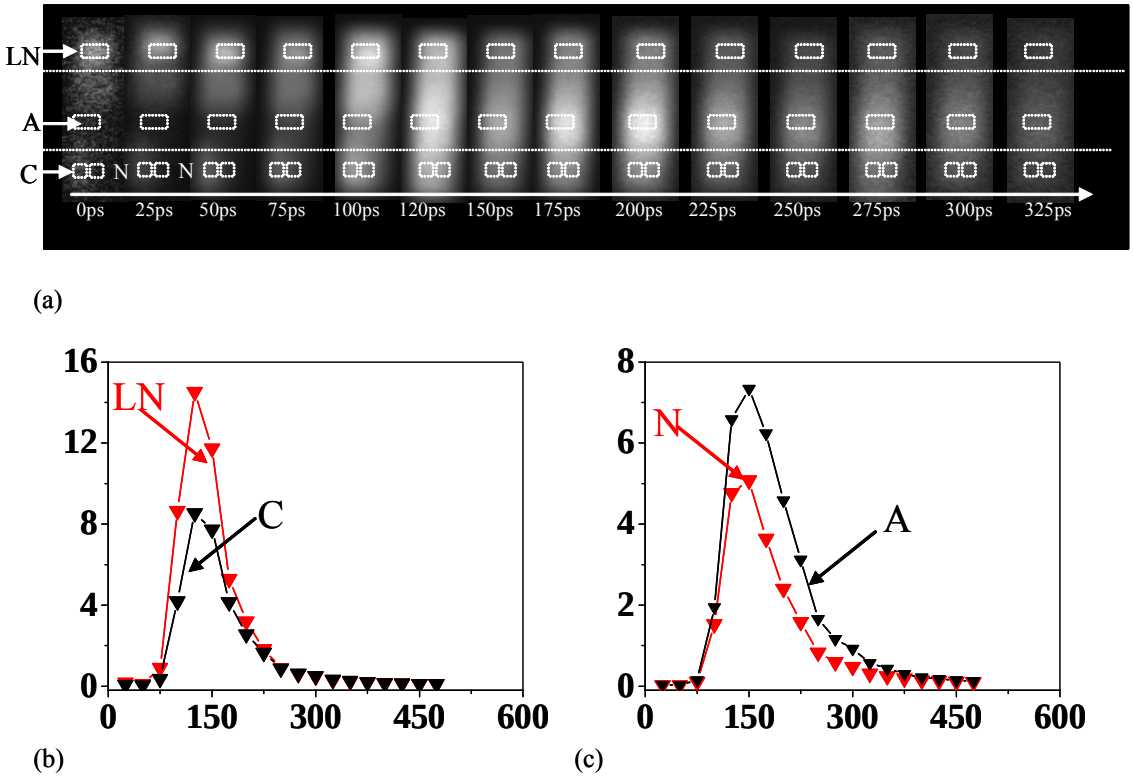


Figure 5.9: (a) Time sliced series images of Sample 3. (b) Lymph node (LN) region in red profile and cancerous (C) region in black profile. (c) Normal (N) in red profile and adipose (A) in black profile.

### 5.5.2 Carcinoma with sarcomatoid features

The next sample is the poorly differentiated carcinoma with sarcomatoid features, and normal tissue (sample #3), this sample feature four distinguished part lymph node (LN), cancerous region (C), Adipose (A), and normal (N). Figure 5.9 (a) shows a sequence of time-sliced 2-D images stretching from time 0 ps to 325 ps. The early-light images high-light lymph node (LN) regions, followed by the cancerous while image recorded with late-arriving light accentuate normal and adipose regions.

The temporal profiles were extracted and plotted for four regions in Figure 5.9 (b) and (c). The MCS ran for giving input parameters: the known thickness of all four regions (~5 mm), $g$ **= 0.8 to 0.975,** $l_t$**. = 1.5 mm to 16 mm** and an input of $10^4$ photons.

The result from the MCS fitting procedures for sample #3 are shown in Figure 5.10 (a)-(d) for lymph node (LN) part and Figure 5.10 (e)-(h) cancerous part. Figure 5.11 (a)-(d) and (e)-(h) show the result for the normal and adipose region respectively. The result for all four regions is presented in Table 5.2; the minimum value of fitting error is picked for g and $l_t$. The table indicates descending order of the effective value of transport length $l_t$, from lymph node (LN) followed by cancerous (C), then normal tissue (N) and finally the adipose part (A). The anisotropy <$g$> value is presented in third column.

Table 5.2: Results from the MCS model of sample #3.

| Tissue Region | Transport length ($l_t$) | anisotropy **<g>** factor |
|---|---|---|
| Lymph node (LN) | 9.7 mm | 0.975 |
| Cancer (C) | 6.5 mm | 0.875 |
| Normal (N) | 4.3 mm | 0.8 |
| Adipose (A) | 3.3 mm | 0.95 |

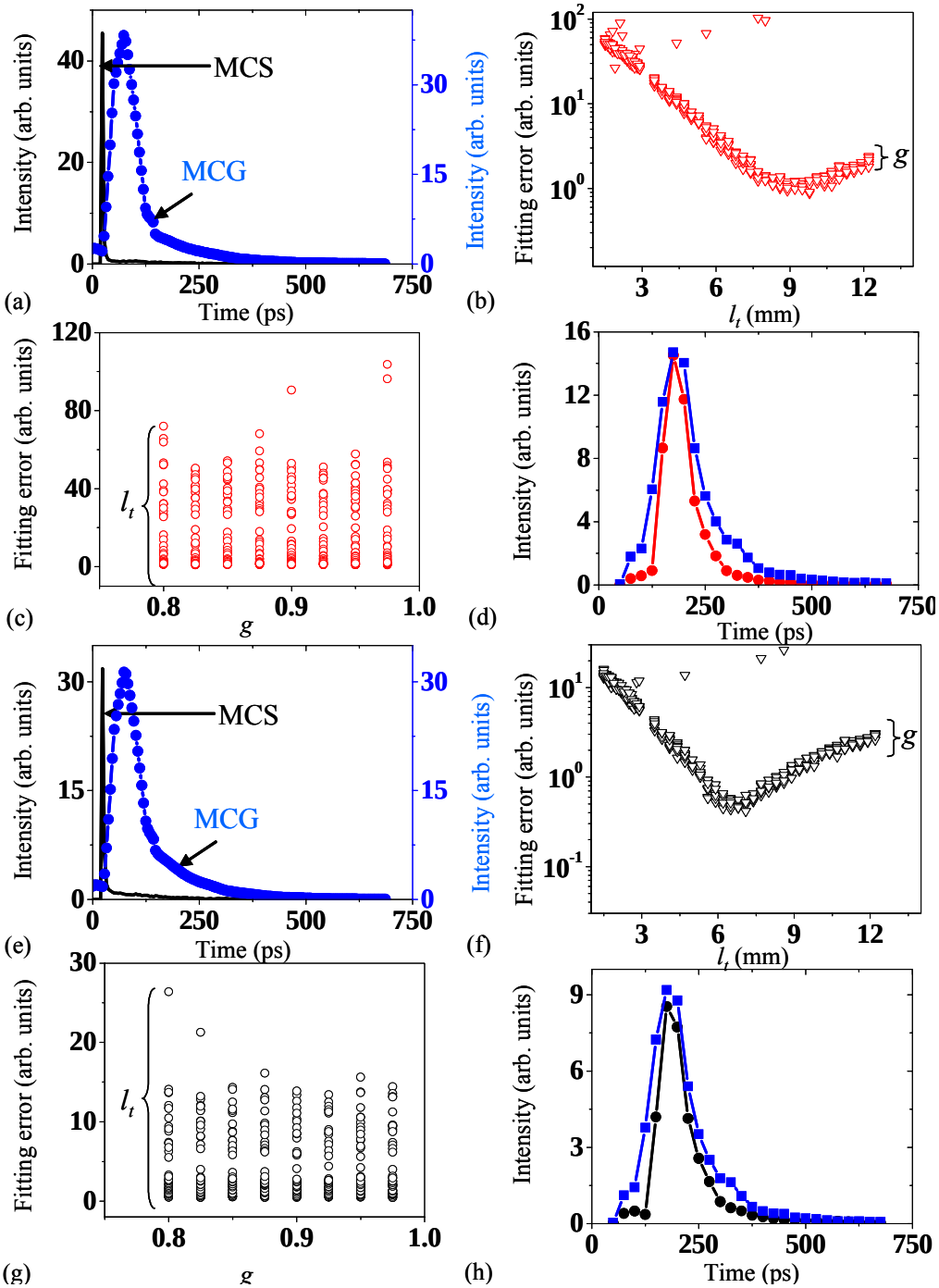


Figure 5.10: (a) and (e) Monte Carlo simulation (MCS black) and convolution with gate (MCG blue) of Sample 3. (b) Lymph node (red) and (f) cancer (black) MCS fitting error for various ranges of $l_t$. (c) Lymph node and (g) cancer MCS fitting error for various ranges of $g$. (d) Lymph node and (h) cancer fitting time data to MCG.

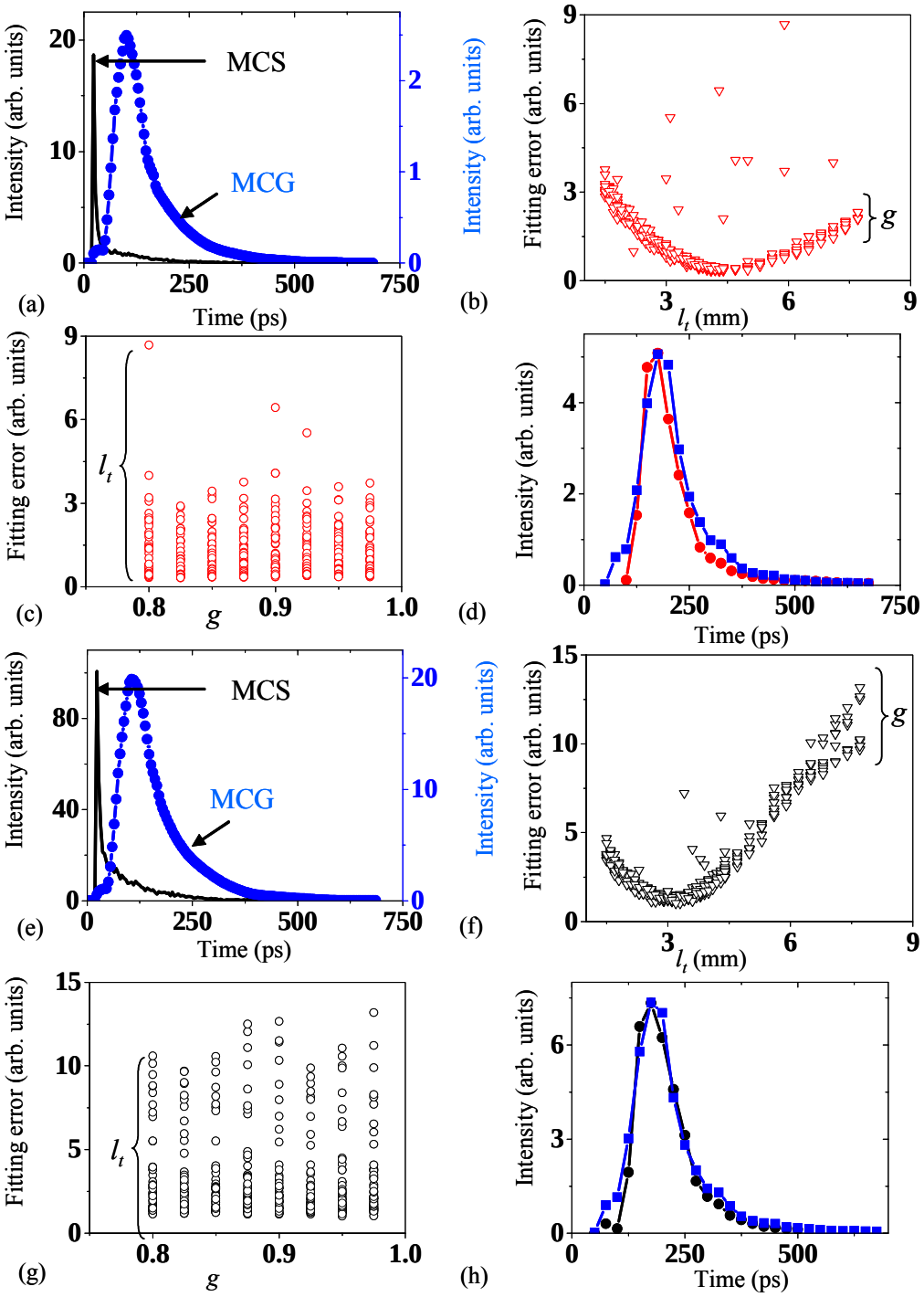


Figure 5.11: (a) and (e) Monte Carlo simulation (MCS black) and convolution with gate (MCG blue) of Sample 3. (b) Normal (red) and (f) adipose (black) MCS fitting error for various ranges of $l_t$. (c) Normal and (g) adipose MCS fitting error for various ranges of $g$. (d) Normal and (h) adipose fitting time data to MCG.

### 5.5.3 Breakdown in the model

In sample #4 MCS was used to attempt to retrieve the optical parameters $l_t$ and g. The input MCS parameters to scan the transport length $l_t$ were extended from 0.5 mm to 18 mm g is same scanning range, the number of photons were left to $10^4$. Figure 5.12 (a) shows profiles of MCS and the convolution gate width with MCS. Figure 5.12 (b)-(c) are the profiles of $l_t$ and g cancerous part it should be noted that Figure 5.12 (b) $l_t$ has being extended to 26 mm, that due to many trials attempts to find if the MCS will converge to the minimum fitting value error, but as it be observed around the $\boldsymbol{l_t}$ **= 12 mm** a split occurred in the model one part begin to increase in error value while another part kept getting smaller asymptotically in value and flatting (not converging) at the bottom, but that value of $l_t$ physically make no sense since the tissue have a thickness of 5 mm.

Figure 5.12 (d) is the fitting solution to the data. As seen, it fit the answer with high accuracy, but this fitting is at any minimum value (not converging) of $l_t$, so the solution doesn't exist. Similar features occur in the normal part of the tissue Figure 5.12 (e)-(h). One key observation is in Figure 5.12 (f) where the split is pronounced around $\boldsymbol{l_t}$ **= 6 mm** again as in the case of cancerous part, the model could not converge to the true minimum value. Another key observation is the behavior of the g profile in both Figure 5.12 (c) and (g): the behavior looks more concentrated, not like the others tissue sections 5.5.1 and 5.5.2 where they more randomly distributed.

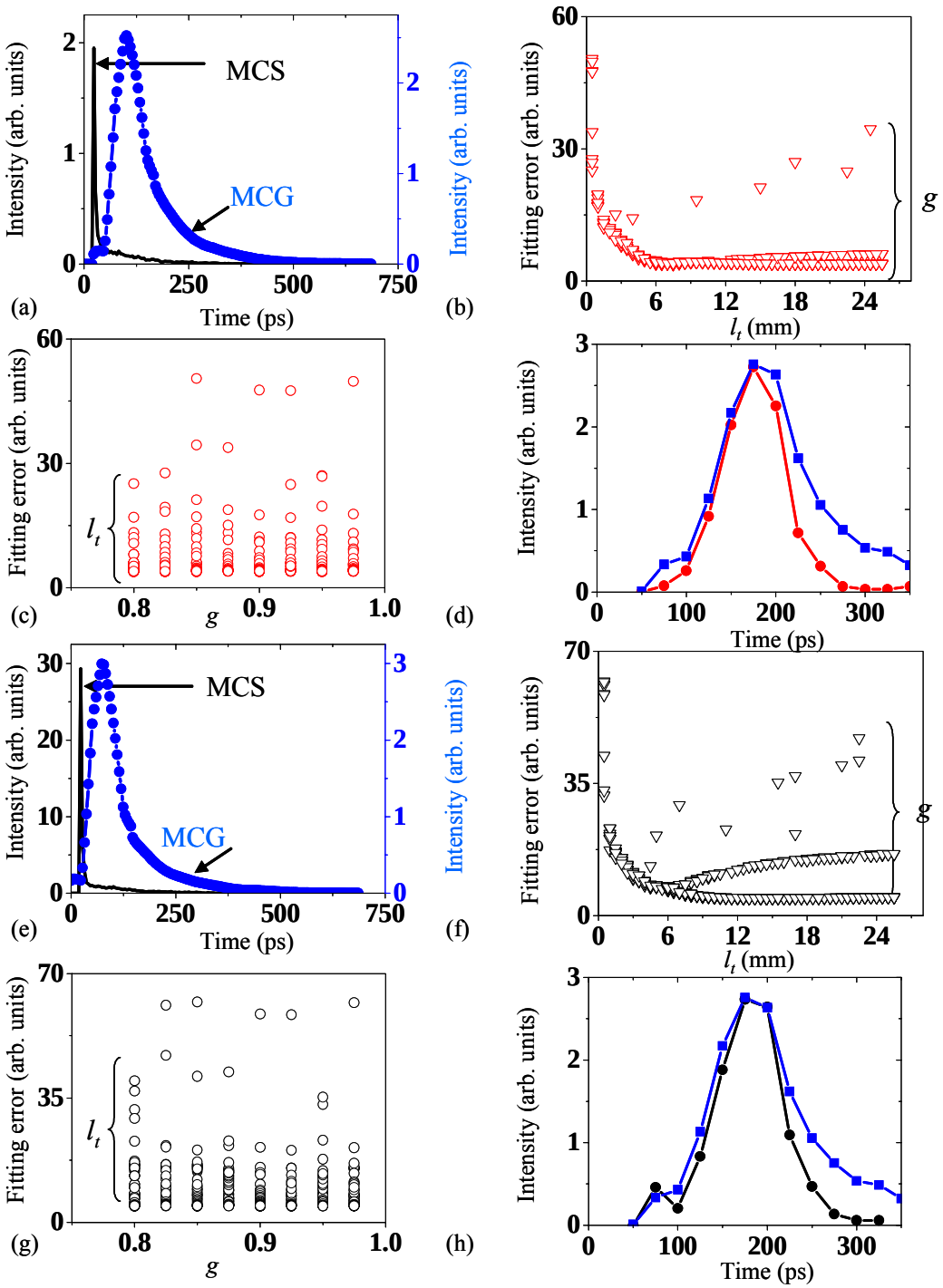


Figure 5.12: (a) and (e) Monte Carlo simulation (MCS black) and convolution with gate (MCG blue) of Sample 4. (b) Cancer (red) and (f) normal (black). MCS fitting error for various ranges of $l_t$. (c) Cancer and (g) normal MCS fitting error for various ranges of $g$. (d) Cancer and (h) normal fitting time data to MCG.

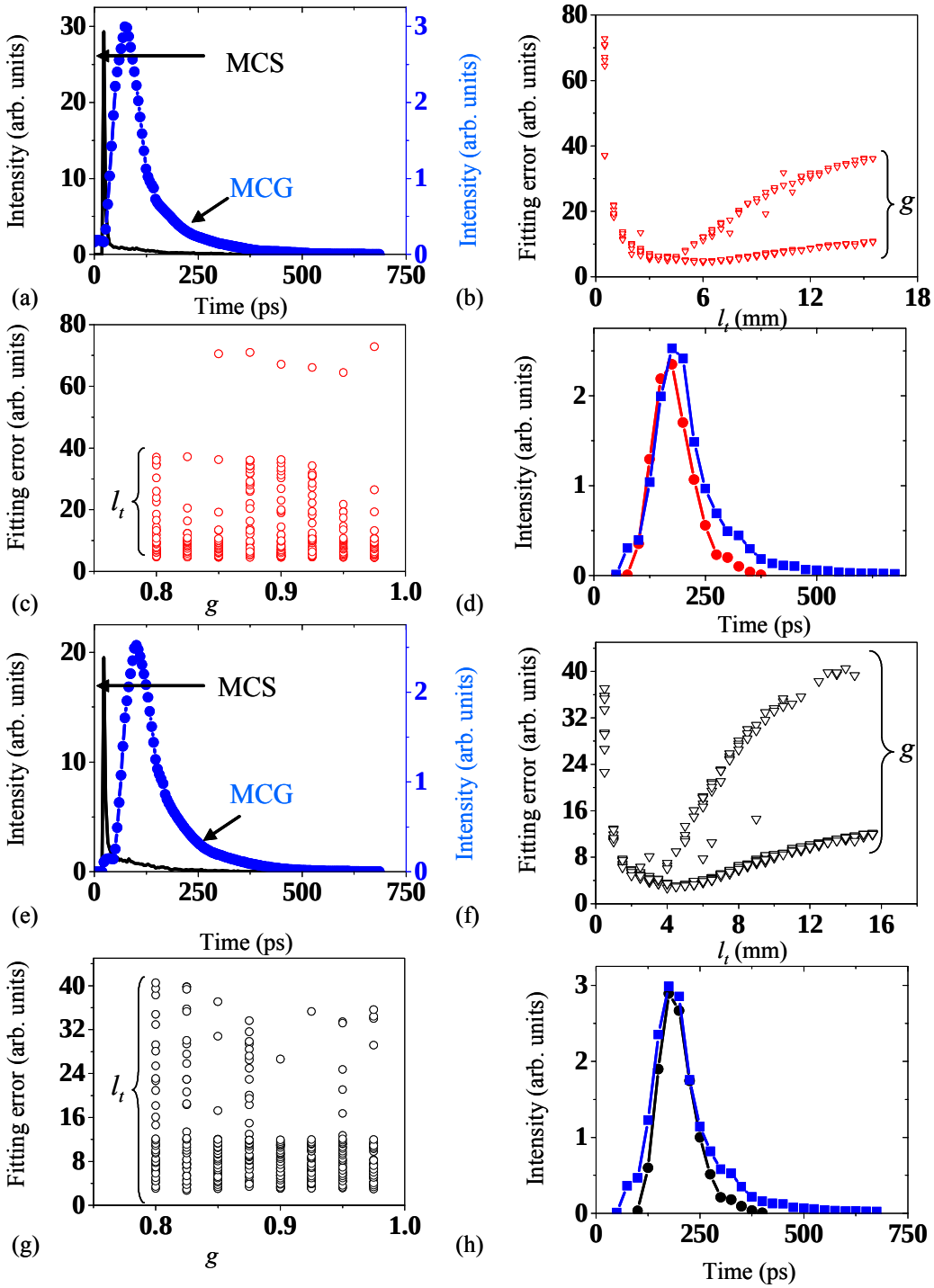


Figure 5.13: (a) and (e) Monte Carlo simulation (MCS black) and convolution with gate (MCG blue) of Sample 5. (b) Cancer (red) and (f) normal (black). MCS fitting error for various ranges of $l_t$. (c) Cancer and (g) normal MCS fitting error for various ranges of $g$. (d) Cancer and (h) normal fitting time data to MCG.

Simulation model was tested on sample #5. Again, Figure 5.13 (a) and (e) show a typical MCS at giving $l_t$ and $g$ value. Figure 5.13 (b)-(d) and (f)-(h) are the

result for cancerous section and normal part respectively. Now, the behavior of transport lengths for both cancerous and normal behaving differently namely the split occurs early in both cases as shown in Figure 5.13 (b) and (f). Moreover, the schism occurs for cancerous around $\boldsymbol{l_t}$ **= 4.5 mm** with minimum value at $\boldsymbol{l_t}$ **= 6 mm.** The normal case, the rift occurs around $\boldsymbol{l_t}$ **= 3.5 mm** with minimum value at $\boldsymbol{l_t}$ **= 4.5 mm.** Furthermore, the behaviors of g for both cancerous and normal cases show fairly normal randomly distributed as seen in Figure 5.13 (c) and (g).

## 5.6 Conclusion

The techniques showed that it has the potential tool to extract the transport length ($l_{te}$). It should be understood that the accuracy of the transport length $l_t$, depends on what the instrumentation (UGICS) observed, since the model took that into account. Plus the absorption coefficient ($\mu_a$) was not consider in detail, the hypothesis is that the tissue is compose of between 70% to 80% water and was set to value 0.002 which is what the value of absorption coefficient ($\mu_a$) of water at $\lambda = 800$ nm. MCS analysis was tested only on five samples of thickness = ~5 mm. for thin tissue analysis. The result from the five samples with exception to one (sample #4) the transport length ($l_t$) had consistently higher values for the cancer region than the non-cancerous (normal, and adipose) region for all four samples. What is even more interesting, when reaching the minimum value of error in the $l_t$ range we see a clustering of the value of g in all cases at the given value of $l_t$. This is observed in Figure 5.8 (b) and (f), Figure 5.9 (b) and (f), Figure 5.10 (b) and (f), Figure 5.11 (b) and (f), and Figure 5.13 (b) and (f). So, interpreting the results shows clearly that $l_t$ is insensitive to $g$ at the given range 0.8 to 0.975.

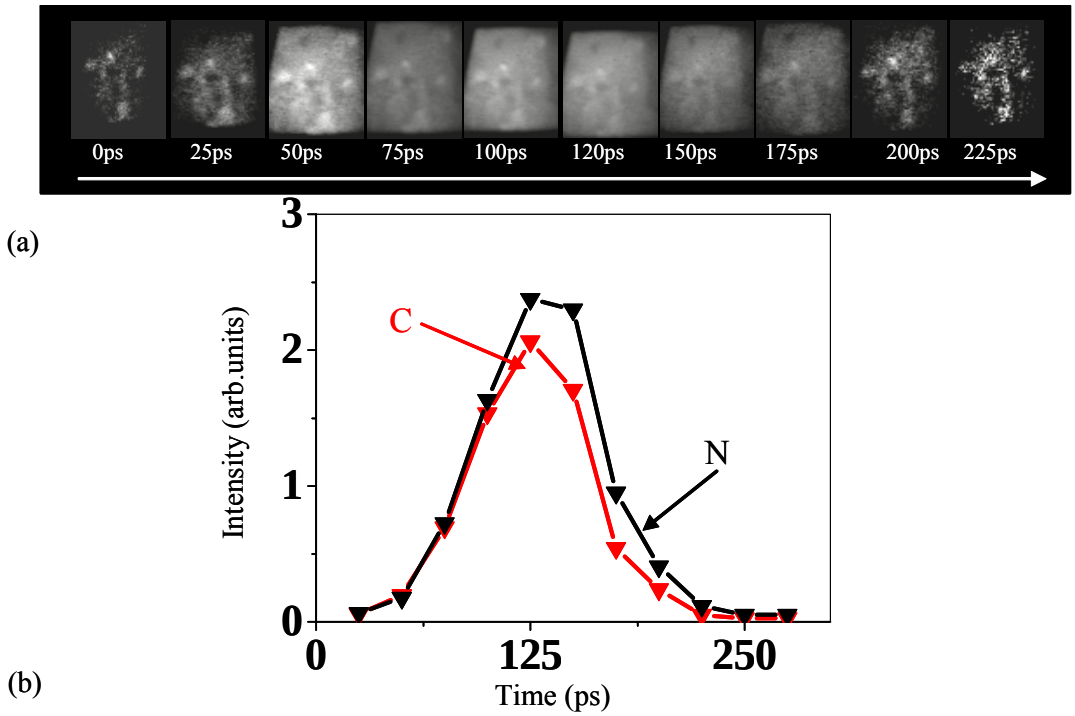


Figure 5.14: (a) Time sliced series images of Sample 4. (b) Cancer (C) region in red profile and normal (N) region in black profile.

Reasons for the breakdown in the model:

- Time sliced images; do the images show differentiation between tissues region as shown in Figure 5.14 (a) and temporal profile Figure 5.14 (b)? From the images and profile the images show slight variation and the temporal profile reflect.
- The number of data plays role in both fitting and retrieving optical information, in all cases, the data points were under twelve. And that made very hard for the fitting algorithm (optimization).
- The MCS program has a floating-point fault (cannot be avoid), which explains the outbreak in the fitting data.
- The UGICS has 15 ps electronic jitter, which threw off the ballistic time ("shine time").
- Finally, the case for absorption coefficient $\mu_a$ of the tissue was not dealt in details

Table 5.3 summarizes all the results for the tissue investigated. The outcome provides a quantitative validation that cancerous (tumors) tissues are less scattering than normal. The NIR time-sliced imaging, combined with MCS analysis, has a potential for improving optical breast mammography / tomography.

Table 5.3: Results of transport length ($l_t$) for tissue investigated.

| Sample # | $l_t$ Cancer | $l_t$ Normal |
|---|---|---|
| 1 | 1.6 mm | 1.1 mm |
| 2 | 0.8 mm | 0.6 mm |
| 3 | 6.5 mm | 4.3 mm |
| 4 | Failed | Failed |
| 5 | 6.0 mm | 4.5 mm |

Detail of the programs that implemented the simulation and fitting are presented in Appendix B. The program was written in the language of Python (v. 2.3), which ran on Debian GNU/Linux platform (v 3.1). The computer processor used a Pentium 4 (2.4 GHz). The computation time for each output file varies from sample to sample and on the average of < 10 minutes.

## 5.7 References


1. Keijzer, M., S.L. Jacques, S.A. Prahl, A.J. Welch: Light distributions in artery tissue: Monte Carlo simulations for finite-diameter lasers beams. *Lasers in Medicine and Surgery* **9**:148-154, 1989.
2. Prahl, S.A., M. Keijzer, S.L. Jacques, A.J. Welch: A Monte Carlo model of light propagation in tissue. In *Dosimetry of Laser Radiation in Medicine and Biology*, G. Mueller, D. Sliney, Eds., SPIE Series Vol. IS **5**:102-111, 1989.
3. Keijzer, M., R. Richards-Kortum, S.L. Jacques, M.S. Feld: Fluorescence spectroscopy of turbid media: Autofluorescence of the human aorta, *Applied Optics* **28**:4286-4292, (1989).
4. Jacques, S.L.: Time-resolved propagation of ultra-short laser pulses within turbid tissues. *Applied Optics* **28**:2223-2229, (1989).
5. Jacques, S.L.: Time-resolved reflectance spectroscopy in turbid tissues. *Transactions IEEE on Biomedical Engineering* **36**:1155-1161, (1989).
6. Wang, L-H, S.L. Jacques: Hybrid model of Monte Carlo simulation and diffusion theory for light reflectance by turbid media. *J. Optical Soc. Am. A* **10**:1746-1752, (1993).
7. Wang, L-H, S.L. Jacques: Optimized radial and angular positions in Monte Carlo modeling. *Med. Phys.* **21**:1081-1083, 1994.
8. Wang, L-H, S.L. Jacques, L-Q Zheng: MCML - Monte Carlo modeling of photon transport in multi-layered tissues. *Computer Methods and Programs in Biomedicine* **47**:131-146, 1995.

9. L.-H. Wang, S. L. Jacques, and L.-Q. Zheng: CONV - Convolution for responses to a finite diameter photon beam incident on multi-layered tissues, *Computer Methods and Programs in Biomedicine* **54**:141-150, 1997.
10. S. L. Jacques and L.-H. Wang, "Monte Carlo modeling of light transport in tissues," in Optical Thermal Response of Laser Irradiated Tissue, edited by A. J. Welch and M. J. C. van Gemert (Plenum Press, New York, 1995), pp. 73-100.
11. S. L. Jacques, L.-H. Wang, and A. H. Hielscher, "Time-resolved photon propagation in tissues," in Optical Thermal Response of Laser Irradiated Tissue, edited by A. J. Welch and M. J. C. van Gemert (Plenum Press, New York, 1995), pp. 305-332.
12. G. L. Coté, S. Rastegar, and L.-H. Wang, "Introduction to Biomedical Optics and Lasers," in Introduction to Biomedical Engineering, J. Enderle, S. Blanchard, and J. Bronzino, eds. (Academic Press, 1999).
13. L. G. Henyey and J. L. Greenstein, 'Diffuse radiation in the galaxy,' Astrophys. J. **93**, 70-83 (1941).
14. M. Xu, “Optical image reconstruction in highly scattering media”, PhD thesis, City University of New York (2001).
15. K. M. Yoo, F. Liu, and R. R. Alfano, Phys. Rev. Lett. **64**, 2647 (1990).
16. W. Cai, M. Xu, and R. R. Alfano, ” Analytical form of the particle distribution based on the cumulant solution of the elastic Boltzmann transport equation” Phys. Rev. E **71**, 041202 (2005).

17. W. Cai, M. Lax, and R. R. Alfano, Phys. Rev. E **61**, 3871 (2000).

18. W. Cai, M. Xu, M. Lax, and R. R. Alfano, Opt. Lett. **27**, 731 (2002).

19. Nelder, J. A. and Mead, R. "A Simplex Method for Function Minimization." Comput. J. **7**, 308-313, (1965).

20. Lagarias, J. C.; Reeds, J. A.; Wright, M. H.; and Wright, P. E. "Convergence Properties of the Nelder-Mead Algorithm in Low Dimensions." AT&T Bell Laboratories Tech. Rep. Murray Hill, NJ, (1995).

# Chapter 6
# Summary and Future work

## 6.1 Summary

This thesis presents a study of the underlying principle, methods and approaches for the development of an optical spectroscopic modality for non-invasive detection and potential diagnosis of breast cancer. The thesis explored combined experimental, analytical, and numerical approaches for addressing the key issues involved in the development of *optical mammography*. The thrust areas of the research carried out in the thesis were: (a) adaptation and development of "time-sliced" (time-resolved) experimental approach for imaging of targets in turbid media, (b) development and adaptation of spectroscopic imaging approach for realizing the diagnostic potential, (c) adaptation of the independent component analysis (ICA) concept from information theory to develop optical tomography using independent component analysis (OPTICA) for detection, three-dimensional localization and cross section imaging of targets embedded in a turbid medium, and (d) application of experimental, analytical and numerical techniques thus developed to model media for initial testing, and *ex vivo* breast tissues for exploring the feasibility and estimating parameters for *in vivo* breast imaging application. The results of optical imaging and spectroscopic study were compared with magnetic resonance imaging and histopathology for validation.

Chapter 2 presents the developments and applications of time-sliced imaging and spectroscopic imaging approaches for obtaining direct images of targets in turbid media, and the applications of those techniques for imaging of normal and cancerous

*ex vivo* human breast tissues. The breast tissue specimens included normal fibroglandular tissues, adipose tissues, and tumors including invasive ductal carcinoma, and tumors with sarcomatoid features. The time-sliced imaging arrangement included the use of a gated image intensified camera system enabling 80-ps temporal resolution. The spectroscopic imaging arrangement made use of Fourier Space gating and polarization gating for reducing multiple-scattered photons, and extended the measurements to 1200-1300 nm spectral range using a Cr:forsterite laser to probe adipose and water signatures in tissues.

The results of time-sliced imaging measurements demonstrated that light transmission properties are different for normal and cancerous tissues, and that images recorded with early-arriving photons highlight cancerous tissues, while those recorded with late-arriving photons accentuate normal tissues. Results of spectroscopic imaging experiments show that overall light transmission is higher through the cancerous tissues compared to that through the same thickness of normal tissues. This difference further depends on the wavelength of light and the proximity of the probing wavelength to the specific resonances of tissue constituents. Diagnostic potential of spectroscopic imaging could be realized by correlating similar wavelength dependent signatures from different tissue constituents, such as, hemoglobin, adipose, water, lipids, and other chromophores.

Chapter 3 details the development of the OPTICA approach and its application to scattering, absorptive, and fluorescent targets embedded in highly scattering turbid media. The results demonstrate that the approach can provide 3-D location of targets with high accuracy. The approach was able to locate all four

targets in a breast phantom where one of the targets had a contrast only 10% higher than the surrounding medium.

In Chapter 4 OPTICA formalism was extended to yield cross sectional image of targets, and tested on realistic breast models assembled using excised breast tissues. The location of a tumor inside a model breast was determined within a few millimeters in all three dimensions, and its cross sectional image provided an estimate of its size. Another measurement of a fluorescent target demonstrated the usefulness of the approach in contrast agent enhanced breast imaging.

Chapter 5 presents a Monte Carlo Simulation based approach to extract key optical parameters of transport length, and anisotropy factor from time-resolved measurements. Although the approach showed right qualitative differences between normal and cancerous tissues in the values of these parameters, the numerical values that were extracted did not conform satisfactorily to those in the literature. We attribute this to inadequacy of data, and the size and thickness limitations of the samples used in the study. The approach has potential and needs further development.

## 6.2 Future Directions

The work carried out and results obtained in this thesis suggests further steps towards realizing the goal of developing optical mammography. These include:

(a) Development of combined spectroscopic and time-resolved imaging approach to capitalize on the scattered light rejection ability of time sliced imaging with the diagnostic potential of optical spectroscopy;

(b) Development of hyperspectral OPTICA that extends measurements to a number of key wavengths to probe different chromophores and fluorophores in breast tissues, and carry out the tasksof detection, localization, cross section imaging, and localized spectroscopy of suspect sites;

(c) Undertake *in vivo* measurements on volunteers using the approaches developed so far which will enable further extraction and accumulation of necessary parameters and specification of design criteria for development of optical mammography systems; and

(d) Continue to develop approaches (such as, oblique incidence backreflection that can be used to extract key optical parameters of tissues to enable non-invasive *in vivo* biopsy for diagnosis.

# Appendix A
# OPTICA computer program

OPTICA computer program is divided into image handling (preparation) part and the actual image detection using independent components analysis (ICA), with help of blind source separation (BSS) and shape reconstruction using backprojection Fourier transforms. The programs are written in Matlab language. (v. 6.5-7.01), which ran on Debian GNU/Linux platform (v 3.1)

1. The program: begin with Config.m file
2. Subroutine findedge.m it find the edge of images
3. Subroutine cropimg.m crops the image at desire size
4. Subroutine Find the value of $\kappa = \sqrt{3\mu_a \mu_s'}$ , the output signal $T(r) = \frac{\exp(-r\kappa)}{4\pi D r}$, $D = 1/3\mu_s'$
5. Subroutine blind source separation (BSS)
6. Subroutines generate the shape of target.

Programs Config.m

```
% config the parameters for one set of experiments
nx = 16; % # of scan images in x-direction
ny = 22; % # of scan images in y-direction
gridsz = 2.0;
pixelsz = 89/477.1;
n = gridsz / pixelsz;
% the boundaries of 0101.tif and 0909.tif
up01 = 320;
```

```
down01 = 550;

left01 = 420;

right01 = 750;

up09 = 310-30;

down09 = 540+15;

left09 = 450-15;

right09 = 700+15;

 samprate = 5;
```

Program findedge.m

```
% the *r.tif files are rotated to upright.

% the edges can be easily found as it is either horizontal or vertial

% search the edges in a region centered at x1, x2, y1, y2

% read the parameters

config;

up = zeros(18, 18);

down = zeros(18, 18);

left = zeros(18, 18);

right = zeros(18, 18);

% the region for 0101r.tif

x1 = up01;

x2 = down01;

d = 30;
```

```
for i=1:nx
 x1 = x1 - floor(n+0.5);
   x2 = x2 - floor(n+0.5);
   y1 = left01;
   y2 = right01;
   for j=1:ny
         y1 = y1 + floor(n+0.5);
         y2 = y2 + floor(n+0.5);
         f = sprintf('%02d%02d.tif', i, j);
         fprintf('%s...\n', f);
         im = imread(f);
         [mx, my] = size(im);
         [bw,thresh] = edge(im, 'log', [], 3);
         % find the peaks along x axis
         a = sum(bw');
         [vx1, px1] = max(a(x1-d:x1+d));
         px1 = px1 + x1 - d - 1;
         [vx2, px2] = max(a(x2-d:x2+d));
         px2 = px2 + x2 - d - 1;
         % find the peaks along y axis
         a = sum(bw);
         if y1 - d < 1
            [vy1, py1] = max(a(11:y1+d));
```

```
            py1 = py1 + 11 - 1;
        else
            [vy1, py1] = max(a(y1-d:y1+d));
            py1 = py1 + y1 - d - 1;
        end
        if y2 + d > my
            [vy2, py2] = max(a(y2-d:my));
        else
            [vy2, py2] = max(a(y2-d:y2+d));
        end
        py2 = py2 + y2 - d - 1;
        fprintf('    %d %d %d %d    %d\n', vx1, px1, vx2, px2, px2-px1);
        fprintf('    %d %d %d %d    %d\n', vy1, py1, vy2, py2, py2-py1);
        % save
        left(i, j) = py1;
        right(i, j) = py2;
        up(i, j) = px1;
        down(i, j) = px2;
    end
end

save edge_findedge.mat up left right down
%mat2nc edge_findedge.mat edge_findedge.nc
```

Program Cropimg.m

```
config;
win0 = [up09 left09 down09 right09];
left = zeros(nx, ny);
up = zeros(nx, ny);
right = zeros(nx, ny);
down = zeros(nx, ny);
for i=1:nx
   for j=1:ny
         f = sprintf('%02d%02d.tif', i, j);
         fc = sprintf('%02d%02dc.tif', i, j);
         fprintf('%s\n', f);
         im = imread(f);
         [w0, w1, w2, w3] = window(n, i, j, 9, 9, win0);
         up(i, j) = w0;
         left(i, j) = w1;
         down(i, j) = w2;
         right(i, j) = w3;
         imc = imcrop(im, [w1, w0, w3-w1, w2-w0]);
         imwrite(imc, fc);
   end
```

```
end


% overwrite edge.mat from findedge.m
save edge_cropimg2.mat up down left right
%mat2nc edge_cropimg2.mat edge_cropimg2.nc
```

Program fit for $\kappa$ value from images

```
% fit for kappa only.
function kappa=fit_kappa(x1, v1, lt, L, doz)
 [M, p] = max(v1);
 x0 = x1(p);
 b = min(v1);
 kappa = 0.1;
 if isreal(kappa)
   a = (max(v1) - b)/gslab(0, L, 0, kappa, lt, L, doz);
 else
   a = (max(v1) - b)/cgslab(0, L, 0, kappa, lt, L, doz);
 end
 opt = optimset('MaxFunEvals', 20000, 'MaxIter', 20000, 'LevenbergMarquardt', 'on');
 [x, feval] = fminsearch(@MSE, [a, b, x0, kappa], opt, x1, v1, lt, ...
                                 L, doz);
 a = x(1); b = x(2); x0 = x(3); kappa = x(4);
 if isreal(kappa)
```

```
  vv1 = a*gslab(x1 - x0, L, 0, kappa, lt, L, doz) + b;
 else
  vv1 = a1*cgslab(x1 - x0, L, 0, kappa, lt, L, doz) + b;
 end
 if isreal(kappa)
  plot(x1, v1, 'o', x1, vv1);
 else
  plot(x1, abs(v1), 'o', x1, abs(vv1));
 end
function f=MSE(x, x1, v1, lt, L, doz)
% calculate the diffrence between a*gslab(rho, 0, z, kappa, lt, L, doz) + b
% and the vector v, where rho = x1 - x0
 a = x(1);                    % scale
 x0 = x(3);                    % center
 kappa = x(4);                   % z
 b = x(2);
 if kappa < 0
  f = 999999999999999999;
  return
 end
 t = a*gslab(x1 - x0, L, 0, kappa, lt, L, doz) + b;
 tv = t - v1;
 %thres = (v1(1) + v1(length(v1)))/2;
```

```
 %tv = tv (find (v1 > thres));
 f = sum(tv.^2);
```

Program blind source separation (BSS)

```
% Experiments
% Data from: reassemeble3.py
% The source grids: 1 16
% The common sensor window: 480 448 [0, 90, 480, 538]
% The sampling rate: 2
lt = 1/0.9;
L = 55;
kappa = 0.127;
samprate = 5;
stepsz1 = 2.5/7*samprate;            % detector step
stepsz2 = 2.5;                       % source step
yc = 245; xc = 405;
% The common sensor window: 480 448 [0, 90, 480, 538]
x1 = -floor((xc-samprate/2-90)/samprate):floor((538-xc-samprate/2)/samprate);
y1 = -floor((yc-samprate/2-0)/samprate):floor((480-yc-samprate/2)/samprate);
x1 = x1*stepsz1; y1=y1*stepsz1;
% x2: 16 15 ... 9 (8) 7 ... 1
x2 = -8:7; x2 = x2*stepsz2;
bg = getnc('bgscanline.nc', 'meas');
X = getnc('scanline.nc', 'dmeas'); XX = X;
```

```
Y = getnc('scanline.nc', 'meas');
nx = 1;
[ny, mx, my] = size(X);
if 1
  Xline = squeeze(X(:, y1>-5 & y1<5, :));  % size: ny x my
  bgline = squeeze(bg(y1>-5 & y1<5, :));  % size: ny x my
  mx = size(Xline, 2);
  X = reshape(Xline, nx*ny, mx*my);
  y1 = y1(y1>-5 & y1 < 5);
else
  X = reshape(X, nx*ny, mx*my);
  Y = reshape(Y, nx*ny, mx*my);
end
% fit for bg
addpath /home/minxu/BSS
bg = mean(bgline, 1);
[kappa, I0, b, v1, vv1] = fit_Shankel(x1, bg, kappa, lt, L);
kappa, I0, b
%return
% find the possible number of ICs
% addpath /usr/local/lib/matlab/icaML
% interval = 1:10;
% P=icaML_bic(X, interval, 1);
```

```
% [most_prop,most_prop_k]=max(P);
% most_prop
% most_prop_k=interval(most_prop_k)
% bar(interval,P);
% drawnow;
n = 2;                          % n components to be extracted
% ---> BEST <---
% runica from eeglab
% In EEGLAB: chans: number of sensors, frames: number of time samplings in
% one epoch, total time samplings is frames*epoch
if 1
  addpath /usr/local/lib/matlab/eeglab4.1
  [weights,sphere,S,bias,sign,lrates] = runica(X, 'pca', n,'maxsteps',1024);
  B = weights*sphere;
  A = pinv(B);
  %[weights, sphere] = binica(X, 'pca', 5);
  %S = weights*sphere*X;
else
  addpath /usr/local/lib/matlab/JADE
  B=jadeR(X,n);
  S=B*X;
  A=pinv(B);
end
```

```
figure(1)
for i=1:n
  subplot(n,3,3*i-2)
  plot(S(i,:))
  subplot(n,3,3*i-1)
  imagesc(x1, y1, reshape(S(i,:), mx, my))
  subplot(n,3,3*i)
  plot(x2, A(:,i))
end
drawnow
S1 = reshape(S(1, :), mx, my);
S2 = reshape(S(2, :), mx, my);
% S1
figure(2)
v1 = mean(S1, 1);
v2 = A(:, 1)';
subplot(1,2,1); plot(x1, v1);
subplot(1,2,2); plot(x2, v2);
drawnow
% [kappa, x0, z, a1, a2, b1, b2, v1, v2, vv1, vv2] = fit_SAhankel_varKappa(x1, v1, x2,
v2, kappa, lt, L);
[x0, z, a1, a2, b1, b2, v1, v2, vv1, vv2] = fit_SAhankel(x1, v1, x2, v2, kappa, lt, L);
z, x0, a1*a2/I0
```

```
% S2
figure(3)
v1 = mean(S2, 1);
v2 = A(:, 2)';
subplot(1,2,1); plot(x1, v1);
subplot(1,2,2); plot(x2, v2);
drawnow
% [kappa, x0, z, a1, a2, b1, b2, v1, v2, vv1, vv2] = fit_SAhankel_varKappa(x1, v1, x2,
v2, kappa, lt, L);
[x0, z, a1, a2, b1, b2, v1, v2, vv1, vv2] = fit_SAhankel(x1, v1, x2, v2, kappa, lt, L);
z, x0, a1*a2/I0
```

Program shape reconstruction

```
% obtain the shape of the inclusion
% used for comparison.m
addpath /home/minxu/research/fluoroscence/trunk/
%[kappa, I0, b, v1, vv1] = fit_Shankel((500:700)*pixelsz, double(im(420,500:700)),
kappa, 1, 33)
kappa = 0.1088
nx = size(A,1); ny = size(A,2);
mx = size(S,1); my = size(S,2);
X = zeros(nx, ny, mx, my);
% for srcno=1, (30,30,30)
```

```
L = 33;
z = 14.6313;
% for srcno=2, (50,60,20)
%z = L - 20;
for i=1:nx
   for j=1:ny
         for k=1:mx
            for l=1:my
                  X(i,j,k,l) = -A(i,j)*S(k,l);         % for srcno=1
                  % X(i,j,k,l) = A2(i,j)*S2(k,l);   % for srcno=2
            end
         end
   end
end
if 0
   % bring the two stepszs to be equal
   mx2 = floor(mx*stepsz1/stepsz2 + 0.5);
   my2 = floor(my*stepsz1/stepsz2 + 0.5);
   Y = zeros(nx, ny, mx2, my2);
   S = fspecial('gaussian', [4 4], 1);
   for i=1:nx
      for j=1:ny
            Y(i,j,:,:) = imresize(squeeze(X(i,j,:,:)), [mx2 my2]);
```

```
            Y(i,j,:,:) = filter2(S, squeeze(Y(i,j,:,:)));
        end
    end
    % effectively, the two step sizes are same now
    X = Y;
    [nx, ny, mx, my] = size(X);
    stepsz1 = stepsz2;
end
% NX = 2*nx+1; NY = 2*ny+1;
% only use psx = psy = 0, no need to expand it
NX = nx; NY = ny;
MX = 2*mx+1; MY = 2*my+1;
Xf = fftn(X, [NX NY MX MY]);
dz = zeros(MX, MY);
a1 = zeros(MX, MY);
a2 = zeros(MX, MY);
ncutoff = 0
mcutoff = mx
doz = 1.68*lt;
b0 = qgslab(0, z, 0, kappa, lt, L, doz)*qgslab(0, z, L, kappa, lt, L, doz)'
for i=-mcutoff+1:mcutoff+1
    qx = (i-1)/MX*2*pi/stepsz1;
    if i < 1; i = i+MX; end
```

```
for j=-mcutoff+1:mcutoff+1
    qy = (j-1)/MY*2*pi/stepsz1;
    if j < 1; j = j+MY; end
  %fprintf('%d %d %f %f\n', i, j, qx, qy);
    f1 = 0; f2 = 0; f3 = 0;
    for is=-ncutoff+1:ncutoff+1
      qsx = (is-1)/NX*2*pi/stepsz2;
      if is < 1; is = is+NX; end
      for js=-ncutoff+1:ncutoff+1
          qsy = (js-1)/NY*2*pi/stepsz2;
          if js < 1; js = js+NY; end
          qdx = qx - qsx;
          qdy = qy - qsy;
          id = qdx*stepsz1/(2*pi)*MX + 1;
          id = mod(floor(id+0.5), MX);
          if id == 0; id = MX; end
          jd = qdy*stepsz1/(2*pi)*MY + 1;
          jd = mod(floor(jd+0.5), MY);
          if jd == 0; jd = MY; end
          qs = sqrt(qsx^2 + qsy^2);
          qd = sqrt(qdx^2 + qdy^2);
          a = Xf(is,js,id,jd);
          b = qgslab(qd, z, 0, kappa, lt, L, doz)*qgslab(qs, z, L, kappa, lt, L, doz)';
```

```
                f1 = f1 + a*b';
                f2 = f2 + b*b';
            end
        end
        a1(i,j) = f1;
        a2(i,j) = f2;
        % 0.00001 is about 0.004*b0=1e-05, where
        % b0 = qgslab(0, z, 0, kappa, lt, L, doz)*qgslab(0, z, L, kappa, lt, L, doz)'
        % dz(i,j) = f1/(f2 + 0.00001^2);
        % dz(i,j) = f1/(f2 + (b0*0.006)^2);
        dz(i,j) = f1/(f2 + (b0*0.005*2)^2);    % for srcno=1
        %dz(i,j) = f1/(f2 + (b0*0.003)^2);   % for srcno=2
    end
end

dz2 = ifft2(dz);
rdz = real(dz2(1:mx, 1:my));
idz = imag(dz2(1:mx, 1:my));
figure(2)
subplot(1,2,1)
imagesc(rdz(1:50,1:45)); colorbar;
subplot(1,2,2)
imagesc(idz); colorbar;
```

# Appendix B

## Monte Carlo simulation program fitting to time-resolved data

The program below calls on Monte Carlo simulation of light propagating in tissue (turbid media), written in C++ language (see *M. Xu 2001* thesis) The programs was written in the python 2.5.1 language, which ran on Debian GNU/Linux platform (v 3.1). The program needs Gnuplot and TableIO.

```
from Numeric import *
import Gnuplot
import OpticalProperty
import TableIO
import ngf2, sys
from scipy.interpolate import interp1d
from Numeric import convolve


# pulse gate with step 25ps
gate = array([1.65278, 1.09375, 17.2882, 20.9618, 12.0903, 1.95486, 0.923611])
gate = gate/sum(gate)
sp = interp1d(arange(7)*25, gate, 'linear')

thickness = 5     # tissue thickness in millimeter
gd = ngf2.grid()
s = ngf2.geometry(0, thickness, gd)
gp = Gnuplot.Gnuplot()

def mc(mus, nph, dt, nt, g):
    o = ngf2.optiparam(1.38, 0, mus, g)  # tissue optical properties
    l = ngf2.layer(s, o)
    c = ngf2.chain(0, thickness, 1, 1)
    c.addLayer(l)
    c.done()
    print 'ls, lt=', c.getLayer(0).ls(), c.getLayer(0).lt()

    ph = ngf2.phMonteCarlo(c)
    ph.setupDetector(dt, 1, nt, 1)
    ph.run(nph)
    tstat, rarr, Tarr = ph.getResult()
```

```
    print tstat
    return Tarr

if __name__ == '__main__':
    nt = 150; nph = 10000          # nph is number of photons
    dt = 1.38/0.2998
    ts = arange(0, dt*(nt-0.5), dt)
    m = TableIO.readTableAsArray('feb1799.TXT', '#')   # input file of samples
    mts = m[2:, 0]  # first column for time
    #mI = m[2:, 2]
    mI = m[2:, 2] # third column for cancer
    out = open('feb1799N.out_2f', 'w')  # output file of samples
    fmc = 'mcfitN5051n1.dat'
    fmcc = 'mc_convN5051n1.dat'
    ffit = 'fitN5051n1.dat'

    muac=0.001
    t0list = [10, 20, 30, 40, 50, 60, 70, 80, 90, 100, 110, 120] # list of t0
    glist = [0.8, 0.825, 0.85, .875, 0.9, 0.925, 0.95, 0.975] # list of g
    for i in range(8):
      g = glist[i]
      muslist = 1/arange(16.0, 26.0, 0.5)/(1-g)
      for k in range(20):
          mus = muslist[k]
       Tarr = mc(mus, nph, dt*0.2998/1.38, nt, g)
       Tarr = Tarr.astype('f')
          TableIO.writeArray(fmc, transpose(array([ts, Tarr])))
       gp.plot(Gnuplot.Data(ts, Tarr, with='lines'))

          gw = sp(arange(floor(6*25/dt))*dt)
          N = len(Tarr)
          Tarr2 = zeros(2*N, 'd')
          Tarr2[int(6*25/dt):len(Tarr)-1+int(6*25/dt)] = Tarr[:-1]
          Tarr = convolve(Tarr2, gw, 1)/sum(gw)
          j = 0
          while Tarr[j] <= 0:
             j = j+1
          Tarr = Tarr[j:N+j]
          gp.replot(Gnuplot.Data(ts, Tarr, with='lines'))
          TableIO.writeArray(fmcc, transpose(array([ts, Tarr])))

       slab = OpticalProperty.UniformSlab(1.38, thickness)
       error_cur = 1e20
          for t0 in t0list:
             # muac = 0.0001
```

```
        muac, t0, a, error, I = slab.fitByMonteCarlo(mI, mts, Tarr, ts, muac, t0,
opt_fixed_t0=0)
            if error < error_cur:
                error_cur = error
                I_cur = I
                muac_cur = muac
                t0_cur = t0
                a_cur = a
        sys.stdout.write('==>OBTAIN\n%d %f %f %f %f %f\n' % (i, g, mus,
muac_cur, t0_cur, a_cur, error_cur))
        sys.stdout.flush()
        out.write('%d %f %f %f %f %f %f\n' % (i, g, mus, muac_cur, t0_cur, a_cur,
error_cur))
        out.flush()
        TableIO.writeArray('ffit_%d'%k, transpose(array([mts, I_cur])))
        TableIO.writeArray('fmcc_%d'%k, transpose(array([ts+t0_cur, a_cur*Tarr*exp(-
muac*ts)])))
        gp.replot(Gnuplot.Data(mts, I_cur/a_cur, with='linespoints', title='g,mus=%f %f'
% (g,mus)))
        gp.replot(Gnuplot.Data(ts+t0_cur, Tarr*exp(-muac*ts), with='lines'))
    out.close()
```

# Appendix C

## PATENTS

1. R. R. Alfano, M. Xu, **M. Alrubaiee**, and S. K. Gayen, "Optical tomography using independent component analysis for detection and localization of targets in turbid media," Provisional patent application #60/633,412 submitted December 7, 2004.

## LIST OF PUBLICATIONS

1. **M. Alrubaiee**, M. Xu, S. K. Gayen, and R. R. Alfano, "Localization and Cross Section Reconstruction of Fluorescent Targets in *Ex Vivo* Breast Tissue Using Independent Component Analysis", Appl. Phys. Lett. **89**, 133902-1 (2006).
2. **M. Alrubaiee**, M. Xu, S. K. Gayen, M. Brito, and R. R. Alfano, "Three-Dimensional Optical Tomographic Imaging of Scattering Objects in Tissue-Simulating Turbid Media Using Independent Component Analysis", Appl. Phys. Lett. **87**, 191112-1 (2005).
3. M. Xu, **M. Alrubaiee**, S. K. Gayen, and R. R. Alfano, "Optical Imaging of Turbid Media Using Independent Component Analysis: Theory and Simulation", J. Biomed. Opt. **10**, 051705-1 (2005).
4. **M. Alrubaiee**, S. K. Gayen, R.R. Alfano, and J. A. Koutcher, "Spectral and Temporal Near-Infrared Imaging of *Ex Vivo* Cancerous and Normal Human Breast Tissues", Tech. Cancer Res. Treat. **4**, 457-469 (2005).
5. M. Xu, **M. Alrubaiee,** S. K. Gayen, R. R. Alfano, "Three-dimensional Localization and Optical Imaging of Objects in Turbid Media with Independent Component Analysis", Appl. Opt. **44**, 1889-1897 (2005).

6. R. R. Alfano, J. L. Birman, X. Ni, **M. Alrubaiee,** and B. B. Das, "Comment on: observation of optical precursors in water," Phys. Rev. Lett. **94**, 239401 (2005)
7. M. E. Zevallos, S. K. Gayen, **M. Alrubaiee**, R. R. Alfano, "Time-gated Backscattered Ballistic Light Imaging of Objects in Turbid Water", Appl. Phys. Lett. **86**, 011115-1 (2005).
8. X. Ni, C. Wang, X. Liang, **M. Al-Rubaiee** and R. R. Alfano, "Fresnel diffraction supercontinuum generation," IEEE *JSTQE* **10**, 1229 (2004).
9. T. K. Gayen, A. Katz, H. E. Savage, S. A. McCormick, **M. Al-Rubaiee**, Y. Budansky, J. Lee, R. R. Alfano, "Aorta and Skin Tissues Welded by Near-Infrared Cr4+:YAG Laser", J. Clin. Laser Med. Surg. **2**1, 259-269 (2003).
10. S. K. Gayen, **M. Alrubaiee**, H. E. Savage, S. P. Schantz, R. R. Alfano, "Parotid Gland Tissues Investigated by Picosecond Time-Gated and Optical Spectroscopic Imaging Techniques", IEEE J. Sel. Top. Quantum Electron. **7**, 906 (2001).
11. W. Cai, S. K. Gayen, M. Xu, M. Zevallos, **M. Alrubaiee,** M. Lax, R. R. Alfano, "Optical Tomographic Image Reconstruction from Ultrafast Time-sliced Transmission Measurements", Appl. Opt. **38**, 4237 (1999).
12. S. K. Gayen, M. E. Zevallos, **M. Alrubaiee**, R. R. Alfano, "Near-Infrared Laser Spectroscopic Imaging: A Step Towards Diagnostic Optical Imaging of Human Tissues", Lasers Life Sci. **8**, 187 (1999).
13. Manuel E. Zevallos, S. K. Gayen, Bidyut Baran Das, **Mohammed Alrubaiee**, R. R. Alfano, "Picosecond Electronic Time-Gated Imaging of Bones in Tissues", IEEE J. Sel. Top. Quantum Electron. **5**, 916 (1999).

14. S. K. Gayen, M. E. Zevallos, **M. Alrubaiee**, J. M. Evans, R. R. Alfano, "Two-dimensional Near-infrared Transillumination Imaging of Biomedical Media with a Chromium-doped Forsterite Laser", Appl. Opt. **37**, 5327 (1998).

**MANUSCRIPTS SUBMITTED**

1. M. Xu, **M. Alrubaiee**, S. K. Gayen, and R. R. Alfano, "Optical diffuse imaging of a human breast model using independent component analysis", PNAS (Submitted 2007).
2. Yimin Wang, S. K. Gayen, **M. Alrubaiee**, and R. R. Alfano, "Detection of a target in a highly scattering turbid medium using near-infrared center of intensity time gated imaging," *Opt. Lett.* (submitted)
3. S. K. Gayen, C. Gonzalez, V. Balogh-Nair, M. Brito, B. B. Das, G. Comanescu, X. C. Liang, A. H. Byro, David. L. V. Bauer, **M. Alrubaiee**, and R. R. Alfano, 'Optical Spectroscopy of a Hybrid CdS-Dendrimer Nanocomposite," *Phys. Rev. B* (submitted).

**PRESENTATIONS:**

1. M. Xu, **M. Alrubaiee,** S. K. Gayen, H. Savage, R. R. Alfano, "Optical High Resolution Cross Section Imaging of a Human Breast Model Using Independent Component Analysis", Proc. of SPIE **6434** (2007).
2. M. Xu, **M. Alrubaiee**, S. K. Gayen, R. R. Alfano, "Determination of Light Absorption, Scattering and Anisotropy Factor of a Highly Scattering Medium Using Back Scattered Circular Polarized Light", Proc. of SPIE **6435** (2007).
3. **M. Alrubaiee**, M. Xu, S. K. Gayen, R. R. Alfano, "Time-sliced imaging and Monte Carlo simulation study of ex vivo cancerous and normal breast tissues."

Presented at the Junior Scientist Conference 2006, April 19 – 21, Vienna University of Technology, Vienna, Austria.

4. M. Xu, **M. Alrubaiee**, R. R. Alfano, "Fractal Mechanism of Light Scattering for Tissue Optical Biopsy, Proc. of SPIE **6091**, 73 (2006).
5. **M. Alrubaiee**, M. Xu, S. K. Gayen, R. R. Alfano, "Independent Component Analysis for Three-Dimensional Optical Imaging and Localization of a Fluorescent Contrast Agent Target Embedded in a Slab of ex vivo Human Breast Tissue", Proc. of SPIE **5859**, 203 (2005).
6. **M. Alrubaiee**, W. Cai, S. K. Gayen, and R. R. Alfano, "Spectral and temporal near-infrared imaging of ex vivo normal and cancerous human breast tissues and model media," Paper P64-1 presented at the Era of Hope, Department of Defense Breast Cancer Research Program Meeting, June 8-11, 2005, Philadelphia, PA.
7. **M. Alrubaiee**, M. Xu, S. K. Gayen, and R. R. Alfano, "Optical tomography using Independent Component Analysis for breast cancer detection," Paper P64-2 presented at the Era of Hope, Department of Defense Breast Cancer Research Program Meeting, June 8-11, 2005, Philadelphia, PA
8. W. Cai, **M. Alrubaiee**, S. K. Gayen, M. Xu, R. R. Alfano, "Three-dimensional Optical Tomography of Objects in Turbid Media using the 'Round-trip Matrix,'" Proc. SPIE **5693**, pp. 4-9, SPIE Conf. on Optical Tomography and Spectroscopy of Tissue VI, San Jose, CA., Jan. 23-26, (2005).
9. M. Xu, **M. Alrubaiee**, S. K. Gayen, R. R. Alfano, "Optical Tomography using Independent Component Analysis to Detect Absorptive, Scattering, or Fluorescent Inhomogeneities in Tubid Media", Proc. SPIE **5693**, pp. 528-535, SPIE Conf. on

Optical Tomography and Spectroscopy of Tissue VI, San Jose, CA, Jan. 23-26, (2005).

10. **M. Alrubaiee**, M. Xu, S. K. Gayen, and R. R. Alfano, "Three-dimensional localization of several scattering targets in a turbid medium using independent component," in Conference on Lasers and Electro-optics/Quantum Electronics and Laser Science and Photonic Applications, System and Technologies 2005 (Optical Society of America, Washington, DC, 2005).
11. M. Xu, **M. Alrubaiee**, S. K. Gayen and R. R. Alfano, "Fluorescence optical imaging in turbid media using independent component analysis," in Conference on Lasers and Electro-optics/Quantum Electronics and Laser Science and Photonic Applications, System and Technologies 2005 (Optical Society of America, Washington, DC, 2005).
12. **M. Alrubaiee**, M. Xu, S. K. Gayen, R. R. Alfano, "Fluorescence Optical Tomography using Independent Component Analysis to Detect Small Targets in Turbid Media", Proc. SPIE **5693**, pp. 221-224, SPIE Conf. on Optical Tomography and Spectroscopy of Tissue VI, San Jose, CA, Jan. 23-26, (2005).
13. X. Ni, C. Wang, X. Liang, **M. Alrubaie**e, and R. R. Alfano, "Supercontinuum interference from Fresnel diffraction caused by periodic filamentation," CLEO/QELS, May 22, 2005, Baltimore, Maryland.
14. **M. Alrubaiee**, M. Xu, S. K. Gayen, W. Cai, R. R. Alfano, "Time-resolved and Quasi-continuous wave Three-dimensional Tomographic Imaging of Objects in Tissue-like Turbid Media", SPIE Proc. **5463**, 82 (2004).

15. **M. Alrubaiee**, S. K. Gayen, J. A. Koutcher, R. R. Alfano, “Cancerous and Normal Human Tissues investigated by Near-infrared Time-resolved and Spectroscopic Imaging Techniques”, SPIE Proc. **4955**, 199 (2003).
16. S..K. Gayen, **M. Al-Rubaiee**, R.R. Alfano, “Time-resolved and Optical Spectroscopic Imaging for Cancer Detection”, Invited talk, 2003 IEEE MTT-S International Symposium, June 8-13, 2003, Philadelphia, PA.
17. **M. Alrubaiee**, S. K. Gayen, W. Cai, M. Xu, J. A. Koutcher, “Near-infrared Photonics Imaging of Human Breast Tissue”, **P48-2**, Era of Hope, Dept. of Defense Breast Cancer Research Program Meeting, Sept. 25-28, 2002, Orlando, FL.
18. S. K. Gayen, **M. Alrubaiee**, R. R. Alfano “Time-Sliced and Spectroscopic Two-dimensional Imaging of Normal and Cancerous Human Breast Tissues”, “Era of Hope,” DOD Breast Cancer Research Program Meeting, pp. 195, June 8-11, 2000, Atlanta, GA
19. S. K. Gayen, **M. Alrubaiee**, M. E. Zevallos, R. R. Alfano, “Temporally and Spectrally Resolved optical Imaging of Normal and Cancerous Human Breast Tissues”, Proc. of Inter-Institute Workshop on In Vivo Optical Imaging, Amir H. Gandjbakhche, ed., NIH (2000).

# BIBLIOGRAPHY

## CHAPTER 1


1. L. Wang, P. P. Ho, C. Liu, G. Zhang, and R. R. Alfano, “Ballistic 2-D Imaging Through Scattering Walls Using an Ultrafast Optical Kerr Gate”, Science **253** 769, (1991)
2. R. R. Alfano and Britton Chance, chairs/editors, “Optical Tomography, Photon Migration, and Spectroscopy of Tissue and Model Media: Theory, Human Studies, and Instrumentation”, Progress in Biomedical Optics, SPIE vol. **2389** Parts 1&2, February (1995).
3. I. D. Campbell and R. A. Dwek, “Biological Spectroscopy”, Benjamin/Cummins Publishing Co. Inc. California (1984).
4. A. Ishimaru, “Wave Propagation and Scattering in Random Media”, Academic, New York, 1978).
5. S. Udenfriend, “Fluorescence Assay in Biology and Medicine”, New York Academic, **1**, (1962), **2**, (1963).
6. B. B. Das, Feng Liu and R. R. Alfano, “Time-resolved fluorescence and photon migration studies in biomedical and model random media”, Rep. Prog. Phys. **60**, 227-292, (1997)
7. R. R. Alfano, S. K. Gayen, A. Katz, “Advances in Mediphotonic Imaging and Biopsy”, IS&T/OSA Optics & Imaging in the Information Age, 299 (1997).
8. Nelson A. Logan, “Survey of some early studies of the scattering of plane waves by a sphere, Selected papers on light scattering”, Milton Kerker, editor, pp.3-15(1988).

9. L. Rayleigh, "On the scattering of light by small particles", Phil. Mag. **41**, 447 (1871).
10. M. I. Mishchenko, L. D. Travis, and A. A. Lacis, “Scattering, Absorption, and Emission of light by Small Particles”, Cambridge University Press, UK, (2002).
11. G. Mie, "Beitzrâge zur optik truber Medien, speziell kolloidaler Metalolsungen," Ann. Phys. **25**, 377 (1908).
12. H. C. van de Hulst, “Light scattering by small particles”, Dover, New York, (1981).
13. J. A. Stratton, “Electromagnetic Theory”, McGraw-Hill, New York, (1941).
14. F. Bohren, D. R. Huffmann, “Absorption and scattering of light by small particles”, Wiley-Innterscience, New York, (1983).
15. S. A. Prahl. “Light Transport in Tissue”. PhD thesis, University of Texas at Austin, (1988).
16. S. A. Prahl, M. J. C. van Gemert, and A. J. Welch, “Determining the optical properties of turbid media by using the adding-doubling method”. Appl. Opt., **32**:559-568, (1993).
17. J. W. Pickering, C. J. M. Moes, H. J. C. M. Sterenborg, S. A. Prahl, and M. J. C. van Gemert. “Two integrating spheres with an intervening scattering sample”, J. Opt. Soc. Am. A, **9**:621-631, (1992).
18. W. F. Cheong, S. A. Prahl, and A. J. Welch. “A review of the optical properties of biological tissues”, IEEE J. Quantum Electron., **26**:2166-2185, (1990).

19. M. Kerker, “The scattering of light and other electromagnetic radiation”, Academic, New York, (1969).
20. S. Chandrasekhar, “Radiative Transfer”, Clarendon, Oxford, (1950).
21. A. Ishimaru, “Diffusion of light in turbid material", Appl. Opt. **28**, 2210 (1989).
22. S. L. Jacques, C. A. Alter, S. A. Prahl, "Angular dependence of HeNe laser light scattering by human dermis," Lasers Life Sci.,**1**, 309-333 (1987).
23. L. G. Henyey, J. L. Greenstein, “Diffuse radiation in the galaxy”, Astrophysical Journal, **93**, 70 (1941).
24. M. Lax, V. Narayanamurti, and R. C. Fulton, “Classical diffusive photon transport in a slab”, in Proc. Symp. on Laser Optics and Condensed Matter, Leningrad, June 1987, edited by J. L. Birman and H. Z. Cummins (Plenum, New York).
25. W. Cai, M. Lax, and R. R. Alfano, “Analytical solution of the polarized photon transport equation in an infinite uniform medium using cumulant expansion”, Phys. Rev. E **61**, 3871 (2000).
26. J. Crank, “The mathematics of diffusion”, Clarendon Press, Oxford, (1956)
27. M. Xu, W. Cai, M. Lax, and R. R. Alfano, "A photon transport forward model for imaging in turbid media," Opt. Lett. **26**, 1066-1068 (2001).
28. B. B. Das, “Time-resolved light scattering and fluorescence spectroscopy in biomedical and model random media”, PhD thesis, City University of New York (1993).

29. M. Xu, “Optical image reconstruction in highly scattering media”, PhD thesis, City University of New York (2001).
30. W. Cai, M. Xu, M. Lax, and R. R. Alfano, “Diffusion coefficient depends on time, not on absorption”, Opt. Lett. **27**, 731 (2002).
31. R. Garg, R. K. Prud’homme, A. Aksay, F. Liu, and R. R. Alfano, “Optical transmission in highly concentrated dispersions”, J. Opt. Soc. Am. A **15**, 932 (1998).
32. R. Garg, R. K. Prud’homme, A. Aksay, F. Liu, and R. R. Alfano, “Absorption length for photon propagation in highly dense colloidal dispersions”, J. Mater. Res. **13**, 3463 (1998).
33. K. M. Yoo, F. Liu, and R. R. Alfano, “When does the diffusion approximation fail to describe photon transport in random media?”, Phys. Rev. Lett. **64**, 2647 (1990).
34. W. Cai, M. Xu, and R. R. Alfano, ” Analytical form of the particle distribution based on the cumulant solution of the elastic Boltzmann transport equation” Phys. Rev. E **71**, 041202 (2005).
35. R. R. Alfano Guest Editor, “Advances in Optical Breast Imaging,” Technology in Cancer Research and Treatment **4** (2005, special issue).
36. S. K. Gayen, M. E. Zevallos, M. Alrubaiee, and R. R. Alfano, “Near-infrared laser spectroscopic imaging: a step towards diagnostic optical imaging of human tissues,” Laser Life Sci. **8**, 187-198, (1999).
37. William R. Hendee and E. Russell Ritenour,” Medical Imaging Physics “,Wiley-Liss; 4$^{th}$ edition (2002)

38. Chance, B. “Near infrared images using continuous, phase modulated and pulsed light with qantitation of blood and oxygenation”. Ann. New Acad. Sci. **838**:29-45. (1997)
39. Cutler M. “Transillumination as an aid in the diagnosis of breast lesions”. Surg Gynecol Obstet;**48**:721–729, (1929)
40. R. R. Alfano, S. G. Demos, S. K. Gayen “Advances in Optical Imaging of Biomedical Media”, Annals of the New York Academy of Sciences **248**, 820, (1997).
41. J. C. Hebden, S. R. Arridge and D. T. Delpy, "Optical imaging in medicine I: experimental techniques," Physics in Medicine and Biology, **42**, 825-840. (1997).
42. S. R. Arridge and J. C. Hebden, "Optical imaging in medicine II: modeling and reconstruction," Physics in Medicine and Biology, **42**, 841-854. (1997).
43. S. K. Gayen and R. R. Alfano, "Emerging optical biomedical imaging techniques," Opt. Photon. News **7**, 17-22 (1996).
44. S. R. Arridge, "Optical tomography in medical imaging," Inverse Probl. **15**, R41-R93 (1999).
45. W. Cai, S. K. Gayen, M. Xu, M. Zevallos, M. Alrubaiee, M. Lax, R. R. Alfano “Optical tomographic image reconstruction from ultrafast time-sliced transmission measurements,” Appl. Opt. **38**, 4237-4246 (1999).
46. A. P. Gibson, J. C. Hebden, and S. R. Arridge, "Recent advances in diffuse optical imaging," Physics in Medicine and Biology, **50**, R1-R43. (2005).

47. Li, X.D., T. Durduran, A.G. Yodh, B. Chance and D.N. Pattanayak, “Diffraction tomography for biochemical imaging with diffuse-photon density waves”. Optics Lett. **22**:573-575. (1997)
48. Arridge, S.R., Schweiger, M., Hiraoka, M., Delpy, D.T., "A Finite Element approach to modeling photon transport in tissue", Medical Physics, **20(2)**, 299-309. (1993)
49. Schweiger, M., Arridge, S.R., Delpy, D.T., "Application of the Finite Element Method for the forward and inverse problem in optical tomography", Journal of Mathematical Imaging and Vision, **3(3)**, 263-283, (1993).
50. http://health.nih.gov/
51. http://www.nci.nih.gov/
52. http://www.cancer.org/docroot/home/index.asp

## CHAPTER 2

1. Cutler, M., “Transillumination as an aid in the diagnosis of breast lesion”, Surg. Gynecol. Obstet. **48**, 721-730 (1929).
2. For a brief review of different optical imaging techniques for biomedical applications see, Gayen, S. K., and Alfano, R. R. “Emerging optical biomedical imaging techniques”. Opt. Photon. News **7(3)**, 17-22 (1996) and references therein.
3. Alfano, R. R., Gayen, S. K., and Zevallos, M. E. “Spectroscopic and time-resolved optical methods and apparatus for imaging objects in turbid media”. U. S. Patent Number: 6,665,557 B1 awarded December 16, 2003.

4. Patterson, M. S., Chance, B., and Wilson, B. C. “Time-resolved reflectance and transmittance for the noninvasive measurement of tissue optical properties”. Appl. Opt. **28**, 2331-2336 (1989).
5. Yoo, K. M. and Alfano, R. R. “Time-resolved coherent and incoherent components of forward light scattering in random media”. Opt. Lett. **15**, 320 – 322 (1990).
6. Wang, L., Ho, P. P., Liu, C., Zhang, G., and Alfano, R. R. “Ballistic 2D imaging through scattering wall using an ultrafast Kerr gate”. Science **253**, 769-771 (1991).
7. O’Leary M. A., Boas, D.A., Chance, B., and Yodh, A. G. “Experimental images of heterogeneous turbid media by frequency-domain diffusing-photon tomography”. Opt. Lett. **20**, 426-428 (1995).
8. Hebden, J. C., Arridge, S. R. and Deply, D. T. “Optical imaging in medicine: I. Experimental Techniques”. Phys. Med. Biol. **42**, 825-840 (1997).
9. Arridge, S. R., and Hebden, J. C. “Optical imaging in medicine: II. Modeling and reconstruction”. Phys. Med. Biol. **42**, 841-853 (1997).
10. Arridge, S. R. “Optical tomography in medical imaging”. Inverse Probl. **15**, R41–R93 (1999).
11. Cai, W., Das, B. B., Liu, F., Zevallos, M., Lax, M., and. Alfano, R. R. “Time-resolved optical diffusion tomographic image reconstruction in highly scattering turbid media”. Proc. Natl. Acad. Sci. USA **93**, 13561-13563 (1996).

12. Cai, W., Gayen, S. K., Xu, M., Zevallos, M., Alrubaiee, M., Lax, M., and Alfano, R. R. "Optical tomographic image reconstruction from ultrafast time-sliced transmission measurements," Appl. Opt. **38**, 4237-4246 (1999).
13. Markel, V. A., Schotland, J. C. "Scanning paraxial optical tomography". Opt. Lett. **27**, 1123 – 1125 (2002).
14. Ntziachristos, V., Yodh, A., Schnall, M., and Chance, B. "MRI-guided diffuse optical spectroscopy of malignant and benign breast lesions". Neoplasia **4**, 347-354 (2002).
15. Grosenick, D., Moesta, K.T., Wabnitz, H., Mucke, J., Stroszczynski, C., Macdonald, R., Schlag, P. M., and Rinneberg. H. "Time-domain optical mammography: Initial clinical results on detection and characterization of breast tumors". Appl. Opt. **42**, 3170-3186, (2003).
16. Dehgani, H., Pouge, B. W., Poplack, S. P., Paulsen, K. D. "Multiwavelength three-dimensional near-infrared tomography of the breast: initial simulation, phantom, and clinical results". Appl. Opt. **42**, 135-145 (2003).
17. Colak, S. B., van der Mark, M. B., 't Hooft, G. W., Hoogenraad, J. H., van der Linden, E. S., and Kuijpers, F. A."Clinical optical tomography and NIR spectroscopy for breast cancer detection". IEEE J. Select. Topics Quantum Electron. **5**, 1143-1158 (1999).
18. Taroni, P., Danesini, G., Torricelli, A., Pifferi, A., Spinelli, L., Cubeddu, R. "Clinical trial of time-resolved scanning optical mammography at 4 wavelengths between 683 and 975 nm". J. Biomed. Opt. **9**, 464-473 (2004).

19. Franceschini, M. A., Moesta, K. T., Fantini, S., Gaida, G., Gratton, E., Jess, H., Mantulin, W. W., Seeber, M., Schlag, P. M., and Kaschke, M. "Frequency-domain techniques enhance optical mammography: initial clinical results". Proc. Natl. Acad. Sci. USA **94**, 6468-6473 (1997).
20. Cheng, X., Mao, J. M., Bush, R., Kopans, D. B., Moore, R. H., Chorlton, M. "Breast cancer detection by mapping hemoglobin concentration and oxygen saturation". Appl. Opt. **42**, 6412-6421 (2003).
21. Webb, S. "The Physics of Medical Imaging". Bristol: Institute of Physics Publishing (1988).
22. Gayen, S. K., Alrubaiee, M., Zevallos, M. E., and Alfano, R. R. "Temporally and spectrally resolved optical imaging of normal and cancerous human breast tissues". Proceedings of Inter-Institute Workshop on In Vivo Optical Imaging at the NIH, Amir H. Gandjebakhche, ed. (Optical Society of America, Washington, DC, 2000), pp. 142-147.
23. Gayen, S. K., Alrubaiee, M., Savage, H.E., Schantz, S. P., and Alfano, R. R. "Parotid gland tissues investigated by picosecond time-gated and optical spectroscopic imaging techniques". IEEE J. Select. Top. Quantum Electron. **7**, 906-911 (2001).
24. Schmidt, F. E. W., Fry, M. E., Hillman, E. M. C., Hebden, J. C., and Deply, D. T. "A 32-channel time-resolved instrument for medical optical tomography". Rev. Sci. Instrum. **71**, 256-265 (2000).

25. Gayen, S. K., Zevallos, M. E., Alrubaiee, M., and Alfano, R. R. “Near-infrared laser spectroscopic imaging: a step towards diagnostic optical imaging of human tissues”. Laser Life Sci. **8**, 187-198 (1999).
26. Gayen, S. K. and Alfano, R. R. “Sensing lesions in tissues with light”. Opt. Express **4**, 475-480 (1999).
27. Fu, Q, Seier, F., Gayen S. K., and Alfano, R. R. “High-average-power kilohertz-repetition-rate sub-100 fs Ti:sapphire amplifier system”. Opt. Lett. **22**, 712-714 (1997).
28. Dolne, J. J., Yoo, K. M., Liu, F., and Alfano, R. R. “IR Fourier space gate and absorption imaging through random media”. Laser Life Sci. **6**, 131-141 (1994).
29. Ntziachristos, V., Yodh, A., Schnall, M., and Chance, B. “Concurrent MRI and diffuse optical tomography of breast after indocyanine green enhancement”. PNAS **97**, 2767-2772 (2000).
30. Merritt S, Bevilacqua, F., Durkin, A. J., Cuccia, D. J., Lanning, R., Tromberg, B. J., Gulsen, G., Yu, H., Wang, J., Nalcioglu, O. “Coregistration of diffuse optical spectroscopy and magnetic resonance imaging in arat tumor model”. Appl. Opt. **42**, 2951-2959 (2003).
31. Bremer, C., Ntziachristos, V., Weitkamp, B, Theilmeier, G., Heindel, W., Weissleder, R. “Optical imaging of spontaneous breast tumors using protease sensing ‘smart’ optical probes”. Investigative Radiology **40**, 321-327 (2005).
32. For details on the MR experimental arrangement, see Koutcher, Jason A., Motwani, M., Zakian, Kristen L., Li, Xiao-Kui, Matei, C., Dyke, Jonathan P.,

Ballon, D., He Yoo H., and Schwartz, Gary K. "The *in vivo* effect of bryostatin-1 on paclitaxel-induced tumor growth, mitotic entry, and blood flow". Clin. Cancer Res. **6**, 1498-1507 (2000).

33. Marks, F. A. "Optical determination of the hemoglobin oxygenation state of breast biopsies and human breast cancer xenografts in nude mice". SPIE **1641**, 227-237 (1992).
34. A 5-point smoothed average of intensity values around pixel #110 was used to reduce the effect of noise in determining the ratio.
35. Perelman, L. T., Backman, V., Wallace, M., Zonios, G., Manoharan, R., Nusrat, A., Shields, S., Seiler, M., Lima, C., Hamano, T., Itzkan, I., Van Dam, J., Crawford, J. M., and Feld, M. S. "Observation of periodic fine structure in reflectance from biological tissue: a new technique for measuring nuclear size distribution". Phys. Rev. Lett. **80**, 627-630 (1998).
36. Backman, V., Gurjar, R., Badizadegan, K., Itzkan, I., Dasari, R. R., Perelman, L. T., and Feld, M. S. Polarized light scattering spectroscopy for quantitative measurement of epithelial cellular structures *in situ*. IEEE J. Select. Top. Quantum Electron. **5**, 1019-1026 (1999).
37. Jakubowski, D. B., Cerussi, A. E., Bevilacqua, F., Shah, N., Hsiang, D., Butler, J., and Tromberg, B. J. "Monitoring neoadjuvant chemotherapy in breast cancer using quantitative diffuse optical spectroscopy: a case study". J. Biomed. Opt. **9**, 230-238 (2004).
38. Osborne, B. G., Fearn T., P. H. Hindle. "Near Infrared Spectroscopy in Food Analysis". 2nd Edition, Longman Group UK Limited, 1993, pp. 13-33.

39. Yoo, K. M., Liu, F., and Alfano, R. R. “Imaging through a scattering wall using absorption”. Opt. Lett. **16**, 1068 – 1070 (1991).

40. Ralph Weissleder, “A clearer vision for in vivo imaging, Nature Biotechnology” **19**, 316 - 317 (2001).

41. Ntziachristos, V., Yodh, A. G., Schnall, Mitchell, Chance, “Concurrent MRI and diffuse optical tomography of breast after indocyanine green enhancement” Proc. Natl. Acad. Sci. USA 97, 2767–2772 (2000).

42. Kristen L Murphy, and Jeffrey M Rosen, “Mutant p53 and genomic instability in a transgenic mouse model of breast cancer”, Oncogene **19**, 1045-1051, (2000)

**CHAPTER 3**

1. G. Muller, R. R. Alfano, S. R. Arridge, J. Beuthan, E. Gratton, M. Kaschke, B. R. Masters, S. Svanberg, and P. van der Zee, eds., “Medical Optical Tomography: Functional Imaging and Monitoring”, Vol. **IS11** of SPIE Institute Series (SPIE, Bellingham, Wash., 1993).

2. A. Yodh and B. Chance, "Spectroscopy and imaging with diffusing light," Phys. Today **48**, 38-40 (1995).

3. M. A. O'Leary, D. A. Boas, B. Chance, and A. G. Yodh, "Experimental images of heterogeneous turbid media by frequency-domain diffusing-photon tomography," Opt. Lett. **20**, 426-428 (1995).

4. S. K. Gayen and R. R. Alfano, "Emerging optical biomedical imaging techniques," Opt. Photon. News **7**, 17-22 (1996).

5. J. C. Hebden, S. R. Arridge, and D. T. Delpy, "Optical imaging in medicine: I. Experimental techniques," Phys. Med. Biol. **42**, 825-840 (1997).
6. S. R. Arridge and J. C. Hebden, "Optical imaging in medicine: II. Modeling and reconstruction," Phys. Med. Biol. **42**, 841-853 (1997).
7. W. Cai, S. K. Gayen, M. Xu, M. Zevallos, M. Alrubaiee, M. Lax, and R. R. Alfano, "Optical tomographic image reconstruction from ultrafast time-sliced transmission measurements," Appl. Opt. **38**, 4237-4246 (1999).
8. S. R. Arridge, "Optical tomography in medical imaging," Inverse Probl. **15**, R41-R93 (1999).
9. D. Grosenick, H. Wabnitz, H. H. Rinneberg, K. T. Moesta, and P. M. Schlag, "Development of a time-domain optical mammograph and first in vivo applications," Appl. Opt. **38**, 2927-2943 (1999).
10. V. Chernomordik, D. Hattery, A. H. Gandjbakhche, A. Pifferi, P. Taroni, A. Torricelli, G. Valentini, and R. Cubeddu, "Quantification by random walk of the optical parameters of nonlocalized abnormalities embedded within tissuelike phantoms," Opt. Lett. **25**, 951-953 (2000).
11. V. A. Markel and J. C. Schotland, "Inverse scattering for the diffusion equation with general boundary conditions," Phys. Rev. E **64**, 035601 (2001).
12. A. H. Hielscher and S. Bartel, "Use of penalty terms in gradient-based iterative reconstruction schemes for optical tomography," J. Biomed. Opt. **6**, 183-192 (2001).
13. M. Xu, M. Lax, and R. R. Alfano, "Time-resolved Fourier optical diffuse tomography," J. Opt. Soc. Am. A **18**, 1535-1542 (2001).

14. B. A. Brooksby, H. Dehghani, B. W. Pogue, and K. D. Paulsen, "Near-infrared (NIR) tomography breast image reconstruction with a priori structural information from MRI: algorithm development for reconstructing heterogeneities," IEEE J. Sel. Top. Quantum Electron. **9**, 199-209 (2003).
15. H. Dehghani, B. W. Pogue, S. P. Poplack, and K. D. Paulsen, "Multiwavelength three-dimensional near-infrared tomography of the breast: initial simulation, phantom, and clinical results," Appl. Opt. **42**, 135-145 (2003).
16. J. C. Hebden, D. A. Boas, J. S. George, and A. J. Durkin, "Topics in biomedical optics: introduction," Appl. Opt. **42**, 2869-3329 (2003).
17. W. Cai, M. Xu, and R. R. Alfano, "Three dimensional radiative transfer tomography for turbid media," IEEE J. Sel. Top. Quantum Electron. **9**, 189-198 (2003).
18. L. Wang, P. P. Ho, C. Liu, G. Zhang, and R. R. Alfano, "Ballistic 2-D imaging through scattering walls using an ultrafast optical Kerr gate," Science **253**, 769-771 (1991).
19. R. R. Alfano, X. Liang, L. Wang, and P. Ho, "Time-resolved imaging of translucent droplets in highly scattering media," Science **264**, 1913-1914 (1994).
20. W. Cai, M. Lax, and R. R. Alfano, "Analytical solution of the elastic Boltzmann transport equation in an infinite uniform medium using cumulant expansion," J. Phys. Chem. B **104,** 3996-4000 (2000).

21. W. Cai, M. Lax, and R. R. Alfano, "Analytical solution of the polarized photon transport equation in an infinite uniform medium using cumulant expansion," Phys. Rev. E **63**, 016606 (2000).
22. M. Xu, W. Cai, M. Lax, and R. R. Alfano, "Photon migration in turbid media using a cumulant approximation to radiative transfer," Phys. Rev. E **65**, 066609 (2002).
23. F. Natterer, “The Mathematics of Computerized Tomography” Wiley, New York, (1986).
24. A. H. Gandjbakhche, G. H. Weiss, R. F. Bonner, and R. Nossal, "Photon path-length distributions for transmission through optically turbid slabs," Phys. Rev. E **48**, 810-818 (1993).
25. A. H. Gandjbakhche, V. Chernomordik, J. C. Hebden, and R. Nossal, "Time-dependent contrast functions for quantitative imaging in time-resolved transillumination experiments," Appl. Opt. **37**, 1973-1981 (1998).
26. P. Comon, "Independent component analysis - a new concept?" Signal Process. **36**, 287-314 (1994).
27. A. J. Bell, "Information theory, independent component analysis, and applications," in Unsupervised Adaptive Filtering, Vol. **I**, S. Haykin, pp. 237-264. ed. Wiley, New York, (2000).
28. D. Nuzillard and J.-M. Nuzillard, "Application of blind source separation to 1-D and 2-D nuclear magnetic resonance spectroscopy," IEEE Signal Process. Lett. **5**, 209-211 (1998).

29. R. Vigário, J. Särelä, V. Jousmäki, M. Hämäläinen, and E. Oja, "Independent component approach to the analysis of EEG and MEG recordings," IEEE Trans. Biomed. Eng. **47**, 589-593 (2000).
30. A. Hyvärinen, J. Karhunen, and E. Oja, “Independent Component Analysis” Wiley, New York, (2001).
31. P. M. Morse and H. Feshbach, “Methods of Theoretical Physics” McGraw-Hill, New York, (1953), Vols. **I** and **II**.
32. M. Xu, W. Cai, M. Lax, and R. R. Alfano, "A photon transport forward model for imaging in turbid media," Opt. Lett. **26**, 1066-1068 (2001).
33. S. Chandrasekhar, “Radiative Transfer” Dover, New York, (1960).
34. M. Lax, V. Nayaramamurti, and R. C. Fulton, "Classical diffusion photon transport in a slab," in Laser Optics of Condensed Matter, J. L. Birman, H. Z. Cummins, and A. A. Kaplyanskii, eds. (Plenum, New York, 1987), pp. 229-237.
35. J. X. Zhu, D. J. Pine, and D. A. Weitz, "Internal reflection of diffusive light in random media," Phys. Rev. A **44**, 3948-3959 (1991).
36. R. C. Haskell, L. O. Svaasand, T.-T. Tsay, T.-C. Feng, M. S. McAdams, and B. J. Tromber, "Boundary conditions for the diffusion equation in radiative transfer," J. Opt. Soc. Am. A **11**, 2727-2741 (1994).
37. S. Roberts and R. Everson, eds., “Independent Component Analysis: Principles and Practice” Cambridge U. Press, Cambridge, UK, (2001).
38. J.-F. Cardoso, "Blind signal separation: statistical principles," Proc. IEEE **86**, 2009-2025 (1998).

39. M. V. Klein, “Optics” Wiley, New York, (1970).

40. H. Heusmann, J. Kölzer, and G. Mitic, "Characterization of female breasts in vivo by time resolved and spectroscopic measurements in near infrared spectroscopy," J. Biomed. Opt. **1**, 425-434 (1996).

41. H. J. van Staveren, C. J. M. Moes, J. van Marle, S. A. Prahl, and M. J. C. van Gemert, "Light scattering in intralipid-10% in the wavelength range of 400-1100 nm," Appl. Opt. **30**, 4507-4514 (1991).

42. D. J. Hall, J. C. Hebden, and D. T. Delpy, "Imaging very-low-contrast objects in breastlike scattering media with a time-resolved method," Appl. Opt. **36**, 7270-7276 (1997).

43. Q. Fu, F. Seier, S. K. Gayen, and R. R. Alfano, "High-average-power kilohertz-repetition-rate sub-100-fs Ti:sapphire amplifier system," Opt. Lett. **22**, 712-714 (1997).

## CHAPTER 4

1. B. Chance and R. R. Alfano, eds., “Optical Tomography and Spectroscopy of Tissue: Theory, Instrumentation, Model, and Human Studies”, SPIE Proc. **2979**, The International Society for Optical Engineering, Bellingham, WA, (1997).

2. R. R. Alfano and J. G. Fujimoto, eds., “Advances in Optical Imaging and Photon Migrations, OSA Trends in Optics and Photonics Series”, vol. **2**, Optical Society of America, Washington, DC, (1996).

3. B. Chance and R. R. Alfano, eds., “Optical Tomography Photon Migration and Spectroscopy of Tissue and Model Media: Theory, Human Studies, and Instrumentation”, SPIE Proc. **2389**, Part 1 and 2, The International Society for Optical Engineering, Bellingham, WA, (1995).
4. A. Yodh , B. Chance, “Spectroscopy and Imaging with diffusing light”, Physics Today **48**, pp. 34-40, (1995).
5. G. Müller, B. Chance, R. Alfano, S. Arridge, J. Beuthan, E. Gratton, M. Kaschke, B. Masters, S. Svanberg, P. van der Zee, “Medical Optical Tomography: Functional Imaging and Monitoring”, SPIE Institutes for Advanced Optical Technologies Series, vol. IS11, Bellingham, WA, (1993).
6. William R. Hendee and E. Russell Ritenour, ”Medical Imaging Physics“ Wiley-Liss; 4th edition (2002)
7. A. Parker, “Image Reconstruction in Radiology”, Boca Rato, FL: CRC Press, 1990.
8. D. A. Benaron, D. C. Ho, S. Spilman, J. P. van Houten, and D. K. Stevenson, "Non-recursive linear algorithms for optical imaging in diffusive media," Advances in Experimental Medicine & Biology: Oxygen Transport to Tissue **XVI**, Plenum Press, New York, pp. 215-222, (1994).
9. S. A. Walker, S. Fantini, and E. Gratton, "Image reconstruction by back-projection from frequency domain optical measurements in highly scattering media," Appl. Opt,**36**, pp. 170-179, (1997).
10. S. B. Colak, D. G. Papaioannou, G. W. 't Hooft, M. B. van der Mark, H. Schomberg, J. C. J. Paasschens, J. B. M. Melissen, and N. A. A. J. van Asten,

"Tomographic image reconstruction from optical projections in light-diffusing media," Appl. Opt. **36**, pp. 180-213, 1997.

11. W. Cai, S. K. Gayen, M. Xu, M. Zevallos, M. Alrubaiee, M. Lax, R. R. Alfano “Optical tomographic image reconstruction from ultrafast time-sliced transmission measurements,” Appl. Opt. **38**, 4237-4246 (1999).
12. Y. Q. Yao, Y. Wang, Y. L. Pei, W. W. Zhu, and R. L. Barbour, " Frequency-domain optical imaging of absorption and scattering distributions by Born iterative method," Journal of the Optical Society of America A, **14**, pp. 325-342, (1997).
13. K. D. Paulsen and H. Jiang, "Spatially varying optical property reconstruction using a finite element diffusion equation approximation," Med. Phys.. **22**, pp. 691-701, (1995).
14. H. Jiang, K.D. Paulsen, and U.L. Österberg, "Optical image reconstruction using DC data: simulations and experiments," Phys. Med. Biol., **41**, pp.1483-1498, (1996).
15. H. Jiang, K. D. Paulsen, U. L. Österberg, B. W. Pogue, M. S. Patterson, "Simultaneous reconstruction of optical absorption and scattering maps in turbid media from near-infrared frequency-domain data," Opt. Lett., **20**, pp. 2128-2130, (1995).
16. D. Y. Paithankar, A. U. Chen, B. W. Pogue, M. S. Patterson, and E. M. Sevick-Muraca, "Imaging of fluorescent yield and lifetime from multiply scattered light reemitted from random media," Appl. Opt., **36**, pp. 2260-2272, (1997).

17. T. R. Lucas, M. V. Klibanov, and R .M. Frank, "Imaging experimental data from optical tomography by the elliptic system method in Computational, Experimental, and Numerical Methods for Solving Ill-Posed Inverse Imaging Problems: Medical and Nonmedical Applications", R.L. Barbour, M.J. Carvlin, and M.A. Fiddy, eds., Proc. SPIE, **3171**, pp. 22-33, (1997) .
18. M. Xu, M. Alrubaiee, S. K. Gayen, and R. R. Alfano, "Three-dimensional localization and optical imaging of objects in turbid media with independent component analysis", Appl. Opt. **44**, 1889 (2005)
19. M. Xu, M. Alrubaiee, S. K. Gayen, and R. R. Alfano, "Optical imaging of turbid media using independent component analysis: theory and simulation", J. Biomed. Opt. **10**, 051705 (2005).
20. M. Alrubaiee, M. Xu, S. K. Gayen, M. Brito, and R. R. Alfano, "Three-dimensional optical tomographic imaging of scattering objects in tissue-simulating turbid media using independent component analysis", Appl. Phys. Lett. **87**, 191112 (2005)
21. M. Alrubaiee, M. Xu, S. K. Gayen, and R. R. Alfano, "Localization and cross section reconstruction of fluorescent targets in ex vivo breast tissue using independent component analysis", Appl. Phys. Lett. **89**, 133902 (2006)
22. P. Comon, "Independent component analysis—a new concept?" Signal Process. **36**, 287–314 (1994).
23. A.J. Bell, "Information theory, independent component analysis, and applications," in Unsupervised Adaptive Filtering, Vol. **I**, S. Haykin, Ed., pp. 237–264, Wiley, New York (2000).

24. A. Hyvärinen, J. Karhunen, and E. Oja, “Independent Component Analysis”, Wiley, New York (2001).
25. J.-F. Cardoso, "Blind signal separation: statistical principles," Proc. IEEE **86**, 2009–2025 (1998).
26. A. Hyvärinen and E. Oja, "Independent component analysis: algorithms and applications," Neural Networks **13**, 411–430 (2000).
27. S. Chandrasekhar, “Radiative Transfer”, Dover, New York (1960).
28. S. R. Arridge and J. C. Hebden, "Optical imaging in medicine: II. Modeling and reconstruction," Phys. Med. Biol. **42**, 841–853 (1997),
29. S. R. Arridge, "Optical tomography in medical imaging," Inverse Probl. **15**, R41–R93 (1999).
30. W. Cai, M. Lax, and R. R. Alfano, "Analytical solution of the elastic Boltzmann transport equation in an infinite uniform medium using cumulant expansion," J. Phys. Chem. B **104**, 3996–4000 (2000).
31. M. Xu, W. Cai, M. Lax, and R. R. Alfano, "Photon migration in turbid media using a cumulant approximation to radiative transfer," Phys. Rev. E **65**, 066609 (2002).
32. M. Xu, W. Cai, M. Lax, and R. R. Alfano, "A photon transport forward model for imaging in turbid media," Opt. Lett. **26**, 1066–1068 (2001).
33. V. Chernomordik, D. Hattery, A. H. Gandjbakhche, A. Pifferi, P. Taroni, A. Torricelli, G. Valentini, and R. Cubeddu, "Quantification by random walk of the optical parameters of nonlocalized abnormalities embedded within tissuelike phantoms," Opt. Lett. **25**, 951–953 (2000).

34. A. H. Gandjbakhche, G. H. Weiss, R. F. Bonner, and R. Nossal, "Photon path-length distributions for transmission through optically turbid slabs," Phys. Rev. E **48**, 810–818 (1993).
35. W. Cai, M. Xu, and R. R. Alfano, "Three dimensional radiative transfer tomography for turbid media," IEEE J. Sel. Top. Quantum Electron. **9**, 189–198 (2003).
36. P.M. Morse and H. Feshbach, “Method of Theoretical Physics”, Vols. **I** and **II**, McGraw-Hill, New York (1953).
37. S. R. Arridge, "Photon-measurement density functions. Part I: Analytic forms," Appl. Opt. **34**, 7395–7409 (1995).
38. S. R. Arridge and M. Schweiger, "Photon-measurement density functions. Part 2: Finite-element-method calculations," Appl. Opt. **34**, 8026–8037 (1995).
39. A. H. Hielscher and S. Bartel, "Use of penalty terms in gradient-based iterative reconstruction schemes for optical tomography, "J. Biomed. Opt. 6, 183–192 (2001).
40. B. A. Brooksby, H. Dehghani, B. W. Pogue, and K. D. Paulsen, "Near-infrared (NIR) tomography breast image reconstruction with a priori structural information from MRI: algorithm development for reconstructing heterogeneities," IEEE J. Sel. Top. Quantum Electron. **9**, 199–209 (2003).
41. Topics in Biomedical Optics, J. C. Hebden, D. A. Boas, J. S. George, and A. J. Durkin, Eds., pp. 2869–3329, a special issue of Appl. Opt.**42** (2003).

42. M. Alrubaiee, S. K. Gayen, J. A. Koutcher, and R. R. Alfano, “Spectral and Temporal Near-Infrared Imaging of Ex Vivo Cancerous and Normal Human Breast Tissues,” Technology in Cancer Research and Treatment **4** (2005).
43. Deans, Stanley R. “The Radon Transform and Some of Its Applications”. New York: John Wiley & Sons. (1983).
44. Bracewell, R.N. "Numerical Transforms". Science **248**: 697-704. (1990)

**CHAPTER 5**

1. Keijzer, M., S.L. Jacques, S.A. Prahl, A.J. Welch:, “ Light distributions in artery tissue: Monte Carlo simulations for finite-diameter lasers beams”. *Lasers in Medicine and Surgery* **9**:148-154, 1989.
2. Prahl, S.A., M. Keijzer, S.L. Jacques, A.J. Welch: “A Monte Carlo model of light propagation in tissue”. In *Dosimetry of Laser Radiation in Medicine and Biology*, G. Mueller, D. Sliney, Eds., SPIE Series Vol. IS **5**:102-111, 1989.
3. Keijzer, M., R. Richards-Kortum, S.L. Jacques, M.S. Feld: “Fluorescence spectroscopy of turbid media: Autofluorescence of the human aorta”, Appl. Opt. **28**:4286-4292, (1989).
4. Jacques, S.L.: “Time-resolved propagation of ultra-short laser pulses within turbid tissues”. Appl. Opt. **28**:2223-2229, (1989).
5. Jacques, S.L.: “Time-resolved reflectance spectroscopy in turbid tissues”. Transactions IEEE on Biomedical Engineering **36**:1155-1161, (1989).
6. Wang, L-H, S.L. Jacques: “Hybrid model of Monte Carlo simulation and diffusion theory for light reflectance by turbid media”. J. Optical Soc. Am. A **10**:1746-1752, (1993).

7. Wang, L-H, S.L. Jacques: “Optimized radial and angular positions in Monte Carlo modeling”. Med. Phys. **21**:1081-1083, 1994.
8. Wang, L-H, S.L. Jacques, L-Q Zheng: “MCML - Monte Carlo modeling of photon transport in multi-layered tissues”. Computer Methods and Programs in Biomedicine **47**:131-146, 1995.
9. L.-H. Wang, S. L. Jacques, and L.-Q. Zheng: “CONV - Convolution for responses to a finite diameter photon beam incident on multi-layered tissues”, ***Computer Methods and Programs in Biomedicine*** **54:**141-150**,** (1997)**.**
10. S. L. Jacques and L.-H. Wang, "Monte Carlo modeling of light transport in tissues," in Optical Thermal Response of Laser Irradiated Tissue”, edited by A. J. Welch and M. J. C. van Gemert pp. 73-100, Plenum Press, New York, (1995).
11. S. L. Jacques, L.-H. Wang, and A. H. Hielscher, "Time-resolved photon propagation in tissues," in Optical Thermal Response of Laser Irradiated Tissue, edited by A. J. Welch and M. J. C. van Gemert, pp. 305-332, Plenum Press, New York, (1995).
12. G. L. Coté, S. Rastegar, and L.-H. Wang, "Introduction to Biomedical Optics and Lasers," in Introduction to Biomedical Engineering, J. Enderle, S. Blanchard, and J. Bronzino, eds. Academic Press, (1999).
13. L. G. Henyey and J. L. Greenstein, 'Diffuse radiation in the galaxy,' Astrophys. J. **93**, 70-83 (1941).
14. M. Xu, “Optical image reconstruction in highly scattering media”, PhD thesis, City University of New York (2001).

15. K. M. Yoo, F. Liu, and R. R. Alfano, “When does the diffusion approximation fail to describe photon transport in random media?” Phys. Rev. Lett. **64**, 2647 (1990).
16. W. Cai, M. Xu, and R. R. Alfano, ” Analytical form of the particle distribution based on the cumulant solution of the elastic Boltzmann transport equation” Phys. Rev. E **71**, 041202 (2005).
17. W. Cai, M. Lax, and R. R. Alfano, “Cumulant solution of the elastic Boltzmann transport equation in an infinite uniform medium “, Phys. Rev. E **61**, 3871 (2000).
18. W. Cai, M. Xu, M. Lax, and R. R. Alfano, “Diffusion coefficient depends on time, not on absorption”, Opt. Lett. **27**, 731 (2002).
19. Nelder, J. A. and Mead, R. "A Simplex Method for Function Minimization.” Comput. J. **7**, 308-313, (1965).
20. Lagarias, J. C.; Reeds, J. A.; Wright, M. H.; and Wright, P. E. "Convergence Properties of the Nelder-Mead Algorithm in Low Dimensions.” AT&T Bell Laboratories Tech. Rep. Murray Hill, NJ, (1995).